Universität Potsdam
Institut für Geowissenschaften
und
Helmholtz-Zentrum Potsdam
Deutsches GeoForschungsZentrum GFZ
Sektion 4.3 – Klimadynamik und Landschaftsentwicklung

Abrupt climate changes and extreme events in two different varved lake sediment records

Kumulative Dissertation

zur Erlangung des akademischen Grades
„doctor rerum naturalium“
(Dr. rer. nat.)
in der Wissenschaftsdisziplin „Paläoklimatologie“

eingereicht an der
Mathematisch-Naturwissenschaftlichen Fakultät
der Universität Potsdam

von
Daniela Müller

Potsdam, November 2021

Supervisor
apl. Prof. Dr. Achim Brauer
Universität Potsdam
Helmholtz-Zentrum Potsdam Deutsches GeoForschungsZentrum GFZ

Published online on the
Publication Server of the University of Potsdam:
https://doi.org/10.25932/publishup-55833
https://nbn-resolving.org/urn:nbn:de:kobv:517-opus4-558331

Erklärung

Hiermit erkläre ich gemäß §12 Abs. 1 Nr. 7 der Promotionsordnung der Mathematisch-Naturwissenschaftlichen Fakultät der Universität Potsdam vom 18. September 2013, dass ich die von mir vorgelegte Dissertation mit dem Titel

Abrupt climate changes and extreme events in two different varved lake sediment records

selbstständig angefertigt habe, die benutzten Quellen und Hilfsmittel vollständig angegeben und wörtliche und sinngemäße Zitate als solche gekennzeichnet habe, sowie Tabellen, Karten und Abbildungen, die anderen Werken in Wortlaut oder dem Sinn nach entnommen sind in jedem Einzelfall als Entlehnung gekennzeichnet habe. Des Weiteren erkläre ich, dass diese Dissertation noch bei keiner anderen Fakultät oder Hochschule vorgelegt wurde, dass sie, abgesehen von den unten angegebenen Teilpublikationen, noch nicht veröffentlicht worden ist und dass ich eine solche Veröffentlichung vor Abschluss des Promotionsverfahrens nicht vornehmen werde. Die Bestimmungen der Promotionsordnung sind mir bekannt.

Teilveröffentlichungen

- Bonk, A., Müller, D., Ramisch, A., Kramkowski, M. A., Noryśkiewicz, A. M., Sekudewicz, I., Gąsiorowski, M., Luberda-Durnaś, K., Słowiński, M., Schwab, M., Tjallingii, R., Brauer, A. & Błaszkiewicz, M. 2021: **Varve microfacies and chronology from a new sediment record of Lake Gościąż (Poland)**. Quaternary Science Reviews 251, 106715.
- Müller, D., Tjallingii, R., Płóciennik, M., Luoto, T. P., Kotrys, B., Plessen, B., Ramisch, A., Schwab, M. J., Błaszkiewicz, M., Słowiński, M. & Brauer, A. 2021: **New insights into lake responses to rapid climate change: the Younger Dryas in Lake Gościąż, central Poland**. Boreas 50, 535–555.

- Neugebauer, I., Müller, D., Schwab, M. J., Blockley, S., Lane, C. S., Wulf, S., Appelt, O. & Brauer, A. 2021: **Cryptotephras in the Lateglacial ICDP Dead Sea sediment record and their implications for chronology**. Boreas 50, 844-861.
- Müller, D., Neugebauer, I., Ben Dor, Y., Enzel, Y., Schwab, Markus J., Tjallingii, R., Brauer, A. Submitted: **Phases of stability during major hydroclimate change ending the Last Glacial in the Levant**. Initial submission to Nature Geoscience.

_____

Ort, Datum Unterschrift (Daniela Müller)

Abstract

Different lake systems might reflect different climate elements of climate changes, while the responses of lake systems are also divers, and are not completely understood so far. Therefore, a comparison of lakes in different climate zones, during the high-amplitude and abrupt climate fluctuations of the Last Glacial to Holocene transition provides an exceptional opportunity to investigate distinct natural lake system responses to different abrupt climate changes. The aim of this doctoral thesis was to reconstruct climatic and environmental fluctuations down to (sub-) annual resolution from two different lake systems during the Last Glacial-Interglacial transition (~17 and 11 ka). Lake Gościąż, situated in the temperate central Poland, developed in the Allerød after recession of the Last Glacial ice sheets. The Dead Sea is located in the Levant (eastern Mediterranean) within a steep gradient from sub-humid to hyper-arid climate, and formed in the mid-Miocene. Despite their differences in sedimentation processes, both lakes form annual laminations (varves), which are crucial for studies of abrupt climate fluctuations. This doctoral thesis was carried out within the DFG project PALEX-II (**Pal**eohydrology and **Ex**treme Floods from the Dead Sea ICDP Core) that investigates extreme hydro-meteorological events in the ICDP core in relation to climate changes, and ICLEA (Virtual Institute of **I**ntegrated **C**limate and **L**andscape **E**volution **A**nalyses) that intends to better the understanding of climate dynamics and landscape evolutions in north-central Europe since the Last Glacial. Further, it contributes to the Helmholtz Climate Initiative REKLIM (Regional Climate Change and Humans) Research Theme 3 “Extreme events across temporal and spatial scales” that investigates extreme events using climate data, paleo-records and model-based simulations. The three main aims were to (1) establish robust chronologies of the lakes, (2) investigate how major and abrupt climate changes affect the lake systems, and (3) to compare the responses of the two varved lakes to these hemispheric-scale climate changes.

Robust chronologies are a prerequisite for high-resolved climate and environmental reconstructions, as well as for archive comparisons. Thus, addressing the first aim, the novel chronology of Lake Gościąż was established by microscopic varve counting and Bayesian age-depth modelling in Bacon for a non-varved section, and was corroborated by independent age constrains from ^{137}Cs activity concentration measurements, AMS radiocarbon dating and pollen analysis. The varve chronology reaches from the late Allerød until AD 2015, revealing more Holocene varves than a previous study of Lake Gościąż suggested. Varve formation throughout the complete Younger Dryas (YD) even allowed the identification of annually- to decadal-resolved leads and lags in proxy responses at the YD transitions.

The lateglacial chronology of the Dead Sea (DS) was thus far mainly based on radiocarbon and U/Th-dating. In the unique ICDP core from the deep lake centre, continuous search for cryptotephra has been carried out in lateglacial sediments between two prominent gypsum deposits – the Upper and Additional Gypsum Units (UGU and AGU, respectively). Two cryptotephras were identified with glass analyses that correlate with tephra deposits from the Süphan and Nemrut volcanoes indicating that the AGU is ~1000 years younger than previously assumed, shifting it into the YD, and the underlying varved interval into the Bølling/Allerød, contradicting previous assumptions.

Using microfacies analyses, stable isotopes and temperature reconstructions, the second aim was achieved at Lake Gościąż. The YD lake system was dynamic, characterized by higher aquatic bioproductivity, more re-suspended material and less anoxia than during the Allerød and Early Holocene, mainly influenced by stronger water circulation and catchment erosion due to stronger westerly winds and less lake sheltering. Cooling at the YD onset was ~100 years longer than the final warming, while environmental proxies lagged the onset of cooling by ~90 years, but occurred contemporaneously during the termination of the YD. Chironomid-based temperature reconstructions support recent studies indicating mild YD summer temperatures. Such a comparison of annually-resolved proxy responses to both abrupt YD transitions is rare, because most European lake archives do not preserve varves during the YD.

To accomplish the second aim at the DS, microfacies analyses were performed between the UGU (~17 ka) and Holocene onset (~11 ka) in shallow- (Masada) and deep-water (ICDP core) environments. This time interval is marked by a huge but fluctuating lake level drop and therefore the complete transition into the Holocene is only recorded in the deep-basin ICDP core. In this thesis, this transition was investigated for the first time continuously and in detail. The final two pronounced lake level drops recorded by deposition of the UGU and AGU, were interrupted by one millennium of relative depositional stability and a positive water budget as recorded by aragonite varve deposition interrupted by only a few event layers. Further, intercalation of aragonite varves between the gypsum beds of the UGU and AGU shows that these generally dry intervals were also marked by decadal- to centennial-long rises in lake level. While continuous aragonite varves indicate decadal-long stable phases, the occurrence of thicker and more frequent event layers suggests general more instability during the gypsum units. These results suggest a pattern of complex and variable hydroclimate at different time scales during the Lateglacial at the DS.

The third aim was accomplished based on the individual studies above that jointly provide an integrated picture of different lake responses to different climate elements of hemispheric-scale abrupt climate changes during the Last Glacial-Interglacial transition. In general, climatically-driven facies changes are

more dramatic in the DS than at Lake Gościąż. Further, Lake Gościąż is characterized by continuous varve formation nearly throughout the complete profile, whereas the DS record is widely characterized by extreme event layers, hampering the establishment of a continuous varve chronology. The lateglacial sedimentation in Lake Gościąż is mainly influenced by westerly winds and minor by changes in catchment vegetation, whereas the DS is primarily influenced by changes in winter precipitation, which are caused by temperature variations in the Mediterranean. Interestingly, sedimentation in both archives is more stable during the Bølling/Allerød and more dynamic during the YD, even when sedimentation processes are different.

In summary, this doctoral thesis presents seasonally-resolved records from two lake archives during the Lateglacial (ca 17-11 ka) to investigate the impact of abrupt climate changes in different lake systems. New age constrains from the identification of volcanic glass shards in the lateglacial sediments of the DS allowed the first lithology-based interpretation of the YD in the DS record and its comparison to Lake Gościąż. This highlights the importance of the construction of a robust chronology, and provides a first step for synchronization of the DS with other eastern Mediterranean archives. Further, climate reconstructions from the lake sediments showed variability on different time scales in the different archives, i.e. decadal- to millennial fluctuations in the lateglacial DS, and even annual variations and sub-decadal leads and lags in proxy responses during the rapid YD transitions in Lake Gościąż. This showed the importance of a comparison of different lake archives to better understand the regional and local impacts of hemispheric-scale climate variability. An unprecedented example is demonstrated here of how different lake systems show different lake responses and also react to different climate elements of abrupt climate changes. This further highlights the importance of the understanding of the respective lake system for climate reconstructions.

Kurzfassung

Verschiedene Seesysteme können unterschiedliche Klimaelemente während Klimaveränderungen wiederspiegeln und auch diverse Seesystemreaktionen aufweisen, wobei letztere bislang noch nicht vollständig verstanden sind. Ein Vergleich von Seesystemen in verschiedenen Klimazonen während der hoch-amplituden und abrupten Klimaveränderung innerhalb des Übergangs vom Letzten Glazial zum Holozän, ermöglicht die Untersuchung deutlicher natürlicher Seesystemreaktionen in Bezug zu abrupten Klimaänderungen. Das Ziel dieser Doktorarbeit war die Rekonstruktion von Klima- und Umweltschwankungen von zwei verschiedenen Seesystemen während des Letzten Glazial-Interglazial-Übergangs (~17.000-11.000 BP) bis hinunter zu saisonaler Auflösung. Der Gościąż See liegt in der gemäßigten Klimazone in Zentralpolen und entwickelte sich im Allerød nach dem Rückgang der Eisschilde des letzten Glazials. Das Tote Meer liegt in der Levante (östlicher Mittelmeerraum) innerhalb eines steilen Gradienten von subhumidem zu hyperaridem Klima und entstand im mittleren Miozän. Trotz ihrer unterschiedlichen Sedimentationsprozesse bilden beide Seen jährliche Laminierungen (Warven) aus. Dies ist essentiell für Studien abrupter Klimaveränderungen. Diese Doktorarbeit wurde innerhalb des DFG-Projektes PALEX-II (Paläohydrologie und Sturzfluten vom ICDP-Kern des Toten Meeres) und ICELA (Virtuelles Institut zur Integrierten Klima- und Landschaftsentwicklungsanalyse) durchgeführt. PALEX-II untersucht hydrometeorologische Extremereignisse im ICDP-Kern in Bezug zu Klimaveränderungen, während ICLEA beabsichtig das Verständnis von Klimadynamiken und Landschaftsevolution in Nord- und Zentraleuropa seit dem letzten Glazial zu verbessern. Zudem, trägt diese Doktorarbeit auch zum Forschungsthema 3 „Extremevents auf unterschiedlichen zeitlichen und räumlichen Skalen“ der Helmholtz-Klimainitiative REKLIM (Regionale Klimaänderungen und Mensch) bei, das basierend auf Klimadaten, Paläoarchiven und modelbasierten Simulationen Extremevents untersucht.

Robuste Chronologien sind Voraussetzung für hochaufgelöste Klima- und Umweltstudien, sowie für den Vergleich von Archiven. Um das erste Ziel zu erreichen, wurde für den Gościąż See mithilfe von mikroskopischer Warvenzählung und einer bayesschen Alters-Tiefen-Modellierung eine neue Chronologie erstellt. Diese wurde durch unabhängige Altersinformationen von ^{137}Cs Konzentrationsmessungen, AMS Radiokarbondatierung und Pollenanalyse bestätigt. Die Warvenchronologie beginnt im späten Allerød und endet AD 2015. Sie offenbart mehr Warven im Holozän als in einer früheren Studie vom Gościąż See gezeigt wurde. Warvenbildung durch die gesamte Jüngere Dryaszeit (JD) hindurch ermöglicht sogar die Identifizierung von jährlich bis dekadisch aufgelösten Abfolgen in Proxyreaktion während der Übergangszonen der JD.

Die spätglaziale Chronologie des Toten Meeres basierte bisher auf Radiokarbon- und U/Th-Datierungen. In den spätglazialen Sedimenten des einzigartigen ICDP-Kern vom tiefen Seezentrum wurde zwischen zwei markanten Gipseinheiten – den Oberen und Zusätzlichen Gipseinheiten (UGU bzw. AGU) – kontinuierlich nach Kryptotephra gesucht. Gläser zweier Kryptotephren korrelieren mit Aschenablagerungen der Süphan und Nemrut Vulkane. Dies deutet darauf hin, dass die AGU ~1000 Jahre jünger ist als bisher angenommen, was sie komplett in die JD verlagert und das darunterliegende warvierte Intervall in das Bølling/Allerød. Diese Ergebnisse widersprechen bisherigen Annahmen.

Unter Verwendung von Mikrofaziesanalysen, stabiler Isotope und Temperaturrekonstruktionen, wurde das zweite Ziel am Gościąż See erreicht. Das Seesystem war während der JD dynamisch und durch höhere aquatische Bioproduktivität, Resuspension und geringere anoxische Bedingungen als das Allerød und frühe Holozän gekennzeichnet. Dies wurde hauptsächlich durch eine verstärkte Wasserzirkulation und Erosion im Einzugsgebiet hervorgerufen, die wiederum durch stärkere Westwinde und geringeren Schutz vor Wind im Einzugsgebiet verursacht wurden. Die Abkühlung am Beginn der JD war etwa 100 Jahre länger als die finale Erwärmung an ihrem Ende, während die Umweltproxies ca. 90 Jahre nach Beginn der Abkühlung, aber gleichzeitig mit der Erwärmung auftraten. Auf Chironomiden basierende Temperatur-rekonstruktionen unterstützen neueste Studien, die milde Sommertemperaturen während der JD anzeigen. Da die meisten europäischen Seearchive keine Warven während der JD erhalten, ist ein solcher Vergleich von jährlich aufgelösten Proxyreaktionen während beiden JD Übergangszonen sehr selten.

Um das zweite Ziel auch am Toten Meer zu realisieren, wurden Mikrofaziesanalysen zwischen der UGU (~17.000 BP) und dem Beginn des Holozäns (~11.000 BP) in Sedimenten aus dem Flachwasserbereich (Masada) und aus dem tiefen Becken (ICDP-Kern) durchgeführt. In diesem Intervall sinkt der Seespiegel gewaltig ab, wobei er von Schwankungen betroffen ist. Daher ist der komplette Übergang in das Holozän nur im ICDP-Kern enthalten, der im tiefen Becken gezogen wurde. In dieser Doktorarbeit wurde dieser Übergang zum ersten Mal kontinuierlich und im Detail untersucht. Während der beiden finalen Seespiegelabfälle wurden die UGU und AGU abgelagert. Zwischen den beiden Gipseinheiten zeugen jedoch Aragonitwarven und nur wenige Extremevents von sedimentärer Stabilität und einem positiven Wasserbudget für beinahe ein Jahrtausend. Selbst innerhalb der UGU und AGU deutet die Ablagerung von Aragonitwarven zwischen Gipslagen auf Dekaden bis Jahrhunderte andauernde Anstiege im Seespiegel hin, was zeigt, dass UGU und AGU nicht kontinuierlich von Trockenheit gekennzeichnet waren. Die kontinuierliche Bildung von Aragonitwarven zeigt hier stabile Phasen über Dekaden, wohingegen mächtigere und häufigere Extremevents generell auf eine erhöhte Instabilität während der Gipseinheiten

hindeuten. Diese Ergebnisse zeigen, dass ein komplexes und variables Hydroklima auf unterschiedlichen Zeitskalen während des Spätglazials am Toten Meer operierte.

Das dritte Ziel wurde basierend auf den individuellen Studien erreicht, die zusammen ein ganzheitliches Bild zu verschiedenen Seesystemreaktionen liefern, die während des Übergangs vom letzten Glazial zum Holozän durch diverse Klimaelemente während abrupter Klimaveränderungen mit hemisphärischen Ausmaßen beeinflusst sind. Grundsätzlich sind die durch Klimaänderungen ausgelösten Faziesänderungen ausgeprägter am Toten Meer als im Gościąż See. Zudem ist der Gościąż See beinahe durchgängig warviert, während die Sedimente des Toten Meeres weithin durch Ablagerungen von Extremevents geprägt sind, welche die Konstruktion einer kontinuierlichen Warvenchronologie verhindern. Die spätglaziale Sedimentation im Gościąż See ist hauptsächlich durch Westwinde beeinflusst und untergeordnet auch durch Vegetationsänderungen im Einzugsgebiet. Im Gegensatz dazu ist die spätglaziale Sedimentation im Toten Meer überwiegend von Schwankungen im Niederschlag während des Winters beeinflusst. Diese wiederum werden durch Temperaturschwankungen im Mittelmeer verursacht. Obwohl die Sedimentationsprozesse so verschieden sind, ist die Sedimentation interessanterweise in beiden Archiven stabiler im Bølling/Allerød und dynamischer in der JD.

Kurz zusammengefasst, präsentiert diese Doktorarbeit saisonal-aufgelöste Sedimentprofile zweier Seearchive während des Spätglazials (ca. 17.000-11.000 BP), um die Auswirkungen abrupter Klimaveränderungen in verschiedenen Seesystemen zu untersuchen. Neue Altersinformationen anhand der Identifizierung von vulkanischen Aschen in den spätglazialen Sedimenten des Toten Meeres erlaubten die erste Lithologie-basierte Interpretation der JD im Sedimentprofil des Toten Meeres und den Vergleich mit dem Gościąż See. Dies hebt die Bedeutung der Erstellung einer robusten Chronologie hervor und liefert einen ersten Schritt für die Synchronisierung des Toten Meeres mit anderen Archiven im östlichen Mittelmeerraum. Des Weiteren haben die Klimarekonstruktionen anhand der Seesedimente Variabilität auf verschiedenen Zeitskalen in den Archiven gezeigt. Diese umfassen dekadische bis tausendjährige Schwankungen im Toten Meer und sogar jährliche und sub-dekadische Schwankungen in Proxys während der rapiden Übergangszonen der JD im Gościąż See. Dies zeigt wie bedeutend es ist verschiedene Seearchive zu vergleichen um die regionalen und lokalen Auswirkungen von hemisphärischen Klimaschwankungen besser zu verstehen. Hier wurde eine beispiellose Fallstudie gezeigt, die die diversen Reaktionen unterschiedlicher Seen beleuchtet und aufzeigt wie diese von verschiedenen Klimaelementen abrupter Klimaveränderungen beeinflusst werden können. Dies hebt auch hervor, wie bedeutsam es für Klimarekonstruktionen ist das jeweilige Seesystem zu verstehen.

Acknowledgements

I would like to thank a number of people without whom this thesis would not have been completed. First of all, I want to thank my supervisor Achim Brauer for his constant support in every scientific aspect, for valuable scientific discussions and for letting me benefit from his profound knowledge. I also want to express special thanks to Markus J. Schwab for his consistent support and motivation throughout the entire thesis, for great field trips and the always warm office atmosphere, including the coffee supply. I further want to thank the DFG for funding and two external reviewers for evaluating this thesis.

Many thanks go to the ICLEA community and especially to those involved in the investigation of Lake Gościąż. I especially want to thank Mirosław Błaskiewicz, Michał Słowiński, Markus J. Schwab, Brian Brademann, Mateusz Kramkowski, Mateusz Płóciennik, and Sabine Wulf. A lot of thanks go to Mirosław Błaskiewicz and Michał Słowiński for their continuous support during field work, scientific input and their always warm hospitality, when visiting Poland.

Further, I would like to thank all of the scientist involved in the Dead Sea project with whom I had the pleasure of working with. Among them Ina Neugebauer, Yehouda Enzel, Jawad Hasan, Yoav Ben Dor, Yael Ebert and Moshe (Koko) Armon. Special thanks go out to Yehouda Enzel, Yoav Ben Dor and Yael Ebert for their great support during field work. I further want to thank Yehouda Enzel and Yoav Ben Dor for the much appreciated scientific discussions and great hospitality.

Additionally, I want to thank Sabine Wulf and Mark Hardiman for their highly valued time to share their knowledge about cryptotephra analyses with me and also for their great hospitality.

Moreover, I very much want to thank everyone from GFZ section 4.3 (and beyond) for their constant support and creation of a welcoming atmosphere. Especially, I would like to thank Ina Neugebauer and Florian Ott for their continuous support in just all areas from lab work to manuscript writing, the much appreciated scientific discussions, and for letting me learn from their experience, Ina Neugebauer for sharing her knowledge about cryptotephra analyses with me, and for her support especially during the end, Brian Brademann, Markus J. Schwab and Matthias Köppl for coring at Lake Gościąż, Brian Brademann and Markus J. Schwab for sampling at the Dead Sea and help with anything lab-related, Brian Brademann for the preparation of so many excellent thin sections, Ina Neugebauer, Markus J. Schwab and Oona Appelt for the tephra work, Rik Tjallingii for all the XRF measurements, insightful scientific discussions and help with manuscript writing, Birgit Plessen, Sylvia Pinkerneil and Petra Meier for the geochemical analyses, Arne Ramisch for help with anything chronology- and writing-related, Jens Mingram for his microscope

expertise, Norbert Nowaczyk for the magnetic susceptibility measurements, Nicolai Klitscher for lab assistance, Matthias Köppl for consistent IT support, Andreas Hendrich and Manuela Dziggel for their great help in figure and poster design, Christine Gerschke for help with any bureaucratic problems and all the students and interns for help in the lab and field. Another big Thank You goes to Christin Lindemann, Julia Kalanke, Ina Neugebauer, Markus J. Schwab, Brian Brademann, Florian Ott and Matthias Köppl for all the much needed laughs, coffee breaks and conversations beyond science. I further want to thank my office mates Christin Lindemann and Sylvia Pinkerneil, as well as our office dog Sheldon for the warm atmosphere. A special thanks goes also to Christin Lindemann for her always friendly ear and constant support. Thank you all for your continuous support even through the unusual situation of a pandemic!

Last but not least, I want to express my deep gratitude to my family and friends beyond my work life for their truly tremendous support, their everlasting patience and friendly ears, as well as for helping me to try to keep the work-life-balance! Especially during this pandemic, I want to thank you for maintaining my mental health.

Vielen Dank! **Thank you!** **Dzikuję!** **תודה רבה!**

Table of contents

List of figures

List of tables

1. Introduction

1.1. Motivation

Climate change during the past decades impacted on natural and human systems worldwide (IPCC 2014 p. 6, 2021 p. 5). For the 21st century further warming and changes in all climate systems are predicted (IPCC 2014 p. 8, 2021 p. 19-22). These entail more intense and frequent heavy precipitation events over most mid-latitude landmasses (IPCC 2014 p. 11), further drying in the Mediterranean region and wetting in central-west Europe (Samuels et al. 2018; Hochman et al. 2020; IPCC 2021 p. 22). Climate projections partly rely on past climatic changes (IPCC 2014 p. 58), which is why the understanding of the natural paleoclimate is crucial. The last time period undergoing a major climatic change with minor human influence was the Last Glacial-Interglacial transition (LGIT). Since instrumental data are not available for this time period, proxy data for environmental and climate reconstructions have to be utilized. These proxy data are obtained from a variety of archives – ice sheets in Antarctica and Greenland (e.g. Dansgaard et al. 1993; EPICA Community Members 2004; Rasmussen et al. 2014), corals (e.g. Fairbanks & Matthews 1978; Fairbanks 1989; Bard et al. 1996), marine sediments (e.g. Shackleton & Opdyke 1973; Lisiecki & Raymo 2005; Blanchet et al. 2021), tree rings (e.g. Schweingruber 1988; Cook et al. 1998; Pauly et al. 2018), speleothems (e.g. Bar-Matthews et al. 1999; Wang et al. 2001; Genty et al. 2006) and lacustrine sediments (e.g. Brauer et al. 1999, 2008; Zolitschka et al. 2015).

Lake sediment archives are available worldwide and are valuable recorders of past climatic changes due to their immediate response and incorporation of information about climate impacts on both the internal lake processes and the catchment (Adrian et al. 2009, 2016). Since lakes occur in all geographical and climate regions, have different morphologies, characteristics and catchments (Adrian et al. 2016), a deep understanding of the respective studied lake system is required for robust climate reconstructions. Internal physical, chemical and biological lake processes can operate on timescales from days to millennia (Adrian et al. 2016; Ramisch et al. 2018), and therefore, to record lake processes at high temporal scales, highly resolved lake archives like annually laminated (varved) lake sediments are vital. To compare different lake records the establishment of independent and robust chronologies is essential. From varve counting of varved lake sediments a seasonally resolved varve chronology can be constructed. However, if the varve chronology is disconnected from the sediment-water-boundary ('floating' varve chronology; (e.g. Brauer 2004)) or varves do not form, other dating techniques are required to anchor the sediment record to the absolute timescale. Radiocarbon dating is mostly performed on terrestrial plant remains in lake sediments and can be applied until ~50 kilo-year calibrated before AD 1950 (ka cal. BP; e.g. Hajdas

2008; Ramsey et al. 2012; Kitagawa et al. 2017). In lake sediment records older than ~50 ka, U/Th-dating performed on lake carbonates provides the opportunity to date back until ~500 ka cal. BP (Haase-Schramm et al. 2004; Stein & Goldstein 2006; Torfstein et al. 2013a, 2015), although it should be mentioned that U/Th-dating is a rather uncommon dating method in lake sediments. A recent (indirect) dating technique is the detection of volcanic ash (tephra) deposits and their correlation to the isochronous dated tephra deposit / volcanic eruption (e.g. Wulf et al. 2004, 2012; Lane et al. 2013) allowing for precise dating and synchronization of records (Lowe 2011; Davies et al. 2012; Lane et al. 2017). Due to novel methodologic developments, macroscopically invisible volcanic ash (cryptotephra) can be investigated and even allows the detection of tephra deposits thousands of kilometres away from the volcanic source (e.g. Wohlfarth et al. 2006; Blockley et al. 2007; Lane et al. 2014; Davies 2015; Wulf et al. 2016; Neugebauer et al. 2017).

Not all lake response mechanisms especially to abrupt climate changes are fully understood yet (Havens & Jeppesen 2018; Botta et al. 2019), and different lake systems might also reflect different aspects of climate changes, like for example the impact of extreme events (Adrian et al. 2016). Past lake responses that can be reconstructed from lacustrine sediments include changes in aquatic biota, lake geochemistry, lake salinity, authigenic mineralization, anoxic conditions, water circulation, extreme event layer deposition, catchment vegetation, detrital input, evaporation, water/air temperature, hydrology, and the water level (e.g. Adrian et al. 2009, 2016; Lotter & Anderson 2012; Havens & Jeppesen 2018). Further, multiple stressors can influence lake responses simultaneously, and lake responses can also occur superimposed (Lotter & Anderson 2012). Therefore, the comparison of different lake systems in different climate settings, but during the same time period, is ideal to improve our understanding of lake system responses to climate changes. Furthermore, of particular interest for paleoclimate reconstructions are locations within climate transition zones that are prone to pronounced changes during climate variability.

In the temperate climate zone, the Baltic region is situated in the transitional zone from oceanic (Atlantic) to continental climate. Related atmospheric pressure systems have shifted in the past, prompting environmental changes, and one area of interest, where these have been recorded, is Poland in the central southern Baltic (e.g. Lauterbach et al. 2011b; Błaszkiewicz et al. 2015; Ott et al. 2016; Słowiński et al. 2017). Paleoclimate and paleoenvironmental reconstructions from varved lake systems in Poland (Fig. 1-1B) cover the Lateglacial and Holocene (e.g. Ralska-Jasiewiczowa et al. 1992; Goslar et al. 1999a; Lauterbach et al. 2011b; Pędziszewska et al. 2015; Bonk et al. 2016; Butz et al. 2016; Ott et al. 2016, 2017; Tylmann et al. 2017; Słowiński et al. 2017; Kinder et al. 2020; Zander et al. 2021). Especially the Younger Dryas cooling period (12,846-11,653 BP in Greenland, Rasmussen et al. 2006) is of particular interest since it is the last abrupt climate change before the onset of the Holocene. However, only two lake records in Poland are

recorded so far that show continuous varve preservation throughout the Younger Dryas – Lake Perespilno (Goslar et al. 1999a) and Lake Gościąż (Ralska-Jasiewiczowa et al. 1987, 1998b; Goslar et al. 1989). Due to the development of novel high-resolution methodologies, the re-investigation of the iconic Lake Gościąż sediment record (Fig. 1-1C) provides the opportunity to study abrupt climatic and environmental fluctuations in detail.

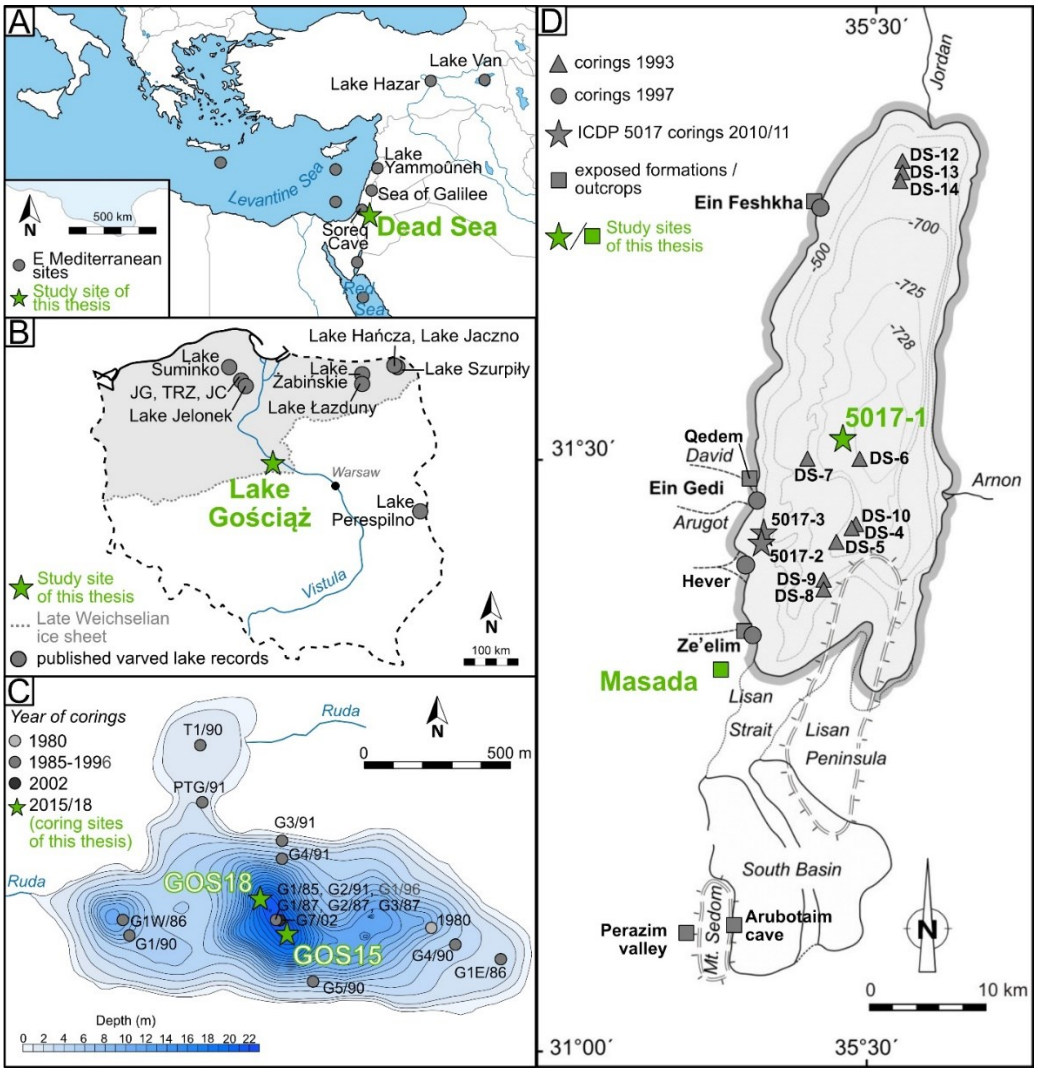

Figure 1-1*: Study sites in (A) the eastern Mediterranean, (B) Poland, (C) at Lake Gościąż and (D) at the Dead Sea. Study sites of this thesis are marked in green. (A) Overview map of the eastern Mediterranean with main studied sites in the region (see text for references). (B) Overview map of Poland* modified after Ralska-Jasiewiczowa et al. (1998c) *with main published varved lake records (see text for references). JG – Lake Głęboczek, TRZ – Trzechowskie palaeolake, JC – Lake Czechowskie. (C) Bathymetric map of Lake Gościąż including previous coring sites from AD 1980 to 2002 (Szymaniak & Wieckowski 1984; Ralska-Jasiewiczowa et al. 1998b, 2003; Rozanski et al. 2010) and the here studied coring sites from 2015 and 2018. Coring site from 1980 is given approximately. (D) Modified after Neugebauer (2015): Bathymetric map of the Dead Sea including coring sites from 1993* (Heim et al. 1997; Ben-Avraham et al. 1999)*, 1997* (Migowski 2001; Migowski et al. 2004, 2006) *and the ICDP coring 5017 in 2010/11* (Stein et al. 2011; Neugebauer et al. 2014)*, as well as the most studied exposed formations / outcrops at the Dead Sea margin* (e.g. Marco et al. 1996; Machlus et al. 2000; Bookman (Ken-Tor) et al. 2004; Haase-Schramm et al. 2004; Prasad et al. 2004; Neumann et al. 2007, 2009; Torfstein et al. 2008, 2009, 2013a; Waldmann et al. 2009; Weber et al. 2021)*. Please note that not all studied sites and corings at the Dead Sea are shown.*

In the subtropical climate zone, the eastern Mediterranean is marked by a sharp gradient from sub-humid Mediterranean to hyper-arid Saharo-Arabian climate. Shifts in this climatic boundary and associated systems have caused environmental changes in the past (e.g. Stein 2014; Stockhecke et al. 2016). Studies in the eastern Mediterranean have focused on the Levantine Sea (e.g. Rossignol-Strick 1985; Cheddadi & Rossignol-Strick 1995; Langgut 2018), Red Sea (e.g. Locke & Thunell 1988; Lamy et al. 2006; Hartman et al. 2020), Lake Van (Landmann et al. 1996; Çağatay et al. 2014; Stockhecke et al. 2016), Lake Hazar (e.g. Eriş 2013; Eriş et al. 2018; Ön et al. 2018), Yammoûneh paleolake (e.g. Develle et al. 2010, 2011; Gasse et al. 2015), Soreq Cave (e.g. Bar-Matthews et al. 1997, 1999, 2003), Sea of Galilee (Lake Kinneret) (e.g. Hazan et al. 2005; Zaarur et al. 2016; Miebach et al. 2017) and the Dead Sea (e.g. Neev & Emery 1967; Stein 2001; Neugebauer et al. 2014) (Fig. 1-1A). In particular, the Dead Sea (DS) is a unique archive due to its steep topography and because its catchment directly covers the boundary between the sub-humid Mediterranean climate in the North and the hyper-arid Saharo-Arabian desert belt in the South (see section 1.3). Shifts in the climate zones and even small changes in precipitation are directly recorded by changes in lake levels and sediment depositions (e.g. Bartov et al. 2002; Torfstein et al. 2008, 2013b; Stein 2014; Neugebauer et al. 2016; Palchan et al. 2017; Ben Dor et al. 2018). Hence, many paleoclimatic and paleoenvironmental studies have been carried out on the sediment formations at the margins and within the Dead Sea (Fig. 1-1D) (e.g. Neev & Emery 1967; Enzel et al. 2003; Migowski et al. 2004; Prasad et al. 2004; Torfstein et al. 2013b; Stein 2014; Neugebauer et al. 2015). Exceptional was the ICDP coring in 2010/11 (Fig. 1-1D) that obtained a ~220 ka BP (~455 m) long sedimentary sequence from the deep centre of the lake (Neugebauer et al. 2014). This sedimentary sequence provides the opportunity to investigate the deep-lake facies for the first time (beyond the last few thousand years, Heim et al. 1997) and compare it with sediment formations at the Dead Sea margins (Neugebauer et al. 2015). Here, of particular interest are time periods of pronounced changes in lake level and lithology that are related to climate variability, i.e. the last Glacial-Interglacial transition.

1.2. Climate during the Last Glacial-Interglacial transition

The Last Glacial was characterized by large-scale climate fluctuations between colder (stadial) and warmer (interstadial) conditions in the Northern Hemisphere that are known as Dansgaard-Oeschger oscillations (e.g. Dansgaard et al. 1982, 1993; Johnsen et al. 1992). In the Greenland ice core record, these fluctuations have been numbered as Greenland Stadials (GS) and Greenland Interstadials (GI) (Rasmussen et al. 2014). At the end of some GS, so-called Heinrich events occur, which are cooling periods triggered by catastrophic discharges of ice bergs probably caused by the weakening of the Atlantic Meridional Overturning

Circulation (AMOC) or internal ice sheet instabilities (e.g. Heinrich 1988; MacAyeal 1993; Broecker 1994; Marcott et al. 2011). The last glacial cycle ended due to warming temperatures after the Last Glacial Maximum at ~19-24 ka BP leading to ice sheet retreat and deglaciation in the Northern Hemisphere (Mix et al. 2001; Denton et al. 2010; Clark et al. 2012). However, this Last Glacial-Interglacial transition (LGIT) was not uniform and like the Last Glacial it was marked by abrupt climate variations, including Heinrich event 1 (H1), GI-1, and GS-1 (Fig. 1-2) (e.g. Rahmstorf 2002; Denton et al. 2010; Rasmussen et al. 2014).

At the end of the Last Glacial, the cold H1 at ~15.5-17 ka BP (e.g. Wang et al. 2001) terminated GS-2, and was followed by warming during GI-1, which is sub-divided into several small-scale climate fluctuations labelled as a-e (b and d representing cooler periods; Fig. 1-2) (Rasmussen et al. 2014). After this initial warming, a pronounced cooling termed GS-1 occurred directly before the onset of the Holocene warming from 12,896 ± 138 to 11,703 ± 99 before AD 2000 (b2k; Rasmussen et al. 2006), which was caused by freshwater influx into the North Atlantic (e.g. Broecker et al. 1988; Teller et al. 2002), a shift in atmospheric circulation (e.g. Seager & Battisti 2007), a large solar minimum (Renssen et al. 2000), an extraterrestrial impact (Firestone et al. 2007) or a combination of these events (Renssen et al. 2015). Yet, most literature agrees that freshwater influx into the North Atlantic leading to weakening of the AMOC was the most probable cause for the cooling (Teller et al. 2002; McManus et al. 2004; Tarasov & Peltier 2005; Broecker 2006; Jennings et al. 2006; Björck 2007). Consequences were a southward expansion of the winter sea ice cover blocking heat release from the North Atlantic, increasing the albedo and causing changes in atmospheric circulation (e.g. more southward deflection of the westerlies), which led to colder temperatures and stronger winds in European sites (Brauer et al. 2008; Broecker et al. 2010; Lane et al. 2013; Słowiński et al. 2017) and colder temperatures and higher aridity in the Levant in the eastern Mediterranean (Rossignol-Strick 1995).

This climate cooling has been recognized throughout the Northern Hemisphere (e.g. Broecker 1994; Brauer et al. 1999; Wang et al. 2001; Lea et al. 2003). In Greenland ice cores, it is defined by stable oxygen isotope ($\delta^{18}O$) curves and is labelled "GS-1" (Rasmussen et al. 2014), but in northern European terrestrial sites this cooling was defined by pollen records and is thus referred to as "Younger Dryas (YD)" (Andersson 1896; Hartz & Milthers 1901; Björck 2007). Within dating uncertainties, ages for GS-1 in Greenland and the YD in Europe coincide (Mangerud et al. 1974; Rasmussen et al. 2006; see also ch. 3), but even if both terms describe the same climate fluctuation, they are derived from different stratigraphies that might show slight temporal offsets. In the synthesis (chapter 6), the lateglacial interstadial and stadial are referred to as Bølling/Allerød and Younger Dryas, respectively, when discussing the lake sites.

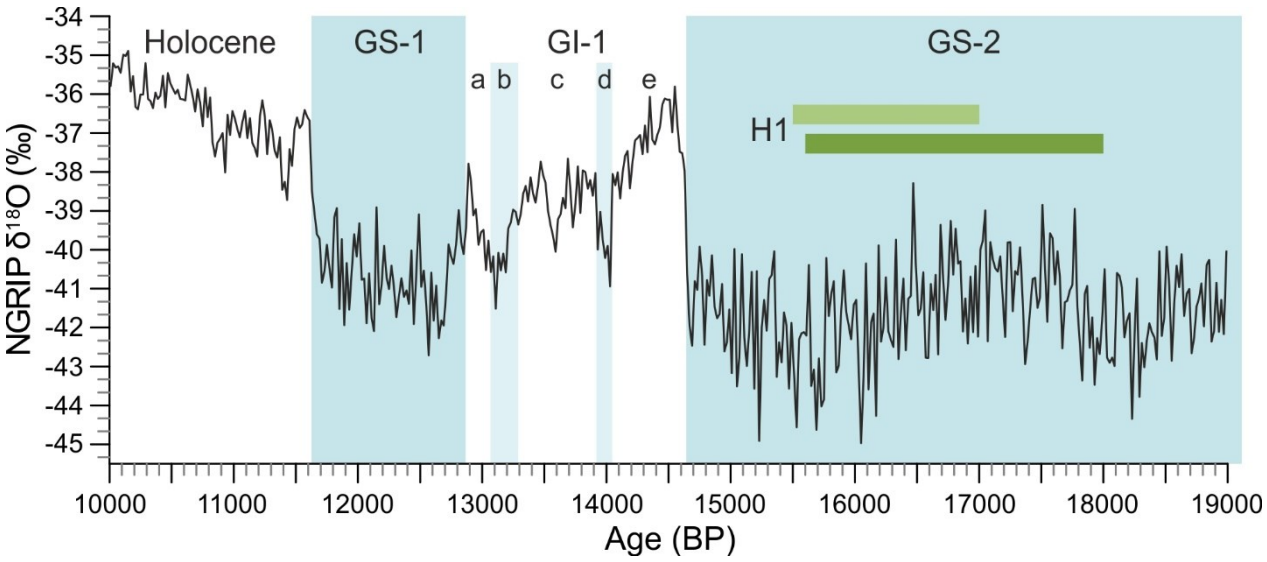

***Figure 1-2**: δ^{18}O data from NGRIP on the GICC05 timescale 19-10 ka BP* (Rasmussen et al. 2006, 2014). *Interstadial in white, stadials in blue. GS-1: Greenland Stadial 1, GI-1: Greenland Interstadial 1, GS-2: Greenland Stadial 2, H1: Heinrich event 1 (dark blue). Timing and duration of H1 is shown for the Hulu Cave* (light green; Wang et al. 2001) *and Greenland ice cores* (dark green; Sanchez Goñi & Harrison 2010).

1.3. Study sites

Lake Gościąż (GOS) is located in central Poland ~80 km WNW of Warsaw (52°35'N, 19°21'E) and is the largest lake of the four-lake Na Jazach lake system in the Płock Basin (Gostynińoskie Lake District, Fig. 1-3A-C, table 1-1). Today the lakes are connected by the Ruda stream draining into the Vistula and since 1970 to the Włocławek Reservoir. GOS is situated at 64.3 m above mean sea level (a.m.s.l), covers an area of 0.417 km^2 and has a catchment area of 5.88 km^2 (Fig. Fig. 1-3C). The open lake consists of a central deep basin (22 m water depth) and a northern shallower basin – the Tobyłka Bay (~2 m water depth). The lake basin formed at 20-19 cal. ka BP during the last ice sheet advance and recession of the Late Weichselian ice sheet (Poznań phase, Marks et al. 2016) as a kettle hole lake within a subglacial channel (Błaszkiewicz et al. 2015). Water to the freshwater lake is supplied predominantly by groundwater (80-90 %) and to a smaller part by the Ruda stream and precipitation (Gierszewski 1993; Giziński et al. 1998; Rozanski et al. 2010). The catchment comprises mainly glacifluvial sediments like aeolian dunes (Rychel et al. 2018; Kruczkowska et al. 2020) and primarily pine forests as present vegetation (Kępczyński & Noryśkiewicz 1998). Central Poland is situated in the temperate climate zone and marked by a warm summer, humid, continental climate (Fig. 1-3A; Dfb in the Köppen-Geiger climate classification, Beck et al. 2018). The monthly mean surface air temperature ranges from -2.8°C in January to +18°C in July, and the annual mean precipitation is 540 mm with highest rainfall during July (Fig. 1-3B; Wójcik & Przybylak 1998; Rozanski et al. 2010).

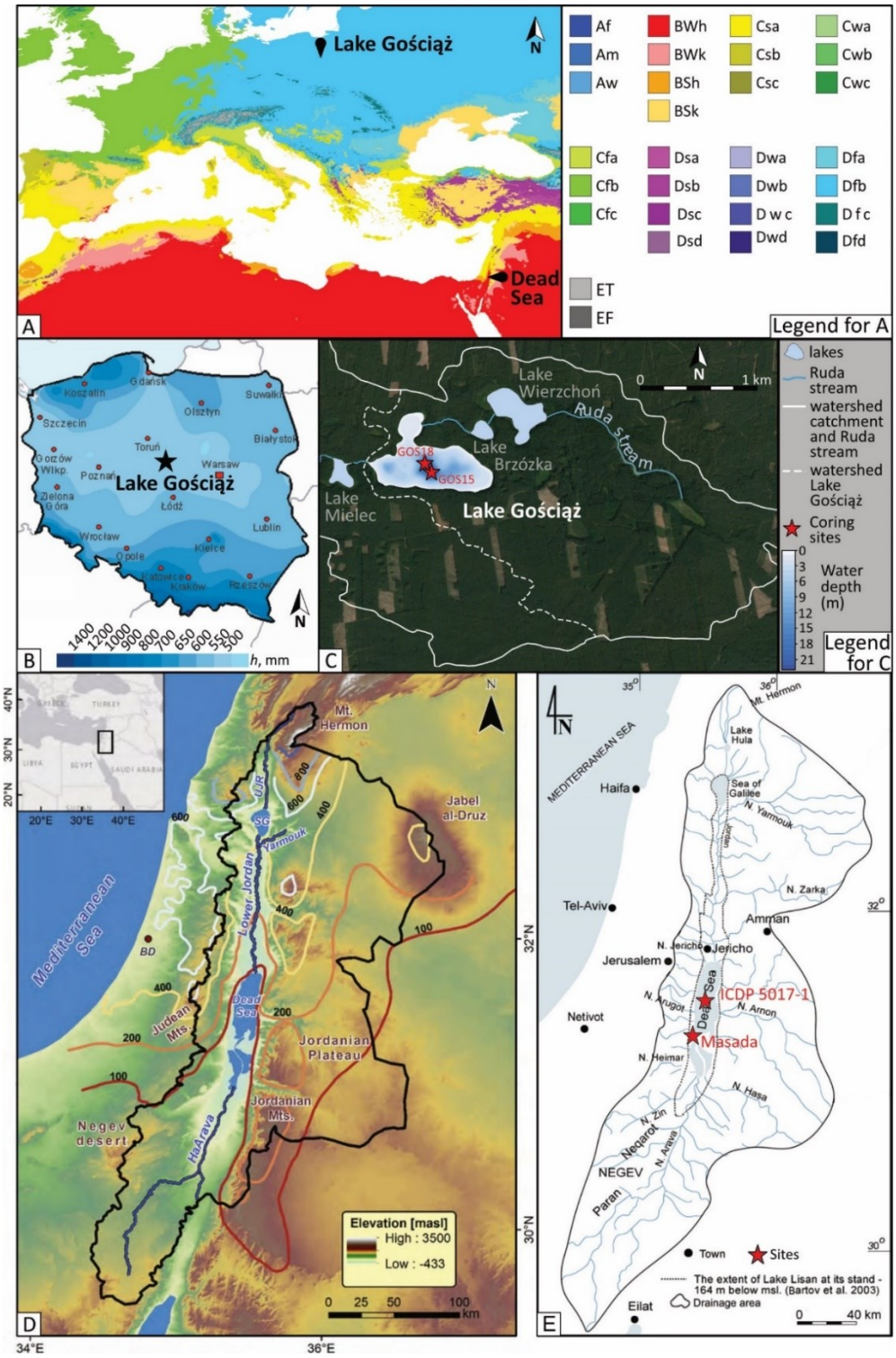

Figure 1-3*: Locations, hydrology and precipitation patterns of Lake Gościąż and the Dead Sea. (A) Köppen-Geiger classifications for the Mediterranean and central Europe from* Beck et al. (2018) *with study sites. Color legend at the right. (B) Mean annual precipitation in Poland from 1970-2019 (weather stations at 19 cities marked by red dots) and location of Lake Gościąż (black star) modified after* Canales et al. (2020)*. (C) Catchment after* Churski & Marszelewski (1998) *and bathymetry of Lake Gościąż and the Na Jazach lake system including coring locations in 2015 and 2018 (red stars). (D) From* Armon et al. (2019)*: Catchment of the Dead Sea (black line) and mean annual rainfall isohyets (mm/yr). SG – Sea of Galilee; UJR – Upper Jordan River. BD – Bet Dagan, atmospheric sounding location. (E) Modified after* Haliva-Cohen et al. (2012)*: Catchment of the Dead Sea (black line), maximum extent of Lake Lisan (dashed line), tributaries in the watershed (blue lines) and locations of sites at the DS (red stars).*

The Dead Sea (DS) is located in the Levant in the eastern Mediterranean (31°34'N, 35°28' E) within one of the deepest continental depressions worldwide – a pull-apart basin that formed along the active Dead Sea Transform (e.g. Garfunkel 1981; Ben-Avraham et al. 2012) (Fig. 1-3A, D-E, table 1-1). As such, the lake is situated at a current (2020) elevation of -434 m a.m.s.l. (Sirota et al. 2020), covers an area of ~609 km^2 (Gertman 2012) and has a catchment area of ~40,000 km^2 (Bentor 1961), which is one of the largest in the Levant. The present DS is ~300 m deep and occupies the northern deep sub-basin. Due to an anthropogenically influenced lake level decline of ~1 m/yr during recent decades (Lensky et al. 2005), the shallower southern sub-basin was disconnected from the main water body in the 1970s and is nowadays filled with artificial shallow evaporation ponds (Gertman 2012). The DS Basin is flanked by steep escarpments in the West (~1000 m a.m.s.l.) and East (~1400 m a.m.s.l.) and characterized by relatively flat topography in the North and South (e.g. Bartov et al. 2002). After its development in the mid-Miocene, the DS Basin was occupied by several water bodies since the late Miocene or Pliocene (~5 Ma) (e.g. Stein 2014). The initial marine Sedom Lagoon was followed by several lacustrine systems (Lake Amora, Lake Samra, Lake Lisan), with the Holocene DS as the most recent one (e.g. Stein 2014). Water to the DS is mainly supplied by the perennial Jordan River in the North and subordinated by the perennial Arnon-Mujib, infrequent flood waters from numerous ephemeral tributaries (Wadis), and springs (Bentor 1961; Lensky et al. 2005; Greenbaum et al. 2006). Due to the lack of an outflow, the DS is a closed lake system that is largely subjected to evaporation processes. With a salinity of ~280 g/kg the DS is hypersaline and even eight times more saline than the ocean (Gertman 2012). Dominant rock types exposed in the DS catchment are Mesozoic to Cenozoic marine sediments (Bentor 1961), while catchment vegetation is largely absent. The DS is located in the subtropical climate zone and its drainage area covers the climate boundary between the sub-humid Mediterranean climate in the North and West, and the semi-arid to hyper-arid Saharo-Arabian desert belt in the South and East (Fig. 1-3A; Csa to BWh in the Köppen-Geiger climate classification, Beck et al. 2018). Accordingly, a steep precipitation gradient from ~1000 mm/year in the North to <40 mm/yr in the South, and >500mm/yr in the West to <100 mm/yr in the East occurs at the DS (Fig. 1-3D; Armon et al. 2019).

In terms of geography, morphology and climate, the two lake systems are quite different, which influences their respective sedimentation processes. However, both lakes are highly resolved due to the formation of varves, which allows for detailed reconstructions of past environments and climates. Summarized climate and morphometric data for both lakes are given below in Table 1-1.

***Table 1-1**: Morphometric and climate data for Lake Gościąż and the Dead Sea (for references see text).*

	Lake Gościąż	**Dead Sea**
Location	Płock Basin, Central Poland	Levant, E Mediterranean
Coordinates	52°35'N, 19°21'E	31°34'N, 35°28' E
Climate zone	Temperate	Subtropical
	warm summer humid continental	*NW*: sub-humid Mediterranean
		SE: semi-arid to hyper-arid desert
Mean annual precipitation (mm/yr)	~540	*N-S:* ~1000 to <40
		W-E: >500 to <100
Lake type	Glacial lake (kettle hole)	Tectonic lake (pull-apart basin)
Lake hydrology	Open	Closed
Salinity	Freshwater	Hypersaline
Surface elevation (m a.m.s.l.)	+64.3	-434 (2020)
Surface area (km^2)	0.417	609
Maximum water depth (m)	22	~300
Catchment area (km^2)	5.88	40,000

1.4. Objectives of this PhD project

The objective of this PhD thesis is to provide a detailed climatic and environmental reconstruction of the Last Glacial-Interglacial transition (LGIT, ~17-11 ka BP) from two different lake systems in two different climatic and geographic settings – the Dead Sea (Levant) and Lake Gościąż (Poland) – by means of high resolution microfacies analyses at seasonal to millennial time scales.

First investigations of the Lake Gościąż sediments were performed in the 1980s to early 2000s (Fig. 1-1C; e.g. Szymaniak & Wieckowski 1984; Ralska-Jasiewiczowa et al. 1987, 1998b, 2003; Goslar et al. 1989) revealing one of the longest and best-preserved varved sediment records in Europe. Recent development of new high-resolution techniques, like e.g. thin section preparation, XRF core scanning and µ-XRF mapping, provides the opportunity to re-investigate this iconic lake sediment record in detail. Therefore, new sediment cores were obtained in 2015 and initial investigations of the lateglacial sediments were performed in 2017 including microfacies analyses, XRF core scanning and bulk geochemical analyses (Müller 2017). However, these analyses showed that the lowermost sediments including the onset of the YD were not recovered in the new cores due to a mass wasting deposit. Thus, in 2018, new sediment cores were obtained from Lake Gościąż and used to complete the new composite profile GOS18 (Fig. 1-4).

The main research questions and aims are as follows:

(1) **What are possibilities to improve chronologies of lacustrine archives?**

Using new cores recovered in 2015 and 2018, a novel chronology based on varve counting is constructed in the varved lake sediments from Lake Gościąż using continuous microscopic thin section analyses, Bayesian age-depth modelling, ^{14}C-dating and gamma measurements.

The existing lateglacial chronology for the ICDP core based on radiocarbon (Neugebauer et al. 2014; Kitagawa et al. 2017) and U/Th-dating (Torfstein et al. 2015), as well as stratigraphic correlation of lithological units (Torfstein et al. 2015; Goldstein et al. 2020) is refined by crypto-tephrochronology and varve counting. At Masada, a floating varve chronology is established.

(2) **How do major and abrupt climate and environmental changes affect lake systems?**

Climatic and environmental changes during the Lateglacial are reconstructed at seasonal resolution in the varved lake sediments from Lake Gościąż using a multiproxy approach, and extending and revising first investigations of the new cores (Müller 2017). Analyses of the new composite profile include continuous thin section microscopy, XRF core scanning and µ-XRF mapping, stable oxygen and carbon isotope measurements, and temperature reconstructions from the beginning of lake sedimentation (late Allerød) until the Early Holocene.

Past climate and environmental changes during the LGIT are reconstructed at seasonal to millennial resolution in the varved sediments from ICDP core 5017-1-A in the deep centre of the Dead Sea and from the Masada outcrop at the southwestern margin of the Dead Sea. Microfacies analyses from thin section microscopy are combined with XRF analyses to investigate and establish a time series of different sediment facies – annual laminations, extreme events and gypsum deposits – and to decode their relation to climate variations during the LGIT. Both sites at the Dead Sea are compared to provide a detailed insight into the temporal dynamics of local hydroclimatic variability.

(3) **How do varved lake systems in different climate zones respond to hemispheric-scale climate changes (during the same time window)?**

The two different lake records – the Dead Sea and Lake Gościąż – that both are high-resolved, but have very different sedimentation processes, are compared during the same period of climate change to decipher the dynamics of complex lake responses to climate variability.

1.5. Related projects

This PhD thesis contributes to (i) the Virtual Institute of **I**ntegrated **C**limate and **L**andscape **E**volution **A**nalyses (ICLEA) of the Helmholtz Association, (ii) the German Research Foundation (DFG) trilateral project **Pal**eohydrology and **Ex**treme Floods from the Dead Sea ICDP Core (PALEX-II), and (iii) the Helmholtz Climate Initiative REKLIM (Regional Climate Change and Humans / **Re**gionale **Klim**aänderungen und Mensch) Research Theme 3 "Extreme events across temporal and spatial scales". This thesis was carried out at the Helmholtz Centre Potsdam GFZ German Research Centre for Geosciences in section 4.3 Climate Dynamics and Landscape Evolution.

i. The **ICLEA** (grant number VH-VI-415, 2012-2018) project is a cooperation between the Helmholtz Centre Potsdam GFZ German Research Centre for Geosciences, Ernst Moritz Arndt University Greifswald (Uni Greifswald), the Brandenburg University of Technology Cottbus (BTU) and the Polish Academy of Sciences (PAN). It aims at a better understanding of the dynamics of climate and landscape evolution of cultural landscapes in the northern central European lowlands (northeastern Germany and northwestern Poland) since the Last Glacial. For this purpose, monitoring data, remote sensing data and proxy data are combined at all relevant time scales and from different sites in this region. In lake sediments, the different landscape forming processes are investigated at high resolution (up to seasonal) and multiple dating techniques are applied to establish a robust chronology and enable synchronization of records. The project is organized in five work packages (WP) with the GFZ Section 4.3 focussing on WP3 ("Tree-ring data") and WP4 ("Lake sediment data"). This thesis is a contribution to WP4.

ii. **PALEX-II** (grant number BR2208/13-1/-2, 2018-2021) is a cooperation of three institutions – the Helmholtz Centre Potsdam GFZ German Research Centre for Geosciences (GFZ), Hebrew University of Jerusalem (HUJ) and Al Quds University of Jerusalem (AQU). The project is related to the ICDP Dead Sea Deep Drilling Project (DSDDP; DFG Priority Program SPP 1006: International Continental Drilling Program) during which a ~450 m long (~220 ka BP long) and quasi-continuous lake sediment record was recovered from the deep central northern Dead Sea basin (longest core 5017-1-A; Neugebauer et al. 2014). Previous studies were restricted to marginal sediment outcrops that are incomplete and discontinuous due to large lake level fluctuations (e.g. Yechieli et al. 1993; Stein 2001) and previous drillings in the deep basin were unsuccessful due to thick salt sequences that could not be penetrated (e.g. Heim et al. 1997). Therefore, this exceptional record provides for the first time mostly continuous information from the deep-lake facies about the last

two glacial-interglacial cycles in the Dead Sea (Neugebauer et al. 2014). The PALEX project combines investigations of extreme hydro-meteorological events (e.g. flash floods) in the ICDP core with meteorological and sedimentological monitoring of recent floods. The main aim is to study changes in flood occurrence and dynamics and their relation to climate changes, while also testing the predicted increase of extreme events in warming climates. The investigation of the origin and mechanisms (e.g. frequency and amplitude) of extreme hydro-meteorological events is crucial to predict their impact on regional environments and humans, especially in terms of recent global warming during which extreme events are expected to increase in frequency and amplitude in this region (Hochman et al. 2018; Myhre et al. 2019; Marra et al. 2021). This thesis was carried out at the GFZ as a contribution to PALEX project P4 "Past extreme event analysis (paleofloods)" that studies in a multiproxy approach the annually laminated sediments and past extreme events from the ICDP core 5017-1.

iii. **REKLIM** (since 2009) integrates disciplines, methods and research centres to investigate regional climate changes and variability also in relation to societies, especially focussing on the "knowledge transfer" to societies (https://www.reklim.de). The network of nine Helmholtz Centres combines regional observation, process studies and coupled climate simulations so that societies are capable to better approach climate protection and climate change adaptation. Within REKLIM Research Theme 3 (RT3) "Extreme events across temporal and spatial scales" climate data, paleo-records and model-based simulations are combined to investigate extreme events and improve the understanding of underlying mechanisms and variability. This is an important aspect since extreme events can affect humans substantially and are an important part in environmental evolution. The main aims of RT3 are to investigate the variability of extreme events, decipher their causes, study their connection to overarching macro-scale changes in e.g. ocean-atmospheric circulations and untangle the causes and dynamics of critical changes in climate.

1.6. Materials and Methods

1.6.1. Sediment cores

In Lake Gościąż (GOS), eight long cores (consecutive ~2 m long cores) and two surface cores (~1 m length) have been retrieved from the deepest lake centre in two coring campaigns in 2015 and 2018 with an UWITEC Piston corer (90 mm diameter) from a floating platform. The long cores are labelled GOS15-A, -B, -C from the 2015 coring and GOS18-D, -E, -G, -H, -I from the 2018 coring. Two surface cores S1 (0.96 m) and S2 (1.05 m) were retrieved at coring locations A and C during the GOS15 coring campaign, respectively.

The cores from 2015 were drilled in the southern section of the deep lake centre (21.3-21.5 m water depth) and encompass a mass movement deposit in the lowermost part that eroded the lowermost lacustrine sediments known from previous corings in the 1980s (Ralska-Jasiewiczowa et al. 1987, 1998b; Goslar et al. 1989). Therefore, in 2018 additional cores were obtained from the northwestern section of the deep lake centre (19.5-21.6 m water depth), which are more distal to the southern mass wasting event and were thus assumed to be less impacted by the mass wasting deposit. These cores only encompass a surface core and the lowermost lake sediments starting at a sediment depth of 8-11 m. In cores GOS18-G and -H the missing lowermost lacustrine sediments were recovered, enabling the construction of a composite profile (labelled GOS18) from overlapping core sections using cores GOS15-S1, -A, -B, -C and GOS18-H (Fig. 1-4). In total, the composite profile is 1897 cm long, starting with lake sedimentation in the late Allerød (see chapter 2 and 3). The cores were opened, cut lengthwise, described macroscopically and photographed at the GFZ, Potsdam. Each two core halves (working and archive half) were stored at 4°C in the core storage at GFZ, Potsdam.

The ICDP DSDDP core 5017-1 (~455 m, ~220 ka BP) was obtained from the deep lake centre (~300 m water depth) with the Deep Lake Drilling System (DLDS) in 2010/11 (Neugebauer et al. 2014). The ICDP cores were first investigated during the PhD thesis of I. Neugebauer (Neugebauer 2015) and details of the drilling campaign, core opening, lithology and first chronological constrains are described in Neugebauer et al. (2014). Here, a ~12 m long section from the Upper Lisan Formation from core 5017-1-A (~101-88.5 m sediment depth; Fig. 1-4) is investigated in detail (chapter 4 and 5). The studied interval in the ICDP core reaches from the base of the so-called Upper Gypsum Unit (UGU) to the base of halite deposition at the onset of the Holocene (Stein et al. 2010; Neugebauer et al. 2014) and is compared to a ~3.8 m long sediment sequence from the marginal Masada outcrop (chapter 5). Cryptotephra analyses have been carried out between ~94-89 m sediment depth (chapter 4).

In the Masada outcrop (MAS) at the southwestern margin of the Dead Sea, the uppermost sediments of the Upper Lisan Formation were sampled in 2018 from the base of the so-called Upper Gypsum Unit (UGU) to the Additional Gypsum Unit (AGU). These sediments comprise the terminal deposits (gypsum and marl sediments) at this site due to a major lake level decline at the Last Glacial-Interglacial transition (e.g. Torfstein et al. 2013a). The complete study interval at Masada is ~3.8 m long, encompassing macroscopic investigations of UGU and AGU and microscopic investigations of the sediments in between including the transition zones into the encircling gypsum units (Fig. 1-4). Using stainless steel boxes (~34x5 cm) with removable side walls that were pressed into the exposed sediments, five consecutive overlapping

sediment blocks (labelled MAS01-MAS05) between the UGU and AGU were obtained from the uppermost part of the outcrop (Fig. 1-4). This section is compared to the deep-lake core 5017-1-A (chapter 5).

An overview of the sediment cores and blocks is given in Appendix A1.

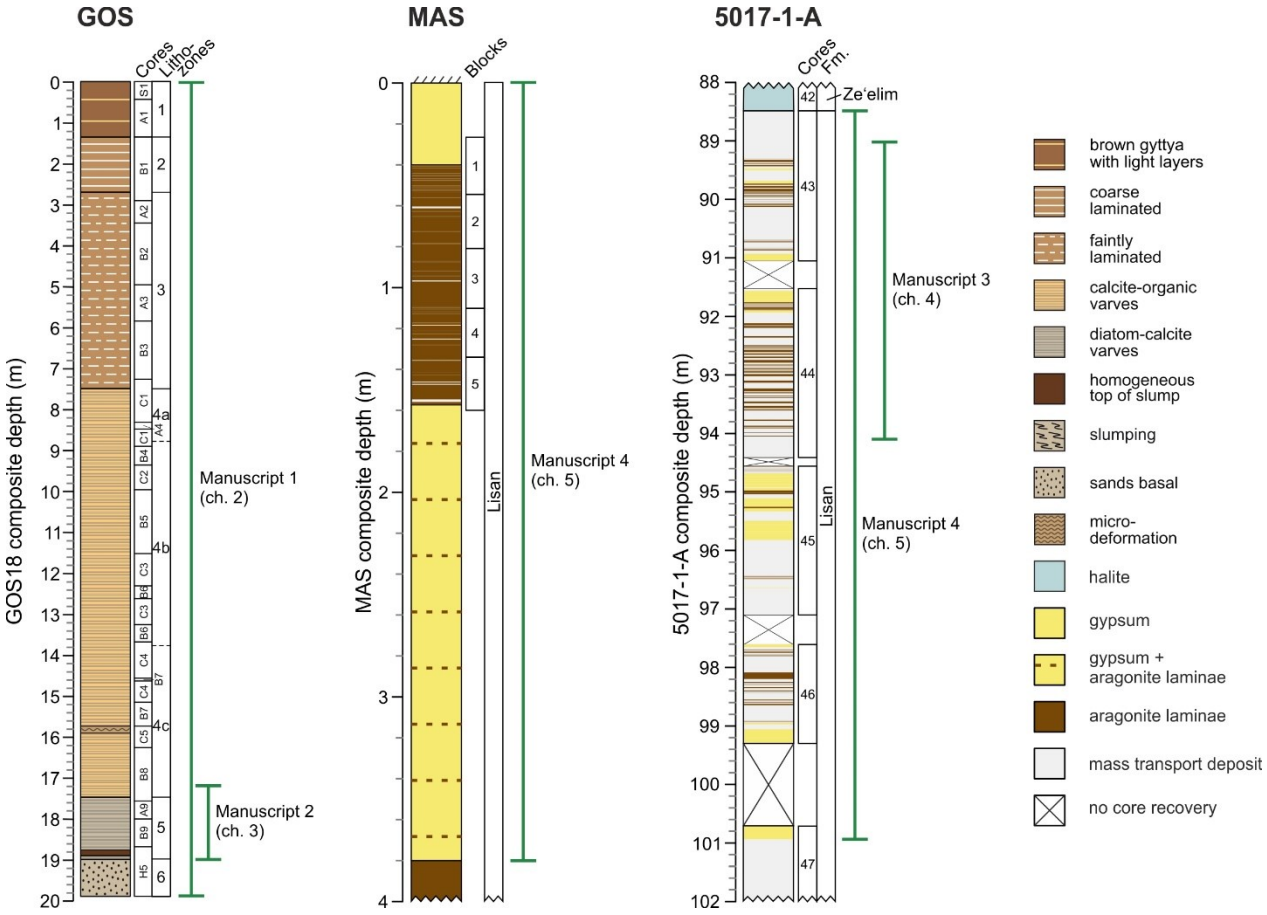

***Figure 1-4**: Overview of the sediment profiles at all three sites. GOS: Lake Gościąż (Poland), MAS: Masada (Dead Sea), 5017-1-A: ICDP core 5017-1-A (Dead Sea). Cores (5017-1-A), core sections (GOS), sediment blocks (MAS) and lithology are detailed for each study section. The related manuscripts of this thesis are marked. Fm: Sediment Formations of the Dead Sea Group.*

1.6.2. Microfacies analyses

Microfacies analyses at seasonal resolution encompassed microscopy of petrographic thin sections (all sites), XRF core scanning at 200 µm resolution (GOS and ICDP core) and µ-XRF mapping at ~20 µm resolution (all sites). In total, 249 thin sections from GOS, 111 thin sections from the ICDP core (Neugebauer 2015) and 29 thin sections from MAS were prepared. The doctoral candidate investigated 26 (GOS), 109 (ICDP core) and 20 (MAS) thin sections during this thesis.

For thin section preparation sediment blocks (10x2x1 cm) were cut from the fresh sediment surface with an overlap of 2 cm and prepared following the procedure by (Brauer & Casanova 2001), which for the Dead Sea was adjusted for the salty sediments (Neugebauer 2015). Varve microfacies investigations and varve counting were performed using a Zeiss Axioplan 2 and Axiolab pol microscope under plane- and cross-polarized light (magnifications 50-400x; chapters 3 and 5). Based on the recognition of varve boundaries and varve composition, varves were counted and the varve and sublayer thicknesses were measured.

XRF core scanning was performed with an ITRAX XRF core scanner (Croudace et al. 2006) at the GFZ in Potsdam (200 µm step size, 10 s measurement time) on the smoothed surface of fresh sediment cores. The attained element intensities in counts per seconds (cps) are further converted into log-ratios that resemble geochemical compositions (Tjallingii et al. 2007; Weltje & Tjallingii 2008; Weltje et al. 2015). Geochemical element data is here produced 1-dimensionally along a vertical profile. µ-XRF mapping was performed with a Bruker M4 Tornado µ-XRF scanner (~20 µm spot size, measurement every ~50 µm, measurement time 30 ms) on selected impregnated sediment blocks that were also used for thin section preparation. Using normalized element intensities, relative element abundancies are visualized in 2-dimensional element maps. Thus, a direct comparison between elemental sediment composition and thin section microscopy can be achieved. Additional details are provided in chapters 3 and 5.

1.6.3. Chronology

The basis for paleoclimatic and paleoenvironmental reconstructions is the construction of a robust age-depth model. In the Lake Gościąż sediment record the here newly constructed chronology is based on varve counting and Bacon age-depth modelling. At the DS, the lateglacial chronologies were thus far based on radiocarbon and U/Th-dating in the ICDP core (Neugebauer et al. 2014; Torfstein et al. 2015; Kitagawa et al. 2017) and at Masada (Prasad et al. 2004; Torfstein et al. 2013a). In this thesis, both DS chronologies are updated by cryptotephrochronology and varve counting (chapters 4 and 5).

Lake Gościąż

In the Lake Gościąż sediment record occur two varve chronologies – one lower floating varve chronology (7.58-18.97 m) and one upper varve chronology reaching the sediment-water boundary (0-5.2 m). The sediments in between are poorly to non-varved (5.2-7.58 m). Therefore, a combination of varve counting and Bayesian age-depth modelling from the Bacon modelling routine (Blaauw & Christen 2011) for the non-varved interval was applied to construct a continuous chronology (chapter 2). The chronology was corroborated by ^{137}Cs activity concentration measurements, AMS radiocarbon dating and pollen analysis (chapter 2).

Varve counting was performed three times based on recognition of varve boundaries under a petrographic microscope. However, the second count during which varve thickness measurements were performed is considered as most accurate (Martin-Puertas et al. 2014). The varve chronologies are 1123 +73/-91 (0-5.2 m) and 10,229 +54/-155 (7.58-18.97 m) varves long, respectively. The mean counting error was calculated for each thin section and cumulatively summed up downcore.

Bacon modelling uses iterated autoregressive gamma walks to establish an age-depth relation between down-core sequences of radiocarbon measurements and to quantify age uncertainties. Using an average age uncertainty of 282 years and the median scenario, Bacon modelling suggested that the non-varved section is 1541 years long. To provide an anchor point for the lower floating varve chronology, a reliable age for the bottom of the non-varved section was calculated. During each iteration, the probability of the age-depth model was evaluated by the sum of all probability density values of all radiocarbon ages below the anchor point. For an age of 2606 cal. yr BP, the cumulative probability was highest.

For gamma measurements, 20 samples were obtained from 7 to 175.5 cm composite depth. The samples were dried for 48 hours at 65°C, homogenized and transferred into polyethylene cups before the ^{137}Cs activity was determined by gamma spectrometry using a Broad Energy Germanium (BE5030) detector (Canberra-Packard). Depending on the minimum detectable ^{137}Cs activity and sample weight, the average counting time for samples varies between 180,000 and 240,000 s. For radiocarbon dating, 15 terrestrial plant remains were sampled, dated using accelerator mass spectrometry (AMS) in the Poznan Radiocarbon Laboratory, Poland, and were calibrated using the IntCal13 calibration curve (Reimer et al. 2013). Pollen analyses were performed consecutively for three sections in the lateglacial part of the core, including the YD transition zones. The 71 samples were prepared following the standard procedure by Berglund & Ralska-Jasiewiczowa (1986) (treatment with 10 % HCl, boiling in 10 % KOH, processing with 40 % HF and acetolysis) and pollen counting followed the method by Stockmarr (1971). 500-1000 Arboreal Pollen were counted per sample. Local pollen assemblage zones (LPAZ) were defined by changes in taxa composition and using numerical analyses from the POLPAL program (Walanus & Nalepka 1999).

Dead Sea

Formation of annual aragonite varves in the Dead Sea has been shown by previous studies (Marco et al. 1996; Migowski et al. 2004; Prasad et al. 2004, 2009; Neugebauer et al. 2015; Ben Dor et al. 2018). However, the deposition of numerous event layers, reworking processes and lake-level related major changes in facies prevent the construction of a continuous varve chronology for the complete profile. Therefore, the existing lateglacial chronology of the ICDP core is primarily constructed from radiocarbon

and U/Th-dating, as well as wiggle matching of lithological units with dated on-shore sites (Neugebauer et al. 2014; Torfstein et al. 2015; Kitagawa et al. 2017; Goldstein et al. 2020). Tephrochronology is an independent dating technique that is also exceptionally well-suited for synchronization of records. Hence, after the first finding of cryptotephra in the DS sediment record (Neugebauer et al. 2017), further cryptotephra analyses have been carried out in the lateglacial ICDP core to further improve the core's chronology (chapter 4). Affirmation is provided by varve counting of varved sequences between the tephra horizons in the ICDP core (chapter 5). The lateglacial chronology for Masada is based on radiocarbon and U/Th-dating (Prasad et al. 2004; Torfstein et al. 2013a) and is here refined by varve counting (chapter 5).

Sampling for cryptotephra analyses was performed in continuous 5 cm steps (samples are 5 cm^3 in volume) in the sediment cores, excluding mass transport deposits thicker than 5 cm. The glass-shard extraction followed established physical and chemical separation procedures (Blockley et al. 2005) and was further adapted to the extreme salinity and sediment recycling of the DS. These adaptations include repeated rinsing with deionized water in a shaking bath, addition of 10 % HCl and 15 % H_2O_2 solutions, wet-sieving and sodium polytungstate (SPT) liquid density mineral separation. Cryptotephra glass shards are then concentrated in the 2- 2.55 g/cm^3 fraction. Because the remaining fraction still contains a high amount of mineral grains, *Lycopodium* spores (1 tablet with a defined number of spores) were added to each sample. Glass shards and *Lycopodium* spores were counted in 5-10 % of the sample mounted on glass slides. Based on the given total number of spores, the glass shard concentration per cubic centimetre of sediment or per gram dry weight can be estimated for the total sample. Picking of glass shards was performed with a 100 µm-diameter gas-chromatography syringe attached to a micromanipulator (Lane et al. 2014). Lastly, the cryptotephra glass shards were embedded in Araldite 2020 epoxy resin, ground and polished for electron probe microanalyses (EPMA).

Based on recognition of varve boundaries, varve counting was performed three times in Masada and two times in the ICDP core under a petrographic microscope. Varve and sublayer thicknesses were measured during the second count and thus are considered as most reliable (Martin-Puertas et al. 2014). The varve chronology at Masada is 968 +15/-64 varves long, whereas in the ICDP core a total of 1509 +44/-55 varves were counted in the individual varved sequences. The longest continuous varved sequence in the ICDP core is 54 varves long. The mean counting error was calculated for each thin section (Masada) or varved sequence (ICDP core) and cumulatively summed up downcore.

1.6.4. Further analyses

Further analyses at Lake Gościąż include (i) powder X-ray diffraction (PXRD), (ii) stable oxygen and carbon isotope analyses, as well as (iii) chironomid-inferred mean July air temperatures. These methods are briefly described below, and presented in more detail in the respective chapters. Further, search for cryptotephra has been carried out at the GOS sediment profile, but provided inconclusive results (Appendix A2).

For the determination of individual minerals in the sediments of Lake Gościąż, PXRD was performed on 19 samples at about every meter within the Holocene (chapter 2). Using side loading technique, disoriented specimens were prepared and collected on an ARL X'tra Thermo Scientific diffractometer (Thermo Electron Corporation, Ecublens, Switzerland) working in Bragg-Brentano geometry. Scanning of samples was performed from 2-65°2Θ using a step size of 0.02°2Θ.

Stable oxygen and carbon isotope analyses were performed for the lateglacial section of the sediment profile (chapter 3). Stable oxygen isotopes were measured in the carbonate sediment fraction ($\delta^{18}O_{carb}$) and stable carbon isotopes in bulk organic matter ($\delta^{13}C_{org}$). Samples were taken continuously in 0.5-1 cm steps from the fresh sediment cores, and include 4-24 varves. Pre-measurement sample treatment included freeze-drying, grinding and homogenization for both, followed by in situ decarbonisation for $\delta^{13}C_{org}$. $\delta^{18}O_{carb}$ was measured with an automated carbonate device (KIEL IV), which is connected to a MAT253 Isotope Ratio Mass Spectrometer (IRMS, Thermo Fisher Scientific), while $\delta^{13}C_{org}$ was measured using an automatic elemental analyser (NC2500 Carlo Erba) coupled with a ConFlow III interface on a DELTAplusXL IRMS. The isotope compositions are given relative to Vienna PeeDee Belemnite (VPDB) standard.

For the chironomid-inferred mean July air temperature reconstruction (chapter 3), chironomid fossils were collected from 233 continuous samples, while samples with less than 50 head capsules were merged for a robust reconstruction (Quinlan & Smol 2001). For the mean July air temperature reconstructions two training sets were applied – the Swiss-Norwegian-Polish Training Set (SNP TS; Kotrys et al. 2020) and the East European Training Set (EE TS; Luoto et al. 2019). The SNP TS includes more lakes (357 vs 212) and a larger temperature range (3.5-20.1°C vs 11.3-20.1°C), but slightly less taxa (134 vs 142) than the EE TS. Both training sets use the weighted averaging-partial least squares transfer function (WA-PLS) and temperature reconstructions were carried out using C2 software (Juggins 2007).

1.7. PhD Thesis structure

This PhD thesis is a cumulative dissertation based on four manuscripts (chapters 2-5). The doctoral candidate is the leading author of two manuscripts (chapters 3 and 5) and second author of two manuscripts (chapters 2 and 4). Three of the manuscripts are published in peer-reviewed international scientific journals (chapters 2, 3 and 4) and one is submitted (chapter 5). The first chapter provides a general introduction followed by the manuscripts in individual chapters and the last chapter 6 concludes and discusses the main results of the thesis, while also providing an outlook and future perspectives. In the following, the manuscripts are summarized and the contribution of the doctoral candidate is provided in detail:

Manuscript #1 (Chapter 2)

Varve microfacies and chronology from a new sediment record of Lake Gościąż (Poland)

Alicja Bonk, **Daniela Müller**, Arne Ramisch, Mateusz A. Kramkowski, Agnieszka M. Noryśkiewicz, Ilona Sekudewicz, Michał Gąsiorowski, Katarzyna Luberda-Durnaś, Michał Słowiński, Markus Schwab, Rik Tjallingii, Achim Brauer, Mirosław Błaszkiewicz

Published in: Quaternary Science Reviews 251, 2021, 106715

(https://doi.org/10.1016/j.quascirev.2020.106715)

This paper describes the new composite profile GOS18 in Lake Gościąż from the onset of annual laminations (varves) in the late Allerød until the time of coring (AD 2015). The almost continuously varved sediment record of Lake Gościąż is one of the most detailed archives of the Lateglacial and Holocene in central Europe as known from previous studies (e.g. Ralska-Jasiewiczowa et al. 1987, 1998b; Goslar et al. 1989). Due to the development of new methodologies it is currently re-investigated at near continuous seasonal resolution. Continuous detailed microscopic data of the microfacies and detailed investigations of the Holocene are provided for the first time from Lake Gościąż. A new and independent chronology is constructed consisting of varve counting and Bayesian age-depth modelling in Bacon of a non-varved interval. Further, variabilities in depositional processes are investigated in relation to climate changes and human impact. It is shown that during the Holocene changes in sedimentology and geochemistry are not only influenced by climatic changes, but also reflect changes in local lake hydrology or water level, processes that apparently can even produce stronger proxy signals than during the YD.

The doctoral candidate contributed about 30 % to the paper. She helped constructing the composite profile, sampled part of the composite profile for pollen, performed varve counting and microfacies analyses of the lower part of the composite profile, provided data for the construction of the age-depth-model, co-designed Figs. 2-2 and 2-3, and contributed to writing and to the general discussion of the manuscript.

Manuscript #2 (Chapter 3)

New insights into lake responses to rapid climate change: the Younger Dryas in Lake Gościąż, central Poland

Daniela Müller, Rik Tjallingii, Mateusz Płóciennik, Tomi P. Luoto, Bartosz Kotrys, Birgit Plessen, Arne Ramisch, Markus J. Schwab, Mirosław Błaszkiewicz, Michał Słowiński and Achim Brauer

Published in: Boreas 50, 2021, 535-555 (DOI 10.1111/bor.12499)

This paper focusses on the lateglacial part of the new composite profile GOS18 from Lake Gościąż (central Poland). As known from previous studies (Ralska-Jasiewiczowa et al. 1987, 1998b; Goslar et al. 1989), Lake Gościąż comprises a remarkably well-preserved sediment record that even features varves throughout the complete Younger Dryas (YD) climate change, which is uncommon for European lake systems. Thus, this record is highly suitable for seasonally-resolved studies of the abrupt YD transitions to improve our understanding of abrupt natural climate coolings (YD onset) and warmings (YD termination). The development of new methodologies (e.g. petrographic thin section analyses, XRF core scanning, µ-XRF mapping) enabled the re-investigation of this record at seasonal resolution using a multiproxy approach. A sediment sequence consisting of 1662 varve years is investigated starting with the beginning of varve formation in the late Allerød and terminating in the Early Holocene. Our findings show complex lake dynamics and responses during an abrupt climate cooling and warming, respectively, but also climatic and environmental variability within the YD.

The doctoral candidate is the leading author and contributed about 80 % to this paper. In detail, she was part of the lake sediment coring, contributed to the establishment of the composite profile, performed varve counting and microfacies analyses on thin sections, sampled part of the composite profile, prepared samples for geochemical analyses, evaluated the data, compiled the figures, and wrote the manuscript. Main contributions were provided from Rik Tjallingii (XRF data), as well as from Mateusz Płóciennik, Tomi P. Luoto and Bartosz Kotrys (chironomid analyses and temperature reconstructions).

Manuscript #3 (Chapter 4)

Cryptotephras in the Lateglacial ICDP Dead Sea sediment record and their implications for chronology

Ina Neugebauer, **Daniela Müller**, Markus J. Schwab, Simon Blockley, Christine S. Lane, Sabine Wulf, Oona Appelt and Achim Brauer

Published in: Boreas 50, 2021, 844-861 (DOI 10.1111/bor.12516)

This paper provides first results from the ongoing cryptotephra search in the ICDP sediment core from the deep centre of the Dead Sea (5017-1-A). Visible tephra layers are absent in the Dead Sea record, but cryptotephra is abundant. Due to the high salinity and sediment recycling of the Dead Sea, a Dead Sea specific glass shard separation protocol and counting procedure were developed. During the Lateglacial (~15-11.4 cal. ka BP) six glass samples from five tephra horizons are investigated showing a heterogenous geochemical composition (primarily rhyolitic and some trachytic glasses). Most glass shards are likely derived from eruptions of the Süphan and Nemrut Volcanoes in the eastern Anatolian volcanic province, but some glasses show a geochemical match with the PhT1 tephra in the Philippon peat record or Santorini Cape Riva Tephra (Y-2), and other glasses tentatively correlate with the St. Angelo Tuff of Ischia (TM-10-1 in Lago Grande di Monticchio). These first cryptotephra findings demonstrate the high potential to improve the chronology of the Dead Sea record and connect it to the Mediterranenan tephrostratigraphy.

The doctoral candidate contributed about 25 % to the paper. She helped to develop the project idea, aided in sampling of the sediments and sample preparation, and contributed to the cryptotephra data evaluation and manuscript writing.

Manuscript #4 (Chapter 5)

Phases of stability during major hydroclimate change ending the Last Glacial in the Levant

Daniela Müller, Ina Neugebauer, Yoav Ben Dor, Yehouda Enzel, Markus J. Schwab, Rik Tjallingii, Achim Brauer

Manuscript submitted to Nature Geoscience

This manuscript presents microfacies data for the Lateglacial (~17-11 ka BP) from the ICDP deep core 5017-1-A and from marginal sediments outcropping at Masada (MAS). This time period is characterized by several abrupt climate fluctuations that are reflected by major lake level and lithological variations in the Dead Sea and its Pleistocene precursor Lake Lisan. Comparison of shallow- (MAS) and deep-water (5017-1-A) sediments provides detailed insights into depositional stabilities and the hydroclimatic variability during the Lateglacial. For the first time the complete transition into the Holocene could be investigated since sedimentation in marginal sites terminated due to the large lake level decline. Decadal- to millennial-long intervals of depositional and hydroclimatic stability are indicated by (i) about one millennium of aragonite varve formation with only a few intercalated mass transport deposits, and (ii) decadal-long intervals of aragonite varves intercalated within gypsum units that reflect elevated lake levels during periods of pronounced lake level decline. Further, a lithology-based interpretation of the Younger Dryas is provided for the first time.

The doctoral candidate is the leading author and contributed about 80 % to this manuscript. In detail, she sampled at Masada, established the composite profile for Masada, performed varve counting and microfacies analyses on thin sections prepared from the Masada blocks and ICDP cores, evaluated the data, compiled the figures, and wrote the manuscript. Main contributions were provided by Rik Tjallingii (XRF data).

2. Varve microfacies and chronology from a new sediment record of Lake Gościąż (Poland)

Alicja Bonk[1, *], Daniela Müller[2, 3], Arne Ramisch[2], Mateusz A. Kramkowski[1], Agnieszka M. Noryśkiewicz[4], Ilona Sekudewicz[5], Michał Gąsiorowski[5], Katarzyna Luberda-Durnaś[6], Michał Słowiński[7], Markus Schwab[2], Rik Tjallingii[2], Achim Brauer[2, 3], Mirosław Błaszkiewicz[1]

(1) Department of Environmental Resources and Geohazards, Institute of Geography and Spatial Organization, Polish Academy of Sciences, Kopernika 19, PL87-100, Toruń, Poland

(2) GFZ -German Research Centre for Geosciences, Section Climate Dynamics and Landscape Evolution, Telegrafenberg, 14473, Potsdam, Germany

(3) Institute of Geosciences, University of Potsdam, Karl-Liebknecht-Str. 24-25, 14476, Potsdam, Germany

(4) Nicolaus Copernicus University in Toruń, Faculty of History, Institute of Archaeology, Bojarskiego 1, PL87-100, Toruń, Poland

(5) Institute of Geological Sciences, Polish Academy of Sciences, Twarda 51/55, PL00-818, Warsaw, Poland

(6) Institute of Geological Sciences, Polish Academy of Sciences, Senacka 1, PL31-002, Kraków, Poland

(7) Past Landscape Dynamics Laboratory, Institute of Geography and Spatial Organization, Polish Academy of Sciences, Twarda 51/55, PL00-818, Warsaw, Poland

* Present address: Division of Geomorphology and Quaternary Geology, Institute of Geography, University of Gdansk, Bażyńskiego 4, PL80-312 Gdańsk, Poland

Published in Quaternary Science Reviews (https://doi.org/10.1016/j.quascirev.2020.106715)

Abstract

The varved sediment of Lake Gościąż (Central Poland) is one of the most detailed and complete climate archives of the Late Glacial and the Holocene in Central Europe. Here, we present microfacies analyses in combination with µXRF core scanning and a detailed varve chronology of a new and continuous GOS18 sediment record.

This record presents six lithozones that mark the most prominent depositional and geochemical changes during the Holocene and Late Glacial. Varve boundaries and five main varve microfacies types were distinguished under petrographic microscope. Analysis provides detailed insights into depositional processes and its changes since the Late Glacial. Microfacies components were used to interpret processes leading to varve formation. A new and independent chronology is obtained by triple varve counting on petrographic thin sections that is complemented by ^{137}Cs measurements and ^{14}C AMS dating of terrestrial plant remains. The age-depth model consists of three parts: (1) the upper part (0-520 cm) that is primarily based on varve counting, (2) the middle part (520-758 cm) obtained through age-depth modelling and (3) the lower part (758-1897 cm) developed by varve counting. The bottom of the composite profile coincides with the onset of lacustrine sedimentation in the late Allerød at 12,834 +134/-233 varve yr BP.

The largest shift in geochemistry, expressed by log(Ca/Ti) and log(Si/Ti) ratios show a rapid increase of calcite precipitation and primary productivity at 7940 +112/-168 varve yr BP. Possible triggers for this include local changes in hydrology as the formation of “Na Jazach” system due to the Ruda River development and fluctuations of lake water level.

Keywords

µXRF; Holocene; Lake sediments; Mn-carbonates; Varve chronology; Paleolimnology; Europe; Sedimentology; Lagoons & swamps; Late glacial

2.1. Introduction

Annually laminated (varved) lake sediments enable detailed reconstructions of environmental and climatic changes in the human habitat. The sedimentological variations of these lacustrine archives record physical, chemical and biological conditions during sediment formation. Individual sublayers represent season-specific sedimentation or even short-term events.

The first sediment record of Lake Gościąż was recovered in 1985 and presented an almost entirely varved archive covering the last 13,000 years (Ralska-Jasiewiczowa et al. 1998b). This record provided the first radiocarbon reference chronology in Central Europe and revealed a detailed environmental history of both climatic and human influences (Goslar 1993; Goslar et al. 1993, 2000; Ralska-Jasiewiczowa et al. 1998b). Multiproxy data analyses were performed at 1-4 year resolution at the Younger Dryas/Preboreal transition (YD/PB) (Ralska-Jasiewiczowa et al. 2003) and revealed, for the first time, details of the origin and nature of this abrupt climate shift in Central Europe. For instance, it was shown, that there was a link between abnormally high ^{14}C concentration and climate changes during the Younger Dryas and the early Holocene (Goslar et al. 1995) and the variations in atmospheric ^{14}C was caused by solar activity (Goslar et al. 2000). Although a wide range of analysis (varve counting, AMS radiocarbon dating, pollen, Cladocera, isotopic and geochemical measures) was applied, the Holocene part of the sediment was only resolved at decadal resolution (ca. 50 years) (Ralska-Jasiewiczowa et al. 1998b). Previous studies of the Lake Gościąż sediment record mainly focused on climate change during the Younger Dryas and human impact during the late Holocene (Ralska-Jasiewiczowa et al. 1998b, 2003). Major lithogenic and geochemical changes were recognized at the YD/PB boundary and its climatic context was highlighted. In contrast, a shift in Mn, Fe, pollen and Cladocera at ca 8000 cal. yr BP were not investigated in detail. The observed changes were described as mostly of anthropogenic origin. In general, previous studies did not include detailed analyses of varves types, structures and composition. In addition, the top part of the core (from 3211 cal. yr BP to the year of coring, 0-7.34 m) has not been varve counted because of disturbed lamination or even homogenous sediments (Ralska-Jasiewiczowa et al. 1998b).

The recent development in analytical techniques (e.g. X-ray fluorescence scanning) and microscopic investigations (i.e. varve microfacies analysis) gives an opportunity to re-analyse the iconic sediments of Lake Gościąż continuously at seasonal resolution. Detailed varve investigation offers a chance to unravel processes that occurred in the lake catchment during sediment formation (Brauer et al. 2008; Bonk et al. 2015a; Dräger et al. 2017; Martin-Puertas et al. 2017; Żarczyński et al. 2019a). The combination of varve microfacies and µXRF scanning allows tracking with high-resolution of the past climatic and environmental changes (Dulski et al. 2015).

It has been shown that microfacial analysis is an excellent tool to recognize varve boundaries and thus improve varve chronologies (Brauer et al. 1999; Bonk et al. 2015b). High-resolution studies and detailed investigations of the lake sediments are crucial to under- stand mechanisms and dynamics of climate changes through examining the analogies in the past. Hence, this paper aims to revise the chronology for the Lake Gościąż record and provide new insights into the Holocene environmental reconstructions using varve microfacies. We introduce detailed microfacial analysis of Lake Gościąż sediment profile (GOS18) in combination with X-ray Fluorescence (XRF) core scanning and Powder X-ray Diffraction (PRXD) of minerals. We also present the full chronology based on thin section counting and supported by radiometric measurements.

2.2. Regional settings

Lake Gościąż is located in Central Poland (52°35'N, 19°21'E, 64.3 m asl) and is one of more than 60 lakes in the Gostynińskie Lake District (Lencewicz 1929). Lake Gościąż is part of the "Na Jazach" lake system including four lakes (Wierzchoń, Brzózka, Mielec and Gościąż) that are connected by the Ruda River (Gierszewski 2000). Lake Gościąż is the biggest of these four lakes with a surface area of 41.7 ha consisting of a large central basin and the shallow Tobyłka Bay in the north (Fig. 2-1). The maximum depth of the lake is 22 m and located in the central basin.

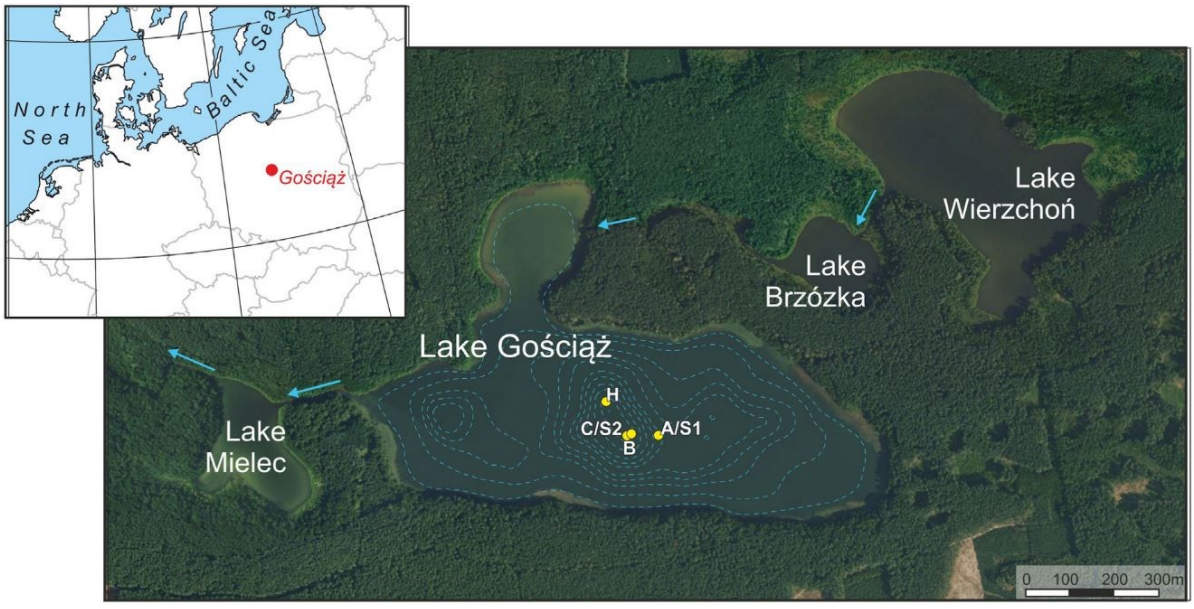

***Figure 2-1**: Location of the study site, bathymetric map and boreholes locations (yellow dots). Arrows show the Ruda River flow direction. The interval between isolines is 2 m. (For interpretation of the references to color in this figure legend, the reader is referred to the Web version of this article.)*

The lake is situated in a dissected subglacial channel and surrounded by the slopes that are up to 5 m high and 5-20° steep. The subglacial channel was formed during the Poznan phase about 18,000 years ago by meltwater of the retreating continental ice sheet after the Last Glacial Maximum. After the ice retreat, this channel was filled with dead ice and covered with fluvio-glacial sediments that maintained permafrost conditions. These conditions prevented the dead-ice blocks from melting until rapid warming at the onset of the Late Glacial and the early Holocene (Błaszkiewicz 2011; Błaszkiewicz et al. 2015; Słowiński et al. 2017). The sand-gravel sediments of the spillway terrace and numerous aeolian dunes formed during cold periods of the Late Glacial in the surroundings of the subglacial channel of Lake Gościąż (Kruczkowska et al. 2020).

2.2.1. Recent climate and seasonality

The region around the study site is classified as humid continental climate with warm summers (Köppen-Geiger climate classification Dfb) (Peel et al. 2007), with highest amounts of precipitation in July and August. The mean annual air temperature is around 8.2°C and the annual mean precipitation ranges from 340 mm yr^{-1} to 780 mm yr^{-1} (over the period 1967-2015 CE; Bartczak et al. 2019). The atmospheric circulation patterns are dominated by westerly surface winds that transport moisture from the Atlantic to the lake region (Ralska-Jasiewiczowa et al. 2003; Rozanski et al. 2010).

The lake is dimictic with a well-pronounced thermal stratification in summer. The ice cover lasts 75 days on average (Choiński et al. 2014). The main periods of highest water flow of the Ruda River are recorded during the late winter and the early spring after the snowmelt. During dry periods and low lake levels the connection between lakes periodically disappears. The most intense phytoplankton bloom takes place during spring but a second one, less intense, is observed during autumn (Fojutowski et al. 2021).

2.2.2. Land cover

The lake is surrounded by forest dominated by *Pinus silvestris* accompanied by *Betula pendula, Quercus robur and Q. petraea*. The more fertile soils are covered with deciduous forests among others with *Carpinus betulus, Tilia cordata, Quercus robur, Q. petraea, Fraxinus excelsior, Ulmus minor, U. glabra, U. leavis* and *Acer platanoides*. Non-forest vegetation is an important part of the land cover in the Lake Gościąż area with the dominance of aquatic, reed swamp, mire, meadow, grassland, scrub, ruderal and segetal communities (Kępczyński & Noryśkiewicz 1998). There is no area related to agriculture in the direct vicinity of the lake. The human activity was reduced in 1979 CE after establishing the Gostynin-Włocławek Landscape Park.

2.3. Material and methods

2.3.1. Coring

In total, four overlapping long sediment sequences and two surface cores were retrieved with a UWITEC Piston Corer (Ø 90 mm) along a N-S transect in deepest part (between 14 m and 22 m in water depth) of the Lake Gościąż (Fig. 2-1). The core sections in the long sequences varied between 178 cm and 198 cm, while for the short cores S1 and S2 it was 95 cm and 97 cm, respectively. The sediment profiles GOS15-A, -B, -C, -S1, -S2 were recovered in 2015, while the sequence GOS18-H was composed from additional cores retrieved during a second coring campaign in 2018 (Fig. 2-2).

After opening and splitting lengthwise, the cores were visually described and photographed at the GFZ Potsdam, Germany. A continuous composite profile GOS18 was constructed from GOS15 and GOS18 cores by visual correlation of macroscopic marker layers (supplementary material, Tab. S2-3 and Fig. S2-8) of overlapping core sections (Fig. 2-2).

2.3.2. Varve microfacies

A total of 249 overlapping thin sections (each 10 cm in length) were prepared from the entire GOS18 composite profile following the procedure described by Brauer and Casanova (2001). All thin sections were scanned on a standard flatbed scanner with 1200 dpi or 2400 dpi resolution between two polarizing foils. Thin sections were microscopically analyzed at 20x to 500x magnification and different varve microfacies were recognized and described. The photos of the microfacies were taken with a Zeiss Axiocam 105 color camera and an Olympus DP72 camera.

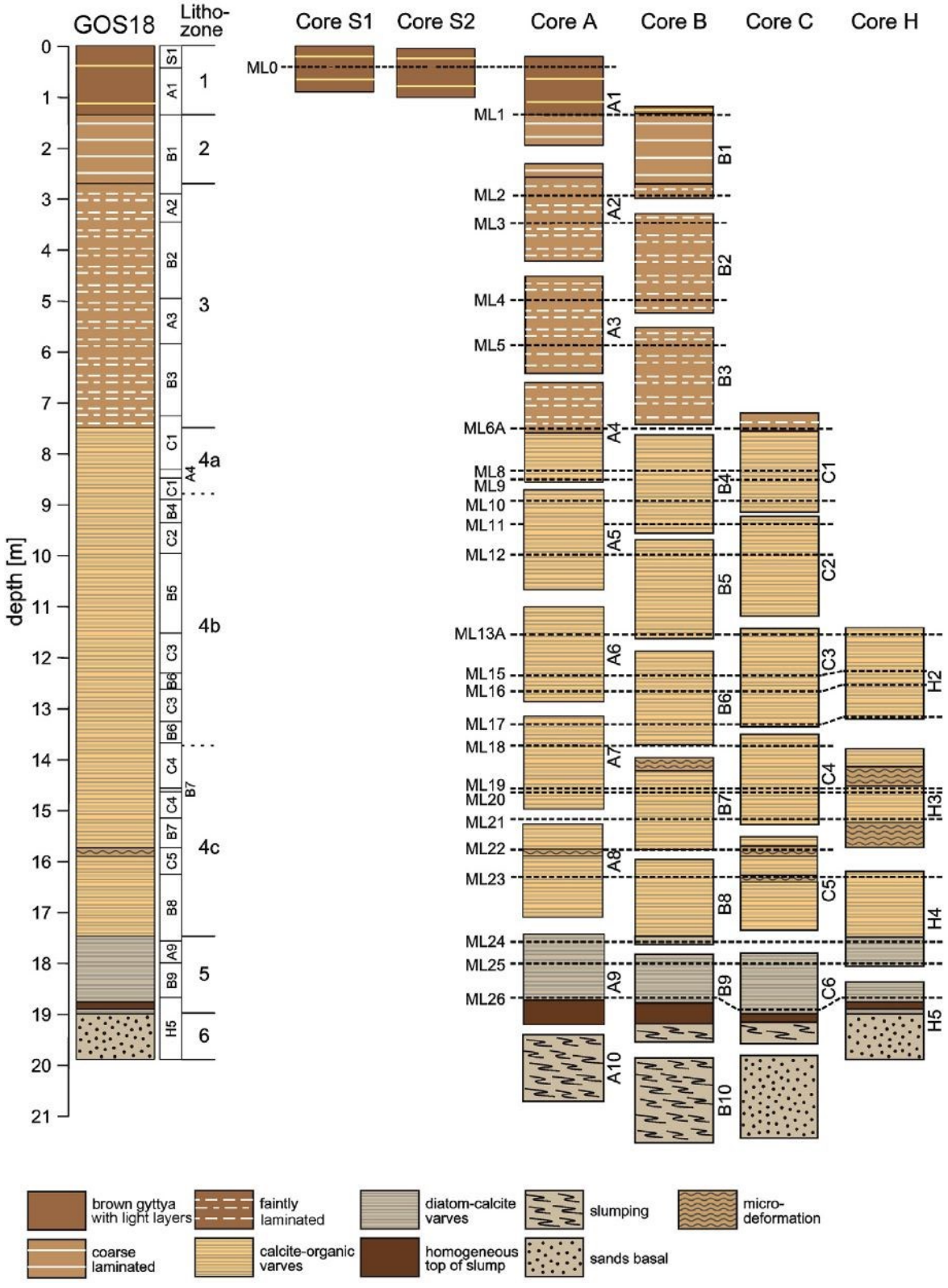

***Figure 2-2**: Composite profile from the Lake Gościąż and sediment cores retrieved from different boreholes with marked marker layers.*

2.3.3. X-ray diffraction

Powder X-ray diffraction (PXRD) was applied to nineteen samples to determine mineral phases in the sediments at the Institute of Geological Sciences PAS, Poland. Samples were taken roughly every meter of the composite profile. The disoriented specimens were prepared using side loading technique and collected on an ARL X'tra Thermo Scientific diffractometer (Thermo Electron Corporation, Ecublens, Switzerland) working in Bragg-Brentano geometry. The conditions of the powder diffraction measurements were as follows: X-ray tube with a copper anode, the fixed anti- scatter slits 1.05 mm and 1.00 mm on primary and secondary side, respectively; Soller slits 1.3° on both sides and scintillation X'ray detector. Samples were scanned from 2 to 65°2Θ with a step size of 0.02°2Θ. The qualitative analysis was performed using DIFFRAC.EVA software ver. 4.2.0.31 and Crystallographic Open Database (COD) (Gražulis et al. 2009). The quantitative analyses were performed using the Qmin program package based on the internal standard methodology (Środoń et al. 2001).

2.3.4. µXRF scanning

Bulk chemical compositions were obtained directly for the split core surface using the ITRAX XRF Core Scanner at GFZ Potsdam, Germany. Measurements were made using a Cr X-ray source (30 kV, 30 mA, 10 s) and are presented at 5 mm resolution for the complete composite profile. Element intensity records are presented as log-ratios, which are linearly related to log-ratios of absolute concentrations and provide the most easily interpretable signals in terms of relative changes in chemical composition (Weltje & Tjallingii 2008).

2.3.5. Varve chronology

The construction of the varve chronology is based on the microfacial analysis of 249 thin sections. Based on varve boundary recognition, three independent counts were performed under the petrographic microscope for the entire profile. The Holocene part of the profile was counted twice by the same person (A. Bonk) and a third time by an independent investigator (M. A. Kramkowski) for providing uncertainty estimates. The late-glacial part was counted three times by the same investigator (D. Müller). Additional counting was made using high-resolution digital images of the fresh cores due to low preservation of varves in topmost thin sections caused by the high water content of the core. The results of the second count for the Holocene and late-glacial parts were used as a master counting, due to the highest reliability.

The counting uncertainty was considered for every individual thin sections following the modified procedure proposed by several authors (Bonk et al. 2015b; Tylmann et al. 2016; Żarczyński et al. 2018). However, the counting uncertainty was calculated not for each varve but for whole thin section. To

evaluate the quality of varve preservation we assigned each varve to one of the three Varve Quality Index (VQI) following the classes described by Bonk et al. (2015b):

- VQI 1: low quality, boundaries interrupted
- VQI 2: high quality, regular varves, boundaries slightly interrupted
- VQI 3: very high quality, regular varves, clear and horizontal boundaries

In addition, we added VQI 0 to show parts of the core, where varves could not be counted. Their number was either modelled with Bacon (between 520 cm and 758 cm) or established using linear interpolation of varve thickness for homogenous non-varved parts of the sequence that occurred above 520 cm (Fig. 2-3).

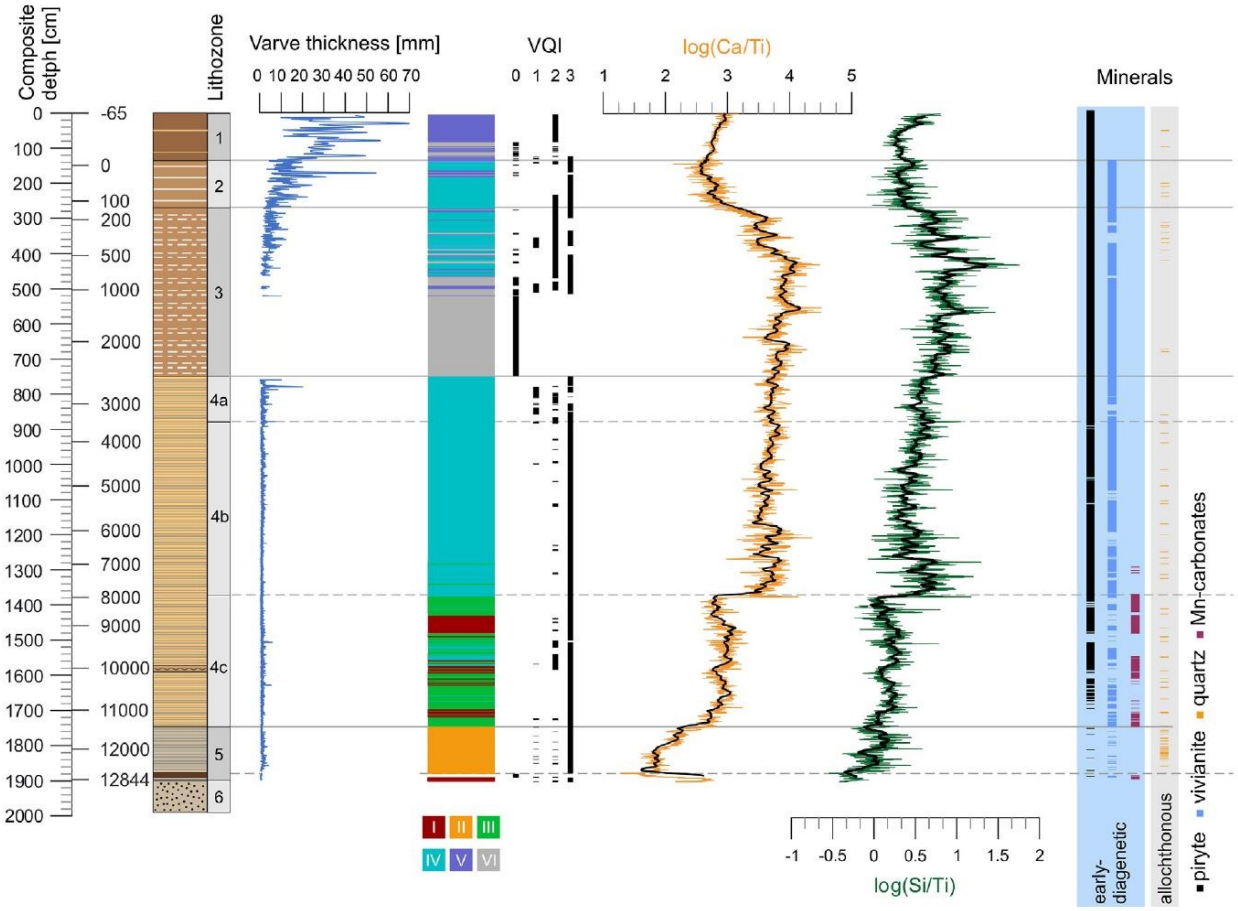

***Figure 2-3**: The sedimentological and geochemical features are shown against composite depth in cm. From the left: Lithological log with lithozones 1 to 6, varve thickness in mm, microfacies types (I- calcite-organic varves (type I), II- diatom-calcite varves (type II), III- calcite-organic varves (type III, a and b), IV- calcite-diatom varves (type IV, a and b), V- calcite-organic varves (type V), 6- homogenous sediment), Varve Quality Index (VQI), XRF ratios of log(Ca/Ti) and log(Si/Ti), minerals appearance within GOS18 composite profile. Grey lines mark the lithozones boundaries.*

2.3.6. Radiocarbon dating

Terrestrial plant remains were hand-picked during the core sampling. Fifteen organic remains were analysed according to the AMS dating procedure used in the Poznan Radiocarbon Laboratory, Poland (Table 2-1). Radiocarbon ages were calibrated using the IntCal 13 calibration curve (Reimer et al. 2013).

***Table 2-1**: Dating results of AMS ^{14}C measurements. Samples are indexed according to numbering in Fig. 2-5. ^{14}C dates were calibrated using MatCal* (Lougheed & Obrochta 2016) *in the Matlab 2018a software environment. Calibrated ages are given as age ranges associated with 95% probability. GOS15 is the code for the Lake Gościąż sequence retrived in 2015; A, B or C indicate the borehole, next two numbers relate to core and sequence, next one or two numbers define the depth at which the macroremains were found.*

Index	Sample	Composite depth [cm]	Material	Lab. code	Age ^{14}C (BP)	Error ^{14}C	Age ranges (cal. BP)
1	GOS15 B1-2 118-119	237.5	*Pinus sylvestris* bark	Poz-95788	85	30	24-264
2	GOS15 A2-1 56.5	289	fragment of terrestrial leaves	Poz-95786	205	30	0-303
3	GOS15 B2-1 18-20	348.5	fragment of terrestrial leaves, *Pinus sylvestris* bark	Poz-114351	330	30	308-473
4	GOS15 B2-1 73-74	403	*Pinus sylvestris* bark	Poz-114348	810	30	681-780
5	GOS15 A3-1 66.5	519	*Pinus sylvestris* bark	Poz-95787	1255	30	1084-1277
6	GOS15 B3-2 112-113	665	*Pinus sylvestris* bark	Poz-95789	2010	30	1886-2040
7	GOS15 C1-1 39-40	758	*Pinus sylvestris* bark	Poz-95790	2425	30	2353-2697
8	GOS15 C1-2 163-164	881.6	*Pinus sylvestris* bark	Poz-88886	3240	30	3389-3558
9	GOS15 B5-1 85-86	1057.9	fragment of terrestrial leaves	Poz-88887	4495	35	4986-5300
10	GOS15 C3-1 80.5	1227.9	*Pinus sylvestris* bark	Poz-88885	5750	40	6450-6651
11	GOS15 C3-2 169-170	1317.9	*Pinus sylvestris* bark	Poz-95791	6460	40	7288-7434
12	GOS15 C4-2 130-131	1487.9	*Pinus sylvestris* bark	Poz-95861	8360	50	9254-9492
13	GOS15 B8-1 51-53	1644.4	Betula sp. bud scale, fragment of terrestrial leaves, *Pinus sylvestris* bark	Poz-114353	9390	60	10426-10767
14	GOS15 B8-2 104-106	1697.4	*Pinus sylvestris* bark and seed, Betula sp. bud scale,	Poz-114352	9620	60	10759-11178
15	GOS15 B8-2 108-110	1701.4	*Pinus sylvestris* bark	Poz-114349	9510	50	10602-11085

2.3.7. Gamma measurements

The ^{137}Cs activity in sediment samples was determined by gamma spectrometry using Broad Energy Germanium (BE5030) detector (Canberra-Packard). Sediment samples were dried (for 48 h at 65°C),

homogenized and transported into polyethylene cups (height 5 mm, diameter 50 mm). The full width at half maximum resolution (FWHM) at 661.7 keV was 1.28 keV. The radioactive standard (POLATOM standard) was used to perform the energy calibration. Data acquisition was investigated using the software Genie 2000. The average counting time for samples varies from 180,000 to 240,000 s. Counting time depended on the minimum detectable ^{137}Cs activity and the weights of sediment samples (approximately from 1 g to 4 g). The ^{137}Cs activity in samples was determined using 661.7 keV gamma line and the activity uncertainty (2s) was around 15-35%.

2.3.8. Age-depth model

Based on the preservation of annual laminae, we divided the profile into three main sections: an upper (0-520 cm) and lower (758-1897 cm) sections with good varve preservation as expressed by VQI ≥ 2 (see Fig. 2-3), separated by a section of poor varve preservation (between 520 cm and 758 cm) with VQI 1 or 0. To establish a reliable age-depth relation for the poorly varved section, we adapted a Bayesian age-depth modelling approach provided by the Bacon modelling routine (Blaauw & Christen 2011). Bacon uses iterated autoregressive gamma walks to establish an age-depth relation between down-core sequences of radiocarbon measurements and to quantify age uncertainties.

2.3.9. Pollen analysis

Pollen analysis was performed for comparison of the new sediment record with the previous study by Ralska-Jasiewiczowa et al. (1998). Seventy one samples, from the bottom of the composite core, were analysed in three intervals: i) from the bottom of GOS15-B9-1 (Fig. 2-2; 13 samples from 1859.9 cm to 1874.4 cm with 2 cm resolution), ii) at the Allerød and the Younger Dryas transition (26 samples from 1880.2 cm to 1896.7 cm with 1-2 cm resolution) and iii) at the Younger Dryas and the Preboreal transition (31 samples from 1741.4 cm to 1798.4 cm with 0.5-3 cm resolution). All samples were prepared according to standard procedure described by Berglund and Ralska-Jasiewiczowa (1986). Calcareous particles were removed with 10% HCl, then samples were boiled in 10% KOH and processed with 40% HF to remove silica if necessary. Next, all samples were acetolyzed. Absolute pollen counting was done according to the method described by Stockmarr (1971). At least 1000 AP (Arboreal Pollen – three and shrubs) per sample were counted in 48 samples and only 500 AP in 23 samples mostly from the Late Glacial. Pollen and spore identification followed the method by Beug (2004) and The Northwest European Pollen Flora I-VIII (Punt et al. 2003). Percentage values were calculated from the sum of trees, shrubs and herbaceous plants (AP + NAP), excluding spores and pollen of aquatic plants. The proportions of the spores/ aquatics/NPPs were calculated respectively on a sum AP + NAP + spores/aquatics/NPPs. The zonation of the diagrams into local

pollen assemblage zones (LPAZ) was based on changes in the composition of the specific groups of taxa and using numerical analyzes from POLPAL program (Walanus & Nalepka 1999).

2.4. Results

2.4.1. Lithology

Three parallel sediment cores (A, B and C) and two surface cores (S1 and S2) were recovered in 2015 (Fig. 2-2) covering a total length of 1818 cm (A), 1849.5 cm (B) and 1282 cm (C), 95 cm (S1) and 97 cm (S2). Due to a slump deposit and the lack of the sediment older than the YD at the base of these cores, additional cores from a more distal position from the slump were retrieved in 2018 (H), to complement the sediment record until the base of the lacustrine sediments. To construct a 1897-cm-long composite sediment profile GOS18, 25 macroscopic marker layers were used (Fig. S2-8 and Tab. S2-3, supplementary material) form cores A, B, C and H (Fig. 2-2).

The mass movement deposit at the bottom of the cores A, B and C is a thick layer (≤2 m) of deformed sediments with faulted sand layers and mixed gyttja with sharp-edged intraclasts of laminated gyttja. The entire slump deposit is covered with a 2 mm thick silt layer, which is overlain by undisturbed calcite lamination and is marked by a sharp transition. In core H, which is part of the composite profile, a 7 cm thick graded layer is deposited within laminated sediments (Fig. 2-2) and reflects the distal deposit of this slump.

Six lithozones are distinguished basing on the main lithological changes observed in composite profile GOS18 and geochemical features (Fig. 2-3).

Lithozone 6 (bottom – 1897 cm) forms the base of the profile. It consists of sands with minor variations in grain size and colour. From the bottom to 1911 cm depth sediments are dominated by homogeneous and beige-coloured fine to medium sands with some scattered black organic particles in the lower part, while in the uppermost 14 cm (1911e1897 cm) grain sizes are slightly finer (fine silt to fine sand) and the colour turns into brownish. The boundary to lithozone 5 is sharp.

Lithozone 5 (1897-1749 cm) is composed of well-preserved, sub-mm light-dark couplets of calcite-organic sediment. At 1885 cm depth the colour changes from light brown-beige to darker brown and the thickness of laminae increases to mm-scale and lamination becomes fainter. From 1872 cm up core the preservation of lamination gradually increases again and occasionally few individual couplets with a thickness >2 mm are intercalated. In the lower part of the lithozone (1880-1872 cm), a 7 cm thick brown and graded sand

to silt-sized layer covered by a distinct 2 mm thick light silt layer on top is intercalated. Weak flame-like structures at the base of this layer suggest minor syn- or post-sedimentary deformations. This layer corresponds to the distal deposit of mass movement deposits in cores A, B and C, up to 200 cm thick, which are located south of core H and thus more proximal with respect to the source of the mass movement. The boundary between lithozone 5 and 4 is sharp and mainly characterized by a change to darker colours and a stronger contrast between light and dark sublayers of the couplets.

Lithozone 4 (1749-758 cm) was divided into three sub-zones due to changes in geochemical composition and different lamination structures:

- Sub-zone 4c (1749-1372 cm) consists of well-preserved calcareous-organic lamination. The dark brown colour of the sediment changes to lighter brown at the depth of 1630 cm and again to reddish-brown at 1398 cm composite depth. The lamination is fine (sub-mm scale) with a coarser (mm scale) lamination around 1500 cm composite depth. A 1 cm-thick silt layer occurs at a depth of 1629 cm. Between 1600 cm and 1580 cm composite depth lamination appears folded in all cores.
- Sub-zone 4b (1372-879 cm) consists of well-preserved calcareous-organic lamination. The colour of the sediment changes from reddish-brown to reddish at 1218 cm depth and darkens to dark brown above 1180 cm towards the top of this sub-zone.
- Sub-zone 4a (879-758 cm) consists of calcareous-organic lamination with less distinct layer boundaries. The colour of the sediment changes from reddish and reddish-brown to light brown at 854 cm depth. The boundary to lithozone 3 is gradual (ca. 5 cm) marked by progressive worsening of the lamination preservation.

Lithozone 3 (758-262 cm) consists of faintly preserved calcareous-organic lamination. The colour of the sediments is light brown. The lamination thickness increases from ca. 2.0 mm at the bottom of the lithozone to ca. 4.7 mm at the top, but layer boundaries are indistinct and disturbed. The boundary to lithozone 2 is gradual (ca. 20 cm).

Lithozone 2 (262-133 cm) is composed of calcareous-organic lamination. The colour varies from light brown at the beginning of the lithozone to the darker brown one on the top. The lamination is coarse and its preservation improves significantly (VQI 1e3) in this part except for 20 cm between 180 cm and 160 cm, where the lamination is invisible or fragmented. The boundary to lithozone 1 is gradual (ca. 40 cm).

Lithozone 1 (133-0 cm) consists of brown gyttja with intercalated light calcareous layers every 2-5 cm. Below 50 cm, however, the lamination is invisible in some parts.

2.4.2. XRF core scanning

The log(Ca/Ti) and log(Si/Ti) records obtained by µXRF scanning (Fig. 2-3) reflect the relative variations of authigenic calcite (Ca) and detrital matter (Ti) as well as relative variations of biogenic silica (Si). Therefore, these records reflect the main variations of allochthonous and authigenic sediment deposition in Lake Gościąż.

The transition from basal sand to lacustrine sediments at 1897 cm is marked by an abrupt drop in the log(Ca/Ti) record (Fig. 2-3) due to the strong decrease of lithogenic sediments. The boundary between diatom-calcite (see section 4.5) varves of lithozone 5 and calcite-organic varves (type II) of lithozone 4 at 1749 cm is not marked by an abrupt shift in the log(Ca/Ti) and log(Si/Ti) records. However, log(Ca/Ti) values start increasing at around 1820 cm indicating a relative increase of Ca prior to the lithozone 5-4c boundary (Fig. 2-3). The log(Si/Ti) record indicates no major changes throughout lithozones 5 and 4c, although values reduce slightly around the lithozone 5-4c boundary (Fig. 2-3). The boundary between sub-zone 4c and 4b at 1372 cm is marked by an abrupt increase of both log(Ca/Ti) and log(Si/Ti), which is also the strongest change recorded by the µXRF scanning of GOS18 (Fig. 2-3). As this abrupt change is observed in both ratios, it is associated with a strong and abrupt decrease of Ti that is indicative for detrital matter. Although both ratios indicate some variation, values remain initially high and decline slightly around 1180 cm depth. They indicate a gradual increase without distinct changes throughout sub-zones 4b, 4a and the beginning of lithozone 3 up to 660 cm, after which occurs a more abrupt decline. Both the log(Ca/Ti) and the log(Si/Ti) records increase again between 660 cm and 430 cm with distinct peak values around 580 cm and 430 cm. Values in both records decrease between 430 cm and the boundary of lithozone 3-2 and stabilize between the boundary of lithozone 3-2 and 180 cm (Fig. 2-3). The upper part of lithozone 2 reveals a decrease of log(Ca/Ti) and an increase of log(Si/Ti), which is one of the few divergences between the two records (Fig. 2-3). Both ratios steadily increase again between the lithozones 1-2 boundary and the sediment surface.

2.4.3. X-ray diffraction

The qualitative and quantitative analysis of PXRD data indicates ten different mineral phases in the sediment profile (Table 2-2): allochthonous minerals (quartz, dolomite/ankerite, feldspar), autochthonous minerals produced in the lake water column (calcite, Mg-calcite, opal A) and early-diagenetic minerals (pyrite, vivianite, gypsum, and Mn-carbonates). Among them, calcium carbonate (CaCO3) is the main mineral phase in Lake Gościąż which occurs abundantly within the whole record. Calcite occurs as a

primary carbonate as a result of precipitation from the water column. This process is mostly associated with the conditions after a spring or summer bloom period with higher surface water temperatures and alkalinity, which cause Ca supersaturation and $CaCO_3$ mineralization respectively (Kelts & Hsü 1978; Stabel 1986).

***Table 2-2**: Mineral composition of sediment samples.*

	Composite depth [cm]	Allochthonous			Autochthonous			Early-diagenetic			
Sample		Quartz	Feld-spar	Dolomite/ Ankerite	Calcite	Mg-Calcite	Opal A	Mn-carbonates	Gypsum	Vivianite	Pyrite
S1 35-36	36	3.3	0	0	56.3	0	38.3	0	1.1	0	1
A1-1 78-79	100	3.4	0	0	60.1	0	35.8	0	0	0	0.7
B1-1 61-62	180.5	10.4	1.8	0	46.9	0	40	0	0.9	0	0
B1-2 131-132	250.5	5.7	0	0.8	54.3	0	37.1	0	1.4	0	0.7
A2-2 112-113	344.5	0.8	0	0.8	82	0	14.9	0	0.8	0	0.7
B2-2 120-121	450.5	0.2	0	0.4	82.7	0	13.5	0	1.2	0.8	1.2
A3-1 97-98	550.5	0.2	0	0.7	87.4	0	9.9	0	1.5	0	0.3
B3-1 98-99	650.5	0.2	0	0	78.9	0	18.3	0	2	0	0.6
C1-1 36-37	755	0.3	0	0	85.4	0	10.1	0	2.7	0.7	0.8
A4-2 189-190	850	0.3	0	0	81.5	0	15.5	0	1.4	0	1.3
C2-1 23-24	950.1	0	0	0	91.2	0	6.7	0	1.2	0	0.9
B5-1 77-78	1049.9	0	3.1	2	82.2	3	5.2	0	2.5	1	1
B5-2 177-178	1149.9	0	0	2	86.1	1.9	7	0	1.8	0	1.2
B6-1 56-57	1250.4	0	0	1	87.3	0	7	0	3.2	0.8	0.7
B6-2 156-157	1349.9	0	0	3.8	67.3	0	20.5	1	6.8	0	0.6
C4-1 80-81	1437.9	0	0	29	47.2	0	19.5	1.3	1.9	1.1	0
C4-1 89-90	1446.9	0	0	21	43.1	0	23.1	10.1	1.7	1	0
B7-2 143-144	1541.9	0	0	25.9	48.7	0	19.1	5.4	0.9	0	0
C5-1 70-71	1627.4	0	0	30	45.4	0	14.6	4.4	5.6	0	0

Formation of Mn-carbonates ($MnCO_3$) is assumed to occur in stratified water column in lakes with high pH values and low redox potential (Jouve et al. 2013). In Lake Gościąż, Mn-carbonates were found in five 1-cm samples mainly from the lower part of the profile until lithozone 4b (Fig. 2-3; Table 2-2) up to ca. 1350 cm. Vivianite ($Fe_3(PO_4)_2 8H_2O$) forms during early diagenesis and has been reported from various reducing environments (Rothe et al. 2014, 2016). It appears throughout the whole profile, except lithozone 1, where no vivianite was observed (Fig. 2-3). Pyrite (FeS_2) is also an early-diagenetic mineral which occurs within the entire record of Lake Gościąż, except for a few short intervals, where pyrite grains were less abundant or even absent (Fig. 2-3). Gypsum was found within the whole profile but there is no clear pattern of its occurrence (Fig. 2-3). However, it was observed more frequently in a light lamina.

Due to the early-diagenetic origin of the Mn-carbonates, vivianite, pyrite, and gypsum none of them can be used as direct paleolimnological indicators in Lake Gościąż as they reflect conditions that occurred within the sediment.

2.4.4. Varve microfacies

Based on detailed microfacies analyses, agreement with seasonal sub-layering, and the dominant mineral phase, we distinguished five main varve types (Fig. 2-4): calcite-organic (type I), diatom-calcite (type II), calcite-organic (type III), calcite-diatom (type IV) and calcite-organic (type V). Their thickness varies through the record from sub-mm to 4-5 mm in lithozones 4c, 4b and 5, through 5-30mm in lithozone 3 up to 70 mm in lithozones 1 and 2:

- Calcite-organic varves (type I) occur during the first ~12 cm of lithozone 5 with an average varve thickness of 0.49 mm. Above this depth they only occur sporadically. Calcite-organic varves (type I) primarily form couplets consisting of a calcite and an amorphous organic sub-layer. The size of calcite grains ranges between ca. 5-20 mm. Some of these varves include an additional sublayer intercalated between the calcite and organic sublayer that consists of fine-grained (2-5 mm) brown- yellowish grains resembling Mn-carbonates (Müller et al. 2021).
- Diatom-calcite varves (type II) consist of up to six sublayers and are the most complex varve type found in the Lake Gościąż sediments. Their occurrence is restricted to lithozone 5 and their mean thickness is 1.15 mm. The main depositional features are several diatom-bearing sub-layers and re-suspended calcite. Further, Mn-carbonate and thin sub-layers of amorphous organic matter occur, as well as rare detrital layers. The Mn- carbonate sublayer at the base was used as the beginning of the varve year or, if it was not deposited, the amorphous organic matter sublayer at the top as the end. In few cases, where neither of the two was deposited, the first sublayer

occurring after the Mn-carbonate sublayer was used as the base, e.g. the spring diatom sublayer. However, the re-suspended calcite sublayer is deposited in almost all varves and was therefore the basis for counting. More detailed description of the late-glacial varves is included in Müller et al. (in press).

- Calcite-organic varves (type III) varves typically consists of three sublayers and have a mean thickness of 1.02 mm. The sedimentation cycle starts with a Mn-carbonate sublayer which was used as an indicator of the beginning of the year. The second sublayer consists of fine (ca. 2 mm) calcite grains deposited during spring and summer. The third sublayer can be either the organic matter in amorphous form (type IIIa) or amorphous organic matter and different species of diatoms (type IIIb). Pyrite grains and vivianite lenses (ca. 250 mm) are visible at the end of the third sublayer. Calcite-organic varves (type III) prevail in the lithozone 4c and 4b. Mn-carbonate grains can be difficult to distinguish from calcite and siderite but the presence of Mn- carbonates is confirmed by PXRD analyses (Table 2-2).
- Calcite-diatom varves (type IV) have a mean thickness of 1.46 mm and mostly contain two layers. The first layer, which represents start of the annual cycle, typically is either diatom layer (type IVa, Fig. 2-4) or a mixed diatom and calcite layer (type IVb, Fig. 2-4) and is the most frequent type within the Lake Gościąż composite profile. The size of the calcite grains is gradual (ca. 2e6 mm) and redeposited calcite (Lyon et al., 2020) grains occur. They form coarse (>6-8 mm) agglomerates in lithozones 4 (especially 4b), 3 and 2. The second layer consists of amorphous organic matter, and early-diagenetic vivianite and pyrite grains along with chrysophycean cysts. This sequence may occur two or three times (Fig. 2-4, type IVb) in the upper part of lithozone 3 and lithozone 2 but the end of the cycle is marked by amorphous organic matter and vivianite crystals not bigger than 20-25 mm within it.
- Calcite-organic varves (type V) are composed of two layers. The first one, calcite (grains of ca. 4-8 mm) layer, is clearly recognizable and hence, served as a marker for the beginning of the year. Diatoms, amorphous organic matter, chrysophycean cysts, vivianite and pyrite grains compose a second, mixed layer but a seasonality of these components cannot be recognized. This varve type is typical for the part of the profile from 133 cm upwards (lithozone 1) and sediment transition from the lithozone 4 to the lithozone 3. This transition is gradual and extends from 758 cm to 578 cm. The mean varve thickness is 15.14 mm (27.30 mm in the lithozone 1 and 2.98 mm in the part between 578 cm and 758 cm).

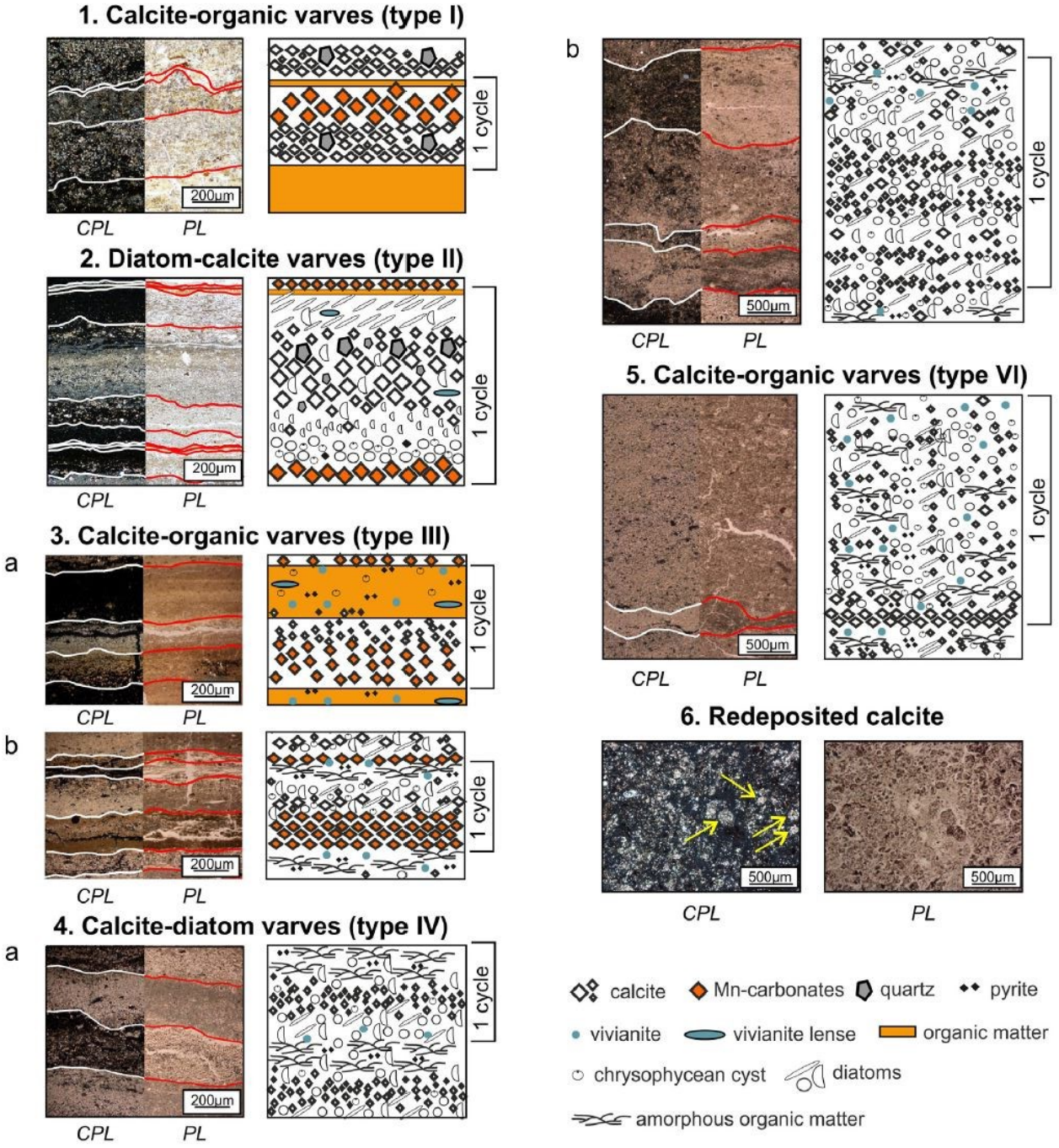

***Figure 2-4**: Major varve microfacies identified in the Lake Gościąż sediment record (1-5). Schemes covers at least 1 cycle of sedimentation (1 varve). Images on the left were taken under cross-polarized light (CPL) and the ones on the right under plain light (PL). White and red lines show boundaries of layers. Examples of redeposited calcite (yellow arrows) are presented in point 6. (For interpretation of the references to color in this figure legend, the reader is referred to the Web version of this article.)*

2.4.5. Chronology

2.4.5.1. Radiocarbon dating

In total, 15 samples from plant macro-remains have been AMS radiocarbon dated (Table 2-1). Most of dates, expect Poz-114352 and Poz-114349, are in stratigraphic order within the composite profile. So far, we have not found datable macrofossils in lithozones 1, 5 and 6.

2.4.5.2. Gamma measurements

The ^{137}Cs activity is incoherently distributed in the top sediment core (Fig. 2-5). Concentrations of ^{137}Cs in the investigated sediment profile are shown in Tab. S2-4 of supplementary materials. Below depth 155.5 cm no ^{137}Cs was measured. The mean ^{137}Cs activity in the topmost 150 cm of sediment record was 17.66 ± 4.89 Bq kg^{-1}. Clear peaks in activity concentration were measured at 140.5 cm and 90 cm depths and were interpreted as as records of the 1960s nuclear weapon tests and the 1986 CE Chernobyl disaster fallout, respectively. The mean deposition rate calculated for the topmost 1.5 m sediment in Lake Gościąż was 28.1 mm yr^{-1}.

2.4.5.3. Age-depth model

The degree of preservation of annual laminae divides profile GOS18 (Fig. 2-5) into three sections: an upper well-varved section with a majority of varves exhibiting a VQI 2 or higher (a), a poorly to non-varved section with VQI equal to 0 or 1 (b) and a lower well- varved section with the majority of varves exhibiting a VQI 3 (c). Accordingly, the age-depth model of profile GOS18 is divided into three sections:

a) Upper varved section (0-520 cm): The age-depth model for this section is based on layer counting which is in good agreement with independent age estimates from ^{137}Cs activity and ^{14}C AMS measurements. One exception is radiocarbon date Poz-114348 (date 4 in Fig. 2-5) which is ~200 years older than varve counting. Where the preservation of varves was not good enough for counting, we interpolated the number of varves by measuring the average thickness above and below the disturbed part (minimal interval taken into consideration was 3 cm and maximal 39 cm). In total, 1123 +73/-91 varves were counted AD) for the base of the upper varved section at 520 cm sediment resulting in an age of 1064 +73/-91 varve yr BP (892 +73/-91 depth. Age uncertainties in this section are based on counting errors and accumulate to 164 years from the top to the bottom of the section.
b) Interpolated section (520-758 cm): Due to the lack of varves, we applied the Bayesian age-depth modelling routine to estimate the age-depth relation for this section. Age information for the Bacon routine in this section is provided by three age estimates: i) the basal age of the upper

section from layer counting in 520 cm depth, adapted for the Bacon routine as normal distribution with a mean of 1064 and an uncertainty of ±45 years (1σ) to enclose the asymmetrical age uncertainty calibrated age of ^{14}C date Poz-95789 (no. 6 in Fig. 2-5) at 665 cm of +73/-91 from counting errors within the 2s range. ii) the depth and iii) the calibrated age of Poz-95790 (no. 7 in Fig. 2-5) at 758 cm depth. The Bacon routine was applied in 5 cm sections, using a default Bayesian accumulation prior (Goring et al., 2012) with an estimated mean of 6.5 yr cm^{-1} and a shape parameter of 1.5, as well as the default for the Bayesian memory prior with a mean of 0.7 and strength of 4. The results of the Bacon routine suggest that the poorly and non-varved interval comprises 1541 years according to the median scenario and with an associated average age uncertainty of 282 years (corresponding to 95% of all accepted Bacon iterations). To calculate a reliable age for the lower varve counted section at the base of the age-modelled interval (758 cm sediment depth; Poz-95790; no. 7 in Fig. 2-5) that lies within the calibrated radiocarbon age range between 2353 and 2697 cal. yr BP, we adapted an iterative modelling approach by increasing the anchor point age within the 95% range of date 7) in one-year steps. At each iteration, we evaluated the probability of the resulting age-depth model by the sum of all probability density values of all radiocarbon dates below the anchor point (dates 8 to 15 in Table 2-1 and Fig. 2-5) for the resulting age-depth relation. The highest cumulated probability (see Fig. S2-9 of supplementary materials) was found for an age of 2606 cal. yr BP. We independently calculated the age uncertainty for the anchor point. Since the cumulated probability distribution for this date as seen in Fig. S2-9 is multimodal and asymmetric, we approximated the multimodal distribution using a normal distribution with a mean of 2606 cal. yr BP and an error of ±80 years (1σ). The approximated probability distribution was passed as basal age information to the Bacon routine.

c) Lower varved section (758-1897 cm): The excellent varve preservation allows the construction of a detailed varve chronology by layer counting. Layer counting resulted in a total of 10,229 identified varves with a mean counting error of about 100 years. The floating varve chronology was anchored at 2606 cal. yr BP ± 80 years (see b). The anchor point uncertainty of ±80 years has been added to the varve counting error summing up to a cumulative uncertainty range of 369 years at the base of profile. The resulting age-depth model thus suggests a basal age of 12,834 +134/-233 varve yr BP for sediment profile GOS18.

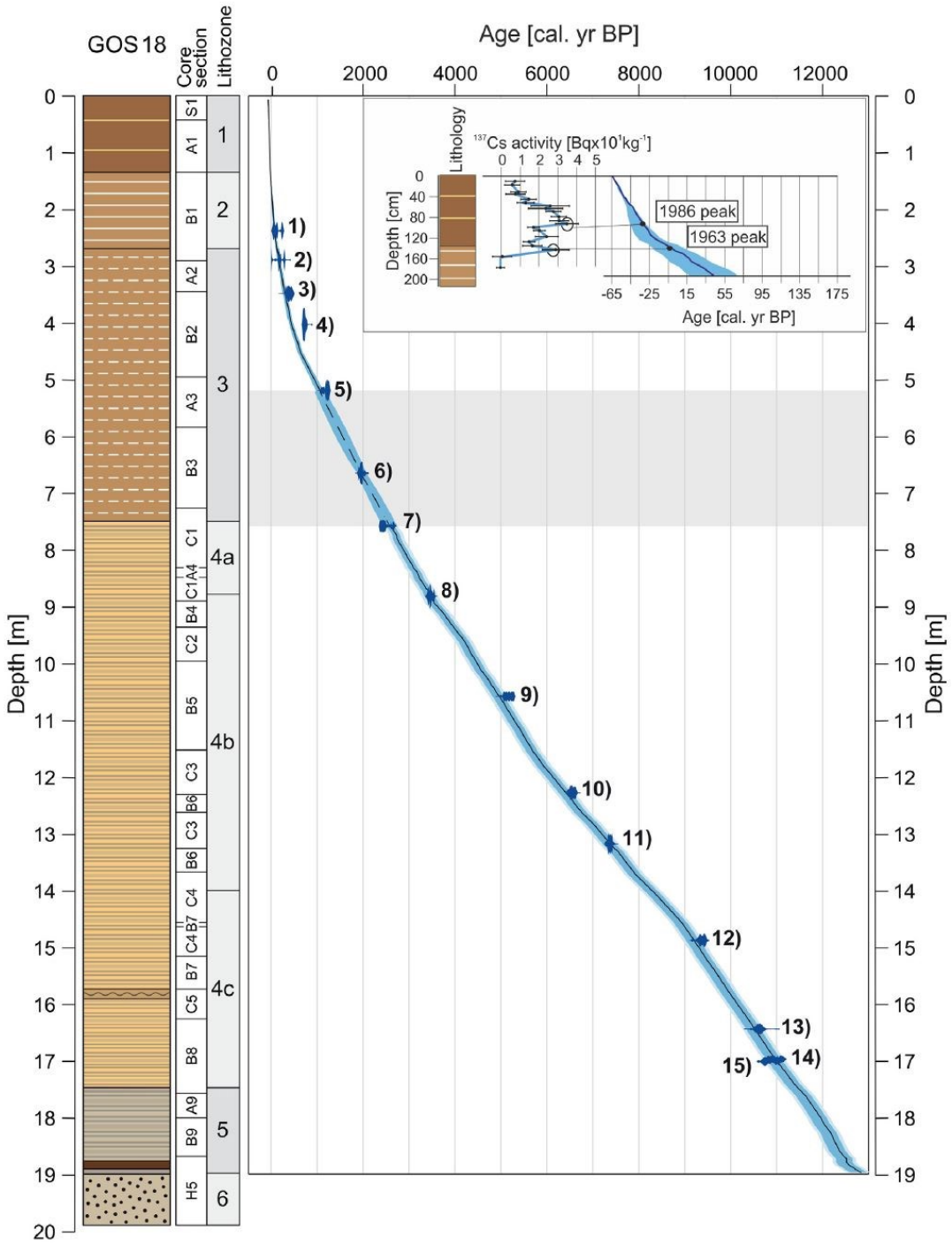

***Figure 2-5**: Age-depth model of sediment profile GOS18. Dark blue areas illustrate the probability distribution of individually calibrated AMS ^{14}C dates 1 to 15 (as indexed in Table 2-1). Solid dark blue lines illustrate the age-depth model based on varve counting and Bayesian age-depth modelling (dashed dark blue line, grey rectangle). Varve counts in the lower section (7.58-18.97 m) are anchored to calibrated ^{14}C date no 7 (for explanation see text). Blue shading illustrates the age uncertainty range associated with layer counting and the interpolation routine (see text). Right top corner: results of ^{137}Cs dating. Black lines shows the uncertainty of the ^{137}Cs dating, solid dark blue line shows the age-depth model with its uncertainty (blue shadding). (For interpretation of the references to color in this figure legend, the reader is referred to the Web version of this article.)*

2.4.6. Bio-stratigraphy

We investigated three short intervals at the base of the varve succession and the onset of the Younger Dryas and the Holocene that allowed us to compare GOS18 results with comprehensive pollen data previously published (Fig. S2-10 of supplementary material; Ralska-Jasiewiczowa et al. 1998b).

The base of the annually laminated sediments was deposited in the Allerød (*Pinus-Betula* L PAZ (local pollen assemblage zones), Fig. 2-6). This phase is characterized by the high concentrations of *Pinus* and *Betula* pollen indicating the development of forest communities. The heliophyte from the open-ground vegetation still exists (*Artemisia*, *Chenopodiaceae*, *Filipendula*). The Allerød (Al.)/ Younger Dryas (YD) boundary between 1886.2 cm and 1886.7 cm is defined by rise of *Juniperus* and NAP and a drop in total concentrations of sporomorphs. This is in agreement with previously published data (Fig. S2-10; Ralska-Jasiewiczowa et al. 1998b).

According to the palynological data, the boundary between the YD/PB (Fig. 2-6, *Pinus-Ulmus-Filipendula* L PAZ) is ambiguous but it can be defined between 1751.9 cm and 1752.4 cm where *Juniperus* and *Artemisia* decreased and *Filipendula* increased. First changes, however, were observed earlier and thus, the boundary may be extended and expressed as a transition zone (between 1755 cm and 1749.4 cm). The percentages and pollen concentration of *Betula* decreased at 1755 cm but *Pinus* slightly increased. At the same depth single grains of *Filipendula* appeared. The final warming is pronounced by increasing forest canopy density at the depth of 1749.4 cm.

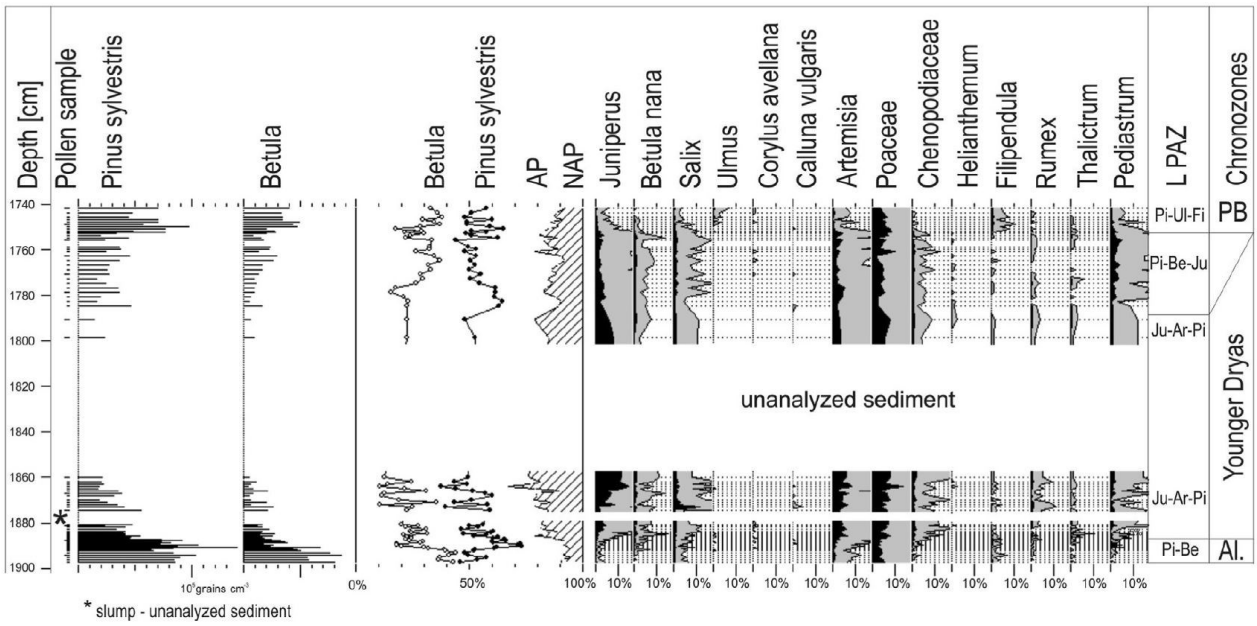

***Figure 2-6**: Bio-stratigraphy of selected pollen and algal taxa from the Lake Gościąż sequence (GOS18) for the Allerød-Younger Dryas and the Younger Dryas-Holocene transitions.*

2.5. Discussion

We performed for the first time microfacies analyses for the entire sediment profile in order to decipher environmental change based on seasonal deposition patterns in Lake Gościąż. We complemented these data with µXRF element scanning data as well as mineralogical analyses.

Late Glacial climate and environment changes were the main focus of previous studies (Goslar et al. 1993, 2000; Pazdur et al. 1995; Ralska-Jasiewiczowa et al. 1998b) and therefore, they are only briefly mentioned in further discussion.

2.5.1. Chronology and varve thickness

We provide the first chronology of Lake Gościąż profile (GOS18) based on thin sections investigation and varve counting supported by radiometric dating and pollen analysis. In a previous study, similar approach was applied only for the Younger Dryas, while on the Holocene part the chronology was obtained from core photo- graphs and only occasionally, on selected intervals, compared with thin section counting (Ralska-Jasiewiczowa et al. 1998b). Here, microfacies analyses of the sediment profile GOS18 reveal detailed seasonal deposition patterns on which the new varve chronology for Lake Gościąż is based. Our thin section data reveals that 1123 +73/-91 varves are preserved in the uppermost 520 cm of the record and another 10,229 +54/-155 varves between 758 cm and 1897 cm sediment depth (Fig. 2-5). The pollen analysis aimed to help correlate the new record from GOS18 core with the analysis performed previously. The pollen data obtained from the GOS18 profile confirms that the beginning of lake sedimentation in the deepest part of Lake Gościąż did not occur earlier than in the middle part of Allerød. At that time, pine-birch forest dominated in the vicinity of the lake. The slump of the sediment in the younger part of YD was rather rapid and short-lived, which is indicated by the undisturbed pollen record. Pollen data support varve counting and radiocarbon dating showing typical taxa for Al./YD transition. Although the YD/ PB is less unambiguous, changes within *Juniperus, Artemisia* and *Filipendula* concentrations between 1755 cm and 1749.4 cm (Fig. 2-6) along with *Betula* and *Pinus* indicated climate warming. The similarity of pollen assemblages presented in this study (Fig. 2-6) and previous research (Fig. S2-10 of supplementary materials) allows correlating these two records.

The ages for the onset of the Younger Dryas (12,620 +133/-231 varve yr BP) and the onset of annual laminations (12,834 +134/-233 varve yr BP) in our chronology are within uncertainties in agreement with published data for the onset of the Younger Dryas of 12,650 ± 90 cal. yr BP (Goslar 1998a) and for the onset of varve formation of 12,872 ± 62 cal. yr BP (Goslar et al. 1999b).

The onset of the Holocene in presented chronology is dated at 11,470 +126/-206 varve yr BP and within age uncertainties in agreement with previously reported ages from Lake Gościąż of 11,510 ± 40 cal. BP obtained through combining AMS radiocarbon dating and tree rings wiggle-matching (Goslar 1998a). These ages are in further agreement with dating from other Polish lake records like the Trzechowskie palaeolake (11,710-11,240 cal. yr BP; Wulf et al. 2013), Lake Perespilno (11,510 ± 40 cal. yr BP; Goslar et al. 1999a) and Lake Szurpiły (11,550 cal. yr BP; Kinder et al. 2020).

The lower part of our varve chronology (from the onset of the Holocene at a depth of 1749 cm up to the top of the lithozone 4) includes 8842 +46/-126 varves obtained entirely from varve counting on thin sections. In comparison, the previous study reported 8300 ± 50 varves for the interval from the Holocene onset until varve cessation.

Above the lower varve section, a 238 cm interval covering the lower part of lithozone 3 could not be varve counted because of a lack of sufficient varve preservation. The basal age of 2606 ± 80 cal. yr BP for this interval has been obtained by Bacon age modelling including three AMS radiocarbon dates from the non-varved part (Fig. 2-5). In the previous study a poorly- and/or non- varved interval also has been reported above 7.34 m (Goslar 1998b). There, the onset of varve cessation was dated at 3140 ± 120 cal. yr BP with 3211 cal. yr BP as most probable age through a combination of radiocarbon and dendro-match method (Goslar 1998a). The apparent difference of roughly 500 years for the age of the onset of the non-varved interval compared to our chronology can be explained by the improved recognition of varves in thin sections that allowed to count varves that were not identified in previous investigations. For this reason, the non-varved interval in our chronology is only 238 cm long (758-520 cm) compared to 734 cm of the non-varved interval in the previous study. Consequently, the lower varved part of GOS18 sediment profile is longer and includes about 500 varves more than reported by Goslar (1998a).

The main new achievement of our study is the identification and counting of varves in the uppermost part of the sediment record up to the year of coring (2015 CE). However, due to poor varve preservation (VQI 1) in the upper 520 cm of the sediment profile about 40% of the varves are interpolated resulting in a larger counting uncertainty than in the lower varved interval. In contrast to a previous study, where the upper part of the record was reported as non-varved (Ralska-Jasiewiczowa et al. 1998b), we were able to prove the annual character of extremely thick laminations (on average 28 mm, max 70 mm) in the upper meter (lithozone 1) through ^{137}Cs measurements. Below these upper varves, which formed after 1983 CE, an about 40 cm poorly-varved interval (bottom part of lithozone 1) was found which likely corresponds to

the non-varved interval reported by Ralska-Jasiewiczowa et al. (1998) because it formed the top of the sediments at the time of coring for the previous study.

The varve thickness in Lake Gościąż is more or less stable through the profile (sub-mm to 4-5 mm) up to ca. 3320 +89/-125 varve yr BP (~860 cm), when the sedimentation rate starts to increase (up to 70 mm $year^{-1}$ in the uppermost sediment). This increase may be related to the decreasing effect of the sediment compaction at first but the last ca. 500 years should be linked to the human activity in the catchment of Lake Gościąż. Higher sedimentation rates have been observed especially in the last 200 years and they can be linked to the development of agriculture (Ralska-Jasiewiczowa et al. 1998b) and longer periods of oxygenated bottom waters (Fojutowski et al. 2021).

2.5.2. Varve microfacies formation and their environmental implications

Lacustrine sedimentation in Lake Gościąż started in the late Allerød at a sharp transition from sandy deposits to annually laminated sediments. The occurrence of well-preserved varves (type I, lithozone 5, Figs. 3 and 4) suggests that the lake was deep at that time. During the early YD a graded layer is intercalated (Fig. 2-2, lithozone 5, 1880-1872 cm), which forms the distal part of a major mass movement deposit originating from the southern shore. This layer likely corresponds to a 60 cm thick sand layer described in previous work (Ralska-Jasiewiczowa et al. 1998b). The final phase of the Late Glacial interstadial is represented by ca. 240 well- preserved calcite-organic varves (type I, lithozone 5, Figs. 3 and 4) mostly deposited during the late Allerød followed by ca. 1130 diatom-calcite varves (type II, lithozone 5, Figs. 3 and 4) formed during the YD. While the late Allerød varves (type I) can be interpreted as presenting calm sedimentation with low inter-annual variability, the YD varves (type II) suggest eutrophication due to nutrient re-mobilization from the sediments caused by increased water mixing. Furthermore, increased varve complexity suggests more instable conditions than in the late Allerød.

The early Holocene (from 11,470 +126/-206 varve yr BP, 1749 cm) is marked by the appearance of calcite-organic varves (type III, lithozone 4c, Figs. 3 and 4). The endogenic calcite layer is followed by an organic layer that formed in the second part of the year. The colour of organic layers varied from yellow to dark brown. It seems that these changes were related to variable content of iron in the sediment that is clearly visible in the occurrence of early-diagenetic vivianite, which formation requires anoxic, organic- and iron-rich conditions in the sediments (Rothe et al. 2016).

Diatom valves appear ca. 9915 +117/-186 varve yr BP in calcite-organic varves (type IIIb, lithozone 4c, Fig. 2-4) and later (from ca. 9745 +116/-184 varve yr BP, lithozone 4c and 4b) in calcite-diatom varves (type IV, Figs. 2-3 and 2-4). The appearance of diatoms suggests increased nutrients upwelling or nutrients delivery

from the catchment either in dissolved form with water or through erosional processes. The later one can be excluded because no detrital matter was observed in the varve composition. Rare grains of quartz (Fig. 2-3) were wind-blown most likely. The higher bioproduction is also shown by a slight increase of log(Ca/Ti) and, although less pronounced, by log(Si/Ti) records at ca. 1580 cm. Appearance of pyrite and vivianite suggests organic matter presence at the bottom of the lake but also anoxic conditions at the water-sediment interference or right below it. Mn-carbonate crystals were less abundant at this time and that could suggest progressive decrease of Mn availability or changes in alkalinity but possible triggers are unknown.

The most prominent change of geochemistry occurs at the boundary of lithozones 4c and 4b at 7940 +112/-168 varve yr BP (1372 cm of the composite depth), when varve deposition changes from calcite-organic (type III, lithozone 4c) to calcite-diatom (type IV, lithozone 4b) varves. This boundary is marked by an abrupt increase of the log(Ca/Ti) and log(Si/Ti) (Fig. 2-3) which likely is related to a relative increase of reworked material. A lack of detrital layer in microfacies shows that the re-suspended calcite, which appears abundantly in the microfacies, come from the littoral zone of the Lake Gościąż basin. Lowering of the water level described by Pazdur et al. (1995) and Starkel et al. (1996) (Fig. 2-7) caused littoral exposure and thus, made the deposited material susceptible for reworking due to wind and wave activity (Dusini et al. 2009).

Climate change as a main driver of the geochemical shift at 7940 +112/-168 varve yr BP is unlikely because the timing does not correspond to any known climate change (Fig. 2-7) and the amplitude of this shift is more pronounced than the shift reflecting the major climate change at the YD/PB transition. The Holocene Thermal Maximum (HTM), however, could strengthen the local geochemical shift though increased summer temperature anomalies (Heikkilä & Seppä 2010), Fig. 2-7) which, depending on the location, occurred between 8200 cal. yr BP and 5700 cal. yr BP (Borzenkova et al. 2015). In Lake Wigry (NE Poland), Tilia and Quercus become widespread between 8000 cal. yr BP and 7000 cal. yr BP (Lauterbach et al. 2011b) that indicates the thermal maximum at that time. High summer temperatures could strengthen the summer stratification and oxygen depletion caused by abundance of phytoplankton fed by nutrients obtained from internal processes (nutrients upwelling).

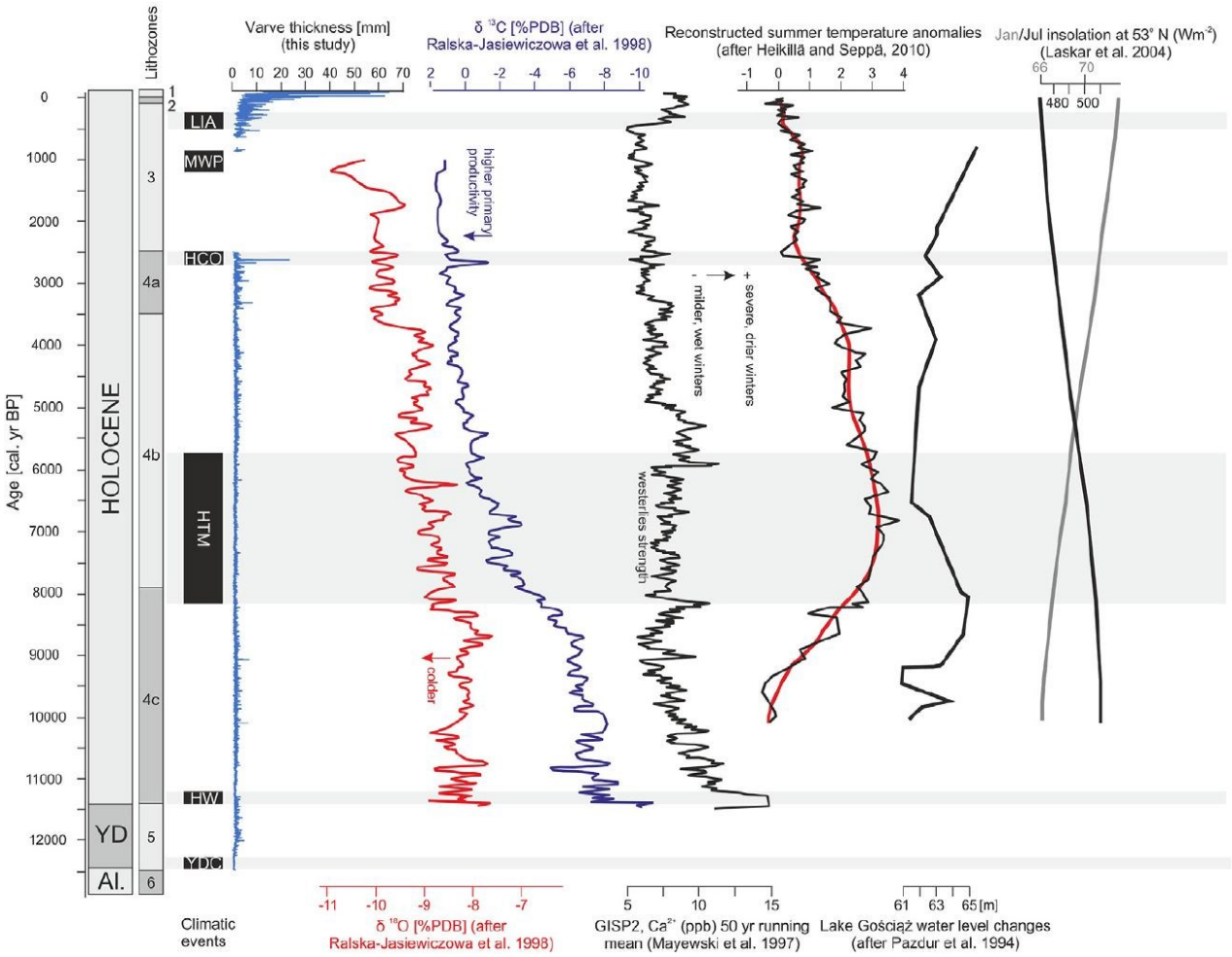

***Figure 2-7**: Possible forcing influencing the varve microfacies occurrence; YDC – Younger Dryas Cooling, HW – Holocene Warming, HTM – Holocene Thermal Maximum, HCO – Homeric Climate Oscillation, MWP – Medieval Warm Period, LIA – Little Ice Age.*

In contrast to the geochemical shift which occurred within a few years, the change within microfacies can be considered as gradual as there was a slow transition (ca. 1500 years) from calcite-organic (type III) to calcite-diatom (type IV) varves started around 8500 +113/-169 varve yr BP (transition from lithozones 4c to 4b). Calcite-organic varves (type III) were observed even a few hundred years after the geochemical shift (Fig. 2-3) and finally disappeared could be caused by the transformation of the drainage system of after 6930 +108/-163 varve yr BP (lithozone 4b). Such a change Lake Gościąż and water composition modification (Delfino & Lee 1971) or the lowering of the water level. It was previously shown (Łącka et al. 1998) that ca. 8300 cal. yr BP Mn content decreased and the isotopic composition of $\delta^{13}C$ and $\delta^{18}O$(Fig. 2-7) changed (Różański et al. 1998). That was linked to the development of the Ruda River as a main drainage of the entire "Na Jazach" system as a response to a substantial increase of precipitation in the region (Rozanski et al. 2010). The gradual filling up of the lake with sediments and increasing summer

temperatures around 8000 cal. yr BP (Heikkilä & Seppä 2010) favoured calcite precipitation and more intense primary productivity through an increase of epilimnion to hypolimnion ratio (Rozanski et al. 2010). In addition, milder and wet winters (Fig. 2-7, westerlies strength after Mayewski et al. 1997) favoured algal blooms in early spring that resulted in higher amount of deposited diatom frustules. It was shown by Bonk et al. (2015a) that in comparison to a severe winter, a mild one is followed by higher biogenic silica (diatoms) deposition.

After the shift at the 4c/4b boundary (ca. 7940 +112/-168 varve yr BP, 1372 cm), sedimentation was uniform with slight increase of varve thickness from subzone 4b up to the 4a boundary at ca. (type IV) show similar sedimentation scheme over 4480 years. The 879 cm (3460 +90/-129 varve yr BP). The calcite-diatom varves sharp boundary between organic winter and calcite-diatom spring layers (Fig. 2-4, type IVa) suggests deposition after calm period (winter) and sudden onset of biochemical carbonate precipitation due to rising temperature, the onset of the photosynthesis and water column circulation in spring (Kelts & Hsü 1978). The end of the year is reflected by a thin layer of organic matter that could be deposited in late autumn or winter under the ice cover. No significant geochemical nor lithological changes were observed at this time, but there is a gradual change in log(Ca/Ti) and log(Si/Ti) showing slow upward increase in bioproductivity. Thus, the sediment record indicates that Lake Gościąż was insensitive to short-term changes within the catchment and the state of the lake was stable from ca. 7940 +112/-168 varve yr BP to 2606 ± 80 cal. yr BP (1372-758 cm). Overall, the sedimentation occurred during warm summers (high bioproductivity) and winters with ice cover.

The onset of VQI decrease from 1 to 0 around 2606 ± 80 cal. yr BP (transition from lithozones 4a to 3, 758 cm) may have been triggered by climatic changes occurring between 2750 cal. yr BP and 2550 cal. yr BP named as Homeric Climate Oscillation (HCO), which is related to low solar activity (van Geel et al. 1999; Gray et al. 2010). The sites located in Western Europe indicate that there was a sharp increase in precipitation at that time. For instance, it was reflected in the increased varve thickness of the Meerfelder Maar lake (Martin-Puertas et al. 2012; Rach et al. 2017) in Germany, the change in vegetation composition in peatlands (van Geel et al. 1996) and the Bog burst (van Geel et al. 2014) in the Netherlands. Unlike in Western Europe, dry episodes and decline of lake waters were observed in several sites of East-Central Europe: Rąbień bog (Słowiński et al. 2016), Lake Biskupin (Piotrowski 1995; Niewiarowski & Noryśkiewicz 1999) and Stążki bog (Gałka et al. 2013) in Poland, an ice core record in a Romanian cave (Perşoiu et al. 2017) or the Mannikjarve bog in eastern Estonia (Sillasoo et al. 2007). Therefore, a decrease in varve preservation accompanied by an increased contribution of redeposited calcite is associated with a decrease in water level and deterioration of hypolimnetic anoxia. The decline of the water table of Lake

Gościąż (Fig. 2-7 after Pazdur et al. 1994) created favouring conditions for deeper water column mixing that resulted in longer periods of oxygenated bottom and the lack of varve preservation. In addition to lower water stands, continuous filling of the basin in sediment, and increased windiness in central Europe (Dräger et al. 2017) caused redeposition of the material from shallower parts of the lake bottom.

One may assume that changes in varve preservation were related to anthropogenic impact but in Lake Gościąż vicinity there was no significant human activity at that time (Ralska-Jasiewiczowa & van Geel 1998).

Between 520 cm and 130 cm (from 1065 +109/-120 varve yr BP to 1969 +8/-12 CE, upper part of lithozone 3 and lithozone 2) the varve preservation improved (VQI 2 and 3). This improvement was, however, gradual which suggests that the factor leading to better varve preservation started to influence the area of Lake Gościąż before 1065 +109/-120 varve yr BP (lithozone 3). The increased varve quality at that time was observed in a previous study (Goslar, 1998a) and was linked to the intensification of human activity in the Early Medieval period. The VQI improves upwards and this coincides with the prominent increase of phosphorus starting from ca. 600 cal. yr BP (Goslar 1998b). The anthropogenic influence affected the lake eutrophication, that resulted in a growing oxygen deficit and better varve preservation. Further improvement of varve preservation might have been related to the cool climatic period known as the Little Ice Age (LIA). According to the documentary data, the LIA in Poland began ca. mid-16th century and ended in the second half of the 19th century (Przybylak 2016). The longer persistence of ice cover on the lake prevented the water column from mixing which extended anoxic conditions in the hypolimnion and, in turn, fostered varve preservation. On the other hand, cold summers during the LIA could have caused higher turbulence and less stable summer stratification. This is visible in the varve structure (type IVb, lithozone 2, Fig. 2-4) through multiple calcite laminae and the autumn-winter sublayer being mixed. Calcite precipitation was possible due to, among others, changes in water chemistry caused by the development of phytoplankton. Hence, the observed multiple algal-calcite layers within one year were possible due to water column mixing and related upwelling of nutrients as well as an increase in insolation and therefore also in temperature during the second part of the year (Fig. 2-7). A similar mechanism has been reported from Lake Żabińskie NE Poland (Bonk et al. 2015a). Increased quartz input with decrease of log(Ca/Ti) and log(Si/Ti) values around 190 varve yr BP (transition from lithozones 2 to 1) suggest more detrital delivery from the catchment that in turn caused higher sedimentation rate.

The gradual change between lithozones 2 and 1 covers 40 cm, which is 35 years long (from 1933 CE to 1968 +8/-12 CE) and is accompanied by the decrease of the varve preservation. Calcite-organic varves

(type V, lithozone 1, Fig. 2-4) are composed of one calcite lamina and mixed second lamina and in some parts the sediment is homogenous. With the shallowing of the water column, the high amount of reworked material consisting of calcite grains and plant tissues suggests intensive column mixing. According to the ^{137}Cs-based chronology, 140 cm of sediment was deposited during the last ~65 years. The high sedimentation rate observed in the top part of the profile could be linked to the increased human impact in the area of Lake Gościąż, which resulted in the eutrophication of the lake water and intense resuspension of material from the littoral zone of the lake.

2.6. Conclusions

The development of new techniques as microfacial analysis of varves and µXRF scanning allowed for the chronology revision of the iconic Lake Gościąż record located in Poland. We developed for this record the first chronology based on varve counting using petrographic thin sections. Due to the presence of a non-varved section, we combined varve counting, radiometric methods and age-depth modelling performed with Bacon software. This approach allowed to revise the varve chronology for the upper 1065 years and to identify extremely thick varves up to present times. Furthermore, thin section analyses enabled to count 500 additional varves in the interval 758-520 cm that were not recognized in previous studies. In total, the part of the sediment record that could not be varve counted was reduced by ca 1500 years. We provided description of five major types varve microfacies with different level of complexity for the whole GOS18 record, from the Allerød to the present time. Our observations show that the Holocene microfacial changes were gradual. There were several abrupt shifts in geochemistry related to lake level fluctuations, the gradual basin filling with the sediment, long periods of oxygenated water as well as human impact. The most pronounced geochemical shift at 7940 +112/-168 varve yr BP could have been strengthened, but not caused, by the Holocene Thermal Optimum which was observed around that time in different locations across Poland. We suspect that the onset of the low varve preservation observed between 2750 cal. yr BP and 2550 cal. yr BP was related to the lowering of the lake level during the Homeric Climate Oscillation. The longer persistence of ice cover and colder and windier summer during the Little Ice Age are reflected in the improved varve preservation and structure. The extremely thick varves at the top of the profile are related to increased eutrophication, depletion of the oxygen at the lake bottom and human activity. The new chronology of the Lake Gościąż sediment record provides a unique opportunity to revise existing records in detail and to extend interpretations of climate change and environmental transformations. Correlation with previous record is possible due to similarity of stratigraphy and pollen data, and hence, previous climate reconstructions and interpretations can be updated. Moreover, the new GOS18 record

has the potential to be included with the other varved sequences (i.e. Meerfelder maar- Rehwiese - Tiefer See, Lake Czechowskie) in a transect of paleoclimatic and paleoenvironmental records across Europe.

Funding sources

This work was supported by the National Science Centre, Poland [2015/19/B/ST10/03039] and DAAD Scholarship [91695826] awarded to Alicja Bonk.

Data availability

Data is available in PANGAEA database: Varve chronology (https://doi.org/10.1594/PANGAEA.924198), varve thickness (https://doi.org/10.1594/PANGAEA.924199), pollen data (https://doi.org/10.1594/PANGAEA.924200), and VARDA database (Ramisch et al., 2020): https://varve.gfz-potsdam.de/database/ details/538cd388-8030-415a-982a-a21ba50c99eb.

Declaration of competing interest

The authors declare that they have no known competing financial interests or personal relationships that could have appeared to influence the work reported in this paper.

Acknowledgements

We would like thank project “Gościąż” team members for their help, comments and fruitful discussions. Special thanks go to Brian Brademann and Matthias Köppl for their help in the field, and Sebastian Tyszkowski for providing the bathymetric map.

2.7. Supplementary material

***Table S2-3**: Marker layers for composite profile GOS18. Numbers in bold shows the core changes. In the lines with two numbers in bold, the first number shows the first marker layer and the second number, the second marker layer.*

Master core				Core depth [cm]		Composite depth [cm]		Marker layers
Exp	hole	core	section	From	To	Top	bottom	
GOS15	S	1		0	**44**	0.0	44.0	**ML0**
GOS15	A	1	1	**23**	92	44.0	113.0	
GOS15	A	1	2	92	**112**	113.0	133.0	**ML1**
GOS15	B	1	1	**14.5**	86	133.0	204.5	
GOS15	B	1	2	86	**173.5**	204.5	292.0	**ML2**
GOS15	A	2	1	**59.5**	100	292.0	332.5	
GOS15	A	2	2	100	**111**	332.5	343.5	**ML3**
GOS15	B	2	1	**14**	95	343.5	424.5	
GOS15	B	2	2	95	**167**	424.5	496.5	**ML4**
GOS15	A	3	1	**44**	100	496.5	552.5	
GOS15	A	3	2	100	**131.5**	552.5	584.0	**ML5**
GOS15	B	3	1	**32.5**	91	584.0	642.5	
GOS15	B	3	2	91	**180**	642.5	731.5	**ML6A**
GOS15	C	1	1	**13.5**	107	731.5	825.0	
GOS15	C	1	2	107	**113.5**	825.0	831.5	**ML8**
GOS15	A	4	2	**171.5**	**190.6**	831.5	850.6	**ML8 - ML9**
GOS15	C	1	2	**133**	**172**	850.6	889.6	**ML9 - ML10**
GOS15	B	4	2	**127**	**175**	889.6	937.6	**ML10 - ML11**
GOS15	C	2	1	**11.5**	**71.5**	937.6	997.6	**ML11 - ML12**
GOS15	B	5	1	**25.7**	96	997.6	1067.9	
GOS15	B	5	2	96	**185**	1067.9	1156.9	**ML13A**
GOS15	C	3	1	**9.5**	**88.5**	1156.9	1235.9	**ML13A - ML15**
GOS15	B	6	1	**42.5**	**73**	1235.9	1266.4	**ML15 - ML16**
GOS15	C	3	2	**118.5**	**182**	1266.4	1329.9	**ML16 - ML17**
GOS15	B	6	2	**137**	**180.5**	1329.9	1373.4	**ML17 - ML18**
GOS15	C	4	1	**16.5**	**102.5**	1373.4	1459.4	**ML18 - ML19**
GOS15	B	7	1	**60**	**65**	1459.4	1464.4	**ML19 - ML20**
GOS15	C	4	2	**107.5**	**163**	1464.4	1519.9	**ML20 - ML21**
GOS15	B	7	2	**122**	**181**	1519.9	1578.9	**ML21 - ML22**
GOS15	C	5	1	**22.5**	**74**	1578.9	1630.4	**ML22 - ML23**
GOS15	B	8		**38**	**166**	1630.4	1758.4	**ML23 - ML24**
GOS15	A	9	1	**14**	**58**	1758.4	1802.4	**ML24 - ML25**
GOS15	B	9	1	**18**	**84**	1802.4	1868.4	**ML26**
GOS18	H	5	1	29.7	60	1868.4	1898.7	
GOS18	H	5	2	60	151	1898.7	1989.7	

***Table S2-4**: Concentrations of ^{137}Cs activity in sediment profile from Gościąż Lake.*

Core No.	Depth (cm)	^{137}Cs activity (Bq kg^{-1})
S1	7	7.55+/-4.54
S1	14	6.15+/-4.25
S1	28	9.42+/-4.13
S1	32	7.79+/-4.55
S1	42	14.81+/-4.4
A1-1	49	11.62+/-4.43
A1-1	55	26.05+/-10.06
A1-1	60	23.72+/-8.79
A1-1	66	27.65+/-4.23
A1-1	76	30.52+/-4.44
A1-1	84	30.66+/-4.56
A1-1	90	34.75+/-6.12
A1-1	97	17.31+/-3.35
A1-1	103	20.45+/-3.2
A1-2	115	24.24+/-5.52
A1-2	125	14.96+/-3.42
A1-2	133	16.65+/-4.66
B1-1	140.5	28.94+/-6.73
B1-1	155.5	under detection limit
B1-1	175.5	under detection limit

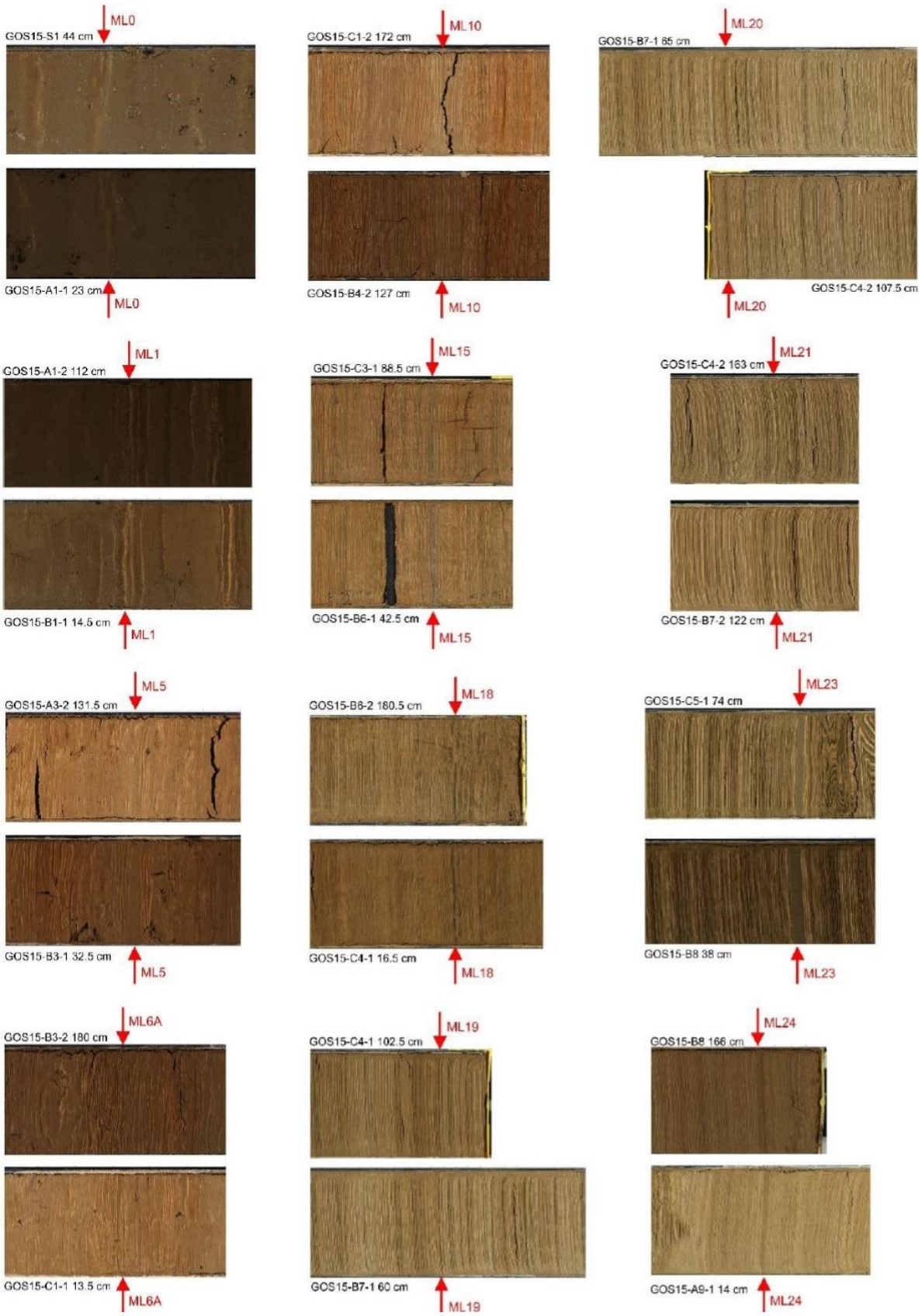

***Figure S2-8**: Examples of section correlation using marker layers.*

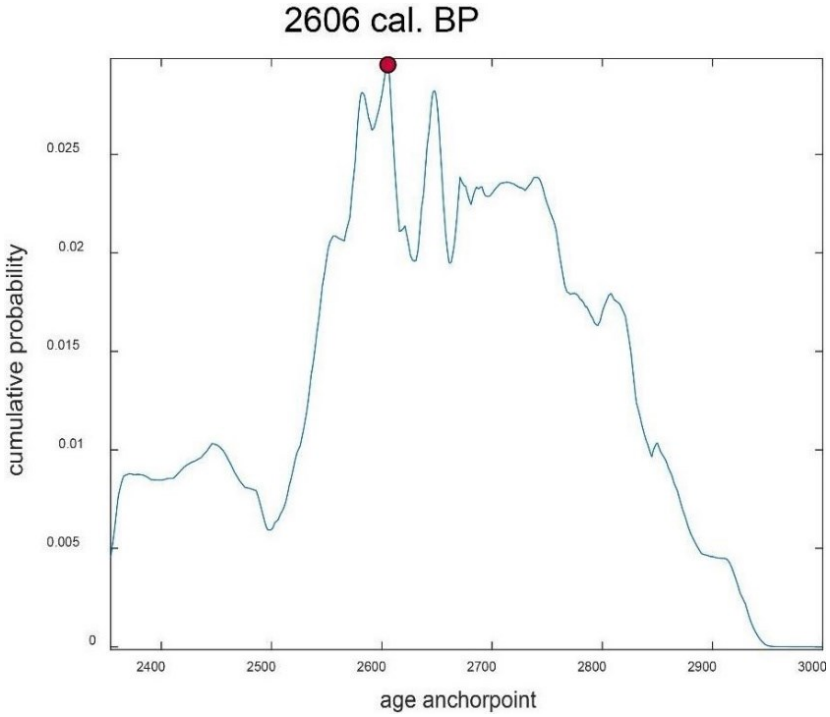

***Figure S2-9**: Cumulative probability of Poz-95790.*

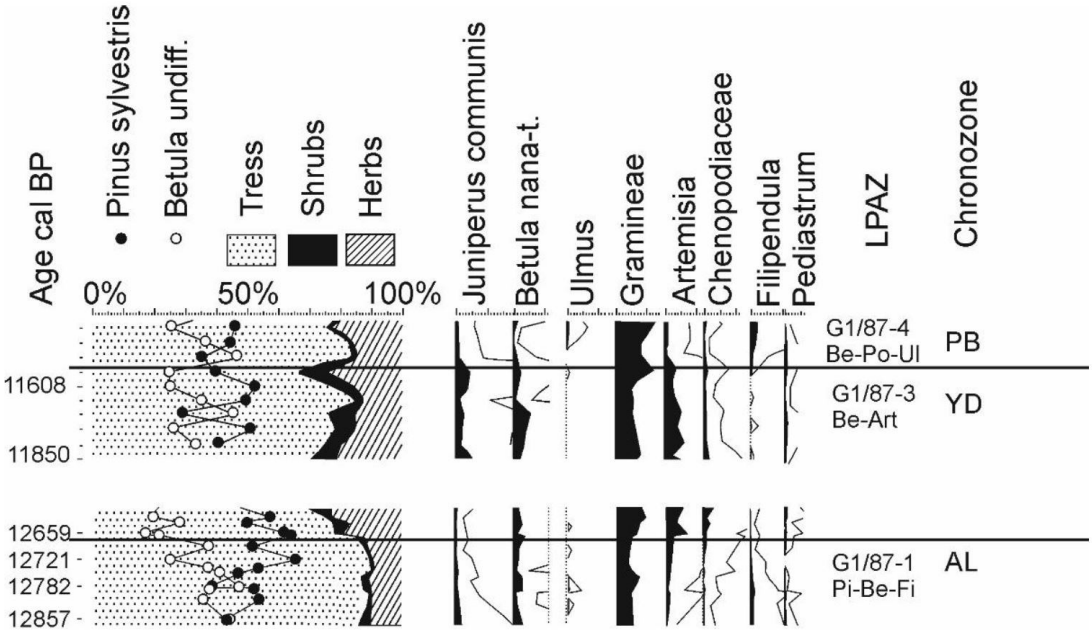

***Figure S2-10**: Simplified polen diagram for the core G1/87 after* Ralska-Jasiewiczowa et al. (1998).

3. New insights into lake responses to rapid climate change: The Younger Dryas in Lake Gościąż, central Poland

Daniela Müller[1,2], Rik Tjallingii[1], Mateusz Płóciennik[3], Tomi P. Luoto[4], Bartosz Kotrys[5], Birgit Plessen[1], Arne Ramisch[1], Markus J. Schwab[1], Mirosław Błaszkiewicz[6], Michał Słowiński[6] and Achim Brauer[1,2]

(1) Section Climate Dynamics and Landscape Evolution, GFZ German Research Centre for Geosciences, Telegrafenberg, Potsdam 14473, Germany

(2) Institute of Geosciences, University of Potsdam, Karl-Liebknecht-Str. 24-25, Potsdam 14476, Germany

(3) Department of Invertebrate Zoology and Hydrobiology, University of Łódź, Banacha st. 12/16, Łódź 90-237, Poland

(4) Faculty of Biological and Environmental Sciences, Ecosystems and Environment Research Programme, University of Helsinki, Niemenkatu 73, 15140 Lahti, Finland

(5) Polish Geological Institute - National Research Institute, Pomeranian Branch in Szczecin, Wieniawskiego 20, 71-130 Szczecin, Poland

(6) Department of Environmental Resources and Geohazards, Institute of Geography and Spatial Organization, Polish Academy of Sciences, Kopernika 19, Toruń 87-100, Poland

Published in Boreas (DOI 10.1111/bor.12499)

Abstract

The sediment profile from Lake Gościąż in central Poland comprises a continuous, seasonally resolved and exceptionally well-preserved archive of the Younger Dryas (YD) climate variation. This provides a unique opportunity for detailed investigation of lake system responses during periods of rapid climate cooling (YD onset) and warming (YD termination). The new varve record of Lake Gościąż presented here spans 1662 years from the late Allerød (AL) to the early Preboreal (PB). Microscopic varve counting provides an independent chronology with a YD duration of 1149 +14/-22 years, which confirms previous results of 1140 ± 40 years. We link stable oxygen isotopes and chironomid-based air temperature reconstructions with the response of various geochemical and varve microfacies proxies especially focusing on the onset and termination of the YD. Cooling at the YD onset lasted ~180 years, which is about a century longer than the terminal warming that was completed in ~70 years. During the AL/YD transition, environmental proxy data lagged the onset of cooling by ~90 years and revealed an increase of lake productivity and internal lake re-suspension as well as slightly higher detrital sediment input. In contrast, rapid warming and environmental changes during the YD/PB transition occurred simultaneously. However, initial changes such as declining diatom deposition and detrital input occurred already a few centuries before the rapid warming at the YD/PB transition. These environmental changes likely reflect a gradual increase in summer air temperatures already during the YD. Our data indicate complex and differing environmental responses to the major climate changes related to the YD, which involve different proxy sensitivities and threshold processes.

Keywords

A new 1662-year seasonal sediment record from late Allerød to early Preboreal from varved Lake Gościąż; Chironomid-based air temperature reconstructions agree well with stable oxygen isotopes; Higher interannual variability of sediment deposition during the Younger Dryas; Delayed lake response to gradual cooling at the onset of the Younger Dryas; Decadal-scale variability at the Late Glacial/Holocene transition

3.1. Introduction

Lakes are considered as sentinels of climate change since they respond immediately, but also incorporate effects of climate change within the catchment (Adrian et al. 2009, 2016). However, lake responses to climate change are complex, due to the involvement of tightly coupled physical, chemical and biological processes that operate on a wide range of time scales from days to millennia (Ramisch et al. 2018). Numerous studies based on modern observations address how different compartments of lake systems respond to climate change (e.g. Adrian et al. 2016). However, there are still synergistic and complex lake response mechanisms that are not fully understood (Havens & Jeppesen 2018). In particular, ecosystem changes to abrupt climate change yet remain elusive (Botta et al. 2019).

Since major hemispheric climatic shifts did not occur during historical times, we need to apply a forensic approach and investigate these climatic changes in lake sediments in the geological past. An ideal time interval for such investigations is the Younger Dryas (YD) cold period at the end of the Last Glaciation, which marks the last major climate fluctuation in the northern hemisphere (e.g. Brauer et al. 2008; Denton et al. 2010; Clark et al. 2012; Rach et al. 2014). The YD is characterized by pronounced seasonality with strong winter cooling (Isarin et al. 1998; Denton et al. 2005) and relatively mild but short summers (Schenk et al. 2018). Changes in seasonality are considered crucial for lake system response, because spring and early summer is a critical time window for the timing and rates of overturn and related biological effects (Peeters et al. 2007; Adrian et al. 2016). Therefore, varved lake sediment records with seasonal time resolution are most suitable recorders of seasonal effects. However, there are only a few lake records reported that are completely varved throughout the YD and document the rapid climatic and environmental changes at the YD transitions with seasonal resolution. In Europe, these lakes include Lake Gościąż (Ralska-Jasiewiczowa et al. 1987, 1998b; Goslar et al. 1989), Meerfelder Maar (Brauer et al. 1999) and palaeolake Rehwiese (Neugebauer et al. 2012). Pioneer studies were carried out on the Lake Gościąż varves starting in the late 1980s (Ralska-Jasiewiczowa et al. 1987; Goslar et al. 1989) that revealed fundamental results on YD varve dating, radiocarbon calibration and vegetation change (Goslar et al. 1989; Ralska-Jasiewiczowa et al. 1998b). Based on varve counting of Lake Gościąż sediments even changes in atmospheric radiocarbon concentrations during the YD were determined (Goslar et al. 1995, 1999b). In addition, regional vegetation changes related to the YD were reconstructed in great detail (Goslar et al. 1992; Ralska-Jasiewiczowa et al. 1992, 1998a, 2003). A truly seminal study was the reconstruction of environmental changes at 1-4 year resolution during the transition to the Holocene (Ralska-Jasiewiczowa et al. 2003) based on pollen and geochemical data. We adopt the principal approach of this study, but include novel analytical methods including continuous X-ray fluorescence (XRF) core scanning and μ-XRF

mapping, continuous microfacies analyses and chironomid-based temperature reconstructions. We further extend the time interval to the entire YD, including the transition from the Allerød (AL) into the YD. This study is part of a larger project re-visiting the entire Holocene and Lateglacial sediment record from Lake Gościąż (Bonk et al. 2021). The main goal of this study is to compare the mechanisms and dynamics of lake system responses to major cooling and warming events. We distinguish between temperature and environmental proxies to decipher in detail the succession of lake-internal and catchment responses to large-scale temperature changes.

3.2. Study area

Lake Gościąż (GOS) is located about 80 km WNW of Warsaw in central Poland (52°35'N, 19°21'E) (Fig. 3-1). It is situated at 64.3 m a.s.l. and has a surface area of 41.7 ha, a maximum water depth of 22 m and a catchment area of 588 ha. GOS is the largest lake of the Na Jazach four lake system, which is today connected by the Ruda stream, draining into the Vistula River (since 1970 to the Włocławek Reservoir). The lake is predominantly groundwater fed with 80-90% of present day inflow from groundwater (Gierszewski 1993; Giziński et al. 1998; Rozanski et al. 2010). GOS is a kettle hole lake within a subglacial channel that formed during the Last Glaciation. The last ice sheet advance of the Scandinavian Ice Sheet (Late Weichselian ice sheet) in this area occurred during the Poznań phase (20-19 cal. ka BP; Marks et al. 2016), leading to the formation of subglacial channels and burial of dead ice during the final stage of ice sheet advance and later recession (Błaszkiewicz et al. 2015). Melting of buried dead ice blocks resulted in formation of kettle hole lakes like Lake Gościąż. Finely laminated lacustrine sediments in this lake are preserved since the late Allerød (Ralska-Jasiewiczowa et al. 1987, 1998b; Goslar et al. 1989).

The lake catchment consists primarily of glaciofluvial sediments and features also aeolian forms (e.g. dunes) (Rychel et al. 2018; Kruczkowska et al. 2020). Present day vegetation predominantly is composed of pine forests and subordinated also by aquatic, reed swamp, mire, meadow, grassland, scrub, ruderal and segetal communities (Kępczyński & Noryśkiewicz 1998). The monthly mean surface air temperature ranges from -2.8 °C in January to +18 °C in July (Wójcik & Przybylak 1998; Rozanski et al. 2010), while the annual mean surface air temperature is 8.2 °C (Rozanski et al. 2010). The monthly mean precipitation ranges from 25.6 mm (February) to 82.5 mm (July) with an annual mean of 540 mm (Wójcik & Przybylak 1998). Westerly winds prevail in the area of the lake (Wójcik & Przybylak 1998).

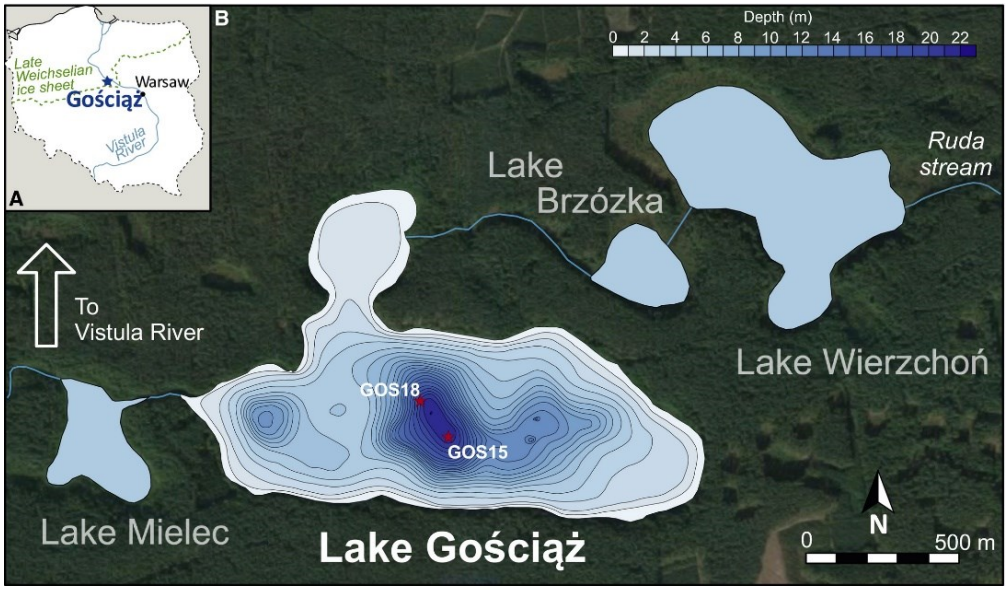

***Figure 3-1**: A. Overview map of Poland including location of Lake Gościąż, Warsaw, the Vistula River and the maximum extent of the Late Weichselian ice sheet according to Ralska-Jasiewiczowa et al. (1998c). B. Aerial photograph of the study site, location of Lake Gościąż as part of the Na Jazach four lake system and lake bathymetry. Coring sites in 2015 (GOS15) and 2018 (GOS18) are marked with red stars.*

3.3. Material and methods

3.3.1. Coring

Coring was conducted with an UWITEC Piston Corer during two coring campaigns in 2015 (GOS15) and 2018 (GOS18) (Fig. 3-1). In 2015, three parallel sediment cores (A, B and C) were obtained from the southern section of the deepest part of the lake basin at 21.3-21.5 m water depth. Since the sediments were disturbed by a ~2 m thick mass movement deposit in the lowermost part of the cores (Fig. S3-10), five new parallel sediment cores (D, E, G, H, I) were obtained in 2018 from the north-western part of the deep basin at 19.5-21.6 m water depth, because this location is more distal with respect to the mass-wasting event that caused the major mass movement deposit. A composite profile with a total length of 1897 cm was established for the finely laminated lacustrine sediments using cores GOS15-A, -B, -C and GOS18-H (Bonk et al. 2021). This study focuses on the lowermost laminated sediments between 1717.8 and 1897 cm depth covering the beginning of limnic sedimentation from the late Allerød (AL) to the early Preboreal (PB) (see table S3-1 and Fig. S3-10).

3.3.2. Microfacies analyses

Microfacies analyses were performed on 26 overlapping large-scale thin sections prepared from 10 cm long freeze-dried and resin impregnated sediment slices (Brauer & Casanova 2001). The analyses included

varve counting and measurements of varve and sublayer thickness based on determination of varve composition, structure and boundaries. We defined a varve quality index (VQI) from VQI 0 (no varve preservation) to VQI 3 (perfect varve preservation with sharp boundaries) that was allocated to each varve. Microscope analysis was conducted with an Axioplan 2 and Axiolab pol imaging microscope with parallel and polarized light using magnifications between 50- and 400x. Thin section photographs were taken with an Olympus BX53F microscope, connected to an Olympus DP72 camera.

3.3.3. Chronology

A floating varve chronology was established by microscopic layer counting on large-scale thin sections. Counting uncertainties are calculated from comparing three independent counts. The count C2 is considered as most accurate, because layer thickness was precisely measured (Martin-Puertas et al. 2014) and was thus used as reference. The counting difference from the other two counts (C1, C3) was calculated for each thin section and summed up. It was distinguished between negative differences (fewer counted varves; under-counting) and positive differences (more counted varves; over-counting). Maximum over- and undercounts are given as counting uncertainty. The varve chronology presented in this study is an integrated part of a long Holocene floating chronology including more than 10,000 varves that has been anchored to the absolute time scale through radiocarbon dating and age modelling with Bacon (Bonk et al. 2021).

3.3.4. XRF element scanning

Non-destructive XRF core scanning was performed on smoothed surfaces of fresh sediment cores using an ITRAX XRF Core Scanner (Croudace et al. 2006) at GFZ Potsdam. Measurements were obtained every 200 µm using a Cr-X-ray source (30 kV, 30 mA) and 10 s measurement time. Element intensities are acquired in counts per second (cps) and displayed as log-ratios that resemble variations of geochemical composition (Tjallingii et al. 2007; Weltje & Tjallingii 2008; Weltje et al. 2015).

For direct comparison of the sediment composition with microfacies analyses, µ-XRF element mapping was performed on two impregnated sediment blocks that were also used for thin section preparation. The two selected samples cover the onset and termination of the YD. Element mapping was conducted with a Bruker M4 Tornado µ-XRF scanner that is equipped with a Rh X-ray source (50 kV, 600 µA) and poly-capillary X-ray optics generating a spot size of approximately 20 µm. Measurements were obtained every 50 µm using a 30 ms measurement time. Normalized element intensities are used to visualize relative element abundances as 2D maps. Both XRF analyses are of sub-annual resolution.

3.3.5. Chironomid analysis and air temperature reconstruction

Chironomidae subfossils were collected from a total of 233 samples from the composite profile. Samples that contained less than 50 head capsules (hc) as required for robust reconstruction (Quinlan & Smol 2001) were merged and also labelled as 'samples'. For this reason, the sample resolution of our temperature reconstruction ranges from 0.5 to 6 cm and the temporal resolution between 3 and 68 varves per sample. For a total of 31 samples the required number of 50 hc was not obtained even after sample merging (table S3-2). Nevertheless, these samples were still included in the reconstruction because either the hc number was very close to 50 and/or the results of temperature reconstruction were consistent with the results based on adjacent samples in which the number of hc reached at least 50. The lowest hc number used for temperature reconstruction is 30 and the highest is 170 with a mean of 61 hc per sample. Two different training sets were used for mean July air temperature (MJAT) reconstructions – the Swiss-Norwegian-Polish Training Set (SNP TS) (Kotrys et al. 2020) and the East European TS (EE TS) (Luoto et al. 2019). The SNP TS includes 357 lakes, 134 taxa and covers the 3.5-20.1 ˚C temperature range. The EE TS includes 212 lakes, 142 taxa and covers the 11.3-20.1 ˚C temperature range. Both TS use the Weighted Averaging-Partial Least Squares transfer function (WA-PLS). The SNP TS root mean squared error of prediction (RMSEP) and R^2_{jack} for the WA-PLS component 3 is 1.39 ˚C and 0.91, respectively and the EE TS RMSEP and R^2_{jack} for the WA-PLS component 2 equals 0.88 °C and 0.88, respectively (Luoto et al. 2019; Kotrys et al. 2020). The temperature reconstructions were carried out with C2 software (Juggins 2007).

3.3.6. Stable isotopes

Stable isotopes of oxygen in carbonates ($\delta^{18}O_{carb}$) and of carbon in bulk organic matter ($\delta^{13}C_{org}$) were determined on bulk sediment samples contiguously taken at 1 cm resolution, except for the sections 1737.4-1757.4 and 1880.2-1891.7 cm depth, which were sampled at 0.5 cm resolution. The temporal resolution of the samples varies between ~4-14 varves cm^{-1} in the intervals from 1717.4-1737.4 and 1757.4-1872.3 cm, ~18-23 varves cm^{-1} from 1891.7 to 1897 cm and ~8-24 varves cm^{-1} in the intervals from 1737.4-1757.4 and 1880.2-1891.7 cm. All samples were freeze-dried, manually ground and homogenized. Measurement of $\delta^{18}O_{carb}$ was performed by an automated carbonate device (KIEL IV) connected to a MAT253 Isotope Ratio Mass Spectrometer (IRMS, ThermoFischer Scientific). $\delta^{13}C_{org}$ was determined after in situ de-carbonization in Ag-capsules first with 3% and second with 20% HCl using an automatic elemental analyser (NC2500 Carlo Erba) coupled with a ConFlowIII interface on a DELTAplusXL IRMS. Both isotope compositions are given relative to the VPDB (Vienna PeeDee Belemnite) standard. $\delta^{18}O_{carb}$ was calibrated against NBS-19 and an internal reference sample (C1), while $\delta^{13}C_{org}$ was calibrated against IAEA-CH7 and

an elemental isotope standard (Urea) and was proved with an internal soil reference sample (Boden3) and Pepton (PEP). Standard errors are 0.06‰ for $\delta^{18}O_{carb}$ and 0.2‰ for $\delta^{13}C_{org}$.

3.4. Results

3.4.1. Lithology

A detailed lithological description of the entire new composite profile is given by Bonk et al. (2021). This study focuses on the interval between 1717.8 and 1897 cm (Fig. 3-2), which comprises lithozones 5a and 5b (1749-1897 cm) and the lower 31.2 cm of lithozone 4 (1717.8-1749 cm) (Fig. S3-10). Briefly summarized, a sharp boundary marks the transition between the basal glacial sands of lithozone 6 and the finely laminated lacustrine sediments of lithozone 5. The transition between lithozones 5b and 5a at ~1885 cm is marked by a colour change of the couplets from light brown and beige to brown and beige. A ~7 cm thick grey-brown graded layer occurs at 1879.6 cm, which is covered by a discrete grey silt-clay layer of ~2 mm thickness. This discrete layer is similar to the layer covering the thick slump deposits observed in cores located closer to the southern shore. Therefore, we interpret the graded layer as distal deposit of a large mass wasting event. The transition from lithozone 5 to lithozone 4 at 1748.6 cm depth is characterized by a sharp and distinct colour change due to the sudden appearance of dark sublayers. The upper boundary of our study interval was defined at a succession of two varves with thick calcite sublayers that form a discrete marker horizon.

3.4.2. Chronology and Younger Dryas definition

The varve chronology of our study interval is the lowest part of a new floating varve chronology for Lake Gościąż that reaches from the Lateglacial to the Late Holocene and has been anchored to the absolute time scale by age modelling and radiocarbon dating (Bonk et al. 2021). The chronology of our study interval includes the lowest 1662 +14/-22 varves of this overall chronology and comprises the period from the onset of lacustrine sedimentation at 12,834 +134/-235 to 11,173 +123/-204 cal. a BP (Fig. 3-2A). The uncertainty for the absolute ages is due to radiocarbon age modelling of a non-varved interval between ~1000 and 2600 cal. a BP (Bonk et al. 2021). In comparison, internal varve counting uncertainty in the study interval is very low due to the mostly excellent varve preservation (mean VQI of 2.6).

In the previous study of Lake Gościąż, the YD boundaries have been defined in the centre of the major shifts in $\delta^{18}O$ of bulk carbonate, nearly coinciding with vegetation changes (Ralska-Jasiewiczowa et al. 1992). We adopt this YD definition, since our record exactly reproduces the published $\delta^{18}O_{carb}$ YD signal

(Kuc et al. 1998) allowing precise correlation of the YD boundaries (Fig. 3-2B). According to this definition the YD is dated at 12,620 +133/-231 cal. a BP to 11,470 +126/-206 cal. a BP in our age model. The late Allerød encompasses 215 varves (1886.4-1897 cm), the YD 1149 varves (1748.5-1886.4 cm) and the early Preboreal 298 varves (1717.8-1748.5 cm).

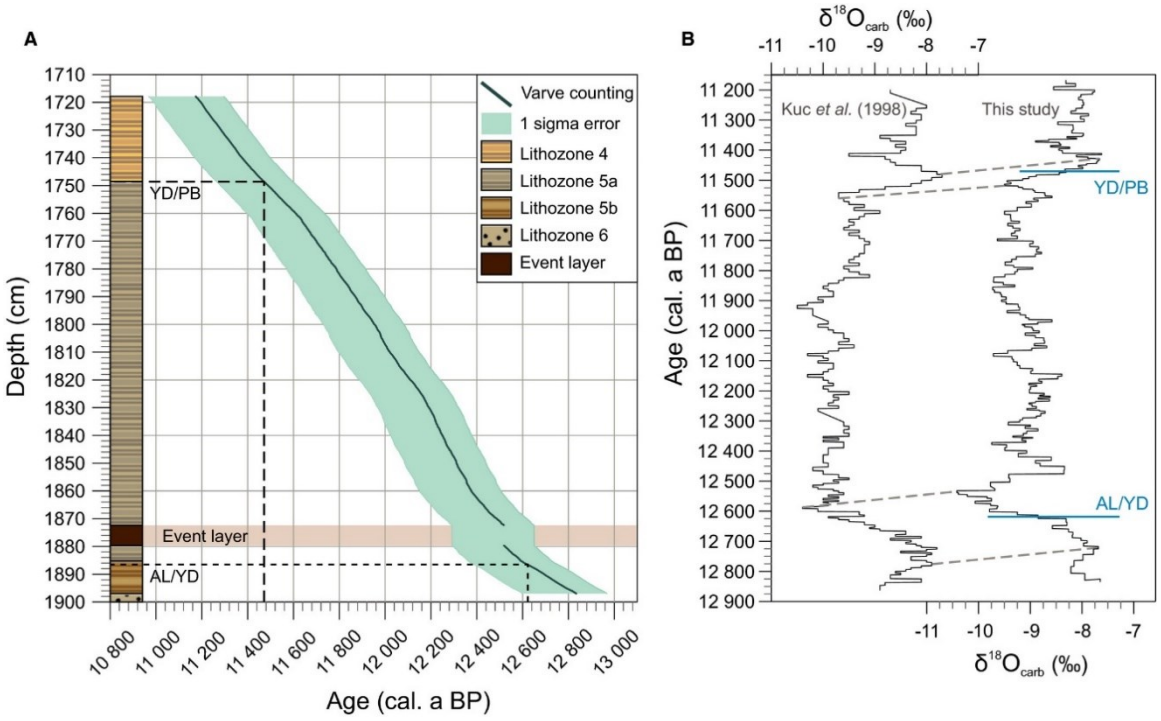

***Figure 3-2**: A. Floating varve chronology for our study interval. Absolute ages are derived from age modelling and radiocarbon dating* (Bonk et al. 2021)*, causing the largest portion of age uncertainties. The varve counting uncertainty is lower (+14/-22) and not possible to show in this figure. Lithological profile on the left. YD/PB = Younger Dryas/Preboreal; AL/YD = Allerød/Younger Dryas. B. Correlation of stable oxygen isotope data from Lake Gościąż with independent chronologies: previous study* (Kuc et al. 1998) *on the left and this study on the right. Dashed grey lines mark the correlation of both curves. Positions of the YD boundaries as defined in our study are marked with blue lines.*

3.4.3. Microfacies analyses

The highest VQI is obtained for the PB (2.8) and mostly during the early YD a few intervals with lower VQI are found (Fig. 3-4).

3.4.3.1. Varve types

The studied sediment section consists primarily of autochthonous material and two calcite varve microfacies types are distinguished: calcite-organic varves (type I) and diatom-calcite varves (type II) (Fig. 3-3). Calcite-organic varves appear slightly different in the lower and upper parts of the study interval. Thus, two sub-types (Ia and Ib) are differentiated.

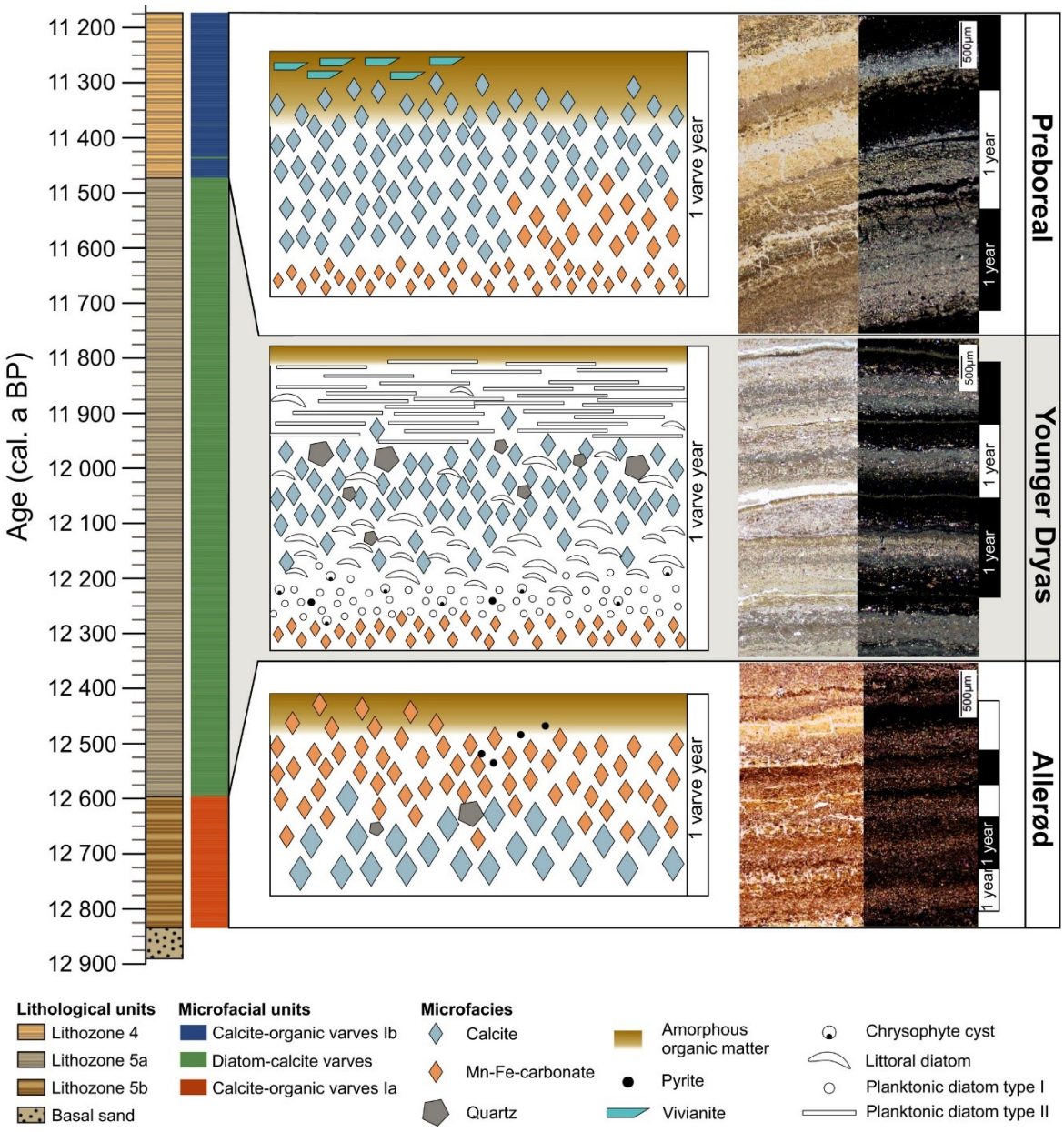

***Figure 3-3**: Left: lithology and varve type distribution over the profile. Centre: microfacies models of calcite-organic varves within the Allerød (subtype Ia) and the Preboreal (subtype Ib), as well as diatom-calcite varves (Younger Dryas). Right: thin section pictures of the different microfacies types (left: non-polarized light, right: polarized light).*

3.4.3.2. Varve type I: calcite-organic varves

The calcite-organic microfacies (subtype Ia) occurs between 1885.4-1897 cm (12,597-12,834 cal. a BP; Fig. 3-3) in 239 varves and comprises up to three sublayers. The sedimentation cycle starts with a sublayer of white idiomorphic calcite grains of 10-20 µm in size, which rarely includes a few scattered quartz grains. The following sublayer consists of fine-grained (2-5 µm) brown-yellowish and rounded grains resembling Mn-Fe-carbonates and rarely includes pyrite framboids. This sublayer only occurs in 58 varves primarily in

the lower part of this interval. The sedimentation cycle terminates with an amorphous organic matter sublayer, which includes scattered brown-yellowish carbonate grains that form the sublayer below.

The calcite-organic microfacies (subtype Ib) appears in 295 varves from 1748.6 cm until the top of the study interval (11,472-11,173 cal. a BP; Fig. 3-3). Similar to subtype Ia, the ideal sedimentation cycle encompasses three sublayers including (i) an idiomorphic calcite sublayer at the base followed by (ii) an amorphous organic matter sublayer, and (iii) a sublayer of brown-yellowish rounded carbonate, which however, appears only in 122 varves of this facies type. The main difference to subtype Ia is that (i) the idiomorphic calcite crystals in the basal sublayer are generally finer grained (2-10 µm), (ii) the amorphous organic matter sublayer frequently includes also scattered calcite and vivianite grains, and (iii) the brown-yellowish carbonate sublayer is generally thinner and appears after the amorphous organic matter sublayer.

3.4.3.3. Varve type II: diatom-calcite varves

The diatom-calcite microfacies is developed in 1128 varves between 1748.6-1885.4 cm (11,473-12 596 cal. a BP; Fig. 3-3) and has a complex and variable structure with up to six sublayers (SL1 to SL6) as described in stratigraphic order from the base to the top in the following:

1 Rounded brown-yellowish carbonate with grain sizes <3 µm that resemble Mn-Fe-carbonates.

2 Planktonic diatoms and a few chrysophyte cysts, interspersed with littoral diatoms and rare pyrite framboids.

3 Primarily diatoms with some patches of white-yellowish idiomorphic calcite. The diatom assemblage consists either of littoral diatoms, planktonic diatoms or a mixture of both. Rare chrysophyte cysts and silt-sized quartz grains occur.

4 Primarily patches of white-yellowish idiomorphic calcite and sub-ordinated littoral diatoms and a few scattered silt-sized quartz grains. In 62 varves a discrete sublayer of detrital quartz of 0.09-0.64 mm thickness (mean 0.3 mm) develops on top of SL4 (Fig. 3-4).

5 Predominantly planktonic diatoms and rarely littoral diatoms. In some varves a few patches of amorphous organic matter and white-yellowish idiomorphic calcite occur.

6 Amorphous organic matter with a few brown-yellowish rounded Mn-Fe-carbonate grains included in some varves.

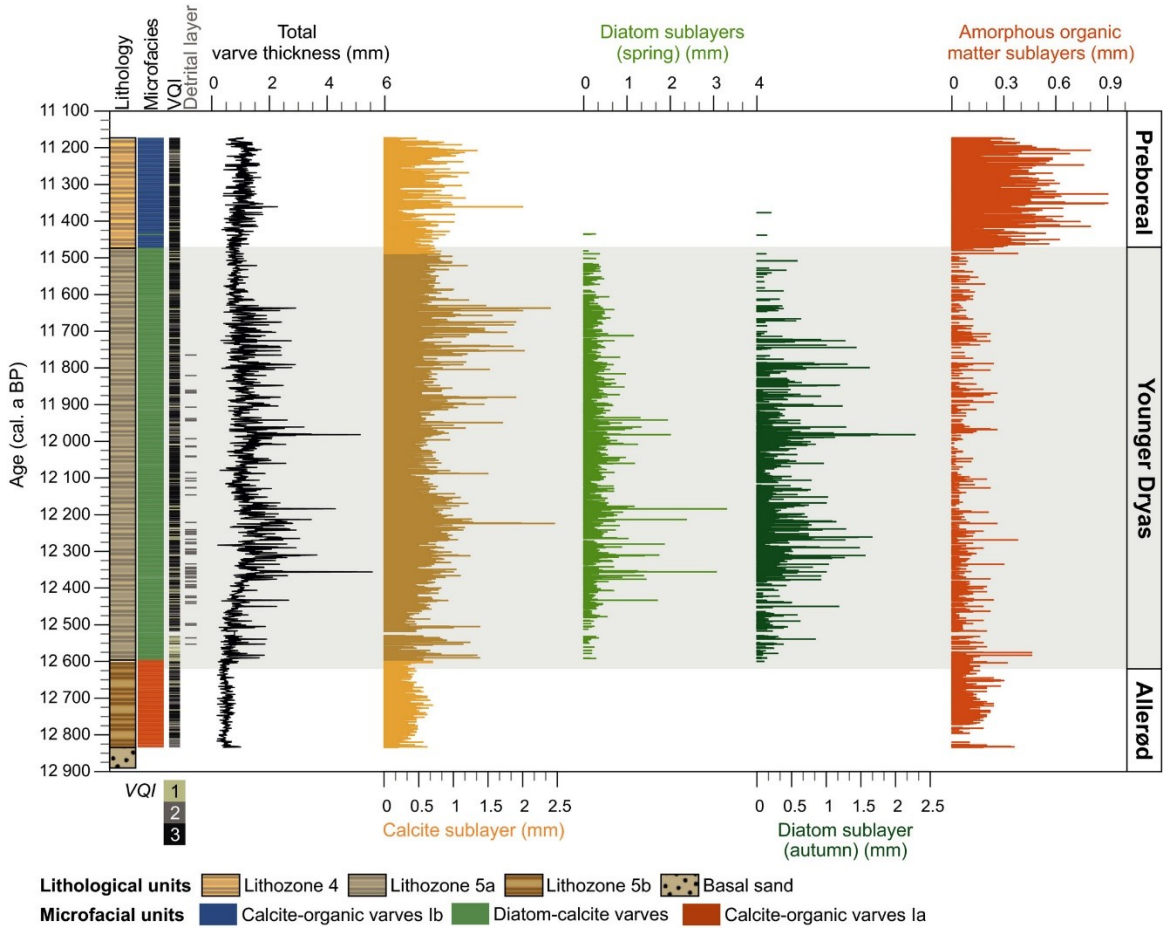

***Figure 3-4**: Lithology, microfacies types, total varve thickness, thickness of selected sublayers, as well as occurrence of detrital sublayers. For diatom-calcite varves: the two diatom-bearing sublayers during spring (SL2 and SL3) are summarized (light green) and autumn diatoms represent SL5. The summer calcite sublayer is differentiated into (i) precipitated calcite with no diatom frustules (light yellow) and (ii) mainly re-suspended calcite with littoral diatom frustules (dark yellow). VQI = varve quality index.*

The frequency of discrete quartz-rich sublayers in SL4 varies within the record (Fig. 3-4). Between 1885.4-1862.4 cm (12,595-12,400 cal. a BP) and 1834.8-1777.5 cm (12,220-11,765 cal. a BP) they occur every 20 to 25 years, while between 1862.4 and 1834.8 cm (12,400-12,220 cal. a BP) these sublayers appear more frequently and occur about every 6 years.

3.4.3.4. Varve thickness

In addition to total varve thickness, we also measured individual sublayer thicknesses for all varves (Fig. 3-4, S3-11). Only calcite and amorphous organic sublayers occur in all varve types, while diatom sublayers are present only in varve type II. We further calculated the coefficient of variation for the AL, YD and PB as an indication of interannual variability (Fig. 3-5).

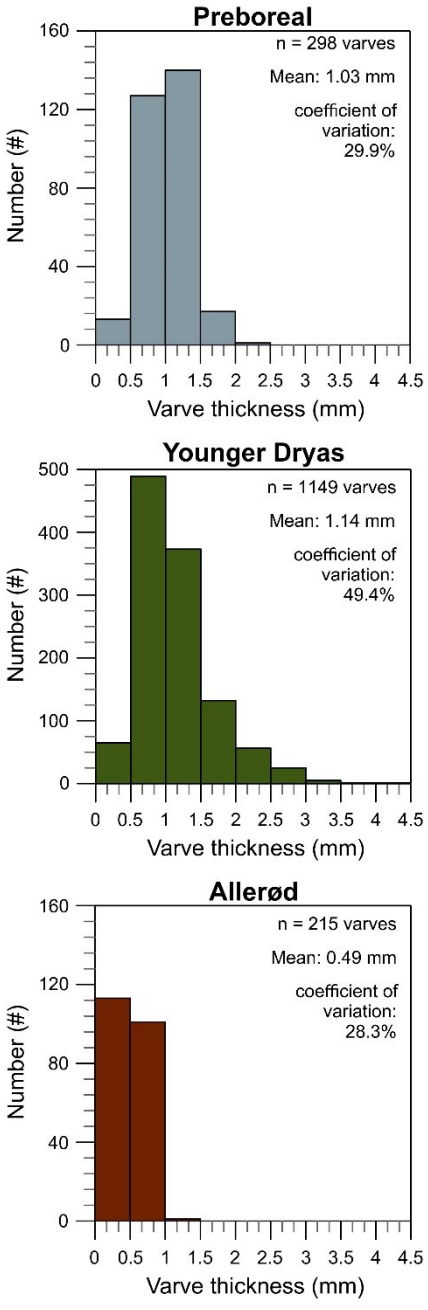

***Figure 3-5**: Frequency distribution plot of varve thicknesses for the late Allerød, Younger Dryas and early Preboreal. Number of varves (n), mean varve thickness (Mean) and coefficient of variation for each period are shown in the upper right corner.*

Calcite-organic varves (subtype Ia) deposited during the late Allerød have a mean varve thickness of 0.49 mm, which is the lowest of the study interval. A low coefficient of variation (28.3%) indicates low interannual variability of varve thickness (Fig. 3-5).

The mean varve thickness of 1.14 mm for diatom-calcite varves formed during the YD is more than doubled compared to the AL. The main reason for the varve thickness increase is the presence of diatom sublayers of up to 3 mm thickness (Fig. 3-4). A slight increase in the re-suspended calcite sublayer further contributes to increased thickness of YD varves. A more detailed view reveals that the period of thickest varves (mean thickness of 1.32 mm) is confined to ~12,375 to 11,635 cal. a BP, mainly because of the frequent occurrence of thick diatom sublayers between ~12,380 and 11,935 cal. a BP. A pronounced decrease in diatom sublayers occurs around 11,700 cal. a BP. In the early phase of the YD, varve thickness shows an increasing trend with occasional occurrence of thicker varves (mean thickness of 0.82 mm), whereas in the last phase of the YD the mean varve thickness of 0.83 mm is similar, but varves thicker than ~1.5 mm do not occur anymore. In general, the interannual variability of varve thickness is distinctly enlarged during the YD as shown by the coefficient of variation of 49.4% (Fig. 3-5).

Mean varve thickness of calcite-organic varves (subtype Ib) formed during the PB is 1.03 mm, which is only slightly lower than the YD mean and even higher than in the late YD (~11,635-11,470 cal. a BP). The reason for the increase of PB varve thickness at the YD/PB transition is the deposition of thick amorphous organic sublayers (Fig. 3-4). The interannual variability of varve thickness (coefficient of variation 29.9%) is similar to the AL and distinctly different from the YD (Fig. 3-5).

3.4.4. XRF element scanning

We first present µ-XRF mapping results because they are directly linked to our varve microfacies allowing us to precisely characterize the geochemical composition even for individual sublayers.

3.4.4.1. µ-XRF mapping

The two epoxy-impregnated sediment blocks selected for µ-XRF element mapping allow direct comparison of the sediment composition with microfacies analyses. The calcite-organic and diatom-calcite varves of the Lateglacial and Early Holocene sediments from Lake Gościąż are best represented by the elements Ca (calcite), Si (diatoms and detrital matter) and Ti (detrital matter). However, XRF scanning does not provide elements associated with organic matter.

The mapping results are not quantified, but clearly reveal the main changes in relative amounts of the elements Ca, Si and Ti (Fig. 3-6). The stepwise transition from calcite-organic (subtype Ia) to diatom-calcite (type II) varves (in phases 1.1 to 1.4) at the onset of the YD is well reflected by the mapping results (Fig. 3-6B). Phase 1.1 (~12,705-12,630 cal. a BP) is dominated by Ca layers, while Ti and Si are only scarce, which agrees with a diatom-free varve microfacies. A slight increase in the log(Si/Ca) record at ~12,630 cal. a BP indicates a relative decrease of calcite at the boundary of phases 1.1 and 1.2. Phase 1.2 (~12,630-12,595 cal. a BP) shows slightly increasing amounts of Si and Ti. The beginning of phase 1.3 at ~12,595 cal. a BP reveals increasing amounts of Si and Ti, while the relative amount of Ca remains constant. Simultaneously, as shown by our microfacies, deposition of diatom sublayers commences and keeps rising, while the increase of quartz grains is only minor in phase 1.3. Hence, the increase of Si and of the log(Si/Ca) record in phase 1.3 mainly reflects a rise in diatoms, while the unvaried log(Si/Ti) ratio represents the concurrent rise in detrital matter. Conditions stabilize again at the boundary between phases 1.3 and 1.4 (at ~12,560 cal. a BP) as indicated by the more or less constant values of the log(Si/Ca) record in phase 1.4 (~12,560-12,530 cal. a BP). This phase is characterized by relatively high amounts of Si and Ti reflecting diatom sublayers and some finely dispersed detrital matter (Fig. 3-6B).

The YD/PB transition reflects a stepwise shift from diatom-calcite (varve type II) to calcite-organic (subtype Ib) varves (in phases 2.1 to 2.3) that is predominantly indicated by a decrease of diatoms (Fig. 3-6A). In addition, the Ti record reveals that detrital matter is generally low during this interval from ~11,555 to 11,435 cal. a BP. The diatom-dominated phase 2.1 (~11,555-11,525 cal. a BP) is characterized by well pronounced diatom sublayers with occasional calcite sublayers resulting in highly variable log(Si/Ca) and log(Si/Ti) records. The boundary between phase 2.1 and 2.2 is marked by a relative increase in Ca, which is indicated by a decrease in the log(Si/Ca) record (Fig. 3-6A). The deposition of diatom sublayers clearly

declines at ~11,490 cal. a BP, which is reflected by a slight decrease in the log(Si/Ca) ratios. However, the boundary of phases 2.2 and 2.3 occurs only at ~11,470 cal. a BP and is marked by a sharp shift from relatively thin to thick amorphous organic matter sublayers. Diatoms and detrital matter (quartz) are absent in phase 2.3 and the origin of Si in this phase is not clear. However, the occurrence of Si in amorphous organic matter sublayers might suggest diatom dissolution in this phase.

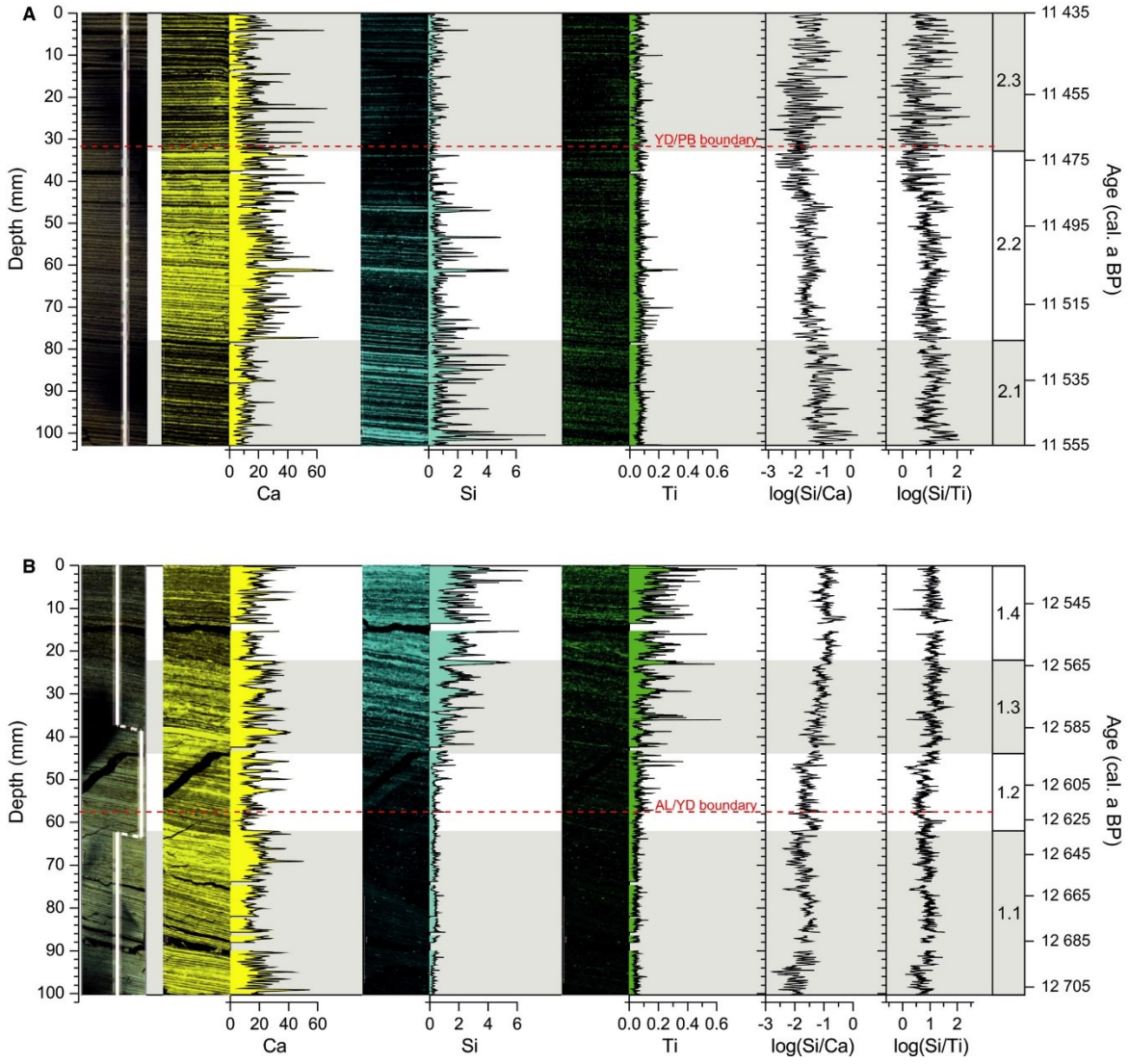

Figure 3-6*: Phases during YD transitions defined by µ-XRF mapping data. XRF counts and log-ratios are directly derived from µ-XRF mapping. From left to right: (i) thin section pictures with pathway of XRF scanning, (ii) maps of Ca (yellow), Si (blue) and Ti (green) with associated relative amounts (% counts), (iii) log-ratios of Si/Ca and Si/Ti. Dashed red lines mark the respective YD boundaries defined by our $\delta^{18}O_{carb}$ record. A. Sample GOS15-B8_153-163 cm: YD/PB transition. B. Sample GOS18-H5-1_42-52 cm: AL/YD transition.*

3.4.4.2. XRF core scanning

The two dominant varve types are diatom-calcite and calcite-organic varves that are best represented by log(Si/Ti), log(Si/Ca) and log(Ca/Ti) records (Fig. 3-7, S3-12). Although detrital matter only occurs in very low amounts, the element Ti seems to play an important role in compositional variations.

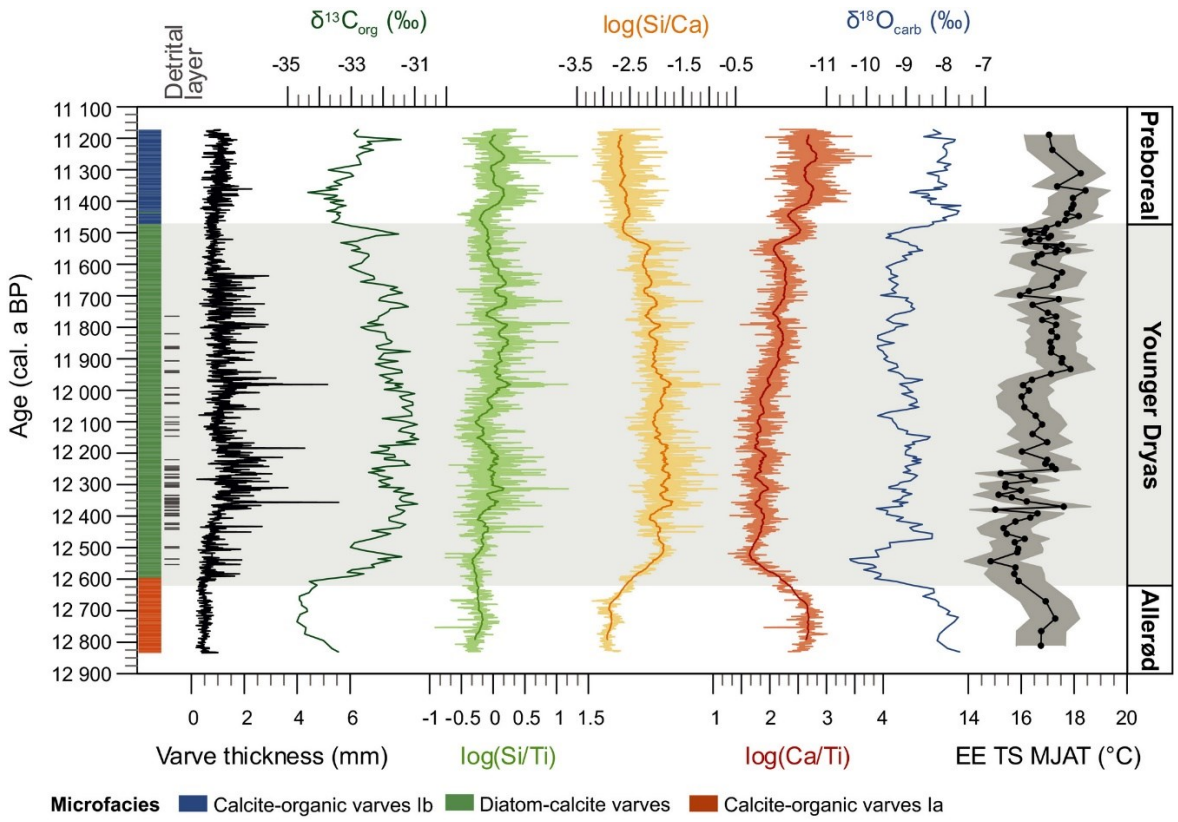

***Figure 3-7**: Comparison of microfacies data (varve types, detrital layer occurrence, varve thickness) with continuous log(Si/Ti), log(Si/Ca) and log(Ca/Ti) records, as well as high-resolution stable isotope ($\delta^{13}C_{org}$, $\delta^{18}O_{carb}$) and chironomid-inferred mean July air temperature (MJAT) data for the Eastern European data training set (EE TS) (shaded background shows the standard error of prediction using bootstrapping cross-validation).*

In the log(Si/Ti) record (Fig. 3-7) distinct variations are absent and values remain relatively stable from the base of the studied interval, but increase slightly and fluctuate much more strongly between ~12,540 and ~11,625 cal. a BP. The interval of slightly higher fluctuation coincides with the frequent occurrence of thick diatom sublayers (Fig. 3-4). Also, the decline of the log(Si/Ti) record between ~11,700 and 11,470 cal. a BP corresponds to the decline of diatom sublayers (Figs 3-4, 3-7). The early PB is marked in the log(Si/Ti) record by an increase, although discrete diatom sublayers are not observed.

Similar to the log(Si/Ti) ratio, the log(Si/Ca) ratio is steady at the base of the studied interval, until it rises gradually from ~12,690 to 12,540 cal. a BP, covering the abrupt transition from calcite-organic (subtype Ia) varves to diatom-calcite (type II) varves (Fig. 3-7). After 12,540 cal. a BP the log(Si/Ca) ratio is generally elevated (coinciding with the frequent occurrence of thick diatom sublayers), but decreases slightly until the YD/PB boundary, which is marked by one negative oscillation coinciding with the abrupt transition from diatom-calcite to calcite-organic (subtype Ib) varves. The early PB shows a continued steady decrease.

The log(Ca/Ti) record shows low variability at the base of the studied interval, but decreases gradually between ~12,690 and 12,540 cal. a BP (Fig. 3-7). This decrease coincides with the transition from calcite-organic (subtype Ia) varves to diatom-calcite varves, but is not as abrupt as observed in the microfacies (Fig. 3-7). After 12,540 cal. a BP, the log(Ca/Ti) record reveals a steady increase until the YD/PB boundary, which is interrupted by distinct fluctuations around the abrupt transition from diatom-calcite to calcite-organic (subtype Ib) varves. The early PB is marked by large-scale fluctuations.

3.4.5. Chironomid analyses

The detrended correspondence analysis (DCA) calculated for chironomid assemblages from the Gościąż sediments reveals a similar trend to mean July air temperature (MJAT) estimations from the EE TS and SNP TS reconstructions (Fig. S3-13), indicating that summer temperature was the main driver of the midge communities during the study interval. Temporal resolution of the reconstructions depended on the availability of head capsules (hc) and ranges between 3 and 68 varves per sample (mean of 17 varves per sample) with lower resolution for samples that had to be merged due to too low hc numbers.

The reconstructions based on two different training sets generally show the same trends and changes (Fig. 3-8, S3-13). However, the amplitudes of changes based on the SNP TS are significantly larger than those based on the EE TS, probably due to the larger temperature range covered by the SNP TS calibration data. The SNP TS includes temperatures down to 3.5 °C, while the EE TS does not include temperatures below 11.3 °C. Reconstructions with the SNP TS generally reveal lower MJAT, which is even more pronounced for the colder YD than for the warmer AL and PB (Fig. 3-8). This is most obvious for the minimum temperatures during the early YD (~12,620-11,950 cal. a BP), which reveal 2.8 °C colder reconstructions using the SNP TS (12.0 °C) compared to the EE TS (14.8 °C). In contrast, reconstructions of the warmest temperatures during the early PB (11,470-11,170 cal. a BP) differ only by 0.7 °C (SNP TS: 17.7 °C; EE TS: 18.4 °C). After relatively warm mean Allerød MJAT of 16.1 °C (SNP TS) and 16.9 °C (EE TS), both reconstructions exhibit a distinct gradual temperature decline of ~5 °C in SNP TS and ~2.5 °C in EE TS commencing at ~12,725 cal. a BP and

lasting for ~140-180 years. Mean MJAT for the YD are ~14 °C (SNP TS) and ~16.5 °C (EE TS), but temperatures before ~11 950 cal. a BP appear to be slightly colder (SNP TS mean: 13.6 °C; EE TS mean: 16.1 °C) than in the later part until ~11,470 cal. a BP (SNP TS mean: 14.7 °C; EE TS mean: 17.0 °C). The main temperature rise at the Holocene onset of 2.1 °C (EE TS) or 4.1 °C (SNP TS) occurred very rapidly in 40 and 60 years, respectively. Interestingly, directly before the onset of this increase a brief ~35 (SNP TS) to 50 (EE TS) year-long cold oscillation appears in both reconstructions. In the first century of the Holocene, MJAT reach highest values of the entire study interval before temperatures slightly decline again (SNP TS mean: 16.6 °C; EE TS mean: 17.8 °C).

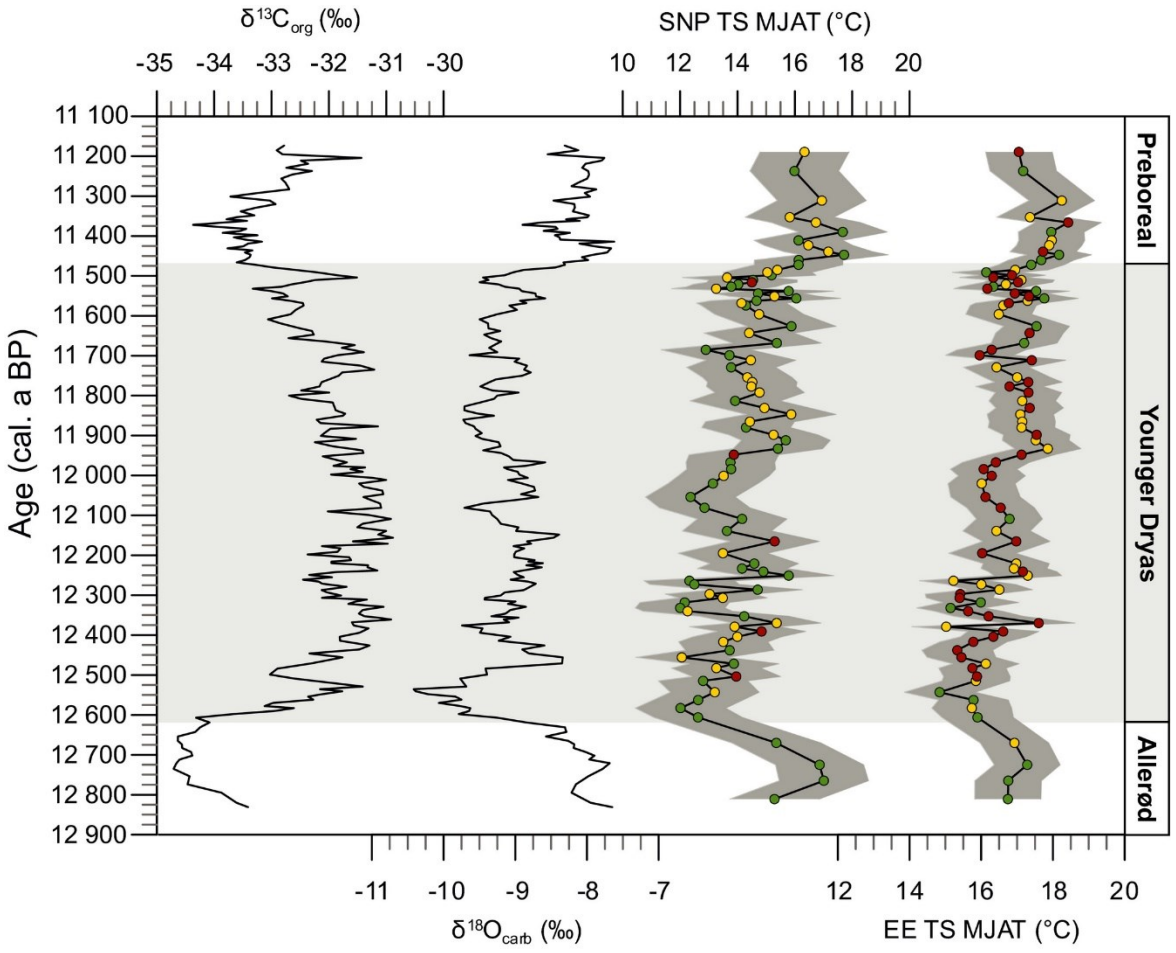

***Figure 3-8**: Stable isotope data and chironomid-inferred mean July air temperature (MJAT) reconstructions using the Swiss-Norwegian-Polish Training Set (SNP TS)* (Kotrys et al. 2020) *and the East European Training Set (EE TS)* (Luoto et al. 2019). *Shaded background of temperature reconstructions shows the standard error of prediction using bootstrapping cross-validation. Statistic basis quality of the temperature reconstructions is represented by green (good), yellow (average) and red (poor) dots.*

According to the EE TS reconstruction, 20 out of 95 samples remain below the 5% percentile threshold (minDC < 8.5053) and represent samples with good modern analogues. 42 samples have values over the 10% percentile threshold (minDC > 9.7531) and represent samples with poor modern analogues. According to the SNP TS reconstruction, 53 out of 95 samples remain below the 5% percentile threshold (minDC < 8.5775) and represent samples with good modern analogues. Five samples have values over the 10% percentile threshold (minDC > 10.0563) and represent samples with poor modern analogues.

3.4.6. Stable isotopes

The temporal resolution of the $\delta^{18}O_{carb}$ and $\delta^{13}C_{org}$ bulk sediment record is derived from contiguous 0.5-1 cm samples and varies between ca 4-14 varves cm^{-1} in the intervals from 11,350-11,170 and 12,520-11,580 cal. a BP, ~18-23 varves cm^{-1} in the interval 12,835-12,725 cal. a BP and ~8-24 varves cm^{-1} in the intervals from 11,580-11,350 and 12,725-12,525 cal. a BP.

3.4.6.1. $\delta^{18}O_{carb}$

$\delta^{18}O_{carb}$ values are isotopically heavier during the late Allerød and Early Holocene with a maximum of -7.62‰ in the Early Holocene and lighter between -8.31‰ and -10.42‰ during the YD (Figs 3-7, 3-8). The $\delta^{18}O_{carb}$ decline of ~2.7‰ at the transition to the YD occurred in two-steps between ~12,720 to 12,535 cal. a BP (185 years). Values increased again after an early YD minimum. Within most of the YD, $\delta^{18}O_{carb}$ values fluctuate around 1‰, but do not show distinct trends. At the transition to the Holocene values rapidly increase by ~1.8‰ within ~75 years (11,505-11,430 cal. a BP). Directly before this transition, a 50-year oscillation with 0.9‰ more negative values occurred. During the first ~80 years of the Holocene values reached a maximum, which was followed by a brief (~50 years) negative oscillation at about 11,400 cal. a BP. From the declining/rising values at the YD transitions, we calculate ~5-7 °C colder annual air temperatures for the YD in agreement with published data (Goslar et al. 1998b). We point out the striking agreement with the $\delta^{18}O_{carb}$ record in previous studies (Kuc et al. 1998; Fig. 3-2B). This very good replicability, the shape of the curves and the measured absolute values confirm that the $\delta^{18}O_{carb}$ record is representative for Lake Gościąż and not influenced by local effects.

3.4.6.2. $\delta^{13}C_{org}$

$\delta^{13}C_{org}$ values are isotopically lighter during the late Allerød and Early Holocene with a minimum of -34.7‰ in the late Allerød and heavier during the YD with a maximum of -30.9‰ (Figs 3-7, 3-8). A rapid increase of ~3‰ at the AL/YD transition occurred within ~80 years from ~12,610-12,530 cal. a BP. Values fluctuate around 1‰ during the early YD (~12,620-12,000 cal. a BP), before they slightly decrease during the late YD until ~11,470 cal. a BP. During the transition to the Holocene, the values rapidly drop by ~2‰ within

~40 years (11,505-11,465 cal. a BP) and after light values during the first ~150 years of the PB start to rise again. Directly before the major drop at the Holocene onset $\delta^{13}C_{org}$ values show a short (~30 year-long) oscillation to heavier values.

3.5. Discussion

The last deglaciation in the Northern Hemisphere is characterized by several short cold setbacks of which the YD was the last and most pronounced one. Cooling during the YD mainly affected the winter season and for central Poland January temperatures of about -20 °C are assumed (Isarin et al. 1998), resulting in a more pronounced seasonality of the climate (Denton et al. 2005). This was recently supported by a model study suggesting mild but short YD summers (Schenk et al. 2018).

3.5.1. Younger Dryas definition and chronology

We define the YD in our new record in the same way as previous studies as the midpoint of the major shifts in $\delta^{18}O$ of bulk carbonate (Ralska-Jasiewiczowa et al. 1992; Kuc et al. 1998), which occurred nearly contemporaneously with vegetation changes (Goslar et al. 1993, 1998a; Kuc et al. 1998; Ralska-Jasiewiczowa et al. 1998a, 2003). Since our $\delta^{18}O_{carb}$ record resembles the previous record to a high degree (Fig. 3-2B), we are confident in adopting this YD boundary definition for further discussion. According to our independently established chronology, the AL/YD boundary is dated at 12,620 +133/-231 cal. a BP and the YD/PB boundary at 11,470 +126/-206 cal. a BP. The relatively large age uncertainties are mainly caused by anchoring the floating varve chronology through radiocarbon dating and age modelling (Bonk et al. 2021) and are considered as conservative estimates. Due to the excellent varve preservation with a mean VQI of 2.6, the counting uncertainty for the YD is low and we report a YD duration of 1149 +14/-22 varve years, which is in good agreement with previous varve counts of 1140 ± 40 (Goslar et al. 1993, 1998a). The absolute ages for the YD boundaries in our chronology also agree within uncertainties with published dates for the Gościąż record (AL/YD boundary: 12,650 ± 60 cal. a BP; 12,580 ± 140 cal. a BP; YD/PB boundary: 11,510 ± 40 cal. a BP; 11,440 ± 120 cal. a BP) (Goslar et al. 1998a, 1999b). Furthermore, these ages are in agreement with the Meerfelder Maar (MFM) chronology (AL/YD boundary: 12,680 ± 40 cal. a BP; YD/PB boundary: 11,590 ± 40 cal. a BP; Brauer et al. (1999)) and support that the YD in central Europe began later than Greenland Stadial 1 (GS-1) in NGRIP (12,846 ± 138 cal. a BP to 11,653 ± 99 cal. a BP) (Rasmussen et al. 2006) due to time-transgressive cooling between Greenland and Europe (Rach et al. 2014).

3.5.2. Proxy interpretation

For the discussion of lake response to climate change we distinguish temperature and environmental proxies. The $\delta^{18}O_{carb}$ signal is interpreted as an annual temperature proxy controlled by the isotopic composition of precipitation and local air temperature (Leng 2006). Chironomid-inferred reconstructions represent MJAT.

$\delta^{13}C_{org}$ is interpreted as a proxy primarily for lake productivity (e.g. Lücke et al. 2003). Microscopic analyses reveal that calcite occurs either as endogenic calcite precipitated in the water column or in patches of re-suspended littoral calcite. This differentiation allows us to distinguish between sedimentation processes and, consequently, environmental conditions. Endogenic calcite precipitation in spring and summer is primarily controlled by temperature and lake productivity (Kelts & Hsü 1978), whereas deposition of re-suspended calcite, together with littoral diatoms, indicates higher lake water circulation and wave activity. Presence and thickness of amorphous organic sublayers are interpreted as a proxy for organic matter preservation in relation to seasonal anoxic conditions. Presence and thickness of diatom sublayers are applied as a proxy for lake productivity.

From (µ-)XRF scanning and mapping we selected Ca, Si and Ti as environmental proxies. Ca reflects calcite without distinction between endogenic and re-suspended calcite. Si is a proxy for both diatom frustules and detrital input (quartz, clay minerals), while Ti is not produced in the water column and thus unambiguously reflects detrital matter input. Since Ca and Si reflect different materials we apply various element ratios for a better distinction of sediment components. Log(Ca/Ti) ratios reflect relative variations of calcite and detrital matter, while log(Si/Ca) ratios show variations of diatoms/detrital matter and calcite. Log(Si/Ti) ratios reflect relative variations of diatoms and detrital matter and can be used as an indicator for diatom productivity.

3.5.3. Overall climate and environmental conditions

First, we discuss the general climatic states and environmental conditions during the study interval comprising the late Allerød (AL), the Younger Dryas (YD) and the early Preboreal (PB). In the second part of the discussion we will focus especially on the dynamic changes during the transitions into and out of the YD.

3.5.3.1. Late Allerød

Chironomid and $\delta^{18}O_{carb}$ data show generally warm conditions during the late Allerød. Chironomid-based reconstructions from both training data sets (SNP TS and EE TS; Fig. 3-8) do not significantly differ and reveal July temperatures around 16-17 °C, which agrees well with previous July temperature

reconstructions of 13-16 °C from pollen and plant macrofossils (Goslar et al. 1998b; Ralska-Jasiewiczowa et al. 1998a) and is only slightly lower than the recent July temperature of 18 °C (Wójcik & Przybylak 1998; Rozanski et al. 2010). The sedimentation during this period is characterized by a simple varve structure comprising an endogenic calcite sublayer with relatively large (~10-20 µm) idiomorphic calcite crystals and an amorphous organic matter sublayer (Fig. 3-3). The observed varve structure indicates a calm and stable lake environment with predominantly anoxic lake conditions (Brauer 2004). Weak lake water mixing is further suggested by the absence of discrete re-suspension sublayers. Catchment erosion was extremely low or even absent as indicated by the almost complete lack of detrital input from the catchment. Despite the warm summer temperatures aquatic bioproductivity was low as inferred from the absence of discrete diatom sublayers (Fig. 3-4), low log(Si/Ti) and log(Si/Ca) ratios, as well as low $\delta^{13}C_{org}$ values (Fig. 3-7), probably due to limited nutrient availability. Low productivity and catchment runoff are reflected in a mean varve thickness of only 0.49 mm, which is the lowest of the entire study interval. The low interannual variability of varve thickness (Fig. 3-5) and varve facies suggests that calm and stable lake conditions with a lack of extremes lasted for at least two centuries starting from the onset of varved lake gyttja formation. Similarly stable lake environment conditions during the late Allerød have been also reported from other lake records in Poland (Słowiński et al. 2017) and from Lake Meerfelder Maar (MFM) in Germany (Brauer et al. 1999; Lücke & Brauer 2004). The striking similarity of depositional processes in these lakes despite different basin morphology and catchment geology suggests a common, probably climatic, trigger.

3.5.3.2. Younger Dryas

Cold conditions during the YD have been reported from many lake and speleothem records in Europe (von Grafenstein et al. 1999; Schwander et al. 2000; Frisia et al. 2005; Lauterbach et al. 2011a; van Raden et al. 2013; Bartolomé et al. 2015), including Lake Gościąż (Kuc et al. 1998). From the Gościąż $\delta^{18}O_{carb}$ record a temperature decline of about 5 °C for the YD has been calculated (Goslar et al. 1998b). Our $\delta^{18}O_{carb}$ data closely resemble these published data (Fig. 3-2B), corroborating them as representative for the Lake Gościąż sediments. Recent studies report a strong seasonality of the YD climate with extremely low temperatures mainly in winter (Isarin et al. 1998), but relatively warm and short summers (Björck et al. 2002; Lücke & Brauer 2004; Birks & Birks 2014; Pawłowski et al. 2015; Schenk et al. 2018). YD summer temperature reconstructions of 14-16 °C for southern Scandinavia (Schenk et al. 2020) agree with our MJAT reconstructions ranging between 14 °C (SNP TS) and 16.5 °C (EE TS), depending on the calibration data applied (Fig. 3-8). These values are slightly higher than mean July temperatures of 10-13 °C derived from pollen and plant macrofossil reconstructions for Lake Gościąż (Goslar et al. 1998b). This difference might be explained by a bias due to the decreased length of the growing season.

The YD sediments generally are characterized by a complex varve structure with up to 6 sublayers (Fig. 3-3) including (i) discrete diatom sublayers, (ii) re-suspension sublayers composed of re-suspended calcite and littoral diatoms, and (iii) occasional up to ~0.6 mm thick sublayers enriched in minerogenic detrital matter (mainly quartz) (Figs 3-4, 3-7). The regular occurrence of up to ~3 mm thick planktonic diatom sublayers (Fig. 3-4) is also reflected in increased log(Si/Ca) and log(Si/Ti) ratios, indicating an enhanced lake productivity as supported by isotopically heavier $\delta^{13}C_{org}$ values (Fig. 3-7). The increased productivity can be explained by nutrient mobilization from the sediments due to intensive water circulation and nutrient input from the catchment. Strong water circulation and wave activity is supported by pronounced lake-internal sediment re-suspension. The intensified water circulation also led to better oxygenated conditions in the hypolimnion, which in turn caused organic matter degradation indicated by the distinct decline of organic matter sublayers. Slightly enhanced catchment erosion is inferred from the lower log(Ca/Ti) ratio and the occurrence of in total 62 sublayers enriched in silt-sized quartz. In addition to the generally dynamic internal lake processes and catchment erosion, the YD sedimentation is characterized by a pronounced interannual variability as inferred from the high variance of varve thickness (Fig. 3-5) and sublayer succession (Fig. 3-4).

Similarly unstable and dynamic sedimentation during the YD has been also reported from other lake records, for example MFM (Brauer et al. 1999, 2008; Lücke & Brauer 2004). However, we do not observe a distinct increase in detrital sediment input as in MFM, Kråkenes and Soppensee (Lotter 1991; Brauer et al. 1999; Bakke et al. 2009) that was also reported from Lake Gościąż (Goslar 1998c). From the obvious but slight increase in detrital matter in our record we infer only moderate catchment erosion during the YD that resembles conditions reported from the Rehwiese palaeolake (Neugebauer et al. 2012).

Environmental conditions were not uniform and gradual proxy changes during the YD suggest a general trend towards warmer and more stable conditions. Chironomid-based MJAT reconstructions reveal approximately 1 °C warmer summer temperatures after ~12,000 cal. a BP (Figs 3-7, 3-8), which is also reflected in the gradually increasing log(Ca/Ti) and decreasing log(Si/Ca) ratios, indicating an intensification in calcite precipitation. A gradual environmental response to warming is expressed by decreasing $\delta^{13}C_{org}$ values and diminution in diatom sublayer occurrence and thickness (Figs 3-4, 3-7), indicating decreasing productivity, probably caused by lower nutrient availability due to less intense lake water circulation. The increasing log(Ca/Ti) curve and the decline of detrital sublayers suggests an attenuation in catchment erosion likely due to soil stabilization in the catchment due to reforestation (Ralska-Jasiewiczowa et al. 1998a). Despite the obvious changes during the YD, we hesitate to state a YD bi-partition in Poland as it has been earlier proposed (Goslar et al. 1998b; Pawłowski et al. 2015), because

these changes are far more gradual than in western European sites located closer to the North Atlantic, which exhibit a distinct bi-partition of the YD (Brauer et al. 1999; Magny et al. 2001; Bakke et al. 2009).

3.5.3.3. Early Preboreal

Our study interval includes the first ~300 years of the Preboreal. Chironomid-based MJAT reconstructions between 16.6 °C (SNP TS) and 17.8 °C (EE TS) are slightly higher than in the Allerød (Fig. 3-8), in agreement with July temperature reconstructions of about ~16 °C from pollen and plant macro-fossils (Goslar et al. 1998b; Ralska-Jasiewiczowa et al. 1998a) and close to recent July temperatures (Wójcik & Przybylak 1998; Rozanski et al. 2010). The $\delta^{18}O_{carb}$ data show, after a short maximum, a ~50-year decline of ~1‰ around 11,400 cal. a BP, which might reflect a brief cold oscillation reported from the Greenland ice cores (Rasmussen et al. 2007, 2014) and/or the Preboreal Oscillation (Björck et al. 1996). Sedimentation during the early PB is characterized by the recurrence of a simple varve structure, primarily consisting of an endogenic calcite and pronounced amorphous organic matter sublayer (Fig. 3-4), similar to those formed in the late Allerød. The main difference compared to the late Allerød varves are thicker amorphous organic matter sublayers, which often also include scattered calcite and vivianite. This suggests better organic matter preservation due to anoxic conditions, likely favoured by increased inflow of mineral-rich groundwater after permafrost thawing during the Early Holocene (Starkel et al. 1998; Błaszkiewicz 2011) and more efficient lake sheltering due to catchment reforestation (Ralska-Jasiewiczowa et al. 1998d; Dräger et al. 2017; Żarczyński et al. 2019b). The absence of diatom sublayers and lighter $\delta^{13}C_{org}$ values (Figs 3-4, 3-7) suggest low lacustrine productivity. However, we cannot exclude growth of other algae species like, for example, green algae that do not leave visible remains in the sediments (Marciniak & Szeroczyńska 1998; Ralska-Jasiewiczowa et al. 1998a) and might explain an increase in productivity suggested by the rise in $\delta^{13}C_{org}$ values. The lack of discrete diatom sublayers might be also explained by dissolution of diatom frustules as suggested by amorphous organic matter sublayers enriched in silicon (Figs 3-6, 3-9). The further decline of already weak catchment erosion, indicated by high log(Ca/Ti) ratios, reflects the full Holocene forest recovery (Ralska-Jasiewiczowa et al. 1998d). In contrast to the YD, the interannual variability in varve thickness (Fig. 3-5) and composition was low, indicating stable environmental conditions.

3.5.4. Lake responses into and out of the Younger Dryas

Due to their seasonal time resolution, varved sediments are ideal to investigate processes and times of lake responses to rapid climate shifts in the past. Previous studies focusing on vegetation changes at the YD/PB transition have established the Lake Gościąż sediments as particularly suitable for such high resolution studies (Ralska-Jasiewiczowa et al. 2003). Here, we extend these investigations with a focus on

novel sedimentological and geochemical proxies and compare periods of rapid warming (YD/PB transition) with periods of rapid cooling (AL/YD transition). For this purpose and in addition to classical XRF element scanning and microfacies analyses, we apply high-resolution µ-XRF element mapping for a ~120-year (YD/PB) and a ~175-year (AL/YD) time window covering the transitions into and out of the YD (Fig. 3-9).

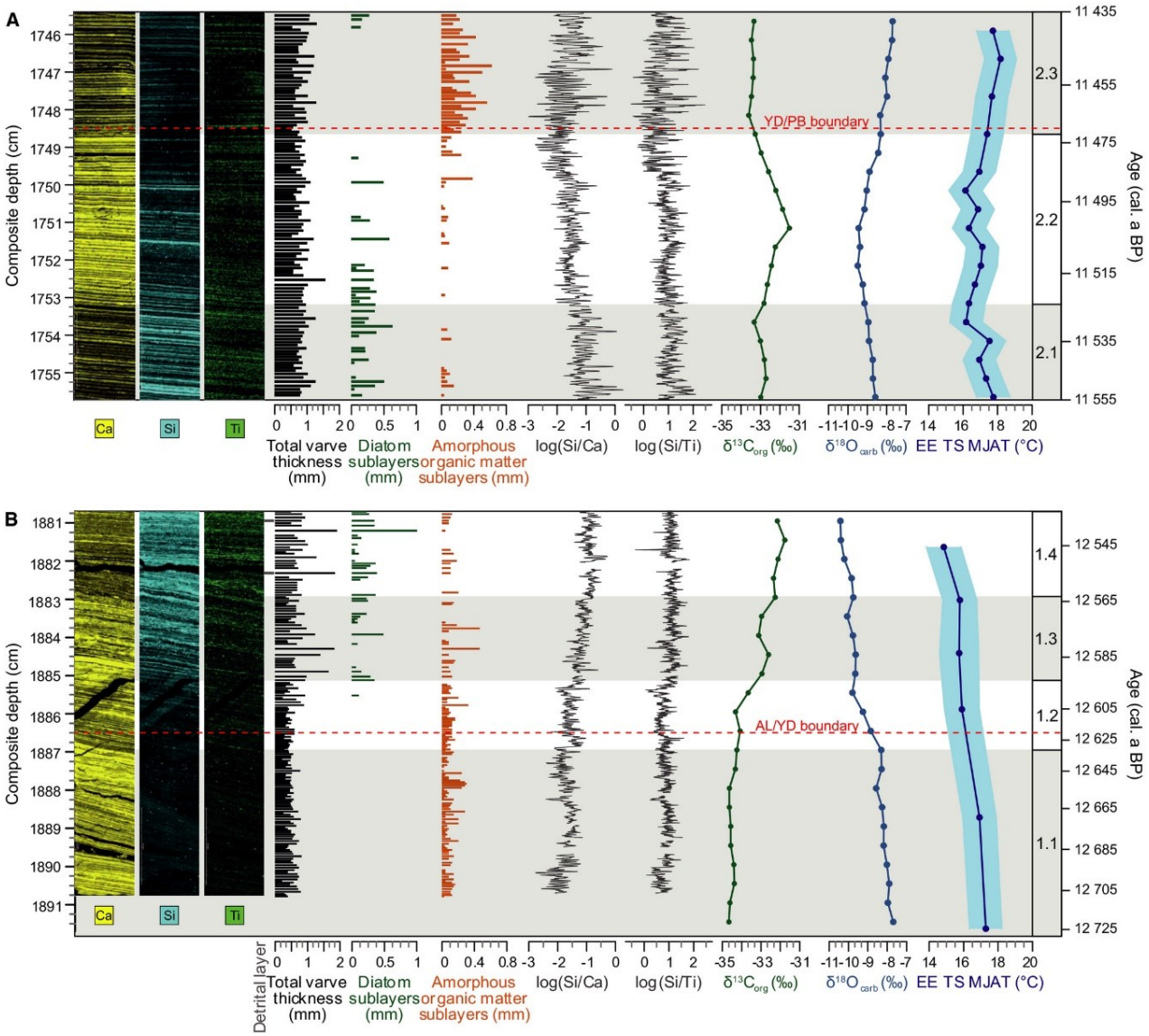

***Figure 3-9**: Zoom in at the A. YD/PB transition (~120 years). B. AL/YD transition (~190 years). Left: µ-XRF mapping of Ca, Si and Ti. Right: selected microfacies data, XRF log-ratios of Si/Ca and Si/Ti, $\delta^{13}C_{org}$, $\delta^{18}O_{carb}$ and chironomid-inferred mean July air temperature (MJAT) for the Eastern European data training set (EE TS). All three diatom sublayers from varve type II (SL2, 3 and 5) are summarized. Dashed red lines mark the respective YD boundaries defined by our $\delta^{18}O_{carb}$ record.*

3.5.4.1. AL/YD transition

Both chironomid- and $\delta^{18}O_{carb}$-based reconstructions show gradually declining air temperatures for about 140 (SNP TS) to 180 years (EE TS and $\delta^{18}O_{carb}$) starting at ~12,720 cal. a BP (Fig. 3-8). The duration of the main decline period is about the same as reported from biomarker isotope reconstructions from MFM (Rach et al. 2014). The resolution of chironomid-based reconstructions for this transition is rather low due to the scarcity of head capsules. In the higher resolved $\delta^{18}O_{carb}$ data a clear two-step decline in air temperature appears, which was moderate before ~12,630 cal. a BP and stronger afterwards (Figs 3-7, 3-8, 3-9).

Lake responses to the temperature lowering occurred as a succession in four phases (1.1-1.4 in Fig. 3-9). During the slow temperature decline in the initial phase 1.1 (~12,720-12,630 cal. a BP), seasonal sublayer composition and element data do not show distinct changes. Phase 1.2 from ~12,630-12,595 cal. a BP reflects a period of accelerated temperature decline and includes the onset of the YD at the midpoint of the $\delta^{18}O_{carb}$ decrease. During this phase, Si and Ti counts show a weak increase, while the log(Si/Ca) ratio is slightly higher, indicating a relative decrease in calcite due to slightly higher diatom productivity and catchment erosion. Higher lake productivity is supported by an increase of $\delta^{13}C_{org}$ values caused by enrichment of ^{13}C in the lake water due to higher photosynthesis (Leng 2006). The onset of phase 1.3 at ~12,595 cal. a BP marks a prominent and abrupt shift in the sedimentation regime due to a sudden increase in diatom productivity. This is expressed by the first occurrence of discrete diatom sublayers leading to an increase in varve thickness, an abrupt rise in the log(Si/Ca) record and in the substantially higher amounts of Si (Fig. 3-9). The abruptness of this shift suggests that a threshold in nutrient availability has been crossed, probably triggered by nutrient remobilization from the sediments due to intensified lake water circulation and by nutrient input from the catchment. Stronger water circulation also explains the concomitant occurrence of re-suspended calcite and littoral diatoms and likely led to an intensified ventilation of the lake bottom as reflected in the decrease of amorphous organic matter sublayers due to organic matter decomposition. Higher Ti amounts further indicate an increase in catchment erosion. During the final phase 1.4 (~12,560-12,530 cal. a BP) conditions stabilize as indicated by regular deposition of diatom sublayers, primarily constant log(Si/Ca) ratios and high amounts of Si (Fig. 3-9). High amounts of Ti and sporadic occurrence of thin discrete detrital sublayers since ~12,553 cal. a BP (Fig. 3-9) reflect finely dispersed detrital matter and small-scale erosion events.

The timing of lake sedimentation response to climate cooling differs between proxies. Main changes in proxies for calcite precipitation, lake productivity and catchment erosion occurred within ~100 years from ~12,630-12,530 cal. a BP during phases 1.2 to 1.4 (Fig. 3-9), broadly coinciding with the second, steeper

decline in $\delta^{18}O_{carb}$. In contrast to the geochemical changes, the seasonal sedimentation pattern changed faster within ~35 years between ~12,595-12,560 cal. a BP, indicating that threshold processes are involved. This applies especially for the occurrence of discrete diatom sublayers, which suddenly appeared ~25 years after the midpoint of $\delta^{18}O_{carb}$ and ~125 years after $\delta^{18}O_{carb}$ started to decline. Similar environmental delays have been reported from MFM (Rach et al. 2014), suggesting a common driver rather than local effects. In both lakes, the sudden appearance of discrete diatom and re-suspension sublayers and the parallel decline in amorphous organic matter sublayers point to a pronounced sensitivity to intensified water circulation changes driven by winds (Brauer et al. 2008) and/or seasonality rather than to declining temperatures. Differences between the lakes appear in the intensity of catchment erosion at the YD onset. After the almost complete lack of detrital matter in the late Allerød in both lake records, the increase in detrital material was far more moderate in Lake Gościąż (Brauer et al. 1999; Litt et al. 2001).

3.5.4.2. YD/PB transition

From the 1.8‰ increase in $\delta^{18}O_{carb}$ within ~70 years at the YD/PB transition an annual air temperature rise of ~5 °C is inferred that agrees with previous results from Lake Gościąż (Fig. 3-2B; Goslar et al. 1998b). The abrupt warming within ~70 years is in agreement with reports from MFM (Rach et al. 2014). The temperature rise is clearly traced also in both chironomid-based reconstructions (Fig. 3-8). The larger amplitude of the warming in the SNP TS (4.1 °C) compared to the EE TS (2.1 °C) reconstruction is due to the lower YD temperatures derived from the SNP TS data. In this respect, the EE TS reconstruction is in better agreement with model results suggesting warm YD summers (Schenk et al. 2018). The major air temperature rise at the Holocene onset was directly preceded by a ~50 year-long drop in $\delta^{18}O_{carb}$ of ~0.9‰, which has been earlier reported from Lake Gościąż and related to changes in seasonal precipitation (Ralska-Jasiewiczowa et al. 2003). Since this fluctuation also appears in our chironomid-based reconstructions we consider an air temperature drop as a more likely explanation. This short cold episode might be related to a brief drop in North Atlantic sea surface temperatures (Bakke et al. 2009).

The main and rapid lake responses at the YD/PB transition in Lake Gościąż as shown in Fig. 3-9 were preceded by gradual environmental changes. About 465 years earlier at ~11,935 cal. a BP diatom sublayer frequency and thickness gradually declined (Fig. 3-4) and between ~11,700-11,630 cal. a BP further decreases in varve thickness, diatom sublayer thickness and occurrence (Fig. 3-4), as well as in log(Si/Ti) ratios and $\delta^{13}C_{org}$ values occurred (Fig. 3-7). All point to more frequent occurrence of years with weaker water circulation and limited nutrient remobilization from the bottom sediments. The absence of years with pronounced diatom blooms might be also related to blooms of green algae, like for example Tetraedron (Ralska-Jasiewiczowa et al. 2003). The attenuation of catchment erosion is reflected in the

increase of the log(Ca/Ti) ratio since about 12,000 cal. a BP (Fig. 3-7) and the cessation of discrete detrital layer deposition at ~11,765 cal. a BP (Fig. 3-7), both reflecting a gradual recovery of forest vegetation and stabilization of slope processes (Ralska-Jasiewiczowa et al. 1998a).

The final transition from the YD into the Holocene occurred in three phases (2.1-2.3 in Fig. 3-9) of which the first phase 2.1 reflects the late YD environment with reduced varve thickness, diatom productivity and nearly absent detrital input. Phase 2.2 commenced abruptly at ~11,525 cal. a BP and appears particularly distinct in the element maps (Figs 3-6, 3-9). High relative amounts of Ca, the decreasing log(Si/Ca) ratio and thin section observations suggest intensified endogenic calcite precipitation. An intensified calcite formation during times of declining temperatures, as expressed in the anti-correlation of the log(Si/Ca) and $\delta^{18}O_{carb}$ curves, is unexpected since log(Si/Ca) generally parallels the temperature curves in all other parts of the study interval. This suggests other controls than temperature on calcite precipitation during this short period. A possible explanation might be higher concentrations of calcium and carbonate ions in the lake water either due to a brief lake level decline (Ralska-Jasiewiczowa et al. 2003) and/or higher groundwater inflow. At ~11,490 cal. a BP, log(Si/Ca) ratios decrease, reflecting the cessation of diatom deposition. The onset of phase 2.3 at ~11,470 cal. a BP is marked by an abrupt shift from one year to the next, when thick amorphous organic matter sublayers begin to regularly form in every year (Fig. 3-9). The abruptness of this shift suggests that a threshold for predominantly anoxic conditions at the lake bottom was crossed. This shift is very distinct in the element maps (Fig. 3-9) and the macroscopically visible colour change of the sediments from light to dark. Interestingly, this main shift in the depositional environment of the lake coincides with the midpoint of the temperature rise, which marks the defined onset of the Holocene (Fig. 3-7). Varve thickness does not change at that point, because calcite sublayer thickness does not change and cessation of diatom sublayers is compensated by amorphous organic matter sublayers.

3.5.4.3. Comparison of the YD transitions

The gradual cooling at the onset of the YD lasted for about one and a half century and thus 2-3 times longer than the warming at the Holocene onset, which in addition was preceded by a brief cold oscillation of about the same duration as the final temperature rise itself. The lake responses are complex and in general, geochemical proxies seem to respond more gradually, whereas seasonal sedimentation can change within a few years, suggesting that threshold effects are involved. Endogenic calcite formation as reflected in log(Ca/Ti) and log(Si/Ca) is the only parameter that mirrors temperature changes directly. Proxies reflecting lake productivity and organic matter preservation respond to lake internal processes largely driven by water circulation, which is considered a major factor for lacustrine sedimentation. Detrital input as a proxy for erosion processes in the catchment is predominantly controlled by vegetation cover

and thus only indirectly by climate change. The detrital portion in our study interval is generally low and shows only a slight increase/decrease at the onset/end of the YD, indicating that despite an obvious reduction in forest cover (Ralska-Jasiewiczowa et al. 1998a) the catchment remained largely vegetated even during the YD.

The main lake response to the cooling at the beginning of the YD was an increase in diatom productivity and lake-internal re-suspension processes accompanied by a decline in organic matter preservation. The shift in seasonal deposition commenced ~125 years after air temperature started to decline and occurred mainly during the second half of the period of cooling (Fig. 3-9). Interestingly, distinct environmental changes commenced ~90 years after onset of cooling at about the mid-point of the air temperature decline that is defined as the onset of the YD. A critical threshold was crossed about 35 years later at ~12,595 cal. a BP when the first discrete diatom blooms occurred. The delayed lake response to the cooling might be rather explained with a particular sensitivity to lake circulation than to temperature. One might speculate that major changes in atmospheric circulation, which ultimately triggered the changes in sedimentation, occurred with a delay of some decades after temperatures started to decline.

Lake responses to the rapid and major warming at the end of the YD occurred instantaneously. However, productivity and erosion proxies showed first signs of changes within the lake and catchment already a few centuries before the main warming (Figs 3-4, 3-7), probably reflecting an initial increase in MJAT, water circulation and catchment vegetation (Ralska-Jasiewiczowa et al. 1998a) in the late YD. During the brief cold oscillation before the final warming, mechanisms of lake responses changed and likely were controlled by local hydrology rather than temperature. At the same time when temperature rise commenced at ~11,505 cal. a BP, the frequency of diatom blooms rapidly decreased further and ceased before the midpoint of the temperature rise. About 20 years later, regular deposition of thicker amorphous organic sublayers began (Fig. 3-9). This reflects the onset of the typical anoxic sedimentation pattern of the PB, even a few decades before the temperature rise came to an end. This immediate lake response suggests a pronounced sensitivity to climate warming compared to a larger resilience with respect to climate cooling.

3.6. Conclusions

Our results provide new insights into rapid climate change and lake system responses at the onset and demise of the YD. The chironomid-based MJAT reconstructions support the hypothesis from several studies that the summer temperature decline was less pronounced during the YD. Sedimentation during

the YD still is predominantly controlled by lake-internal processes and the increase of catchment material is only weak to moderate in Lake Gościąż, which is uncommon but not unique. The seasonal sedimentation pattern of Lake Gościąż during the YD indicates a dynamic lake system, primarily controlled by intensified water circulation and wave activity. Furthermore, the YD in Lake Gościąż is characterized by a pronounced interannual variability suggesting unstable weather conditions.

In Lake Gościąż, the rapid transitions into and out of the YD exhibit distinct differences in both the temperature changes itself and lake system responses provoked by these changes. The major warming at the end of the YD occurred in 40-70 years and thus faster than the cooling at the onset of the YD (140-180 years). The lake system was more resilient to the cooling at the YD onset and first changes in environmental proxies lagged the cooling by ~90 years. In contrast, lake responses to the terminal PB warming occurred instantaneously.

In general, different environmental proxies derived from microfacies, XRF element scanning and stable isotope analyses do not respond synchronously, but with small leads and lags. Element and stable isotope geochemistry commonly changes slightly more gradually, while seasonal sublayer formation tends to change abruptly within a few years suggesting that threshold processes are involved. Such potential differences in proxy responses to climate change should be considered for proxy-based synchronization of sediment records from different lakes.

Acknowledgements

The authors thank both coring teams including Mateusz A. Kramkowski and Matthias Köppl and especially our coring engineer Brian Brademann for the excellent core recovery. We further thank Brian Brademann for thin section preparation, Sylvia Pinkerneil for help with geochemical analyses, Sebastian Tyszkowski for providing the bathymetric map, Olga Antczak, Marta Rudna and Małgorzata Mielczarek for chironomid sample preparation and Jens Mingram for technical help. Florian Ott and Ina Neugebauer are thanked for their technical and scientific support and valuable discussions. We further thank B. Zolitschka and an anonymous reviewer, as well as editor J. A. Piotrowski for their constructive comments and corrections on the manuscript. This study is funded by project No. 2015/19/B/ST10/03039 of the National Science Centre, Poland and the Virtual Institute of Integrated Climate and Landscape Evolution Analysis (ICLEA) (grant number VH-VI-415). The study is a contribution to the Helmholtz Association (HGF) climate initiative REKLIM Topic 8 “Rapid climate change derived from proxy data”. We confirm that we have no conflict of interest to declare for this study.

Author contributions

DM performed the microfacies analyses, was part of the sediment coring and wrote the manuscript with contributions from all co-authors. Figures were prepared by DM and partly by RT. XRF analyses have been performed by RT. MP, TPL and BK performed the chironomid analyses and temperature reconstructions. BP performed stable isotope analyses and AR provided the age model. MJS selected drilling points, was part of the sediment coring and did sedimentological work. MB and MS provided information about local lake catchment, morphology and hydrology. MS did micropaleontological work and was part of the sediment coring. MB, MS and AB designed the project and acquired funding. AB supervised analyses and improved the manuscript. All co-authors contributed to the manuscript by proofreading and discussions, especially AB.

Data availability statement

Data of this article will be publicly available on PANGAEA (mean July air temperature reconstructions (https://doi.org/10.1594/PANGAEA.924337), $\delta^{18}O_{carb}$ and $\delta^{13}C_{org}$ (https://doi.org/10.1594/PANGAEA.924342), varve chronology (https://doi.org/10.1594/PANGAEA.924343)) and on the VARDA varve database (Ramisch et al. 2020): https://varve.gfz-potsdam.de/database/details/538cd388-8030-415a-982a-a21ba50c99eb. XRF-data will be made available upon reasonable request from Rik Tjallingii.

3.7. Supplementary material

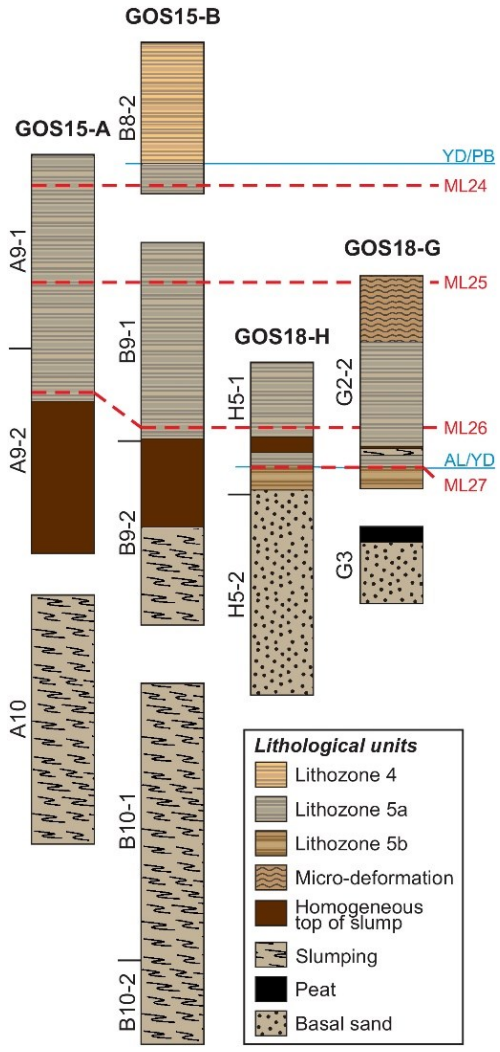

***Figure S3-10**: Core correlation of the here observed interval of the composite profile GOS18 (Bonk et al. 2021).*

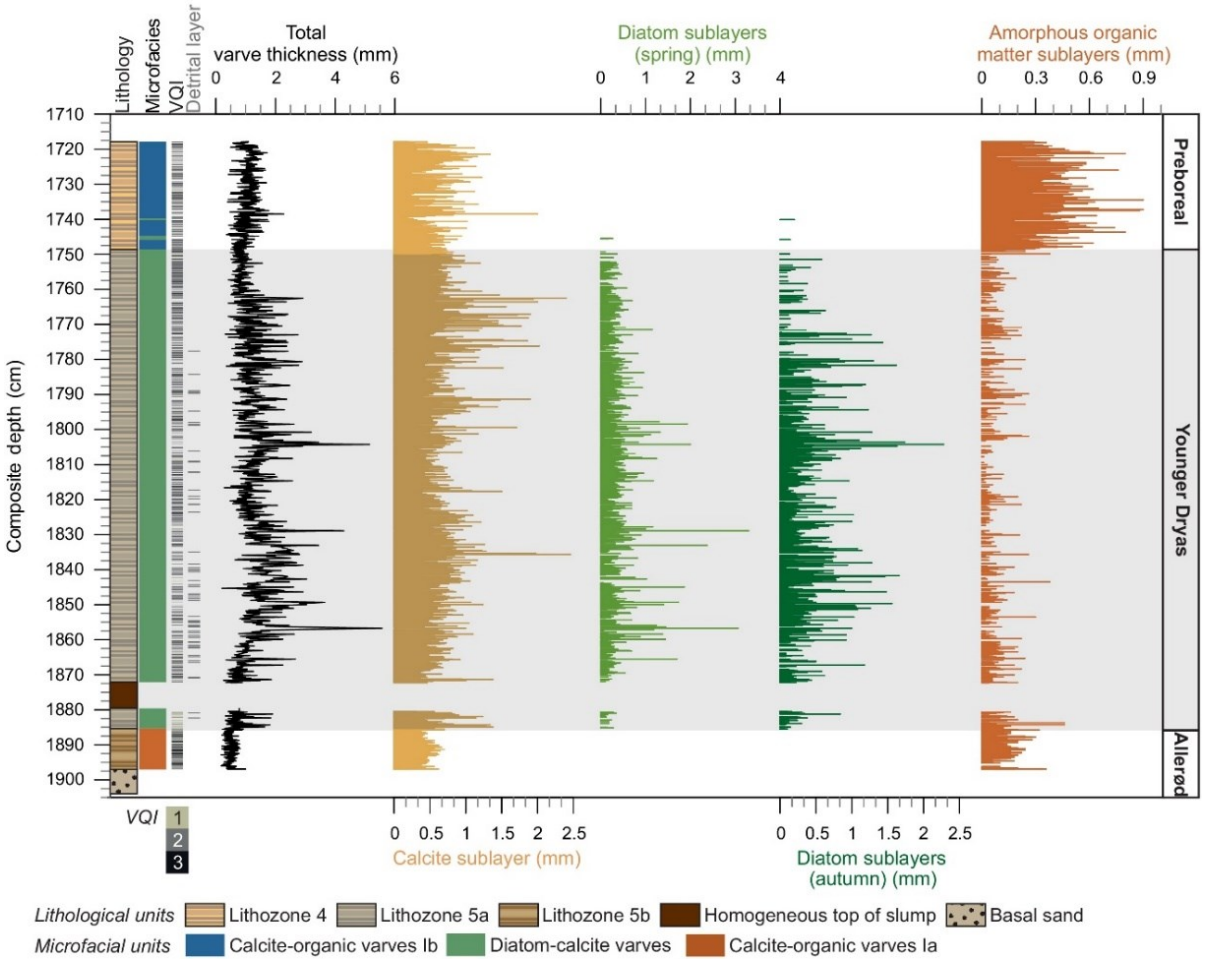

***Figure S3-11**: Lithology and microfacies data against composite depth.*

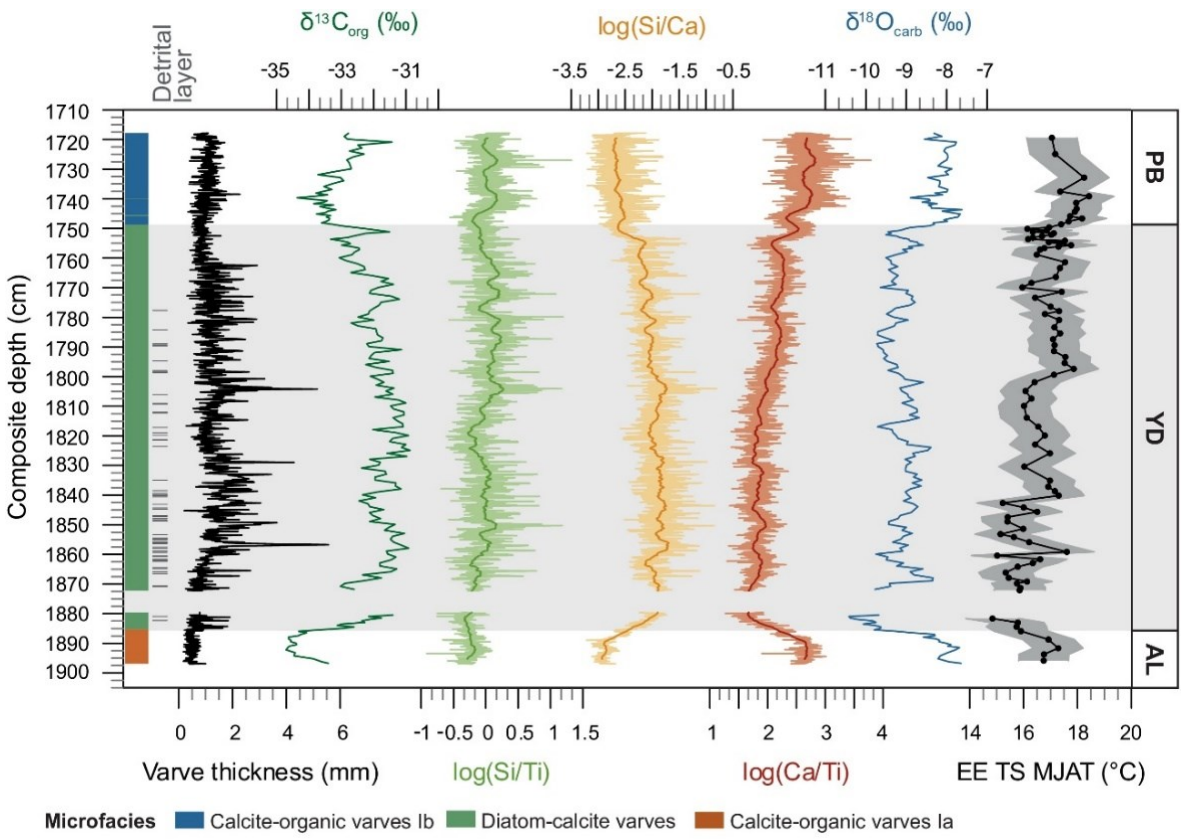

***Figure S3-12**: Selected microfacies data, XRF-data, $\delta^{13}C_{org}$, $\delta^{18}O_{carb}$ and chironomid-inferred mean July air temperature (MJAT) reconstruction using the East European Training Set (EE TS) against composite depth.*

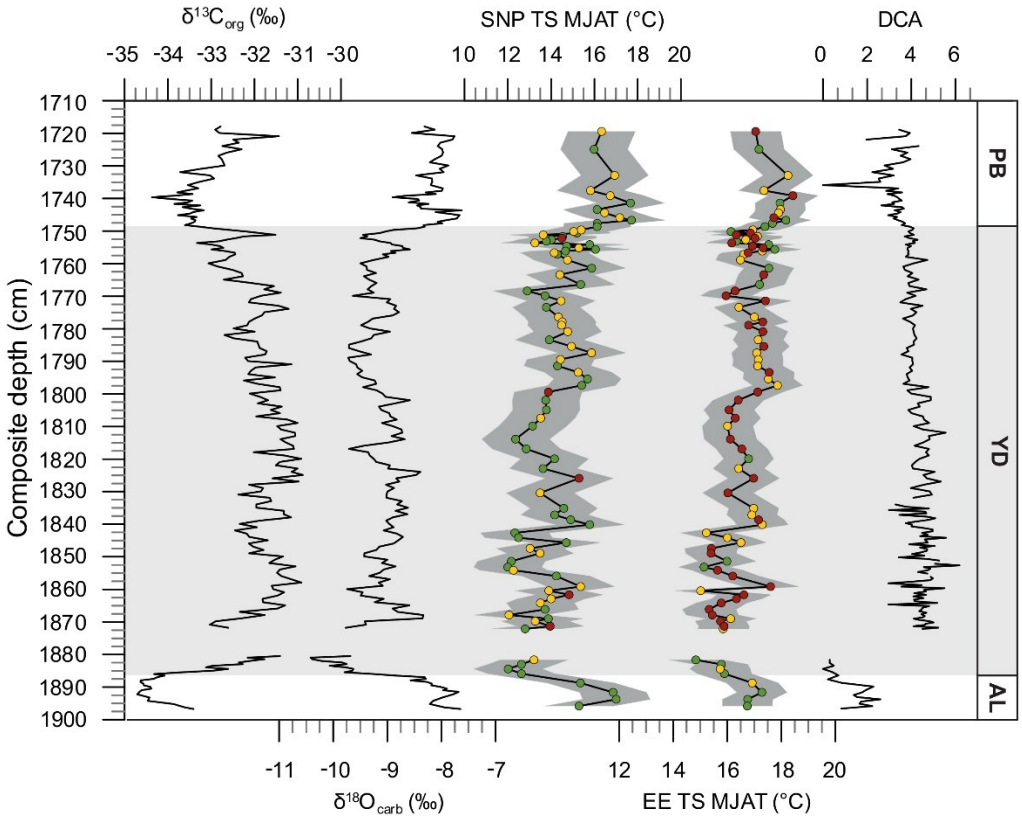

***Figure S3-13**: $\delta^{13}C_{org}$, $\delta^{18}O_{carb}$, chironomid-inferred mean July air temperature (MJAT) reconstructions using the Swiss-Norwegian-Polish Training Set (SNP TS) (Kotrys et al. 2020) and the East European Training Set (EE TS) (Luoto et al. 2019) and detrended correspondence analysis (DCA) against composite depth.*

***Table S3-1**: Table Marker layers (ML) of the here observed interval from the composite profile GOS18.*

Master core				Core depth [cm]		Composite depth [cm]		Marker layers
Exp	hole	core	section	from	to	top	bottom	
GOS15	B	8		**38**	**166**	1630.4	1758.4	**ML23 - ML24**
GOS15	A	9	1	**14**	**58**	1758.4	1802.4	**ML24 - ML25**
GOS15	B	9	1	**18**	**84**	1802.4	1868.4	**ML26**
GOS18	H	5	1	**29.7**	60	1868.4	1898.7	
GOS18	H	5	2	60	151	1898.7	1989.7	

***Table S3-2**: Chironomid samples included in the mean July air temperature reconstruction with head capsule (hc) counts below 50.*

Sample	Composite depth [cm] from	to	number of head capsules (hc)
GOS15-B8-113 to -118	1704.4	1710.4	35
GOS15-B8-126 to -129	1717.4	1721.4	49
GOS15-B8-161	1752.9	1753.4	48
GOS15-A9-26	1769.4	1770.4	48
GOS15-A9-32 to -33	1775.4	1777.4	44
GOS15-A9-34	1777.4	1778.4	49
GOS15-A9-43 to -44	1786.4	1788.4	49
GOS15-B9-23 to -24	1806.4	1808.4	41
GOS15-B9-38 to -40	1821.4	1824.4	42
GOS15-B9-41 to -43	1824.4	1827.4	41
GOS15-B9-44 to -49	1827.4	1833.4	44
GOS15-B9-55.5 to -56.5	1839.4	1840.9	49
GOS15-B9-58 to -59	1841.9	1843.4	46
GOS15-B9-59.5 to -60.5	1843.4	1844.9	48
GOS15-B9-61 to -62	1844.9	1846.4	41
GOS15-B9-64 to -65.5	1847.9	1849.9	35
GOS15-B9-66.5 to -68	1850.4	1852.4	48
GOS15-B9-68.5 to -69.5	1852.4	1853.9	43
GOS15-B9-70.5 to -73	1854.4	1857.4	46
GOS15-B9-74.5 to -75.5	1858.4	1859.9	30
GOS15-B9-76 to -76.5	1859.9	1860.9	44
GOS15-B9-77 to -78	1860.9	1862.4	36
GOS15-B9-79.5 to -80.5	1863.4	1864.9	32
GOS15-B9-83 to -84.5	1866.9	1868.79	36
GOS15-B9-85.5 to -86.5	1869.18	1870.35	48
GOS15-B9-89	1871.91	1872.3	42
GOS18-G2-2_168-169	1883.95	1884.87	49
GOS18-G2-2_169-170 to GOS18-G2-2_170-171	1884.87	1887.06	40
GOS18-G2-2_171-172 to GOS18-G2-2_173-174	1887.06	1890.4	36
GOS18-G2-2_174-175 to GOS18-G2-2_177-178	1890.4	1892.77	46
GOS18-G2-2_178-179 to GOS18-G2-2_180-181	1892.77	1894.75	43

4. Cryptotephras in the Lateglacial ICDP Dead Sea sediment record and their implications for chronology

Ina Neugebauer[1], Daniela Müller[1,2], Markus J. Schwab[1], Simon Blockley[3], Christine S. Lane[4], Sabine Wulf[5], Oona Appelt[6], and Achim Brauer[1,2]

(1) Section Climate Dynamics and Landscape Evolution, GFZ German Research Centre for Geosciences, Telegrafenberg, Potsdam 14473, Germany
(2) Institute of Geosciences, University of Potsdam, Karl-Liebknecht-Str. 24-25, Potsdam 14476, Germany
(3) Department of Geography, Royal Holloway University of London, Egham TW20 0EX, UK
(4) Department of Geography, University of Cambridge, Cambridge CB2 3EN, UK
(5) School of the Environment, Geography and Geosciences, University of Portsmouth, Portsmouth PO1 3HE, UK
(6) Section Chemistry and Physics of Earth Materials, GFZ German Research Centre for Geosciences, Telegrafenberg, Potsdam 14473, Germany

Published in Boreas (DOI 10.1111/bor.12516)

Abstract

Due to a lack of visible tephras in the Dead Sea record, this unique palaeoenvironmental archive is largely unconnected to the well-established Mediterranean tephrostratigraphy. Here we present first results of the ongoing search for cryptotephras in the International Continental Drilling Program (ICDP) sediment core from the deep Dead Sea basin. This study focusses on the Lateglacial (~15-11.4 cal. ka BP), when Lake Lisan – the precursor of the Dead Sea – shrank from its glacial highstand to the Holocene low levels. We developed a glass shard separation protocol and counting procedure that is adapted to the extreme salinity and sediment recycling of the Dead Sea. Cryptotephra is abundant in the Dead Sea record (up to ~100 shards cm-3), but often glasses are physically and/or chemically altered. Six glass samples from five tephra horizons reveal a heterogeneous geochemical composition, with mainly rhyolitic and some trachytic glasses potentially sourced from Italian, Aegean and Anatolian volcanoes. Most shards likely originate from the eastern Anatolian volcanic province and can be correlated using major element analyses with tephra deposits from swarm eruptions of the Süphan Volcano ~13 ka BP and with ashes from Nemrut Volcano, presumably the Lake Van V-16 volcanic layer at ~13.8 ka BP. In addition to glasses that match the TM-10-1 from Lago Grande di Monticchio (15,820 ± 790 cal. a BP) tentatively correlated with the St. Angelo Tuff of Ischia, we further identified a cryptotephra with glass analyses which are chemically identical with those of the PhT1 tephra in the Philippon peat record (13.9-10.5 ka BP), and also a compositional match for the glass analyses of the Santorini Cape Riva Tephra (Y-2 marine tephra, 22,024 ± 642 cal. a BP). These first results demonstrate the great potential of cryptotephrochronology in the Dead Sea record for improving its chronology and connecting the Levantine region to the Mediterranean tephra framework.

Keywords

Tephrochronology; Cryptotephra; Eastern Mediterranean; Dead Sea; Palaeoclimate

4.1. Introduction

In the drought-affected eastern Mediterranean region, a better understanding of the past hydroclimate variability is a prerequisite to improving our capability for estimating future changes of the water balance. In this respect, palaeoclimate records from marine or lake sediments provide invaluable information about natural hydroclimate changes. The hypersaline Dead Sea is a key palaeoclimate archive in the southeastern Mediterranean region, situated at a critical position between more humid Mediterranean climate and the hyper-arid Saharo-Arabian desert belt (e.g. Enzel et al. 2003; Migowski et al. 2006; Stein et al. 2011; Torfstein & Enzel 2017). As such, the Dead Sea is particularly sensitive for recording even small changes in the atmospheric circulation and precipitation by varying lake levels and sedimentary facies (e.g. Stein 2001). The ~450-m-long International Continental Drilling Program (ICDP) drill-core 5017-1, recovered from the deepest part of the Dead Sea, spans the last ~220,000 years (Stein et al. 2011; Neugebauer et al. 2014; Torfstein et al. 2015). Despite the recent refinement of the age model of the ICDP Dead Sea core (Goldstein et al. 2020), it still mainly relies on wiggle matching of $\delta^{18}O$ data and U-Th ages with comparably large dating uncertainties, hence, hampering the identification of lead- and lag-phase relationships of changing hydroclimate in comparison to other palaeoclimate records.

The timing and hydroclimatic response to abrupt climate change can only be unequivocally synchronized and compared between different climate records if each of their chronologies are precise and robust. In this respect, tephrochronology, i.e. identifying volcanic ash (tephra) of past volcanic eruptions in lacustrine and marine sediment records and using them as time-parallel markers, is the ideal method to achieve unambiguous synchronization (Lowe 2011; Davies et al. 2012; Lane et al. 2017). In recent years, methodological advances have enabled the identification of macroscopically invisible traces of volcanic ash – so-called cryptotephras – in sedimentary climate records, which have multiplied the number of identified tephras, in regions that can be several thousand kilometres away from the volcanic source (Lane et al. 2014; Davies 2015).

For the central and eastern Mediterranean region (Fig. 4-1A), comprehensive tephrostratigraphical efforts have led to a good understanding of the chemical compositions and spatial distribution of late Quaternary tephras deposited in marine and terrestrial sediment records (e.g. Keller et al. 1978; Narcisi & Vezzoli 1999; Bourne et al. 2010; Wulf et al. 2012; Matthews et al. 2015). The main volcanic source regions for late Quaternary tephra dispersals in the eastern Mediterranean region are the Italian volcanic provinces, the Hellenic Arc including Santorini, central Anatolia and eastern Anatolia (Fig. 4-1A). So far, there is no evidence for regionally significant volcanic eruptions and tephra dispersal from the Arabian volcanic province including the Harrat Ash Shaam field (Fig. 4-1A) of the southern Levant and northern Arabia in

the late Quaternary (Hamann et al. 2010; Zanchetta et al. 2011). Therefore, the tephrostratigraphical work accomplished in recent decades is mainly based on the study of visible tephra layers identified in marine and lacustrine sediment records located in relative proximity to the highly active Italian and Aegean provinces (e.g. Keller et al. 1978; Federman & Carey 1980; Narcisi & Vezzoli 1999; Wulf et al. 2012, 2020, 2004, 2008; Bourne et al. 2010, 2015; Çağatay et al. 2015; Matthews et al. 2015; Tomlinson et al. 2015).

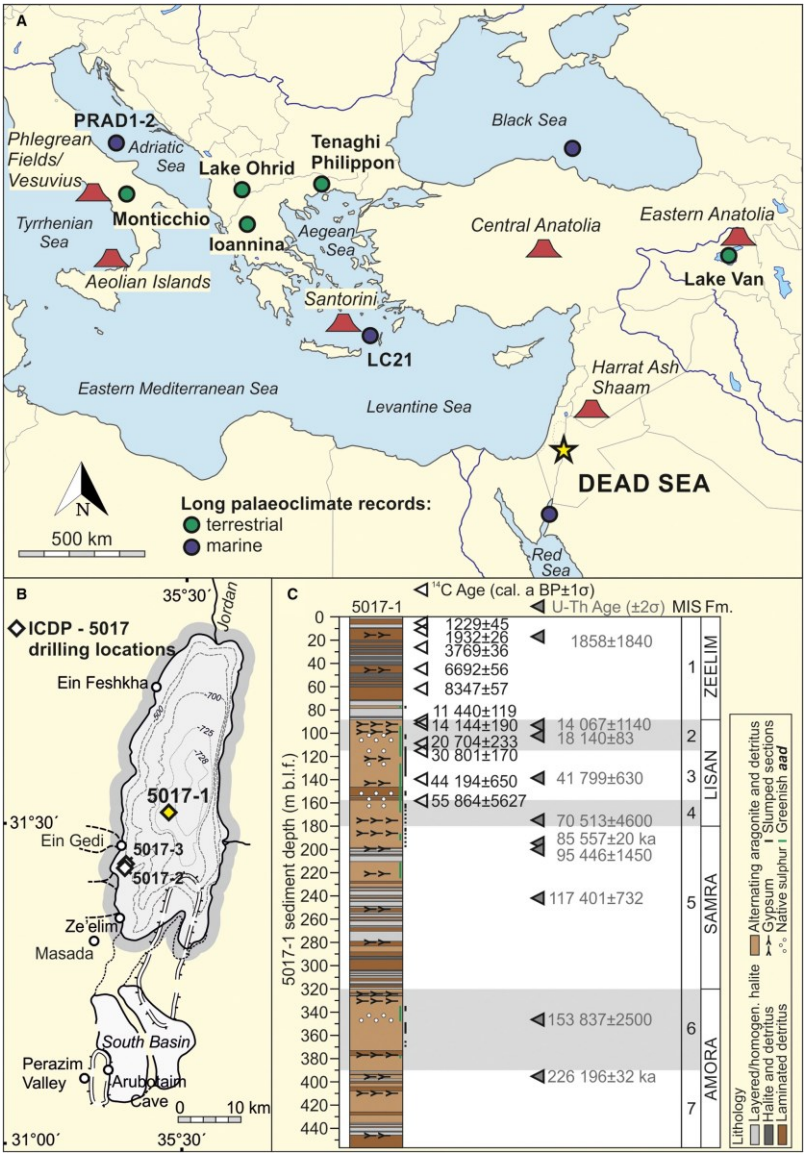

***Figure 4-1**: A. Distribution map of central and eastern Mediterranean volcanic provinces and selected palaeoenvironmental sediment records with established late Quaternary tephrochronologies; the Dead Sea is highlighted (yellow star). B. Dead Sea map with drilling locations of the ICDP 5017 expedition (diamonds; core 5017-1 is analysed in this study) and selected onshore sites studied earlier (circles). C. Core 5017-1 lithostratigraphy* (Neugebauer et al. 2014) *and selected ^{14}C* (Kitagawa et al. 2017) *and U-Th ages* (Torfstein et al. 2015)*; corresponding marine isotope stages (MIS) and Dead Sea sediment formations (Fm.) are also marked.*

Despite being located in a favourable wind direction for receiving tephra from the central and eastern Mediterranean volcanoes via the westerlies, there are so far no tephra layers reported in palaeoclimate records from the southeastern Levantine region. The only exception is the Early Holocene (~9000 cal. a BP) Dikkartin eruption of the Erciyes Dagi in central Anatolia that was identified as a distal tephra layer in

the Yammouneh palaeolake record in Lebanon, and in a marine sediment core from the SE Levantine Sea (Develle et al. 2009; Hamann et al. 2010). Recently, the first finding of this so-called 'S1' tephra as a cryptotephra in the Dead Sea and in the Tayma palaeolake record from NW Arabia allowed precise synchronization of these records and a discussion of lead- and lag-phase relationships of precipitation patterns in the Levantine-Arabian region during the Early Holocene humid period (Neugebauer et al. 2017). Moreover, this discovery encouraged a systematic search for tephra time-markers in the ICDP deep-basin core 5017-1 (Fig. 4-1B, C), with the aim of improving the chronology of the deep record and providing a tool for precise regional synchronization of proxy records.

The present study focusses on the last glacial-interglacial transition in the ICDP Dead Sea sediment core. Strong lake level fluctuations occurred at the last glacial precurser of the Dead Sea (Lake Lisan) during the Lateglacial; however, the hydroclimatic conditions in the central Levantine region in particular during Greenland Stadial 1 are uncertain (Stein et al. 2010). An improved chronology of the Dead Sea sediment record is a prerequisite for a precise synchronization with other palaeoclimate records, particularly in the eastern Mediterranean, in order to prove or disprove apparent large regional hydroclimatic differences like, for example a wet Younger Dryas in the Levant (Stein et al. 2010) and an arid Younger Dryas in Anatolia (e.g. Wick et al. 2003). This study aims at deciphering the Lateglacial hydroclimatic conditions in the Levantine region through the identification of cryptotephras in the Dead Sea sediment record and the improvement of its Lateglacial chronology. Such advanced insights into past regional climatic responses to global change are crucial to better anticipate possible future developments.

4.2. The ICDP Dead Sea record

Previous studies of the Dead Sea sediments were mainly restricted to sediment formations that are exposed at the margins of the lake (e.g. Bartov et al. 2002; Bookman (Ken-Tor) et al. 2004; Torfstein et al. 2009; Waldmann et al. 2009), or that were drilled along the western shoreline (Migowski et al. 2006). These outcrops and shallow cores, however, lack information especially about drier periods and low lake stands. Earlier attempts to drill in the deep basin were hampered by thick salt sequences that could not be penetrated (Heim et al. 1997). Therefore, a promising way to gain a continuous, long sediment record from the deep Dead Sea basin was through an ICDP drilling. From the ICDP Dead Sea Deep Drilling Project (DSDDP; 'The Dead Sea as a Global Paleoenvironmental, Tectonic, and Seismological Archive'), a ~450-m-long sediment record was recovered from the deepest part of the Dead Sea basin in 2010/11, comprising

a continuous record of the last ~220,000 years of climate history in the southern Levantine region (Stein et al. 2011; Neugebauer et al. 2014).

The efforts to establish a robust chronology for the exposed sequences of the Dead Sea lacustrine formations have continued for more than two decades, applying radiocarbon, U-Th dating and floating $\delta^{18}O$ stratigraphy methods (see Stein & Goldstein 2006 for an overview; Torfstein et al. 2009, 2013a). Accordingly, this approach has also been applied to constrain the chronology of the ICDP deep core 5017-1. For the upper ~150 m of the core, the age-depth model is based on 38 ^{14}C dates of terrestrial plant remains that provide a relatively solid chronology for the last ~50 ka, i.e. back to the limit of the radiocarbon dating method (Neugebauer et al. 2014, 2015; Kitagawa et al. 2017). Unfortunately, this chronology includes unknown uncertainties because all dated plant remains could only be extracted from the base of turbidites so that reworking and resulting age/depth reversals cannot be excluded. Slumping of sediments and erosion by mass-transport deposits are very common features in the core (Neugebauer et al. 2014; Kagan et al. 2018) and further add to the uncertainty of the chronology, but this can hardly be quantified. The age model of the older part of the core, reaching to ~220,000 years, was constructed by U-Th dating on primary aragonite that was combined with wiggle matching of stable oxygen isotope signals from aragonite layers and lithological changes that have been tied to exposed sediment formations, and to stable oxygen isotope data from the Soreq Cave speleothem and the LR04 global marine stack (Torfstein et al. 2015; Goldstein et al. 2020). Also, this approach is problematic, since (i) U-Th dating of authigenic carbonate requires a comprehensive correction procedure to account for the presence of detrital U and Th, and hydrogenic Th in Dead Sea sediments (Stein & Goldstein 2006 and references therein), which results in large age uncertainties of U-Th ages of up to several thousand years (Torfstein et al. 2013a); and because (ii) wiggle matching of oxygen isotope and lithological data to very different types of records is not independent.

Sediments of the ~450-m-long 5017-1 core, retrieved from a water depth of ~300 m (in 2010), mainly consist of alternating aragonite-detritus laminae, massive gypsum deposits, laminated marl, and halite sequences that are characteristic for the Amora (MIS 7-6), Samra (MIS 5), Lisan (MIS 4-2) and Zeelim (Holocene) sediment formations deposited in the Dead Sea basin (Fig. 4-1C; Neugebauer et al. 2014). One of the best-studied sections of the Dead Sea sediment formations is the Upper Lisan Formation, deposited in the Dead Sea basin during MIS 2 and building iconic sediment exposures in Masada (M1 outcrop) and the Perazim Valley (PZ1 outcrop) (e.g. Begin et al. 1980; Machlus et al. 2000; Bartov et al. 2002; Prasad et al. 2004, 2009; Torfstein et al. 2013b). The so-called 'White Cliff', finely laminated white aragonite and detritus sediments, formed during the Last Glacial Maximum when Lake Lisan was at its maximum

highstand of ~160 m below sea level (b.s.l.; Torfstein et al. 2013b). The White Cliff is topped by the 'Upper and Additional Gypsum Units', which announce the Lake Lisan level retreat at the end of the last glacial at ~17.1-15.5 ± 0.5 and at ~14.5 ± 0.5 ka (Torfstein et al. 2013a) down to Holocene levels of ~400 ± 30 m b.s.l. (Migowski et al. 2006). Due to this lake level decline, Lateglacial sediments and the transition to the Holocene between ~13 and 11 cal. ka BP are not exposed in the onshore deposits, but these can now be studied in the ICDP deep-basin core.

4.3. Material and methods

4.3.1. Sampling and glass shard extraction

Sediment cores of ICDP expedition 5017 are stored at the Marum Core Repository in Bremen, Germany. Sampling for glass shard analyses of cryptotephras of core 5017-1 is principally done in contiguous 5-cm steps with sample volumes of 5 cm^3, excluding mass-transported deposits (turbidites and slumps) thicker than 5 cm. Rock salts and other consolidated sediment sections that are too hard for sampling with a spatula were cut using a band saw at GFZ Potsdam, Germany.

The cryptotephra glass extraction protocol followed established physical and chemical separation procedures (Blockley et al. 2005), and has been further developed to account for the specific conditions of Dead Sea sediments. First, samples were repeatedly rinsed with deionized water in a shaking bath to dissolve salts and remove highly saline pore waters. Second, 10% HCl and 15% H2O2 solutions were added to remove carbonates and organic matter. This step was followed by wet-sieving into a 20-100 µm grain-size fraction, and sodium polytungstate (SPT) liquid density mineral separation, with volcanic glass shards being concentrated in the 2-2.55 g cm^{-3} fraction. Residual clays that disaggregated during this process were then removed by a second sieving through a 20-µm mesh.

The remaining sediment material still contains high concentrations of mineral grains (Fig. 4-2), which would prevent time-efficient glass shard counting of these samples. Therefore, Lycopodium spores (Fig. 4-2) with a defined number of spores per tablet (10,679 ± 426 spores per tablet, batch no. 938934, Laboratory of Quaternary Geology University Lund, Sweden; Stockmarr 1971) were added to the samples. About 10% (at least 5%) of the total residue was mounted on glass slides for glass shard counting under a transmitted light polarization microscope. Along with counting Lycopodium spores in this subsample, the glass shard concentration per cubic centimetre of sediment or per gram dry weight can be estimated based on the given total number of spores (one tablet) in the total sample residue.

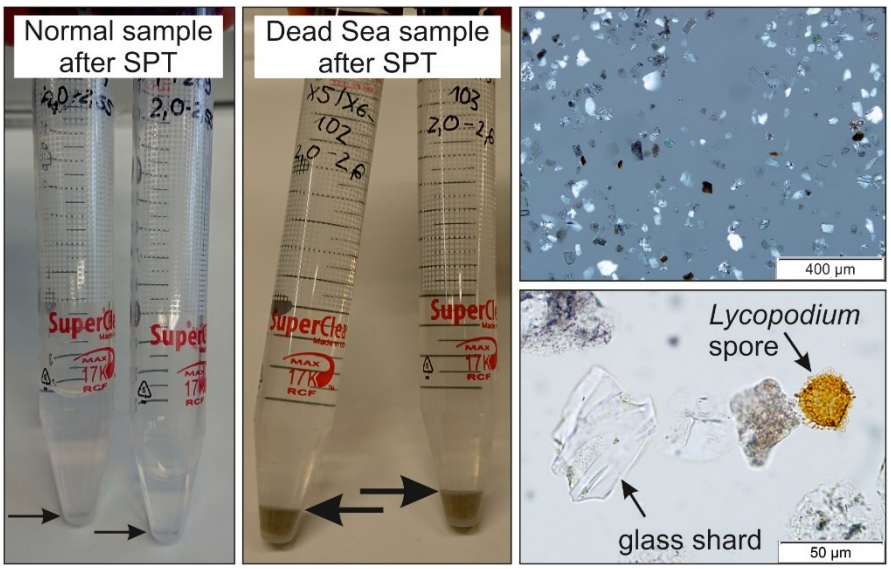

***Figure 4-2**: Comparably large amounts of mineral grains (e.g. quartz, feldspars; upper right) in Dead Sea samples are left after physical-chemical treatment, requiring a specific protocol (adding Lycopodium spores to estimate tephra concentration from a ~10% aliquot of the 20-100 µm grain size and 2-2.55 g cm^{-3} density fraction). The comparison sample has been taken from evaporitic sediments of a high-altitude lake in Argentina.*

4.3.2. Geochemical characterization of tephra-derived glass

Glass shards of identified tephra horizons were picked under the microscope from the remaining ~90% of suspended sample material using a 100-µm-diameter gas-chromatography syringe attached to a micromanipulator (see Lane et al. 2014). Shards were transferred into single-hole-stubs, embedded in Araldite 2020 epoxy resin, ground and polished for electron probe microanalyses (EPMA). The major element composition of individual glass shards was measured using a JEOL JXA-8230 electron microprobe at GFZ Potsdam, Germany, with operating conditions of 15 kV voltage, 5 nA beam current, and a beam size of 5-10 µm depending on glass shard size. Exposure times were for each analysis 20 s for the elements Fe, Cl, Mn, Ti, Mg and P, and 10 s for Si, Al, K, Ca and Na. Instrumental calibration used natural mineral standards, and the glass standards Lipari obsidian (Hunt & Hill 1996; Kuehn et al. 2011) and MPI-Ding glasses ATHO-G, StHs-6-80-G and GOR-132-G (Jochum et al. 2006) were used during analytical runs to monitor the precision and accuracy of measurements (Table S4-2).

4.3.3. Lateglacial Dead Sea samples

For the present study, 56 samples between 89.30 and 94.09 m sediment depth below lake floor (m b.l.f.) from cores 5017-1-A-43 and 5017-1-A-44 were analysed for crypto-tephrostratigraphy, following the procedure illustrated above. These samples cover the top-most ~5 m of the Upper Lisan Formation in the ICDP core (Figs 4-1C, 4-3), i.e. immediately underlying the Early Holocene salt section (~73-89 m b.l.f. in 5017-1; Fig. 4-1C). From six of these samples, at least 10 glass shards per sample were measured by EPMA. Replicate measurements on a different set of glass shards from the sample were performed initially using

10 nA and later 5 nA beam currents for three samples, resulting in a total of 107 glass geochemical measurements (Table S4-3). Five values with raw totals of <90% were excluded from further evaluation.

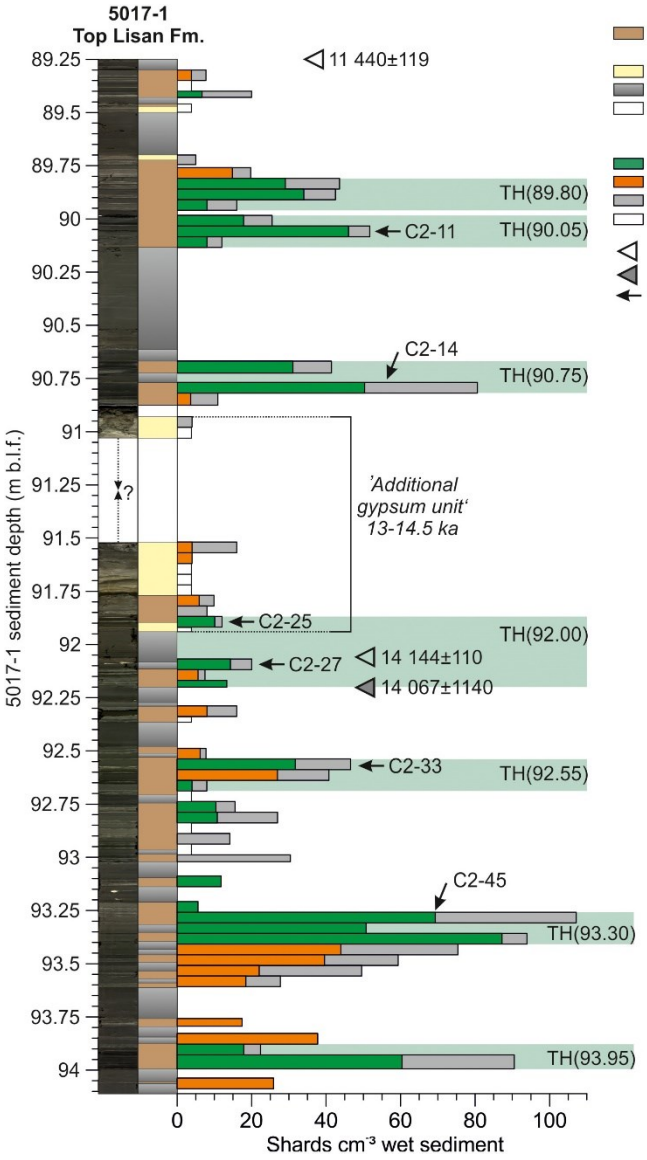

***Figure 4-3**: Detailed lithology and glass counting results of the uppermost ~5 m of the Lisan Formation in the ICDP core 5017-1 from the deep Dead Sea basin. The alteration of shards has been defined by their optical appearance (rounded or sharp) under the microscope. Tephra horizons (TH) are highlighted by light green bars. Glass shards of the uppermost and lowermost tephra horizons could not be prepared for glass geochemical measurements because shards were too small (tiny platy shards in TH(89.80)), or had an unfavourable morphology (very thin butterfly shards in TH(93.95)).*

4.4. Results

4.4.1. Glass shard counting

Of the 56 samples inspected here, 45 contain volcanic glass shards with concentrations of 4 to 107 shards cm^{-3} wet sediment (Fig. 4-3). Shards are concentrated in several 10-20 cm thick tephra horizons (TH) within finely laminated aad (alternating aragonite and detritus) sediments around 89.80, 90.05, 90.75, 92.00,

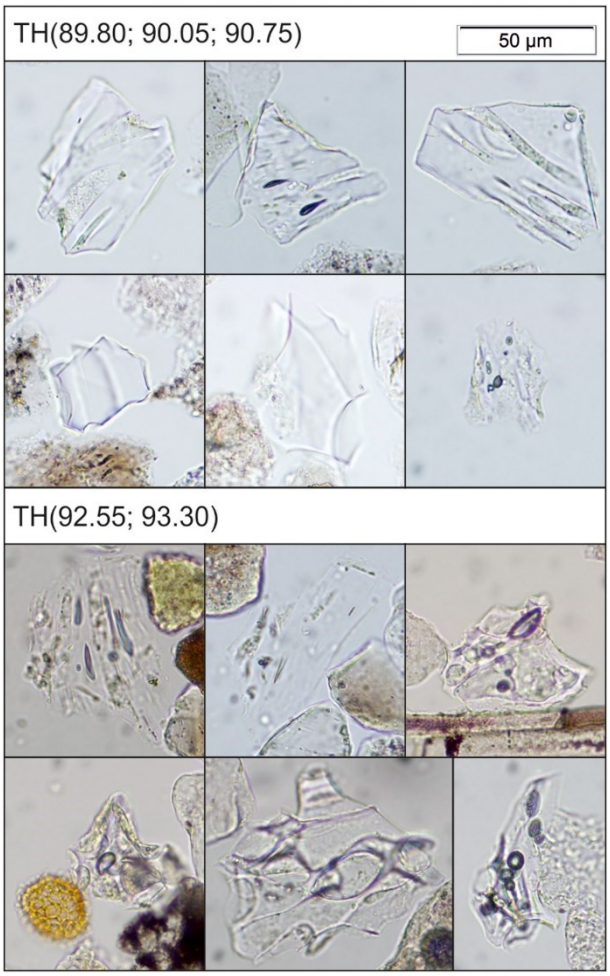

***Figure 4-4**: Glass shard morphologies of different tephra horizons (TH); see text for details.*

92.55, 93.30 and 93.95 m b.l.f. (Fig. 4-3). Even though turbidites thicker than 5 cm were excluded from cryptotephra sampling, evidence of smaller reworking events is still common and included in the samples. This reworking likely explains the physical alteration (rounding) of glass shards of at least 17 samples. In addition, particularly vesicular shards are often chemically altered at their surface and rims (Fig. 4-4), potentially as a result of the alkaline composition of the Dead Sea brine. The frequent occurrence of 'volcaniform' phytoliths, which have similar optical properties to these altered volcanic glasses, further complicates glass and hence tephra identification under the microscope. The maximum estimate of the shard concentration in Fig. 4-3 considers such ambiguous cases.

4.4.2. Glass shard morphologies

Glass shards are typically clear, devoid of microlites or other inclusions, and range in size mostly between 30 and 80 µm (Fig. 4-4). Some glass morphologies are preferentially found within specific TH. In the upper tephra horizons TH(89.80; 90.05; 90.75), glasses are mostly cuspate/butterfly-shaped or contain elongated vesicles (Fig. 4-4), and some are fluted. Tiny platy shards almost exclusively occur in TH(89.80). Glasses in TH(92.00) have cuspate or fluted shapes. In TH(92.55), glasses with elongated vesicles are noticeably thin. Vesicular and highly vesicular bubble-wall shards are characteristic in TH(93.30). Very thin butterfly shards occur in the lowermost tephra horizon TH(93.95).

4.4.3. Glass geochemical compositions

Major element EPMA data (n = 102; Table S4-3) of glass from the six samples analysed here show mostly rhyolitic and some trachytic glass compositions (Fig. 4-5). Seven tephra populations can be distinguished that are mostly spread over several samples, i.e. they occur in several tephra horizons. These tephra

populations (POP) are described in the following; their major element glass chemistry is shown in Figs 4-5 and 4-6 and summarized in Table 4-1. The analyses reported in the following text are on a normalized (volatile-free) basis (Table 4-1).

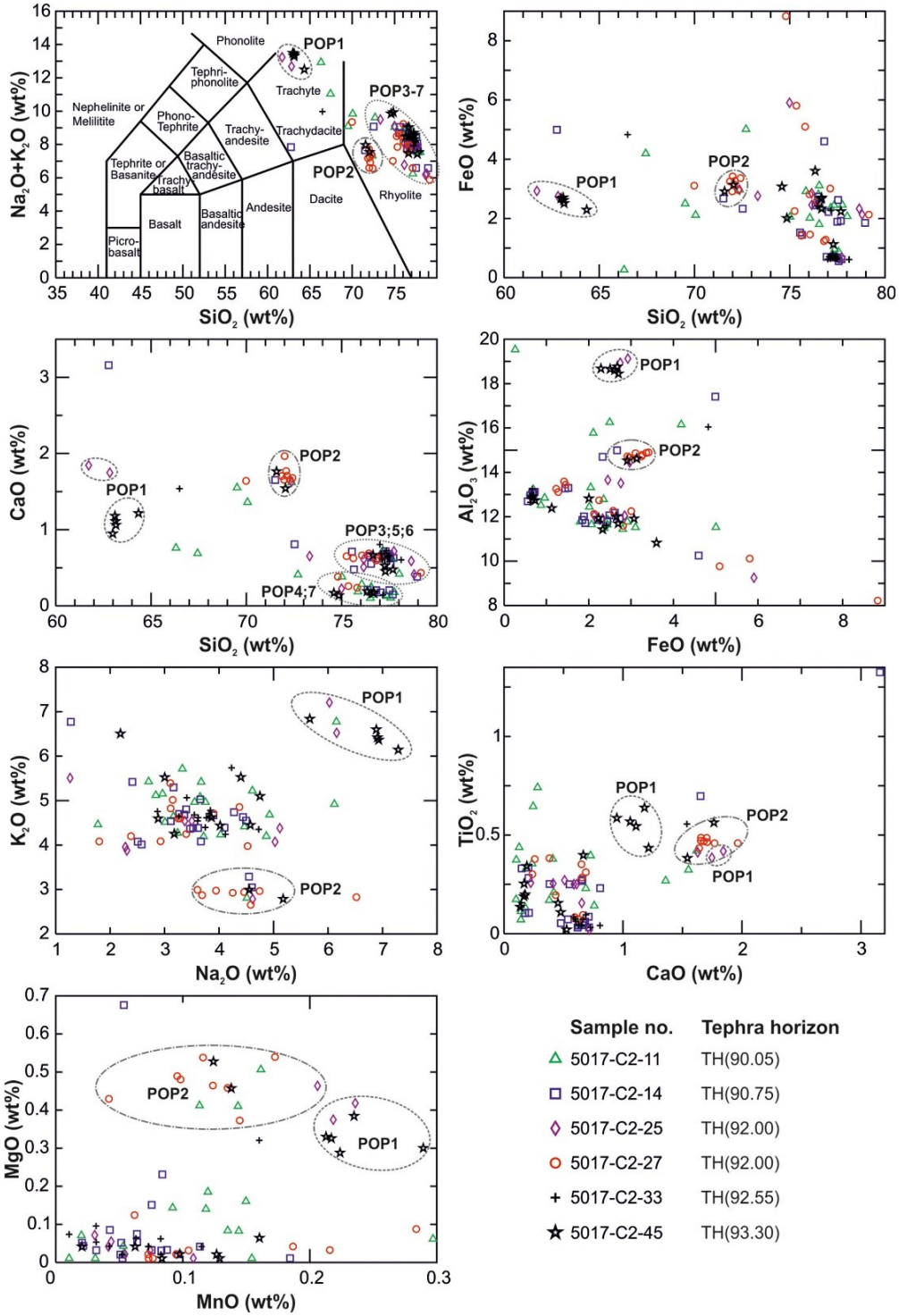

***Figure 4-5**: Total alkali-silica diagram and bivariate elemental plots of EPMA normalized glass data from Lateglacial Dead Sea sediments (~15-11 cal. ka BP). Note that analytical errors are smaller than the symbol size.*

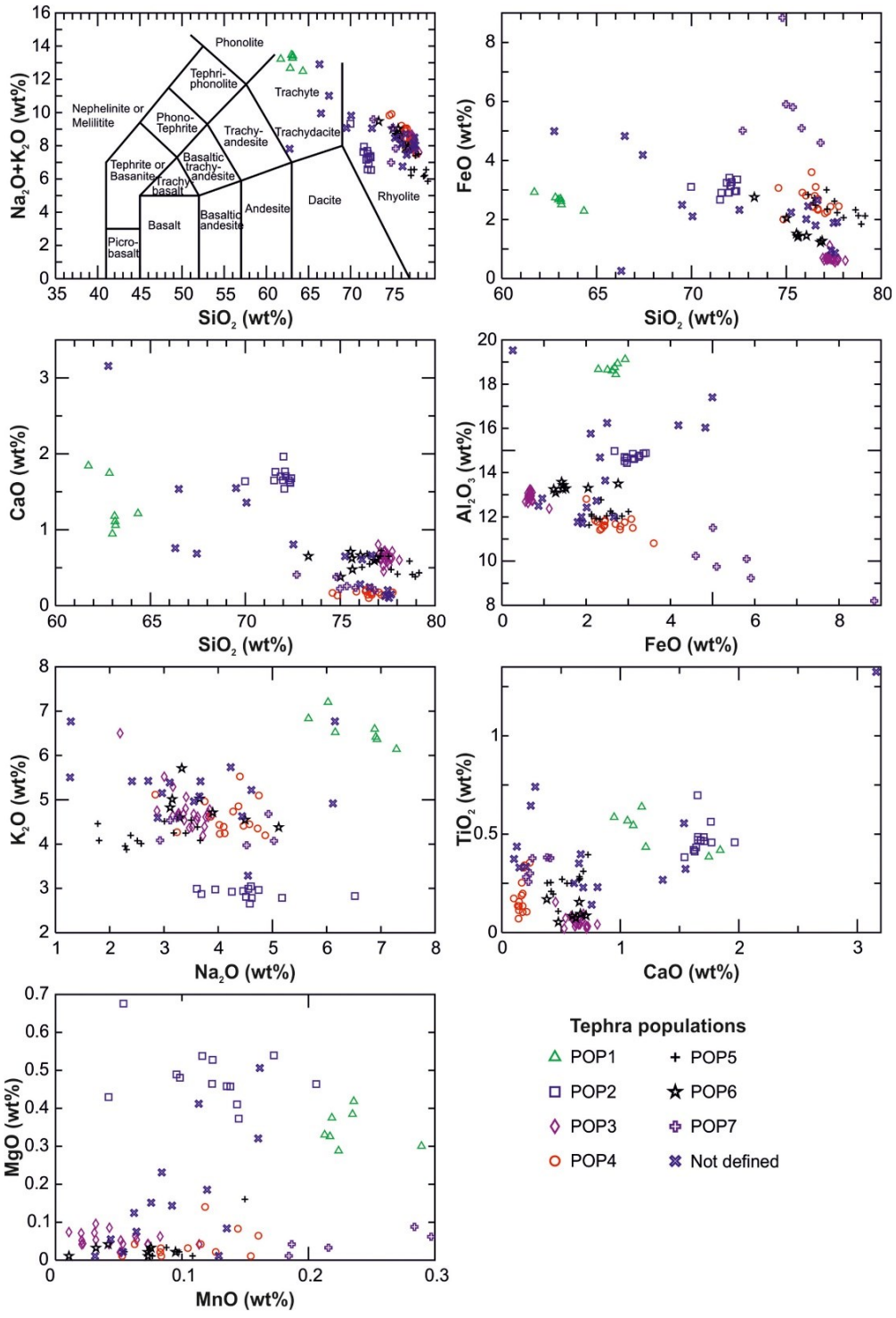

***Figure 4-6**: Total alkali-silica diagram and bivariate elemental plots of EPMA normalized glass data of tephra populations identified in Lateglacial Dead Sea sediments (~15-11 cal. ka BP). Tephra populations were defined visually and by sorting the EPMA data table. Note that analytical errors are smaller than the symbol size.*

***Table 4-1**: Mean glass geochemical data in wt% (normalized, volatile-free) of the identified tephra populations (POP). Std = standard deviation; * = total iron is reported as FeO.*

Tephra population	Total	SiO_2	TiO_2	Al_2O_3	FeO*	MnO	MgO	CaO	Na_2O	K_2O	P_2O_5	Na_2O+K_2O	K_2O/Na_2O
POP1 (*n* = 7)	93.76	63.04	0.51	18.74	2.64	0.23	0.35	1.3	6.55	6.58	0.05	13.13	1.02
std	1.11	0.71	0.09	0.21	0.19	0.02	0.04	0.32	0.55	0.32	0.02	0.36	0.13
POP2 (*n* = 13)	95.14	71.9	0.48	14.72	3.08	0.12	0.49	1.69	4.56	2.89	0.08	7.45	0.65
std	1.81	0.61	0.08	0.15	0.2	0.04	0.07	0.1	0.7	0.11	0.02	0.68	0.1
POP3 (*n* = 23)	95.75	77.39	0.05	12.93	0.68	0.04	0.05	0.64	3.43	4.77	0.02	8.2	1.43
std	1.6	0.26	0.03	0.2	0.1	0.03	0.02	0.07	0.38	0.46	0.02	0.3	0.37
POP4 (*n* = 16)	95.93	76.43	0.19	11.69	2.62	0.11	0.03	0.16	4.15	4.62	0.01	8.77	1.14
std	1.45	0.79	0.09	0.39	0.4	0.03	0.04	0.05	0.53	0.38	0.01	0.61	0.21
POP5 (*n* = 13)	92.96	77.59	0.26	12.08	2.41	0.1	0.02	0.55	2.77	4.21	0.01	6.97	1.6
std	1.54	1.01	0.06	0.26	0.32	0.03	0.04	0.12	0.64	0.21	0.01	0.74	0.39
POP6 (*n* = 8)	94.9	75.61	0.1	13.35	1.65	0.06	0.02	0.59	3.75	4.85	0.02	8.61	1.34
std	1.12	1.05	0.04	0.14	0.48	0.03	0.01	0.1	0.67	0.39	0.02	0.54	0.28
POP7 (*n* = 6)	93.92	75.08	0.33	9.85	5.87	0.24	0.04	0.29	3.96	4.32	0.01	8.28	1.15
std	2.26	1.25	0.05	1	1.4	0.04	0.03	0.08	0.88	0.29	0.02	0.88	0.28

4.4.3.1. POP1 (trachytic)

Seven shards are trachytic in composition (five in sample 5017-C2-45, two in sample 5017-C2-25), close to the phonolite boundary, with 61.7-64.3 wt% SiO_2 and on average 6.5 wt% Na_2O and 6.5 wt% K_2O. These glasses are further characterized by ~18.7 wt% Al_2O_3, 0.5 wt% TiO_2 and 2.6 wt% FeO (total iron sum reported as FeO). CaO values in glass differ between the two samples, with ~1.1 wt% in sample 5017-1-C2-45 and ~1.8 wt% in sample 5017-C2-25 (Fig. 4-5).

4.4.3.2. POP2 (rhyolitic)

The composition of glass in population POP2 (n = 13) is characterized by a rhyolitic, close to dacitic, narrow cluster of 71.5-72.4 wt% SiO_2 and total alkalis of 6.6-8 wt%, whereas K_2O values are constant and low (~2.9 wt%). One glass shard with lower SiO_2 (70 wt%), but high Na_2O (6.5 wt%) was assigned to this cluster as well (Fig. 4-6), as all other major elements occur in similar concentrations, e.g. ~14.7 wt% Al_2O_3, 3.1 wt% FeO, 0.5 wt% MgO and 1.7 wt% CaO (Table 4-1). Single glass shards of this population occur in nearly all

analysed samples, except for sample 5017-C2-33, but most of them are located in sample 5017-C2-27 of TH(92.00) (Fig. 4-5).

4.4.3.3. POP3-POP7 (rhyolitic)

The majority of the glass shards analysed have rhyolitic compositions with 74-79 wt% SiO_2 and 6-9.5 wt% total alkalis (Fig. 4-5). Based on small differences in Ti, Al, Fe and Ca oxide contents and alkali ratios, five different tephra populations (POP3 to POP7) can be differentiated that describe n = 66 of all analysed shards (Fig. 4-6).

POP3 (n = 23) is characterized by particularly low TiO_2 (~0.05 wt%) and FeO (0.7 wt%), CaO is ~0.6 wt% and Na_2O is <4 wt%, and most glasses of this population were analysed in sample 5017-C2-33. Of the 14 analysed shards from this sample, 11 shards have compositions that fall into POP3 (Table S4-3).

POP4 (n = 16) shows very depleted CaO values (0.1-0.2 wt%), lower Al_2O_3 (~11.7 wt%) compared to POP3 (~12.9 wt%), higher FeO values (~2.6 wt%), and Na_2O >4 wt%. Glasses of POP4 occurred in all analysed samples; most in both the lowermost and uppermost samples 5017-C2-45 and 5017-C2-11, respectively.

The composition of POP5 (n = 13) is overall very similar to that of POP3 and POP4, with slightly higher TiO_2 (0.3 wt%) and Al_2O_3 (12.1 wt%), but similar FeO (2.4 wt%) compared to that of POP4, whereas CaO values of ~0.6 wt% compare with those of glass of POP3. However, the very low alkali-sum (~7 wt%) and higher K_2O/Na_2O (~1.6) ratio clearly distinguish POP5 from POP3 and POP4. Shards of this population occur in all analysed samples, except for sample 5017-C2-33.

POP6 (n = 8) shows the largest similarity with POP3; only SiO_2 is slightly lower (~75.6 wt%), and Al_2O_3 (13.4 wt%) and FeO (1.7 wt%) are somewhat higher. This population (POP6) mostly occurs in sample 5017-C2-27 of TH(92.00) and only occasionally in the overlying tephra horizons.

POP7 (n = 6) differs from POP3 to POP6 by having lower SiO_2 (72.7-76.8 wt%) and Al_2O_3 (8.2-11.7 wt%) concentrations, but much enhanced FeO values (4.6-5.9 wt%) (Fig. 4-6). Like POP6, most shards of this population were analysed in sample 5017-C2-27, while analyses of only single shards occur above.

4.4.3.4. Undefined glasses

Sixteen glass compositions, eight of which were from sample 5017-C2-11, could not be assigned to any of the tephra populations defined above, and do not build a separate cluster (Figs 4-5, 4-6). Some of these glasses show apparent similarities with POP3, 4, 5 and 6, and others plot in between trachytic and rhyolitic compositions. One single glass shard is of trachydacitic composition.

4.5. Discussion

4.5.1. Lateglacial tephra record ~15-11 cal. ka BP in the Dead Sea

Considering that the Dead Sea in the southern Levantine region is largely influenced by westerly winds from the Mediterranean Sea, we would expect the majority of cryptotephras detected in the Dead Sea record to originate from Italian and Aegean volcanic centres. As the only visible tephra layer in the Levant – the Early Holocene 'S1' tephra from Erciyes volcano (Develle et al. 2009; Hamann et al. 2010), detected as a cryptotephra in the Dead Sea record (Neugebauer et al. 2017) – originates from central Anatolia, we also include the western, central and eastern Anatolian volcanic provinces as potential tephra sources.

Due to the large number and frequent activity of highly explosive volcanoes in the central and eastern Mediterranean during the Lateglacial and beyond, and because successive eruptions from the same source often have very similar glass compositions (e.g. Tomlinson et al. 2012a, 2015), assigning a particular volcanic eruption to a tephra population defined in our data is difficult. Also, a very distal cryptotephra record with low shard concentrations, as is the case for our record, may not represent the full compositional range of an eruption (Tomlinson et al. 2015), which might lead to false correlation, if the full geochemical range of a proximal deposit is also unknown. A further complication is the strong reworking of sediments in the Dead Sea basin, which requires extending the search for tephra correlatives beyond the Lateglacial period analysed here to consider those from older eruptions.

We first followed the attempt by Tomlinson et al. (2015) to discriminate the Mediterranean volcanic centres captured in our data, based on major element glass variations that are typical for different tectonic settings and volcanic provinces, before discussing the correlation of tephra populations with particular eruptives. In addition, we consulted the RESET Database (https://c14.arch.ox.ac.uk/resetdb/db.php; Bronk Ramsey et al. 2015b; Lowe et al. 2015) for available tephra data also from Anatolian provinces. Accordingly, we can distinguish at least three different sources – (i) the Neapolitan volcanic centre/and probably western Anatolia, (ii) Santorini, and (iii) eastern Anatolia/and probably central Anatolia (Fig. 4-7).

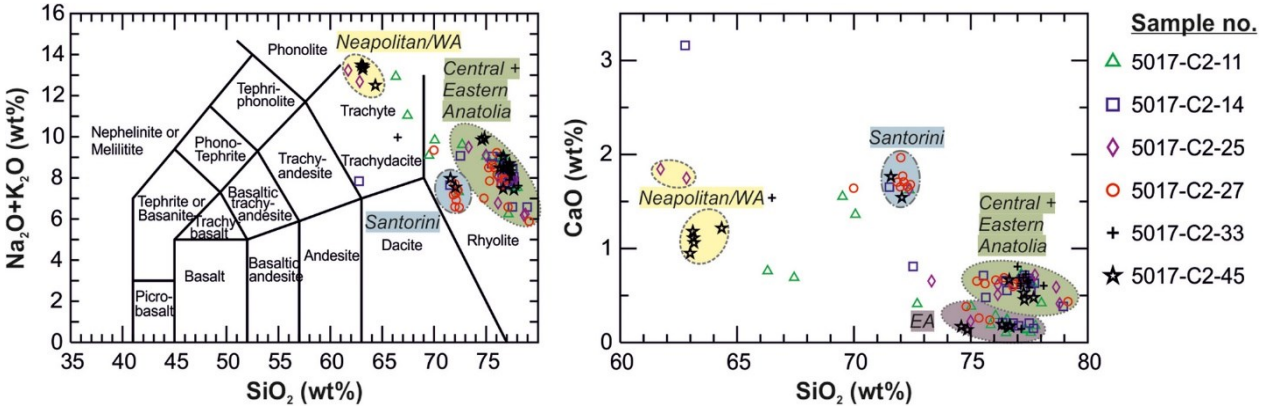

***Figure 4-7**: Discrimination of Mediterranean volcanic centres captured in tephra data of Lateglacial Dead Sea sediments (~15-11 cal. ka BP). Note that the highlighted fields do not represent the full range of geochemical glass compositions of tephras from Neapolitan, Santorini and western, central and eastern Anatolian volcanic centres, and that available proximal tephra data from central and eastern Anatolia largely overlap. Only glasses from Nemrut volcano (eastern Anatolia) can be discriminated due to characteristically low CaO.*

4.5.1.1. POP1 (Campanian and potentially western Anatolian volcanic provinces)

The trachytic composition of POP1 is similar to products of the Neapolitan volcanic district (Campi Flegrei, Ischia and Somma Vesuvius) that formed in a post-subduction setting (Tomlinson et al. 2015). Chemical biplots of Ca-Si, Na/K-Ca and Ca-Mg oxides, which are useful to discriminate Neapolitan volcanic products, place the five glass shards of POP1 from sample 5017-C2-45 that have low CaO (~1.1 wt%) in the field of the Ischia Island (Tomlinson et al. 2015). We found a good correlation of four glasses of this low-Ca subgroup of POP1 (Fig. 4-8) with the glass analyses of Ischia tephra layer TM-10-1 (15,820 ± 790 cal. a BP) in the Lago Grande di Monticchio (LGdM) record (Wulf et al. 2008), which was suggested to relate to the St. Angelo Tuff from the Campotese volcano of Ischia (17,800 ± 3200 K/Ar a; Poli et al. 1987). Glass of the marine C-3 tephra in deep-sea cores in the Tyrrhenian Sea has similar age and trachytic composition (Paterne et al. 1988), and was considered to represent the same explosive event (Wulf et al. 2008). Finding the product of a sub-Plinian eruption in the Dead Sea record, more than 2000 km away from the source, is noteworthy. In addition, the cryptotephra age of ~14.5 cal. ka BP in the Deep Sea core (sample 5017-1-C2-45, TH(93.30)) would be younger than TM-10-1 by at least ~500 years. Therefore, a correlation of the low-CaO glasses of POP1 with those of the TM-10-1 tephra from Ischia must be considered with caution.

Two POP1 glasses in sample 5017-C2-25 (~1.8 wt% CaO) overlap with Campi Flegrei Campanian Ignimbrite (CI)/pre-CI products in Tomlinson et al. (2015), and are similar to the glass composition of the Campanian Ignimbrite super-eruption (~39 ka, marine Y-5 tephra) itself (e.g. Tomlinson et al. 2012a; Giaccio et al. 2017) (TM-18 in LGdM, Fig. 4-8; Wulf et al. 2004). However, CI glasses in this stratigraphical position in the Dead Sea record are unlikely, and Tomlinson et al. (2012a) reported that Post-CI/Pre-NYT (Neapolitan

Yellow Tuff) tephras can hardly be discriminated based on major element compositions alone (see TM tephra layers of LGdM originating from the Phlegrean fields in Fig. 4-8; Wulf et al. 2004, 2008). Therefore, we do not consider the CI as a likely source of the two 'high-CaO' glasses of POP1, even though reworking of older CI glasses cannot be entirely excluded.

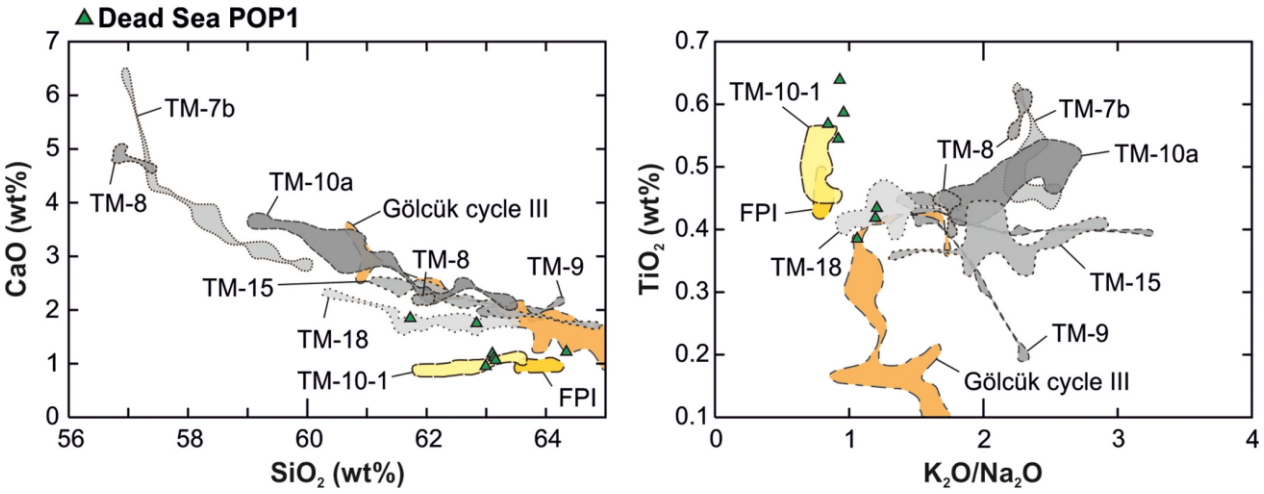

***Figure 4-8**: Elemental biplots (normalized to 100%, volatile-free) of Dead Sea POP1 EPMA glass data (green triangles) compared with data of Ischia/Campanian eruptives, as recorded in the Lago Grande di Monticchio record* (*TM tephra layers*; Wulf et al. 2004, 2008). *Tephras related to the Phlegrean fields (grey shades): TM-7b = Pomici Principali; TM-8 = Neapolitan Yellow Tuff; TM-9 = Tufi Biancastri; TM-10a = Lagno Amendolare; TM-15 = marine Y-3 tephra; TM-18 = Campanian Ignimbrite (CI)/marine Y-5 tephra. Tephras related to Ischia (yellow shades): TM-10-1 = tentative correlation to St. Angelo Tuff/marine C-3 tephra* (Wulf et al. 2008, and S. Wulf, unpublished data)*; FPI = Faro di Punta Imperatore in marine core PRAD 1-2, central Adriatic Sea* (Bourne et al. 2010). *Also shown are pumice data of Gölcük cycle III (orange field) from western Anatolia* (Tomlinson et al. 2015).

A widely dispersed trachytic phreato-plinian deposit is the Neapolitan Yellow Tuff (NYT, marine C-2 tephra) that is the product of a high-magnitude, caldera-forming eruption of Campi Flegrei (Deino et al. 2004; Siani et al. 2004). Its $^{40}Ar/^{39}Ar$ isochron age of 14.9 ± 0.4 ka (2σ) (Deino et al. 2004) and revised age of 14,194 ± 172 cal. a BP (Bronk Ramsey et al. 2015a), considering ^{14}C dating and varve counting in Lago Grande di Monticchio (Wulf et al. 2004, 2008), would make the NYT a likely candidate for correlation with POP1. However, the NYT was rather dispersed to the north and has never been reported from eastern Mediterranean archives (Bronk Ramsey et al. 2015a). The slight mismatch of the major element compositions of the NYT (TM-8 in LGdM, Fig. 4-8; Wulf et al. 2004) and POP1 leave us to reject the NYT as a tephra correlative.

Trachytic tephra of the western Anatolian Gölcük volcano (Isparta, SW Turkey; Platevoet et al. 2008; Çoban et al. 2019), located much closer to the Dead Sea than the Campanian province and with most recent

activity during the Lateglacial ((U–Th)/He zircon eruption ages 14.1 ± 0.5 and 12.9 ± 0.4 ka, 1σ; Schmitt et al. 2014), is considered as a more likely candidate for correlation with 'high-CaO' glasses of POP1. Indeed, geochemical data of glass from the most recent eruption sequence Gölcük cycle III (Tomlinson et al. 2015) plot very close to our data, of which one glass lies directly within this field (Fig. 4-8).

4.5.1.2. POP2 (Santorini)

The major element composition of glass of the rhyolitic POP2 can be correlated with the active subduction setting of the Aegean volcanic province (Tomlinson et al. 2015), and more specifically with glass of the rhyodacitic Cape Riva Ash of Santorini (marine Y-2 tephra) (Federman & Carey 1980; Druitt et al. 1999; Fabbro et al. 2013; Wulf et al. 2020; Fig. 4-9). The Cape Riva eruption, radiocarbon-dated at 22,024 ± 642 (2σ) cal. a BP (Bronk Ramsey et al. 2015a), formed prominent proximal pyroclastic fall deposits and far-spread distal tephra layers in the eastern Mediterranean region (e.g. St. Seymour et al. 2004; Satow et al. 2015; Wulf et al. 2020). Still, the appearance of the ~22 ka Cape Riva Ash in Lateglacial sediments of the Dead Sea is considered unlikely due to the large age difference that would imply considerable reworking of sediments.

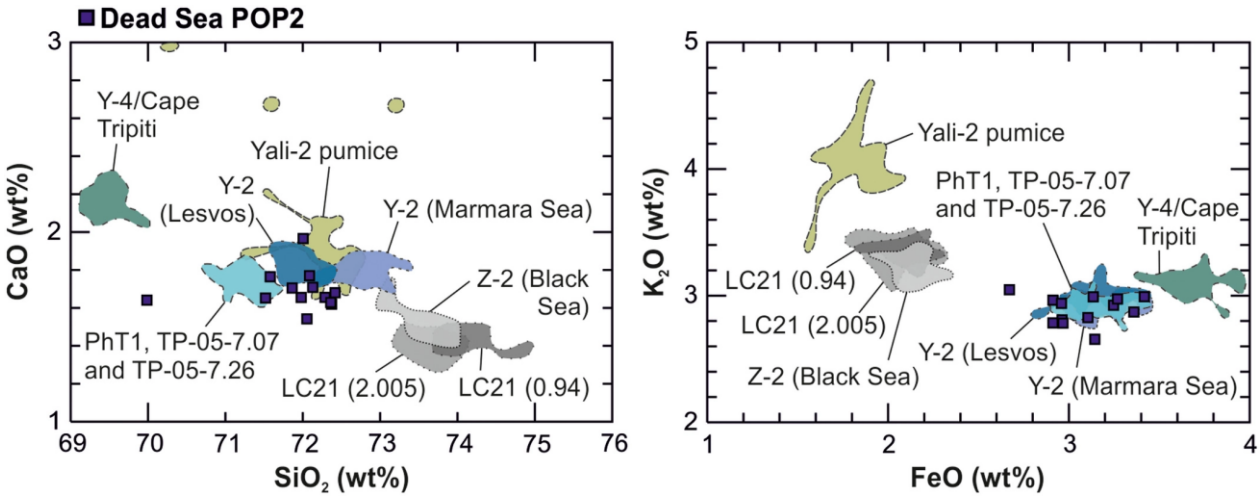

***Figure 4-9**: Elemental biplots (normalized to 100%, volatile-free) of Dead Sea POP2 EPMA glass data (blue squares) compared with data of Santorini/Hellenic Arc eruptives. Minoan Ash/marine Z-2 tephra (Santorini; grey shades) recorded in SW Black Sea cores* (Kwiecien et al. 2008) *and in Aegean Sea core LC21 (LC21 (0.94))* (Satow et al. 2015)*; the older, Lateglacial cryptotephra layer LC (2.005) with identical chemical composition is also shown. Cape Riva/Y-2 tephra (Santorini; blue shades) recorded in the Marmara Sea* (Wulf et al. 2002) *and in Lesvos (Margari et al. 2007); the glass shards of cryptotephra layers of Lateglacial age in the Tenaghi Philippon record* (PhT1, St. Seymour et al. 2004; TP-05-7.07 and TP-05-7.26, Wulf et al. 2018) *have a similar, Cape Riva-like composition. The much older Hellenic Arc Yali-2 tephra (RESET Database, pumice collected inside Nisyros caldera by H. Kinvig) and the Cape Tripiti/Y-4 tephra from Santorini* (Wulf et al. 2020) *are plotted in green shades.*

However, there is distal evidence from the Tenaghi Philippon peat basin of northern Greece for deposition of a Lateglacial Santorini eruption that has glass chemically identical to that of Cape Riva tephra (St. Seymour et al. 2004; Wulf et al. 2018), but this has not yet been proven in the proximal or marine distal database (Druitt et al. 1999; Wulf et al. 2020). St. Seymour et al. (2004) described a visible tephra layer (PhT1) in the Philippi peat basin, radiocarbon-dated to 11,818 ± 139 cal. a BP (IntCal13) but with conflicting estimates from ~13.9 to 10.5 cal. ka BP, which has glass with a chemical affinity to Y-2 and which was recognized some decimetres above the primary, several-centimetre-thick Y-2 (PhT2) tephra. Similarly, Wulf et al. (2018) identified two cryptotephra layers (that have comparably high shard concentrations >10 000 shards g-1 dwt; TP-05-7.07 and TP-05-7.26 in Fig. 4-9) that are chemically identical to those of the Cape Riva/Y-2 tephra in the Tenaghi Philippon TP-2005 core ~40-60 cm overlying the Y-2 tephra. Due to the lack of field and geochronological evidence for a Lateglacial eruption of Thera (Santorini) volcano, and because of the identical trace element composition of glass with that of the Y-2 tephra, the PhT1 tephra has been interpreted as a result of postdepositional recycling of Y-2 material (Wulf et al. 2018). Although we cannot exclude reworking in the Dead Sea sediments either, the occurrence of a cryptotephra with Cape Riva glass chemical affinity also in the Lateglacial sediments of the Dead Sea (sample 5017-C2-27 of TH(92.00); previously dated to ~14 cal. ka BP, see discussion below) might be another hint for a yet unknown Inter-Plinian eruption of the Santorini volcano during this period that so far has not yet been found in proximal sites.

4.5.1.3. POP3-POP6 (central/eastern Anatolia)

Glasses of the highly evolved, silicic tephra populations POP3 to POP6 overlap in their chemical composition with those of the products of several active subduction volcanic centres in the eastern Mediterranean; these are the Hellenic Arc islands Nisyros, Kos and Yali (without Santorini) and central Anatolia (Kuzucuoglu et al. 1998; Tomlinson et al. 2015), as well as eastern Anatolia (Sumita & Schmincke 2013; Schmincke & Sumita 2014). Only for four major eruptives from Hellenic Arc volcanoes, geochemical glass data are available: the Yali-2 tephra, dated to ~35 ka BP based on orbitally tuned marine core KB28 (Vinci 1985), shows a similar glass chemical composition as that of the Cape Riva Ash (Tomlinson et al. 2015) and may be considered for potential correlation with POP2 (Fig. 4-9). The Nisyros Upper and Lower Pumices (~47 and 52 ka BP, respectively; Limburg & Varekamp 1991; Tomlinson et al. 2012b), and the Kos Plateau Tuff (KPT, marine W-3 tephra, ~166 ka BP; Bachmann et al. 2010) overlap in their glass shard compositions with POP3 to POP6. Even though we cannot entirely exclude these tephras as potential correlatives to our data, we also do not consider these as very likely due to their much older eruption ages.

The tephrostratigraphical framework for central and eastern Anatolian volcanic provinces is sparse in comparison to that of the comprehensive Italian and Aegean databases. While the Early Holocene Dikkartin, Perikartin and Karagüllü eruptives of Erciyes Dagi in central Anatolia (Hamann et al. 2010) do not match with POP3 to POP6 data (Fig. 4-10), eruptives of the central Anatolian Acigöl volcano at ~25-20 ka BP or younger, the so-called western Acigöl rhyolites, might fit in composition with our data (Schmitt et al. 2011; Siebel et al. 2011). However, only mean chemical analysis data of six rock samples are available for comparison (Fig. 4-10), restricting a proper interpretation of these data in comparison to our glass-based cryptotephra record. Kuzucuoglu et al. (1998) reported three rhyolitic tephras of Lateglacial age (GÖL T1, GÖL T5 and GÖL T11) from the Eski Acigöl lacustrine sequence and one (GÖCÜ 1 potentially correlating with the Korudagi Tuff of Acigöl) from the Göcü beach deposit sequence in the Konya Plain. The major element glass compositions, given only as mean values for these tephras (Kuzucuoglu et al. 1998), do not agree well with Dead Sea POPs when several elements are considered (Fig. 4-10).

Our POP3 to POP6 major element glass data show the best correlation with eastern Anatolian Süphan swarm eruptives around 13 cal. ka BP and with glass analyses of Nemrut Dagi ashes, as reported from tephra layers in the ICDP Lake Van sediment core (Schmincke & Sumita 2014). The Lateglacial Süphan tephra swarm occurred during a short time interval of ~338 years between ~13,078 and 12,740 varve years BP, labelled as V-8 to V-15 volcanic layers in Lake Van varved (annually laminated) sediments (Schmincke & Sumita 2014). POP3 and likely POP5 correlate with these chemically very similar Süphan eruptives around 13 cal. ka BP, and POP6 might correlate with V-13 that has glass with a somewhat higher FeO than other Süphan eruptives of this swarm (Fig. 4-10; Schmincke & Sumita 2014). POP4 most likely represents the V-16 layer of a Nemrut eruption ~13.8 cal. ka BP, as can be seen in the characteristically low CaO values (~0.2-0.3 wt%) of glass of the rhyolitic Nemrut tephras. However, higher FeO in glass of POP4 could also suggest a correlation to Nemrut V-17 that is dated to >30 ka BP in the Lake Van core. Schmincke & Sumita (2014) postulate a tephra gap between 30 ka BP (V-17) and ~14 ka BP (V-16); hence, a match with V-17 in our data would imply reworking of tephra over more than 15,000 years in the Dead Sea record, which we consider as highly unlikely. It should also be noted that only single representative values of glass compositions for Lake Van tephra layers are reported, which cannot illustrate the whole range of glass compositions of these tephras.

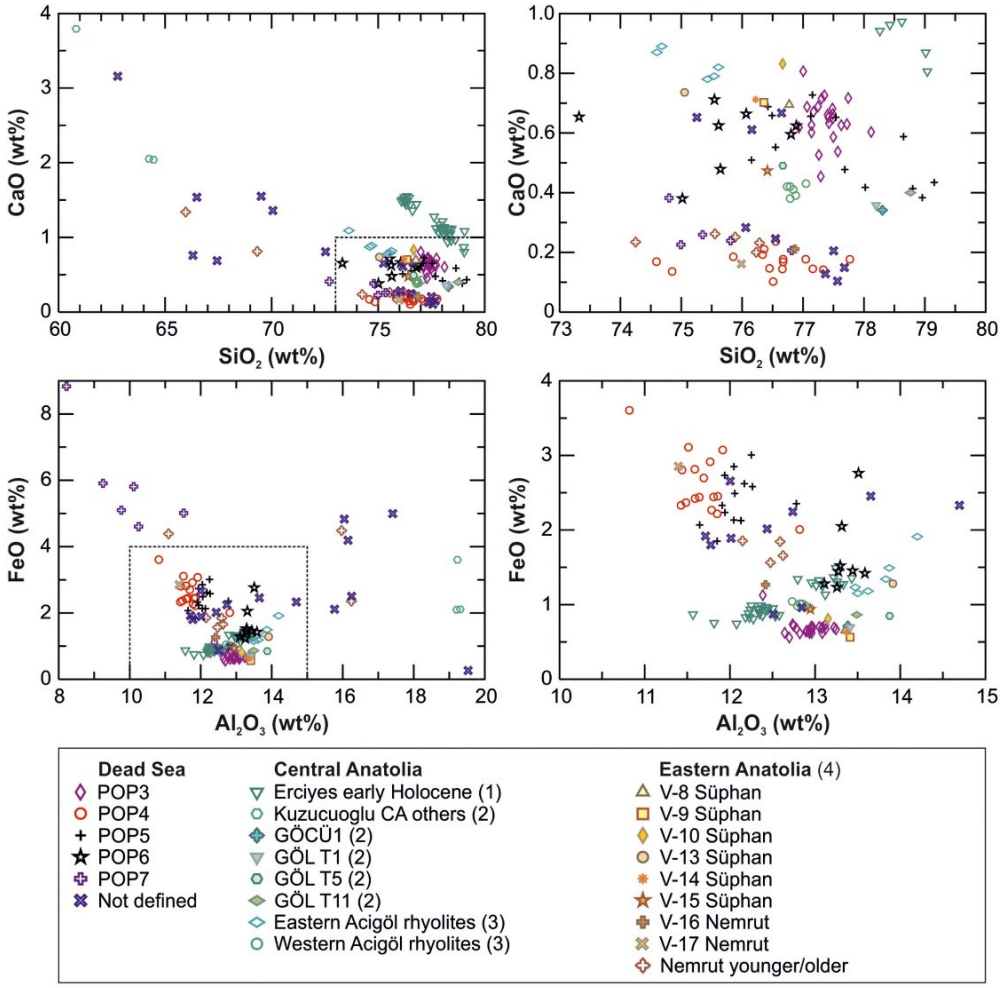

***Figure 4-10**: Elemental biplots (normalized to 100%, volatile-free) of Dead Sea POP3-POP7 EPMA glass data (including 'not defined' glasses, i.e. glasses that do not correlate with glass of any tephra population) compared to data from central and eastern Anatolian volcanic provinces. Central Anatolia: (1) Early Holocene eruptions of Erciyes Dagi* (Hamann et al. 2010)*; (2) GÖCÜ 1 (Korudagi tuff of Acigöl), GÖL T1, GÖL T5 and GÖL T11 (Acigöl)* (Kuzucuoglu et al. 1998)*; (3) eastern Acigöl (~150-200 ka BP) and western Acigöl (~25-20 ka BP) rhyolites* (Siebel et al. 2011). *Eastern Anatolia: (4) Lateglacial Süphan swarm (V-8 to V-15 in Lake Van) and Nemrut data V-16 (~13.8 ka BP), V-17 (~30 ka BP), as well as younger (V3a-V6; Holocene) and older (V-18) Nemrut tephra layers in Lake Van* (Schmincke & Sumita 2014).

4.5.1.4. POP7 and 'not defined' glasses (not identified)

The tephra population POP7 and glasses that could not be defined here potentially originate from eruptives of central and eastern Anatolian volcanic centres as well (Fig. 4-10). Unfortunately, the current, very limited proximal glass chemical database does not allow any conclusive correlation with our cryptotephra-derived glass data set.

4.5.2. Implications for the Lateglacial chronology of the Dead Sea record

The Lateglacial is of particular interest for palaeoclimate research at the Dead Sea because several strong lake level drops occurred between the Last Glacial Maximum highstand of Lake Lisan and the Holocene

low-level of the Dead Sea. However, the last glacial-interglacial transition (LGIT) could not be studied for its entire duration before the ICDP deep drilling because of the lack of exposed sediments dating to this time. This gap particularly concerns the sedimentological and hydroclimatic signature of the Greenland Stadial 1 (GS-1) in the Levantine region, which is under debate (Stein et al. 2010).

The oldest Holocene Dead Sea sediments comprise the 'Early Holocene salt section' that has been radiocarbon-dated in marginal shallow cores to between 10 and 11 cal. ka BP (Stein et al. 2010). In the ICDP core, this Early Holocene salt is evident at ~71 to 88.5 m sediment depth (Figs 4-1C, 4-11). No radiocarbon or U-Th ages exist from this section of the core, but a ~75-cm-thick turbidite directly below is radiocarbon-dated at its base at 89.25 m b.l.f. to 11,440 ± 119 cal. a BP (Neugebauer et al. 2014; Kitagawa et al. 2017), supporting an age for the start of the salt sequence of ~11 cal. ka BP in the marginal cores (Stein et al. 2010) if significant reworking of the dated sample is excluded. So far, the only available age estimates for the LGIT in the ICDP core are from below a massive gypsum deposit at ~91-92 m b.l.f. (Fig. 4-11): a ^{14}C age of 14,144 ± 110 cal. a BP retrieved from the base of a ~15-cm-thick turbidite at 92.06 m b.l.f. (Neugebauer et al. 2014; Kitagawa et al. 2017) and an U-Th isochron age of 14,067 ± 1140 a BP measured on aragonite at 92.20 m b.l.f. (Torfstein et al. 2015). These ages suggest deposition of this gypsum unit, labelled as 'Additional Gypsum Unit' (AGU) in the Masada section by Torfstein et al. (2013a), during Greenland Interstadial 1a-c. In contrast, our tephrochronological correlation provides evidence for a ~1000-years younger bottom-age of the gypsum deposit. Volcanic glass shards directly below the gypsum deposit (tephra horizons TH(92.00) and TH(92.55)) correlate with products of the Süphan swarm eruptions, which have been varve-dated at between 12,740 and 13,078 varve years BP in the Lake Van core (V8-V15 tephra layers) (Schmincke & Sumita 2014). Furthermore, we are confident that glass shards found at ~93 m b.l.f. in the ICDP core (TH(93.30)) correlate with those of the V-16 tephra layer in Lake Van, originating from an eruption of Nemrut Volcano at ~13.8 cal. ka BP (Schmincke & Sumita 2014). Our revised age for the gypsum deposit in the core further agrees within dating uncertainties with U-Th ages of ~13-14.5 ka BP for the corresponding onshore 'Additional Gypsum Unit'that has been dated at the M1 section in Masada and the PZ1 section in Perazim Valley (Figs 4-1B, 4-11; Haase-Schramm et al. 2004; Torfstein et al. 2013a). Moreover, the age supports the average single sample U-Th age of 12,858 ± 363 a BP obtained at 92.20 m b.l.f. in the ICDP core (Torfstein et al. 2015) instead of the above-mentioned, parallel U-Th isochron age of 14,067 ± 1140 a BP. Therefore, we are confident that the massive gypsum unit, which correlates with the AGU section at Masada, formed during the early GS-1 rather than during the Lateglacial interstadial (GI-1a-c) as previously suggested. Since the AGU represents the final deposits of the Lake Lisan highstand period, this further implies that the major lake level decline did not occur at the onset of the

Lateglacial interstadial as previously assumed (Torfstein et al. 2013a) but only at around the transition to the Younger Dryas. Consequently, also previous interpretation of the Younger Dryas as a wet period in the Levant (Stein et al. 2010) must be questioned. An arid Younger Dryas as indicated by gypsum deposition is in accord with the observed coupling between millennial-scale lake level declines of the Dead Sea and cold Heinrich events in the North Atlantic (Torfstein et al. 2013b). This would reconcile the apparent contradiction of the Younger Dryas as the only cold period in the North Atlantic causing lake level rise (Stein et al. 2010) rather than decline of the Dead Sea. Furthermore, an arid Younger Dryas in the Levant is congruent with a dry eastern Mediterranean (Rossignol-Strick 1995) and major lake level lowering in Lake Van (Landmann et al. 1996; Wick et al. 2003) during that time.

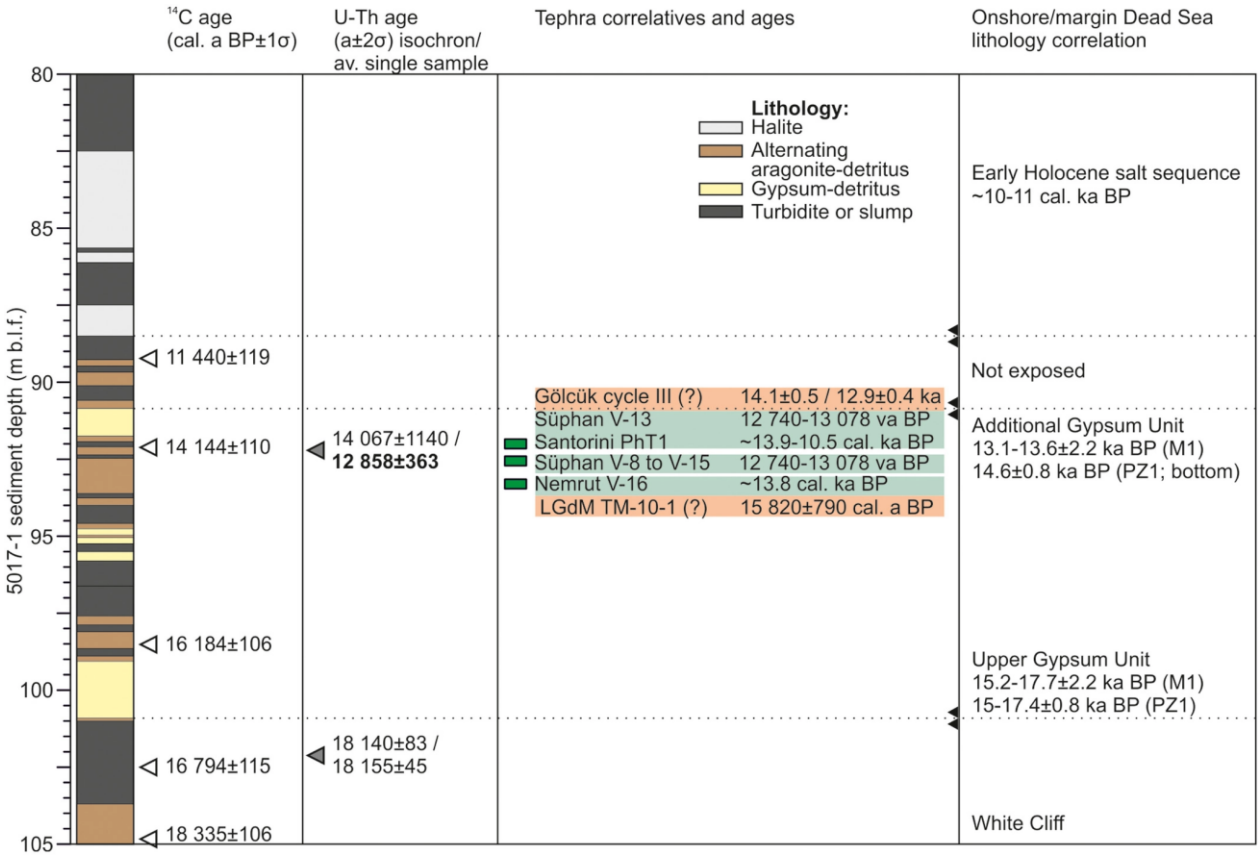

***Figure 4-11**: Lithology, available ^{14}C and U-Th ages* (Torfstein et al. 2015; Kitagawa et al. 2017)*, identified cryptotephras in the Lateglacial 5017-1 core* (St. Seymour et al. 2004; Schmincke & Sumita 2014)*, and correlation of 5017-1 lithologies with onshore sediment formations. We also included tentative tephra correlations in this plot; these are TM-10-1 in the LGdM record* (Wulf et al. 2008) *that is located at the same sediment depth as Nemrut V-16, and Gölcük cycle III tephra at the same sediment depth as Süphan V-13 and Santorini PhT1. The Early Holocene salt sequence is the bottom-section of the Zeelim Formation, radiocarbon-dated to between 10 and 11 cal. ka BP in numerous shallow drill-cores at the western margin of the Dead Sea* (Stein et al. 2010). *The 'Additional' and 'Upper Gypsum Units' form the top of the last glacial Lisan Formation and have been dated by U-Th in outcrops at Masada* (M1 section; Torfstein et al. 2013a) *and Perazim Valley* (PZ1 section; Haase-Schramm et al. 2004). *va = varve years.*

4.6. Conclusions

In the Lateglacial (~11-15 cal. ka BP) time interval of the ICDP Dead Sea core, we have identified numerous cryptotephra horizons, from at least three different sources of Italian, Aegean and Anatolian volcanic centres. First glass geochemical data suggest that the majority of volcanic ash in the Dead Sea sediments originates from eruptions of the Anatolian volcanic provinces. Even though proximal Anatolian tephra data (glass shard analyses) for comparison are still limited, the identification of cryptotephra in the long Dead Sea record provides novel opportunities to advance the tephrostratigraphical framework in this region, e.g. not only through synchronizing the Dead Sea and Lake Van (eastern Anatolia) sediment records, but also with archaeological and palaeoenvironmental sites that are currently investigated in the Levant and in Arabia. Furthermore, the glass composition-based correlation of tephra populations in the Dead Sea with well-dated Lateglacial tephras of the Süphan and Nemrut volcanoes at Lake Van enabled us to improve the chronology of the Dead Sea record significantly, in a critical time-window for better understanding the hydroclimatic conditions in the region during abrupt climate changes at the end of the last glacial. The results of this study pave the way for extending the tephra work at the Dead Sea, and for synchronization with other important palaeoclimate records in the Mediterranean region, like Lago Grande di Monticchio, Italy, Lake Ohrid, Albania/Macedonia, Tenaghi Philippon, Greece, and Lake Van, Turkey.

Acknowledgements

We like to thank Jan A. Piotrowski for editing this article, and David J. Lowe and an anonymous reviewer for their very constructive suggestions that helped to improve the quality. This study has received funding by the German Academic Exchange Service (DAAD postdoc grant to IN) and the German Research Foundation (DFG research grant to IN, grant no. NE 2295/1-1) and is a contribution to the projects 'TEPH-ME: CryptoTEPHrochronology in the ICDP Dead Sea deep core as a key to synchronise past hydroclimate changes in the eastern MEditerranean' and 'PALEX: Paleohydrology and Extreme Floods from the Dead Sea ICDP core' (DFG grant no. BR2208/13-1/-2). We thank our student helpers Miriam Seidel, Anna Beer (University Münster) and Daniel Redant (Free University Berlin) for assistance in the Potsdam Tephra Lab, and Brian Brademann and Nicolai Klitscher (both GFZ) for help with technical and practical issues. Part of the laboratory work was carried out in the Cambridge Tephra Lab during a research visit of IN in the Department of Geography, University of Cambridge, and we thank Alma Piermattei, Amy McGuire and Erin

Martin-Jones for their help with method development. We confirm that there is no conflict of interest to declare for this study.

Author contributions

IN, DM and MJS developed the project idea, and performed the sampling and sample preparation. IN and OA analysed glass shards using EPMA. Data evaluation was done by IN, DM, SB, CSL and SW. IN and AB wrote the manuscript with contributions from all co-authors.

Data availability statement

Data of this article will be publicly available on PANGAEA.

4.7. Supplementary material

***Table S4-2**: EPMA glass geochemical data (raw and normalised, volatile-free) of Lateglacial cryptotephra from the ICDP Dead Sea core and glass standards measurements (raw data).*

Instrument:	JEOL-JXA8230 (GFZ Potsdam)												
Voltage:	15 kV												
Beam current:	10/5 nA												
Beam size:	10 µm												
Date: 17/09/2019													
Samples 5017-C2-11, -14, -27 (10 nA beam current)													
Glass standard	**SiO_2**	**TiO_2**	**Al_2O_3**	**FeO**	**MnO**	**MgO**	**CaO**	**Na_2O**	**K_2O**	**P_2O_5**	**Cl**	**F**	**Total**
Lipari obsidian	74.31	0.10	13.12	1.64	0.00	0.07	0.73	4.14	5.13	0.00	0.26	0.00	99.50
GOR-132-G	46.09	0.29	11.20	10.24	0.15	22.29	8.27	0.91	0.05	0.02	0.00	0.00	99.51
St-Hs-6-80-G	63.62	0.68	17.90	4.38	0.08	2.23	5.25	4.37	1.29	0.15	0.02	0.00	99.97
ATHO-G	74.87	0.26	12.21	3.29	0.12	0.14	1.67	3.77	2.68	0.01	0.04	0.00	99.06
Date: 16/01/2020													
Samples 5017-C2-11, -14, -25, -27 (5 nA beam current)													
Glass standard	**SiO_2**	**TiO_2**	**Al_2O_3**	**FeO**	**MnO**	**MgO**	**CaO**	**Na_2O**	**K_2O**	**P_2O_5**	**Cl**	**F**	**Total**
Lipari obsidian	73.41	0.08	13.02	1.52	0.07	0.03	0.72	4.01	5.00	0.01	0.37	0.00	98.24
GOR-132-G	45.31	0.29	10.81	10.18	0.17	22.63	8.39	0.75	0.01	0.05	0.01	0.00	98.60
St-Hs-6-80-G	63.73	0.72	17.76	4.30	0.07	2.02	5.21	4.50	1.20	0.17	0.03	0.00	99.71
ATHO-G	75.49	0.23	12.34	3.16	0.11	0.10	1.65	3.92	2.57	0.03	0.03	0.00	99.63
Date: 10/03/2020													
Samples 5017-C2-33, -45 (5 nA beam current)													
Glass standard	**SiO_2**	**TiO_2**	**Al_2O_3**	**FeO**	**MnO**	**MgO**	**CaO**	**Na_2O**	**K_2O**	**P_2O_5**	**Cl**	**F**	**Total**
Lipari obsidian	74.33	0.09	13.02	1.57	0.05	0.04	0.76	4.05	5.02	0.00	0.34	0.00	99.28
GOR-132-G	45.34	0.31	10.95	10.33	0.18	22.48	8.15	0.89	0.01	0.06	0.00	0.00	98.71
St-Hs-6-80-G	63.77	0.69	17.82	4.33	0.08	2.08	5.01	4.61	1.33	0.15	0.01	0.00	99.89
ATHO-G	75.30	0.24	12.13	3.41	0.11	0.08	1.67	3.61	2.76	0.00	0.04	0.00	99.35

***Table S4-3 (Part I)**: EPMA glass geochemical data (raw and normalised, volatile-free) of Lateglacial cryptotephra from the ICDP Dead Sea core and glass standards measurements (raw data).*

			raw data													normalised, volatile-free												
analysis date	sample	nA	SiO_2	TiO_2	Al_2O_3	FeO	MnO	MgO	CaO	Na_2O	K_2O	P_2O_5	Cl	F	Total	SiO_2	TiO_2	Al_2O_3	FeO	MnO	MgO	CaO	Na_2O	K_2O	P_2O_5	Na2O +K2O	POP	Tephra correlative
17.09.2019	5017-C2-11-1	10	69.83	0.68	11.42	1.85	0.11	0.17	0.26	2.72	4.73	0.04	0.03	0.00	91.85	76.05	0.74	12.44	2.01	0.12	0.19	0.29	2.96	5.15	0.04	8.11	nd	?
17.09.2019	5017-C2-11-3	10	64.55	0.30	15.09	2.32	0.15	0.47	1.44	3.41	5.03	0.10	0.25	0.00	93.11	69.52	0.32	16.25	2.50	0.17	0.50	1.55	3.67	5.42	0.11	9.09	nd	?
17.09.2019	5017-C2-11-4	10	71.20	0.33	10.71	2.89	0.11	0.13	0.22	2.64	4.76	0.02	0.06	0.00	93.06	76.56	0.35	11.52	3.11	0.11	0.14	0.23	2.84	5.12	0.03	7.96	4	V-16 Nemrut
17.09.2019	5017-C2-11-7	10	72.58	0.41	12.05	0.90	0.05	0.02	0.12	2.54	5.09	0.05	0.03	0.00	93.84	77.37	0.44	12.85	0.96	0.05	0.02	0.12	2.71	5.43	0.06	8.13	nd	?
17.09.2019	5017-C2-11-8	10	71.05	0.16	12.61	1.94	0.01	0.01	0.36	3.15	5.41	0.01	0.18	0.05	94.93	75.02	0.17	13.32	2.05	0.01	0.01	0.38	3.33	5.71	0.01	9.04	6	V-13 Süphan
17.09.2019	5017-C2-11-9	10	65.52	0.14	19.30	0.26	0.01	0.00	0.75	6.08	6.69	0.06	0.00	0.00	98.81	66.31	0.14	19.53	0.27	0.01	0.00	0.76	6.15	6.77	0.06	12.92	nd	?
17.09.2019	5017-C2-11-10	10	74.90	0.13	11.42	2.36	0.10	0.00	0.17	3.12	4.11	0.00	0.28	0.00	96.59	77.77	0.13	11.86	2.45	0.11	0.00	0.17	3.24	4.27	0.00	7.51	4	V-16 Nemrut
17.09.2019	5017-C2-11-11	10	72.79	0.04	12.42	0.65	0.05	0.04	0.61	2.97	4.36	0.00	0.02	0.00	93.95	77.49	0.05	13.22	0.69	0.06	0.04	0.65	3.16	4.64	0.00	7.80	3	Süphan
16.01.2020	5017-C2-11-1	5	74.81	0.63	11.51	1.76	0.09	0.14	0.24	3.57	4.96	0.02	0.05	0.01	97.78	76.55	0.64	11.78	1.80	0.10	0.14	0.24	3.65	5.08	0.02	8.73	nd	?
16.01.2020	5017-C2-11-2	5	76.39	0.07	11.50	2.41	0.11	0.00	0.14	3.98	4.18	0.00	0.37	0.04	99.21	77.33	0.08	11.64	2.44	0.12	0.00	0.14	4.03	4.23	0.00	8.26	4	V-16 Nemrut
16.01.2020	5017-C2-11-3	5	76.89	0.05	12.96	0.61	0.02	0.07	0.62	3.68	4.15	0.00	0.04	0.00	99.08	77.63	0.05	13.08	0.62	0.02	0.07	0.62	3.72	4.19	0.00	7.91	3	Süphan
16.01.2020	5017-C2-11-4	5	68.06	0.26	15.32	2.05	0.11	0.40	1.32	4.48	5.07	0.07	0.29	0.00	97.42	70.07	0.27	15.77	2.11	0.11	0.41	1.36	4.61	5.22	0.07	9.83	nd	?
16.01.2020	5017-C2-11-5	5	73.67	0.32	11.43	2.83	0.14	0.08	0.18	3.64	4.82	0.01	0.06	0.00	97.17	75.86	0.33	11.77	2.91	0.14	0.08	0.18	3.75	4.96	0.01	8.71	4	V-16 Nemrut
16.01.2020	5017-C2-11-6	5	74.50	0.11	11.16	2.30	0.15	0.01	0.14	4.73	4.08	0.00	0.38	0.00	97.56	76.66	0.11	11.48	2.37	0.16	0.01	0.14	4.87	4.20	0.00	9.07	4	V-16 Nemrut
16.01.2020	5017-C2-11-7	5	72.14	0.37	11.95	2.20	0.14	0.15	0.68	1.66	4.17	0.04	0.04	0.00	93.53	77.16	0.40	12.78	2.35	0.15	0.16	0.73	1.78	4.46	0.04	6.24	5	Süphan/Nemrut
16.01.2020	5017-C2-11-8	5	74.72	0.36	12.05	0.84	0.03	0.01	0.10	3.42	4.78	0.02	0.03	0.00	96.35	77.57	0.37	12.51	0.88	0.03	0.01	0.10	3.55	4.96	0.02	8.51	nd	?
16.01.2020	5017-C2-11-9	5	74.70	0.20	11.15	1.98	0.11	0.00	0.40	2.88	4.32	0.00	0.05	0.00	95.80	78.02	0.21	11.65	2.07	0.12	0.00	0.42	3.01	4.51	0.00	7.52	5	Süphan/Nemrut
16.01.2020	5017-C2-11-10	5	70.99	0.37	11.25	4.89	0.29	0.06	0.40	4.81	4.57	0.01	0.12	0.00	97.77	72.70	0.38	11.52	5.01	0.29	0.06	0.41	4.93	4.68	0.01	9.61	7	CA/EA?
16.01.2020	5017-C2-11-11	5	75.04	0.17	11.22	2.75	0.09	0.00	0.10	4.38	4.33	0.00	0.32	0.01	98.40	76.51	0.17	11.44	2.80	0.09	0.00	0.10	4.47	4.41	0.00	8.88	4	V-16 Nemrut
16.01.2020	5017-C2-11-12	5	70.60	0.41	14.30	2.89	0.14	0.40	1.58	4.40	2.74	0.09	0.28	0.00	97.84	72.37	0.42	14.66	2.96	0.15	0.41	1.62	4.51	2.81	0.09	7.32	2	Santorini Y2/PhT1
16.01.2020	5017-C2-11-13	5	64.73	0.22	15.50	4.02	0.13	0.08	0.66	5.87	4.72	0.05	0.27	0.21	96.46	67.44	0.23	16.15	4.19	0.14	0.09	0.69	6.12	4.92	0.05	11.03	nd	?
17.09.2019	5017-C2-14-1	10	71.42	0.04	12.07	0.63	0.02	0.04	0.61	3.10	4.32	0.02	0.01	0.00	92.28	77.41	0.05	13.08	0.68	0.02	0.04	0.66	3.36	4.68	0.02	8.04	3	Süphan
17.09.2019	5017-C2-14-2	10	72.48	0.05	12.29	0.65	0.04	0.08	0.63	3.19	4.51	0.00	0.02	0.00	93.94	77.17	0.05	13.08	0.69	0.05	0.09	0.67	3.40	4.80	0.00	8.20	3	Süphan
17.09.2019	5017-C2-14-3	10	72.41	0.03	12.29	0.68	0.06	0.05	0.67	3.06	4.40	0.02	0.03	0.00	93.70	77.30	0.04	13.12	0.73	0.07	0.05	0.71	3.27	4.70	0.02	7.96	3	Süphan
17.09.2019	5017-C2-14-4	10	66.67	0.65	13.97	2.49	0.05	0.63	1.54	4.29	2.84	0.09	0.15	0.00	93.37	71.51	0.70	14.99	2.67	0.06	0.68	1.65	4.60	3.05	0.10	7.65	2	Santorini Y2/PhT1
17.09.2019	5017-C2-14-5	10	70.80	0.26	9.45	4.24	0.17	0.01	0.19	2.87	4.18	0.00	0.14	0.00	92.30	76.82	0.29	10.25	4.60	0.19	0.01	0.20	3.11	4.54	0.00	7.65	7	CA/EA?
17.09.2019	5017-C2-14-6	10	72.55	0.10	11.22	2.32	0.05	0.01	0.20	4.06	4.50	0.00	0.30	0.00	95.32	76.36	0.10	11.81	2.44	0.05	0.02	0.21	4.27	4.74	0.00	9.01	4	V-16 Nemrut
17.09.2019	5017-C2-14-7	10	59.21	1.25	16.42	4.71	0.20	1.79	2.98	4.29	3.10	0.37	0.33	0.00	94.64	62.78	1.32	17.41	4.99	0.21	1.90	3.16	4.55	3.29	0.39	7.84	nd	?
17.09.2019	5017-C2-14-8	10	70.06	0.08	12.33	1.41	0.07	0.03	0.66	3.39	4.66	0.05	0.29	0.00	93.03	75.55	0.08	13.30	1.52	0.07	0.04	0.71	3.66	5.03	0.05	8.68	6	V-13 Süphan
16.01.2020	5017-C2-14-1	5	76.16	0.06	12.90	0.66	0.05	0.02	0.67	3.46	4.31	0.00	0.01	0.00	98.30	77.49	0.06	13.12	0.67	0.05	0.02	0.68	3.52	4.39	0.00	7.91	3	Süphan
16.01.2020	5017-C2-14-2	5	75.32	0.04	12.56	0.60	0.11	0.04	0.61	3.36	4.23	0.04	0.03	0.00	96.93	77.72	0.05	12.96	0.62	0.11	0.04	0.63	3.47	4.37	0.04	7.83	3	Süphan
16.01.2020	5017-C2-14-3	5	69.10	0.22	14.00	2.22	0.08	0.22	0.77	4.23	4.41	0.02	0.24	0.00	95.52	72.53	0.23	14.69	2.33	0.09	0.23	0.81	4.44	4.63	0.02	9.07	nd	?
16.01.2020	5017-C2-14-4	5	73.51	0.24	11.58	2.39	0.07	0.00	0.53	3.47	4.21	0.03	0.06	0.00	96.10	76.55	0.25	12.06	2.49	0.08	0.00	0.55	3.61	4.38	0.03	8.00	5	Süphan/Nemrut
16.01.2020	5017-C2-14-5	5	72.50	0.25	11.38	2.45	0.09	0.02	0.61	2.41	3.75	0.04	0.04	0.00	93.55	77.53	0.27	12.17	2.62	0.10	0.03	0.65	2.58	4.01	0.04	6.59	5	Süphan/Nemrut
16.01.2020	5017-C2-14-6	5	72.09	0.23	10.82	1.69	0.08	0.03	0.35	2.29	3.72	0.00	0.05	0.00	91.34	78.96	0.26	11.85	1.85	0.09	0.03	0.38	2.51	4.07	0.00	6.58	5	Süphan/Nemrut
16.01.2020	5017-C2-14-7	5	69.70	0.25	10.88	2.49	0.14	0.00	0.60	3.34	3.72	0.00	0.04	0.00	91.16	76.49	0.27	11.94	2.73	0.15	0.00	0.66	3.67	4.08	0.00	7.75	5	Süphan/Nemrut
16.01.2020	5017-C2-14-8	5	71.18	0.05	12.49	1.36	0.03	0.03	0.45	4.23	4.28	0.00	0.23	0.12	94.45	75.64	0.05	13.27	1.45	0.03	0.03	0.48	4.50	4.55	0.00	9.04	6	V-13 Süphan
16.01.2020	5017-C2-14-9	5	72.88	0.31	10.99	1.80	0.06	0.07	0.14	1.20	6.35	0.02	0.08	0.00	93.91	77.67	0.34	11.71	1.92	0.07	0.08	0.15	1.28	6.77	0.02	8.05	nd	?
16.01.2020	5017-C2-14-10	5	75.02	0.07	12.28	0.54	0.02	0.05	0.52	3.06	5.12	0.03	0.17	0.00	96.88	77.57	0.08	12.70	0.56	0.03	0.05	0.53	3.16	5.29	0.03	8.46	3	Süphan
16.01.2020	5017-C2-14-11	5	74.64	0.03	12.66	0.68	0.05	0.05	0.60	3.78	4.53	0.00	0.01	0.00	97.02	76.94	0.03	13.05	0.70	0.05	0.05	0.62	3.90	4.67	0.00	8.57	3	Süphan
16.01.2020	5017-C2-14-12	5	74.04	0.10	11.39	2.13	0.08	0.03	0.17	3.94	4.22	0.00	0.40	0.04	96.54	77.05	0.10	11.85	2.22	0.08	0.03	0.18	4.10	4.39	0.00	8.49	4	V-16 Nemrut
16.01.2020	5017-C2-14-13	5	71.80	0.31	11.13	1.75	0.07	0.14	0.19	2.23	5.02	0.00	0.10	0.00	92.75	77.50	0.34	12.01	1.89	0.07	0.16	0.20	2.41	5.42	0.00	7.83	nd	?

Table S4-3 (Part II): *EPMA glass geochemical data (raw and normalised, volatile-free) of Lateglacial cryptotephra from the ICDP Dead Sea core and glass standards measurements (raw data).*

			raw data													normalised, volatile-free												
analysis date	sample	nA	SiO_2	TiO_2	Al_2O_3	FeO	MnO	MgO	CaO	Na_2O	K_2O	P_2O_5	Cl	F	Total	SiO_2	TiO_2	Al_2O_3	FeO	MnO	MgO	CaO	Na_2O	K_2O	P_2O_5	Na2O +K2O	POP	Tephra correlative
16.01.2020	5017-C2-25-1	5	70.29	0.25	11.12	2.63	0.10	0.01	0.47	3.23	4.19	0.01	0.08	0.00	92.39	76.15	0.27	12.05	2.85	0.11	0.01	0.51	3.50	4.54	0.02	8.04	5	Süphan/Nemrut
16.01.2020	5017-C2-25-2	5	72.25	0.23	10.94	2.14	0.05	0.02	0.54	2.12	3.56	0.01	0.04	0.00	91.89	78.65	0.25	11.91	2.33	0.06	0.02	0.59	2.31	3.88	0.01	6.18	5	Süphan/Nemrut
16.01.2020	5017-C2-25-3	5	69.82	0.24	8.61	5.50	0.25	0.00	0.21	4.68	3.79	0.00	0.23	0.13	93.46	75.00	0.26	9.25	5.91	0.27	0.00	0.22	5.03	4.07	0.00	9.10	7	CA/EA?
16.01.2020	5017-C2-25-4	5	70.66	0.15	13.02	2.66	0.04	0.04	0.63	4.93	4.22	0.02	0.19	0.00	96.56	73.32	0.16	13.51	2.76	0.04	0.04	0.65	5.12	4.38	0.02	9.49	6	V-13 Süphan
16.01.2020	5017-C2-25-5	5	57.58	0.39	17.84	2.73	0.22	0.39	1.72	5.62	6.72	0.07	0.84	0.09	94.21	61.73	0.42	19.13	2.93	0.24	0.42	1.84	6.02	7.20	0.07	13.23	1	WA
16.01.2020	5017-C2-25-6	5	60.40	0.37	18.20	2.64	0.21	0.36	1.68	5.92	6.27	0.07	0.78	0.20	97.10	62.84	0.38	18.94	2.75	0.22	0.37	1.75	6.16	6.52	0.07	12.68	1	WA
16.01.2020	5017-C2-25-7	5	69.83	0.23	12.52	2.25	0.04	0.05	0.56	1.16	5.05	0.00	0.07	0.02	91.79	76.15	0.25	13.65	2.45	0.05	0.06	0.61	1.26	5.51	0.01	6.77	nd	?
16.01.2020	5017-C2-25-8	5	75.90	0.02	12.48	0.66	0.03	0.07	0.70	3.29	4.43	0.05	0.02	0.00	97.65	77.74	0.02	12.78	0.68	0.03	0.08	0.72	3.37	4.54	0.05	7.91	3	Süphan
16.01.2020	5017-C2-25-9	5	74.31	0.24	11.36	2.01	0.07	0.03	0.39	2.15	3.73	0.01	0.07	0.00	94.38	78.79	0.26	12.05	2.13	0.08	0.03	0.41	2.28	3.96	0.02	6.23	5	Süphan/Nemrut
16.01.2020	5017-C2-25-10	5	70.22	0.40	14.02	2.88	0.20	0.45	1.58	4.48	2.70	0.11	0.25	0.00	97.28	72.37	0.41	14.45	2.97	0.20	0.46	1.63	4.62	2.78	0.11	7.40	2	Santorini Y2/PhT1
17.09.2019	5017-C2-27-1	10	70.57	0.26	11.21	2.75	0.07	0.01	0.60	2.18	3.84	0.01	0.05	0.00	91.54	77.13	0.29	12.25	3.01	0.08	0.01	0.66	2.38	4.20	0.01	6.58	5	Süphan/Nemrut
17.09.2019	5017-C2-27-2	10	72.21	0.09	12.76	1.38	0.09	0.02	0.63	2.99	4.76	0.00	0.28	0.00	95.21	76.06	0.09	13.44	1.45	0.10	0.02	0.67	3.15	5.01	0.00	8.16	6	V-13 Süphan
17.09.2019	5017-C2-27-3	10	66.61	0.45	13.64	3.01	0.16	0.50	1.58	3.94	2.71	0.09	0.20	0.00	92.90	71.86	0.49	14.71	3.25	0.17	0.54	1.70	4.25	2.92	0.09	7.17	2	Santorini Y2/PhT1
17.09.2019	5017-C2-27-4	10	68.40	0.44	14.02	3.10	0.11	0.51	1.62	3.74	2.82	0.07	0.21	0.00	95.04	72.13	0.47	14.78	3.27	0.11	0.54	1.71	3.94	2.97	0.07	6.92	2	Santorini Y2/PhT1
17.09.2019	5017-C2-27-5	10	72.95	0.18	11.18	1.96	0.07	0.00	0.40	1.66	3.76	0.00	0.05	0.00	92.21	79.16	0.20	12.13	2.13	0.07	0.00	0.43	1.80	4.08	0.00	5.88	5	Süphan/Nemrut
17.09.2019	5017-C2-27-6	10	68.11	0.44	13.99	3.16	0.09	0.46	1.58	3.47	2.70	0.05	0.21	0.00	94.26	72.42	0.46	14.88	3.36	0.09	0.49	1.68	3.69	2.87	0.06	6.56	2	Santorini Y2/PhT1
17.09.2019	5017-C2-27-7	10	65.95	0.42	13.64	3.13	0.09	0.44	1.80	3.30	2.74	0.08	0.23	0.00	91.82	72.01	0.45	14.89	3.42	0.10	0.48	1.97	3.60	2.99	0.09	6.59	2	Santorini Y2/PhT1
17.09.2019	5017-C2-27-8	10	69.82	0.35	9.37	5.38	0.20	0.03	0.24	3.01	4.26	0.00	0.12	0.00	92.76	75.36	0.37	10.11	5.81	0.21	0.03	0.26	3.25	4.60	0.00	7.85	7	CA/EA?
17.09.2019	5017-C2-27-9	10	68.51	0.35	7.53	8.09	0.26	0.08	0.35	2.68	3.74	0.00	0.80	0.08	92.48	74.79	0.39	8.22	8.83	0.28	0.09	0.39	2.93	4.08	0.00	7.01	7	CA/EA?
16.01.2020	5017-C2-27-1	5	71.09	0.29	11.41	2.40	0.08	0.00	0.64	3.16	3.95	0.00	0.06	0.00	93.08	76.43	0.31	12.27	2.58	0.08	0.00	0.69	3.40	4.25	0.00	7.64	5	Süphan/Nemrut
16.01.2020	5017-C2-27-2	5	71.41	0.07	12.83	1.34	0.05	0.00	0.59	3.68	4.45	0.02	0.30	0.00	94.74	75.61	0.07	13.59	1.42	0.05	0.00	0.63	3.90	4.71	0.03	8.61	6	V-13 Süphan
16.01.2020	5017-C2-27-3	5	68.72	0.45	14.05	2.78	0.04	0.41	1.58	4.53	2.83	0.08	0.23	0.00	95.69	71.98	0.47	14.72	2.91	0.04	0.43	1.66	4.75	2.96	0.08	7.71	2	Santorini Y2/PhT1
16.01.2020	5017-C2-27-4	5	69.86	0.47	14.17	2.86	0.14	0.36	1.60	4.31	2.84	0.03	0.28	0.00	96.92	72.29	0.49	14.66	2.96	0.15	0.37	1.66	4.46	2.94	0.03	7.40	2	Santorini Y2/PhT1
16.01.2020	5017-C2-27-5	5	69.24	0.44	14.07	3.02	0.13	0.44	1.70	4.40	2.55	0.06	0.28	0.00	96.33	72.09	0.45	14.65	3.14	0.13	0.46	1.77	4.58	2.65	0.06	7.24	2	Santorini Y2/PhT1
16.01.2020	5017-C2-27-6	5	67.83	0.42	14.40	3.01	0.12	0.45	1.59	6.32	2.74	0.04	0.27	0.00	97.19	69.99	0.43	14.86	3.11	0.12	0.46	1.64	6.52	2.83	0.04	9.35	2	Santorini Y2/PhT1
16.01.2020	5017-C2-27-7	5	72.69	0.18	11.08	2.69	0.10	0.03	0.00	4.18	4.64	0.01	0.22	0.00	95.83	76.03	0.19	11.59	2.81	0.10	0.03	0.00	4.37	4.85	0.01	9.23	4	V-16 Nemrut
16.01.2020	5017-C2-27-8	5	72.72	0.34	12.31	2.17	0.06	0.12	0.63	3.00	5.21	0.07	0.04	0.00	96.67	75.26	0.36	12.74	2.25	0.06	0.12	0.65	3.10	5.39	0.07	8.50	nd	?
16.01.2020	5017-C2-27-9	5	73.90	0.07	12.60	1.23	0.07	0.02	0.60	3.16	4.42	0.04	0.36	0.00	96.47	76.89	0.07	13.11	1.28	0.08	0.02	0.62	3.29	4.60	0.04	7.89	6	V-13 Süphan
16.01.2020	5017-C2-27-10	5	73.57	0.08	12.70	1.18	0.07	0.01	0.57	2.98	4.62	0.01	0.32	0.00	96.10	76.81	0.08	13.26	1.23	0.07	0.01	0.59	3.11	4.82	0.01	7.94	6	V-13 Süphan
16.01.2020	5017-C2-27-11	5	73.06	0.29	9.41	4.91	0.18	0.04	0.23	4.36	3.83	0.06	0.17	0.00	96.55	75.81	0.31	9.76	5.09	0.19	0.04	0.24	4.52	3.97	0.06	8.50	7	CA/EA?
10.03.2020	5017-C2-33-1	5	74.05	0.08	12.33	0.62	0.07	0.04	0.56	3.58	4.20	0.02	0.06	0.00	95.61	77.49	0.08	12.90	0.65	0.07	0.05	0.58	3.75	4.40	0.03	8.14	3	Süphan
10.03.2020	5017-C2-33-2	5	73.63	0.04	12.30	0.62	0.06	0.06	0.62	3.43	4.32	0.03	0.03	0.03	95.16	77.42	0.04	12.93	0.65	0.06	0.07	0.65	3.61	4.54	0.03	8.15	3	Süphan
10.03.2020	5017-C2-33-3	5	72.62	0.04	12.14	0.60	0.03	0.05	0.59	3.59	4.43	0.05	0.01	0.00	94.16	77.14	0.04	12.90	0.64	0.04	0.05	0.63	3.81	4.71	0.06	8.52	3	Süphan
10.03.2020	5017-C2-33-4	5	74.64	0.00	12.49	0.68	0.02	0.00	0.61	3.42	4.51	0.03	0.03	0.00	96.43	77.43	0.00	12.96	0.71	0.02	0.00	0.63	3.55	4.68	0.03	8.23	3	Süphan
10.03.2020	5017-C2-33-5	5	73.53	0.03	12.32	0.63	0.01	0.00	0.69	3.44	4.39	0.02	0.02	0.00	95.07	77.35	0.03	12.96	0.66	0.01	0.00	0.73	3.62	4.62	0.03	8.24	3	Süphan
10.03.2020	5017-C2-33-6	5	73.09	0.07	12.08	0.68	0.04	0.04	0.57	3.64	4.53	0.01	0.03	0.00	94.78	77.14	0.07	12.75	0.72	0.04	0.04	0.60	3.84	4.78	0.02	8.62	3	Süphan
10.03.2020	5017-C2-33-7	5	62.25	0.52	15.02	4.52	0.15	0.30	1.44	3.96	5.37	0.09	0.08	0.00	93.70	66.50	0.56	16.04	4.83	0.16	0.32	1.54	4.23	5.74	0.10	9.97	nd	?
10.03.2020	5017-C2-33-8	5	73.60	0.07	12.01	0.59	0.01	0.07	0.63	3.58	4.38	0.04	0.03	0.00	95.02	77.49	0.08	12.64	0.62	0.01	0.08	0.66	3.77	4.61	0.04	8.38	3	Süphan
10.03.2020	5017-C2-33-9	5	75.12	0.06	12.33	0.59	0.07	0.04	0.58	2.76	4.57	0.04	0.02	0.00	96.18	78.12	0.07	12.82	0.61	0.07	0.04	0.60	2.87	4.75	0.04	7.62	3	Süphan
10.03.2020	5017-C2-33-11	5	74.47	0.04	12.51	0.60	0.08	0.06	0.78	3.69	4.46	0.02	0.02	0.00	96.73	77.01	0.04	12.94	0.62	0.09	0.06	0.81	3.82	4.61	0.02	8.43	3	Süphan
10.03.2020	5017-C2-33-12	5	73.27	0.15	11.11	2.32	0.11	0.04	0.14	4.53	4.17	0.00	0.34	0.06	96.23	76.45	0.15	11.59	2.42	0.12	0.04	0.15	4.73	4.35	0.00	9.08	4	V-16 Nemrut
10.03.2020	5017-C2-33-13	5	74.56	0.13	11.39	2.19	0.08	0.02	0.14	3.98	4.10	0.04	0.42	0.00	97.04	77.16	0.14	11.79	2.27	0.08	0.02	0.14	4.12	4.24	0.04	8.36	4	V-16 Nemrut
10.03.2020	5017-C2-33-14	5	72.89	0.09	12.50	0.63	0.03	0.09	0.65	3.08	4.38	0.02	0.02	0.00	94.38	77.25	0.10	13.25	0.67	0.03	0.09	0.69	3.26	4.64	0.02	7.91	3	Süphan
10.03.2020	5017-C2-33-15	5	73.96	0.00	12.45	0.67	0.05	0.02	0.66	3.27	4.86	0.03	0.02	0.00	95.97	77.08	0.00	12.97	0.69	0.05	0.02	0.69	3.41	5.06	0.03	8.47	3	Süphan

***Table S4-3 (Part III)**: EPMA glass geochemical data (raw and normalised, volatile-free) of Lateglacial cryptotephra from the ICDP Dead Sea core and glass standards measurements (raw data).*

			raw data													normalised, volatile-free												
analysis date	sample	nA	SiO_2	TiO_2	Al_2O_3	FeO	MnO	MgO	CaO	Na_2O	K_2O	P_2O_5	Cl	F	Total	SiO_2	TiO_2	Al_2O_3	FeO	MnO	MgO	CaO	Na_2O	K_2O	P_2O_5	Na2O +K2O	POP	Tephra correlative
10.03.2020	5017-C2-45-1	5	71.64	0.13	12.27	1.92	0.08	0.01	0.13	4.21	5.29	0.03	0.26	0.00	95.97	74.86	0.13	12.82	2.01	0.08	0.02	0.13	4.40	5.53	0.03	9.93	4	V-16 Nemrut
10.03.2020	5017-C2-45-2	5	73.63	0.19	11.23	2.59	0.06	0.04	0.17	3.86	4.26	0.00	0.33	0.26	96.63	76.67	0.20	11.69	2.70	0.06	0.04	0.18	4.02	4.44	0.00	8.46	4	V-16 Nemrut
10.03.2020	5017-C2-45-3	5	69.64	0.37	14.13	3.03	0.12	0.51	1.49	4.40	2.89	0.07	0.27	0.00	96.92	72.05	0.38	14.62	3.14	0.12	0.53	1.54	4.55	2.99	0.07	7.54	2	Santorini Y2/PhT1
10.03.2020	5017-C2-45-4	5	71.39	0.32	10.12	3.37	0.15	0.06	0.18	3.61	4.32	0.00	0.11	0.23	93.86	76.33	0.35	10.82	3.60	0.16	0.07	0.19	3.86	4.62	0.00	8.48	4	V-16 Nemrut
10.03.2020	5017-C2-45-5	5	71.26	0.37	11.16	2.47	0.12	0.01	0.62	2.68	4.27	0.01	0.05	0.00	93.02	76.65	0.39	12.00	2.66	0.13	0.01	0.67	2.88	4.59	0.02	7.48	nd	?
10.03.2020	5017-C2-45-8	5	73.07	0.18	10.89	2.22	0.16	0.00	0.16	4.36	4.24	0.02	0.34	0.01	95.65	76.67	0.19	11.43	2.33	0.17	0.00	0.17	4.57	4.45	0.02	9.02	4	V-16 Nemrut
10.03.2020	5017-C2-45-9	5	59.10	0.55	17.60	2.51	0.21	0.27	0.89	6.46	6.19	0.04	0.64	0.13	94.60	62.99	0.58	18.76	2.68	0.23	0.29	0.95	6.89	6.60	0.04	13.48	1	Campanian/Ischia TM10-1
10.03.2020	5017-C2-45-10	5	59.13	0.51	17.43	2.45	0.22	0.36	1.04	6.49	5.96	0.07	0.76	0.21	94.62	63.14	0.55	18.61	2.62	0.23	0.38	1.11	6.93	6.36	0.07	13.29	1	Campanian/Ischia TM10-1
10.03.2020	5017-C2-45-11	5	59.30	0.60	17.33	2.54	0.20	0.31	1.11	6.49	6.03	0.06	0.65	0.04	94.66	63.11	0.64	18.44	2.70	0.21	0.33	1.18	6.91	6.42	0.06	13.32	1	Campanian/Ischia TM10-1
10.03.2020	5017-C2-45-12	5	59.30	0.40	17.21	2.11	0.20	0.30	1.12	5.22	6.30	0.00	0.42	0.16	92.74	64.34	0.43	18.67	2.29	0.22	0.33	1.22	5.66	6.84	0.00	12.50	1	Campanian/Ischia TM10-1
10.03.2020	5017-C2-45-13	5	70.67	0.24	11.29	2.91	0.12	0.02	0.16	4.50	4.83	0.00	0.33	0.03	95.09	74.59	0.26	11.92	3.07	0.12	0.02	0.17	4.75	5.10	0.00	9.85	4	V-16 Nemrut
10.03.2020	5017-C2-45-14	5	67.35	0.53	13.67	2.74	0.13	0.43	1.66	4.87	2.62	0.09	0.23	0.00	94.31	71.58	0.56	14.53	2.91	0.14	0.45	1.76	5.18	2.78	0.10	7.96	2	Santorini Y2/PhT1
10.03.2020	5017-C2-45-15	5	71.62	0.10	11.01	2.06	0.09	0.02	0.44	2.93	3.92	0.00	0.05	0.00	92.23	77.69	0.11	11.94	2.23	0.09	0.02	0.48	3.18	4.25	0.00	7.43	5	Süphan/Nemrut
10.03.2020	5017-C2-45-16	5	74.85	0.02	12.34	0.71	0.00	0.03	0.51	2.12	6.30	0.00	0.09	0.00	96.97	77.26	0.02	12.74	0.73	0.00	0.03	0.53	2.19	6.50	0.00	8.69	3	Süphan
10.03.2020	5017-C2-45-17	5	74.88	0.15	12.00	1.09	0.02	0.04	0.44	2.91	5.35	0.00	0.25	0.00	97.14	77.29	0.16	12.39	1.13	0.02	0.04	0.46	3.00	5.52	0.00	8.53	3	Süphan-V15?
10.03.2020	5017-C2-45-18	5	58.92	0.53	17.40	2.34	0.27	0.28	0.99	6.80	5.73	0.03	0.69	0.24	94.22	63.16	0.57	18.65	2.51	0.29	0.30	1.07	7.29	6.14	0.04	13.43	1	Campanian/Ischia TM10-1

5. Phases of stability during major hydroclimate change ending the Last Glacial in the Levant

Daniela Müller[1,2,*], Ina Neugebauer[1], Yoav Ben Dor[3,4], Yehouda Enzel[4], Markus J. Schwab[1], Rik Tjallingii[1], Achim Brauer[1,2]

(1) Section Climate Dynamics and Landscape Evolution, GFZ German Research Centre for Geosciences, Telegrafenberg, Potsdam 14473, Germany

(2) Institute of Geosciences, University of Potsdam, Karl-Liebknecht-Str. 24-25, Potsdam 14476, Germany

(3) Geological Survey of Israel, 32 Yesha'ayahu Leibowitz, Jerusalem 9692100, Israel

(4) The Fredy and Nadine Herrmann Institute of Earth Sciences, The Hebrew University of Jerusalem, Givat Ram, Jerusalem, 91904, Israel

Manuscript submitted to Nature Geoscience (initial submission)

Abstract

The substantial level drop (~240 m) of the terminal Lake Lisan provides a unique record of hydroclimatic reorganization of the eastern Mediterranean during the Pleistocene-Holocene transition, recorded by gypsum layers deposited during pronounced periods of decline. However, despite their importance for understanding the hydroclimatic response in the eastern Mediterranean to global climate change, little is known about the intervals between periods of major lake level falls. Here, we present an unprecedented, seasonally-resolved record of Lake Lisan that shows decadal to millennial-long periods of hydroclimatic stability before its termination. An interval of almost 1000 regular aragonite varves with a few intercalated mass transport deposits indicates stable or rising lake levels under a positive water balance. Even the surrounding phases of pronounced lake level drops include decadal periods of regular varves suggesting depositional stability and elevated water inflow. Our results highlight that even during a major hydroclimatic shift and pronounced long-term lake level drop, decadal to millennial periods of relative stable moisture supply occurred, which might have impacted human migration through the region at the demise of the Last Glacial.

Keywords

Eastern Mediterranean; Dead Sea; Lateglacial; Hydroclimate; Varves

5.1. Introduction

The Last Glacial-Interglacial climate warming of the Northern Hemisphere was marked by short and long climate fluctuations, such as Heinrich cold event 1 (H1), Greenland Interstadial 1 (GI-1) and Greenland Stadial 1 (GS-1) (Rahmstorf 2002; Denton et al. 2010; Rasmussen et al. 2014). The most prominent expression of this climate transition in the hydroclimatically sensitive Levant is the major lake level fall by ~240 m (Torfstein et al. 2013a) of Lake Lisan and its transition into the hypersaline Dead Sea (DS) (e.g. Bartov et al. 2002; Stein et al. 2010; Torfstein et al. 2013b; Neugebauer et al. 2014; Stein 2014), during which distinct evaporation phases causing lake level declines are reflected by massive gypsum horizons (Torfstein et al. 2008, 2013b; Neugebauer et al. 2014; Stein 2014). Gypsum precipitation occurs due to a reduction of the upper freshwater layer under a negative water budget, increasing its density and favoring a complete mixing of the water column (Stein et al. 1997; Torfstein et al. 2008), and is supported by the increased inflow of sulfate-rich brines from formerly submerged aquifers (Torfstein et al. 2008). Between the major deglacial gypsum units – the Upper Gypsum Unit (UGU) and the Additional Gypsum Unit (AGU) – a period of seasonally resolved sediments provides unprecedented insights into the in situ response of local hydroclimatic fluctuations during a major reorganization of global climate. The deposition of alternating aragonite detritus laminae between the two gypsum units (Stein et al. 1997; Machlus et al. 2000; Torfstein et al. 2008) indicates a positive water budget, and a relatively higher lake level stand (Torfstein et al. 2013b) lasting approximately one millennium based on ages from the bounding gypsum units (Torfstein et al. 2013a). While the mechanism for gypsum formation during falling water levels was established (e.g. Torfstein et al. 2008; Stein et al. 2010), the details of the depositional processes between the gypsum intervals, and their climatic implications remain largely unknown. The climate-sensitive Levant is part of one of the cradles of ancient cultural developments (e.g. Beit-Arieh 1997; Müller et al. 2011; Hershkovitz et al. 2018). Therefore, reconstructions from the Dead Sea and its latest Pleistocene predecessor, Lake Lisan, can provide insights into causes for human migration, cultural rises and declines (e.g. Maher et al. 2012; Stein 2014; Miebach et al. 2019).

In order to analyze these millennial-scale climate changes, we compare marginal lake sediments from the Masada outcrop with deep-lake facies from core 5017-1-A of the ICDP Dead Sea Deep Drilling Project (DSDDP) (Neugebauer et al. 2014), deposited between the UGU and AGU (Figs. 5-1, S5-5). Both segments cover the final Lisan Formation, before deposition at Masada terminated due to the lake level decline. The following transition into the Holocene is recorded only by the deep-basin ICDP core providing the only archive of this important transition in the Dead Sea basin.

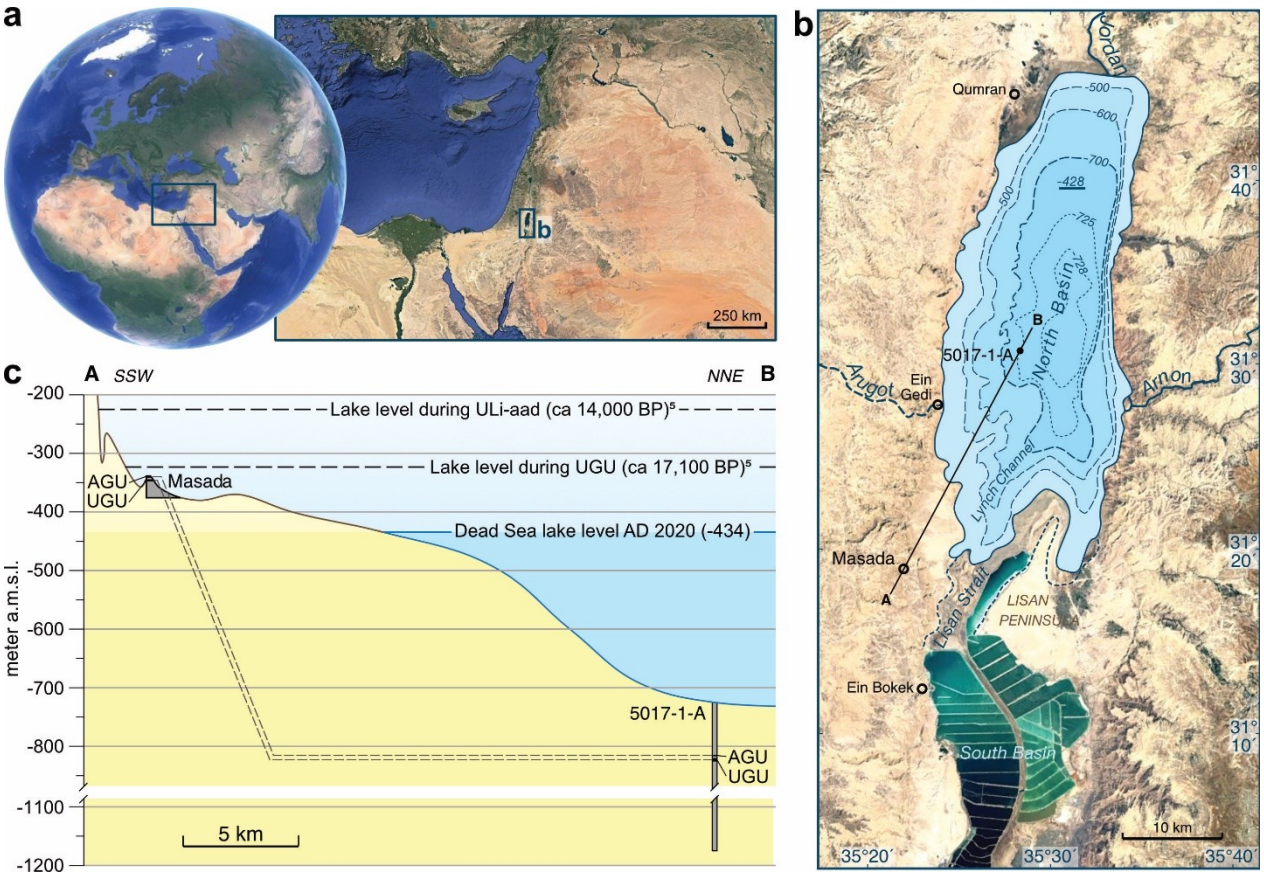

***Figure 5-1**: Dead Sea location, sampling sites and lake levels of the investigated time interval. (a) Satellite images of the location of the Dead Sea. (b) Bathymetric map and satellite image of the Dead Sea with sampling sites onshore (Masada) and in the deep lake center (core 5017-1-A). (c) Topographic/bathymetric profile from Masada to 5017-1-A. Approximate lake levels during the study interval are from* Torfstein et al. (2013b)*, and are shown in comparison to the water level in AD 2020. The dashed lines connect the Upper Gypsum Unit (UGU) and Additional Gypsum Unit (AGU; see supplement S1) at both sites.*

Assuming that the gypsum units coincide with Heinrich events (Bartov et al. 2003; Haase-Schramm et al. 2004; Stein et al. 2010; Torfstein et al. 2013b, 2013a; Torfstein & Enzel 2017), U/Th- and radiocarbon ages for the UGU and AGU in Masada were tuned to the Hulu Cave record revealing ages of 17.1-15.5 ± 0.5 ka BP (UGU) and 14.5 ± 0.5 ka BP (AGU base) (Torfstein et al. 2013a) (Fig. S5-5, table S5-1). The lateglacial chronology of the ICDP core, based on radiocarbon dating of macro-debris, U/Th-ages, and its lithological correlation with shelf deposits, reveals comparable ages of ~17 and ~14.1 ka BP for the bases of the UGU and AGU, respectively (Neugebauer et al. 2014; Torfstein et al. 2015; Kitagawa et al. 2017), although tephrochronological dating indicates a ~1000-years younger age for the AGU base, shifting it entirely into the Younger Dryas chronozone (Neugebauer et al. 2021) (Fig. S5-5, table S5-1).

In this study, microfacies and more objective sub-millimeter XRF analyses from marginal (Masada) and deep-water (core 5017-1-A) sediments are utilized to determine the seasonally-resolved geochemical, sedimentary and hydroclimatic variability during the final stage of Lake Lisan between 17 and 11 ka.

5.2. Results

5.2.1. Lithology of the ICDP core 5017-1-A

Four lithozones (C1-C4) with sharp transitions were distinguished (Fig. 5-2, table S5-2) in the ~12 m thick section of the ICDP core, and microfacies investigations are confirmed by the independent XRF element data (Fig. 5-2, supplement S5). These sections comprise (i) alternating aragonite and detritus (aad) varves, accumulated by aragonite deposition during summer and detrital flood material during winter (e.g. Machlus et al. 2000; Neugebauer et al. 2014; Ben Dor et al. 2019), and marked by high log(Sr/Ca) and log(Ti/Ca) ratios, (ii) laminated and massive gypsum deposits (Torfstein et al. 2008; Neugebauer et al. 2014) indicated by high log(S/Ca) ratios, and (iii) mass transport deposits (MTDs)(Neugebauer et al. 2014) that are mostly mass flow deposits (MFD) (table S5-2, supplement S2). Ages in the following refer to the updated chronology of the ICDP core using radiocarbon (Kitagawa et al. 2017) and tephra (Neugebauer et al. 2021) ages (supplement S1.4.).

Lithozone C1 is coeval with the UGU (~17-14 ka) and comprises seven discrete gypsum intervals intercalated with mm- to dm-scale, often erosive, MTDs and a total of ~340 aragonite varves. Almost all gypsum deposits are laminated (facies gd-l1, -l2, -l3: supplement S2.1), and precipitated from the water column due to evaporation during the summer season (supplement S2.1) supporting seasonal formation processes (Magee 1991; Kirkland 2003; Mees et al. 2012). Gypsum intervals are interrupted by four ~30-230 varve-long phases of aragonite varves and MTDs including sequences of up to ~40 varves without MTD intercalation. Most varves comprise couplets of authigenic aragonite and fine-grained detritus (‘aad’ varves (Machlus et al. 2000; Neugebauer et al. 2014)), but some include diagenetic gypsum within the detrital sublayer (‘aadg’ varves) and some ld-type varves (laminated detritus (Haliva-Cohen et al. 2012; Neugebauer et al. 2014)) were also identified (supplements S2.1, S2.2). Especially log(S/Ca) ratios are high for aadg varves, with similar values as seen for the gypsum beds.

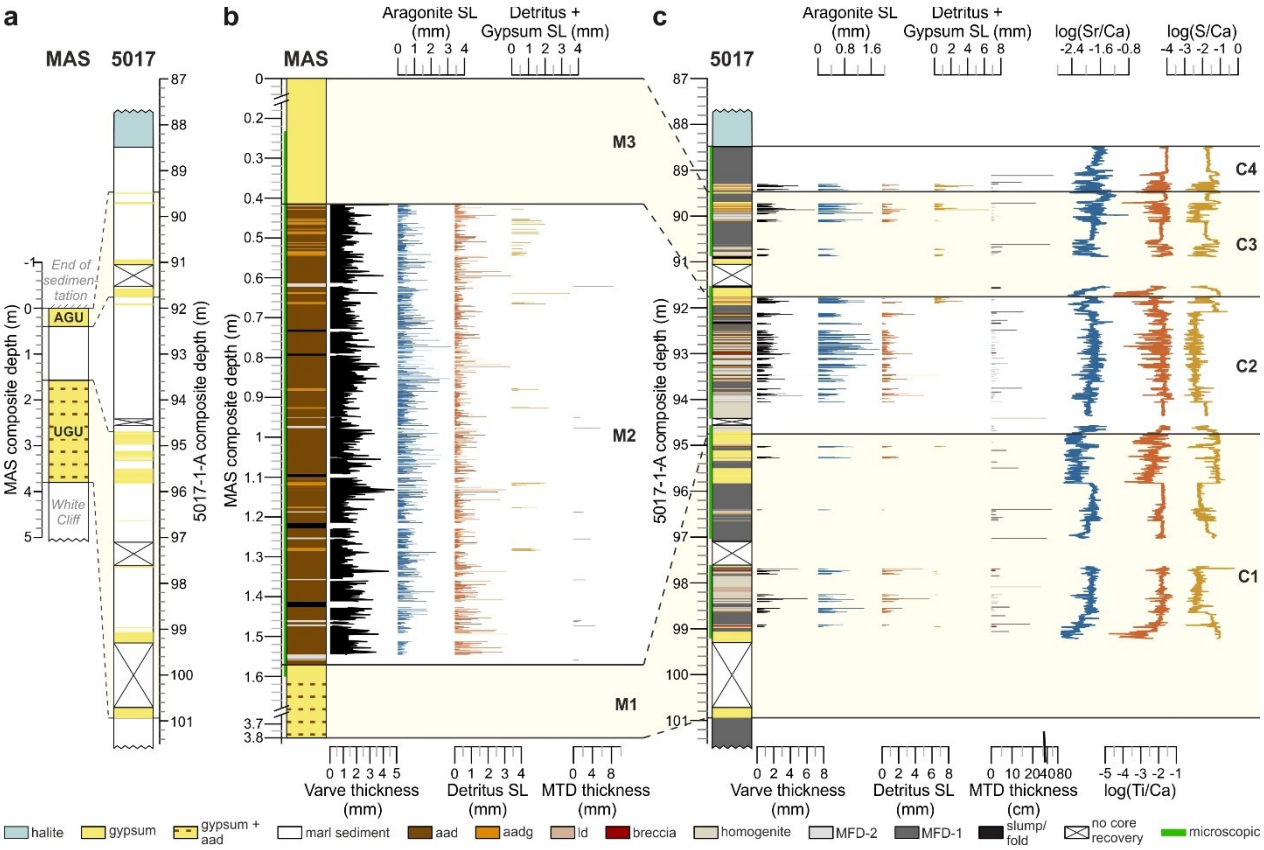

***Figure 5-2**: (a) Overview of study intervals at Masada (MAS) and the deep ICDP core (5017) on the same scale intervals for thickness comparison (see Fig. S5-5 for details). UGU: Upper Gypsum Unit, AGU: Additional Gypsum Unit. (b) Zoom in at the MAS study interval. From left to right: lithological column, varve thickness (mean 1.1 mm), aragonite, detritus and detritus + gypsum sublayer (SL) thicknesses, thickness of MFDs and lithozones M1 – M3. (c) Study interval of the ICDP core. From left to right: lithology, varve thickness (mean 0.82 mm), aragonite, detritus and detritus + gypsum sublayer (SL) thicknesses, thickness of MTDs, log(Sr/Ca), log(Ti/Ca) and log(S/Ca) ratios, lithozones C1 – C4.*

Lithozone C2 (~14-13 ka) comprises ~910 aad/aadg varves (Fig. 5-3, supplement S2.2, S3) intercalated with mostly mm- to cm-scale, non-erosive MFDs (C2 hereafter labelled as ULi-aad – Upper Lisan aad varves). The basal ~50 aad varves are frequently intercalated with MFDs, which distinctly decrease in number upcore, where sequences of up to ~60 continuous and undisturbed varves occur. The elemental compositions of the alternating aragonite and detrital sublayers are clearly depicted by µ-XRF mapping (Fig. 5-3a). The upper varved part is interrupted by a series of primary (Magee 1991; Kirkland 2003; Mees et al. 2012) gypsum laminae (facies gd-l1, -l3: supplement S2.1) followed by ~60 aadg varves marking the top of this lithozone.

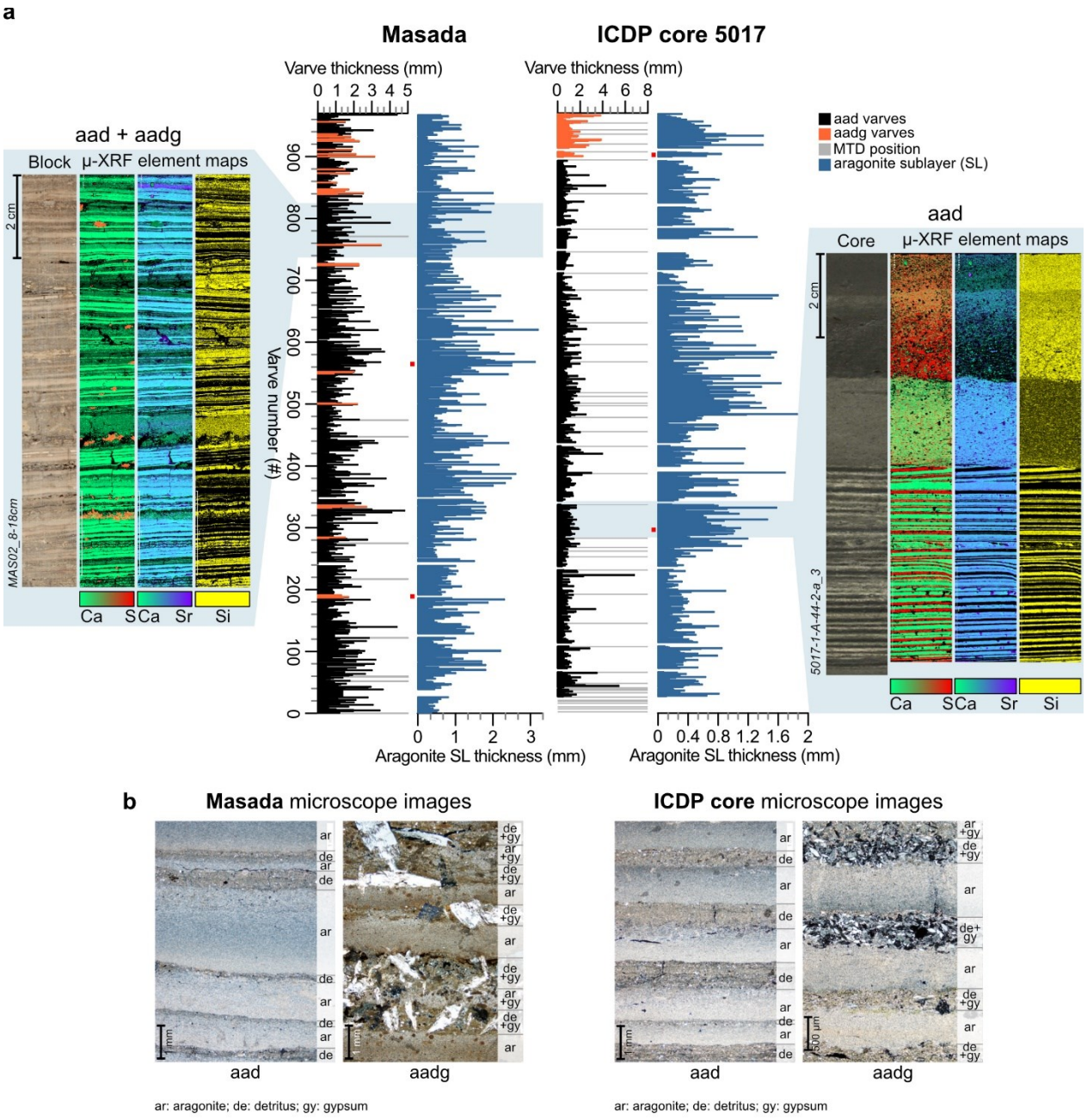

***Figure 5-3**: Aragonite varves of the ULi-aad. (a) Varve and aragonite sublayer thicknesses for Masada (center left) and the ICDP core (center right). In the varve thickness plots aadg varves are marked in orange and MTDs as grey bars. Gaps in the ICDP core are due to erosion and were estimated from parallel Masada varve counts. Gaps in the Masada profile are due to folded varves that were counted without thickness measurements. Note: three phases of increased aragonite sublayer thickness at both sites. Red points mark position of thin section images in (b). Blue shading indicates position of 2D µ-XRF element maps of resin-impregnated sediment blocks shown to the left and right. Left: prolonged period of 89 continuous varve formation at Masada. Right: 54 years of calm and undisturbed aragonite varve formation followed by MTDs in the ICDP core. Aragonite sublayers (blue colors in Ca+Sr maps) alternate with detrital sublayers (yellow Si maps) in aad varves. Orange colors in Ca+S maps indicate gypsum. (b) Microscope images of aad and aadg varves from Masada (left) and the ICDP core (right). Note the different scales.*

Lithozone C3 corresponds to the AGU (~13-11.5 ka) and includes four gypsum beds intercalated with cm- to dm-scale partly erosive MTDs and a total of ~210 varves. Gypsum deposits are partly laminated (facies gd-l1, -l2, -l3: supplement S2.1) and interpreted as precipitated during summer (supplement S2.1) (Magee 1991; Kirkland 2003; Mees et al. 2012). Varved intervals comprise up to 40 years-long sequences of aad and aadg varves, and are deposited intercalated with MTDs in one sequence between gypsum beds.

The lower part of lithozone C4 (~11.5-11 ka) comprises ~50 aadg varves intercalated with some MFDs, while the upper part represents a series of dm-scale erosive MFDs (supplement S2). The lithozone ends with the sharp onset of halite deposition.

5.2.2. Lithology at Masada

The uppermost ~3.8 m of the Lisan Formation at Masada represent the final deposition of Lake Lisan before sedimentation terminated at this site due to the lake level fall (~17-13 ka). Three lithozones M1 – M3 (Fig. 5-2, table S5-2) consisting of aragonite varves and laminated gypsum are distinguished (supplement S2). Our microfacies analyses concentrate on the finely laminated interval.

Lithozone M1 corresponds to the UGU and includes nine coarsely laminated gypsum beds intercalated with sequences of aragonite varves. The upper gypsum bed comprises laminated gypsum facies gd-l4 (supplement S2.1).

Lithozone M2 (ULi-aad) comprises ~930 aad and ~40 aadg varves (Fig. 5-3, supplement S2.2, S3). Continuous sequences of up to ~300 varves occur and only very few cm-scale, non-erosive MFDs are intercalated. In the uppermost ~130 varve years the number of aadg varves in between regular aad varves increases, which are clearly recorded by µ-XRF mapping (Fig. 5-3a).

Lithozone M3 is a ~40 cm thick pure gypsum deposit known as AGU and consists of undulating gypsum layers. Microfacies analyses of the lowest part show laminated gypsum facies gd-l5 (supplement S2.1). The top of this lithozone marks the end of sedimentation at Masada.

5.2.3. Shallow *versus* deep-water sedimentation

The correlation of Masada and ICDP core sediments is based on the UGU and AGU observed in both records (Fig. 5-2, supplement S1.4), revealing the main differences in the sedimentary sequences between the AGU and the Early Holocene halite (Stein et al. 2010; Neugebauer et al. 2014) in the deep basin (lithozone C4, Fig. 5-2). Thus, the core reveals additional record with no corresponding sediments at Masada due to the falling lake level and erosion. Therefore, the transition into the Holocene is not recorded, and was not studied in detail thus far. The dominance of MFDs in the depocenter with only ~50 intercalated aadg varves

indicates slope instability, probably due to rapid lake level change, runoff or earthquakes (e.g. Machlus et al. 2000; Haase-Schramm et al. 2004; Neugebauer et al. 2014; Kagan et al. 2018). The preservation of only ~50 varves therefore provides the minimum estimate for the duration of this interval.

Another distinct difference between the two depositional environments is the increased frequency and thickness of MTDs in the depocenter. MTDs in the deep-water gypsum deposits expand C1 and C3 by a factor of ~2.5 and ~5.5 with respect to M1 and M3 thicknesses at Masada. Even the gypsum beds themselves are up to ~1.5 times thicker in the deep water environment likely due to longer submergence under a thicker water column (Torfstein et al. 2008). At Masada, gypsum is primarily reworked or diagenetic with fine-grained detrital aggregates of pellets, whereas precipitated gypsum and fine-grained detritus or cement dominate the deep-water site (supplement S2.1).

The varved ULi-aad (Fig. 5-3) unit bound by the two gypsum units also differs between the two sites. The frequency and thickness of MTDs is higher in the deep basin leading to a ~2.5 times higher sedimentation rate than at Masada (Fig. 5-2). Yet, the duration of independently established floating varve chronologies is strikingly similar at both sites (M2: 968 +15/-64 varves; C2: 912 +15/-24 varves; Fig. 5-3, supplement S3) indicating only minor erosion by MTDs in the deep-water site. Interestingly, mean varve thickness is by a factor of 1.3 higher in the M2-chronology (1.1 mm *versus* 0.82 mm in the C2-chronology) due to thicker aragonite sublayers (Fig. 5-3; supplement S3). Aragonite sublayers in the shallow-water site are likely thicker because of proximity to the freshwater inflow, inhomogeneous aragonite accumulation in the basin (Ben Dor et al. 2021a) and/or dissolution in the depocenter. In both sites, the three oscillations of higher aragonite sublayer thickness lasting between ~30 and ~200 years (Fig. 5-3; supplement S3) suggest decadal to centennial-scale intervals of elevated freshwater inflow that could have supported aragonite precipitation (Stein et al. 1997; Ben Dor et al. 2021b), although other mechanisms, like dust or sulfate-reducing bacteria, could have contributed bicarbonate as well (Ben Dor et al. 2021a).

5.3. Discussion: a millennium of stability

During the major lake level decline of Lake Lisan at the end of the last deglaciation, two discrete gypsum units formed across the basin (Torfstein et al. 2008) that record intervals of proposed accelerated lake level fall (Torfstein et al. 2008, 2013b) of more than 100 m each (Stein 2014). However, the interval between the two gypsum units, the UGU and AGU, which record the in situ climatic response of the eastern Mediterranean to the reorganization of global climate, was not studied in detail. Thus, although the deposition of aad facies (ULi-aad) in between these gypsum units indicates an interval of positive water

budget and perhaps of elevated lake level (e.g. Torfstein et al. 2008, 2013b; Stein et al. 2010), the duration, internal structure and variability of this period are unknown. Furthermore, newer ages (Neugebauer et al. 2021) may shift this interval in time, reforming the formerly climates associated with the Bølling/Allerød and Younger Dryas.

The first ~50 varves following the sharp termination of the UGU are frequently intercalated with event layers (Fig. 5-3) suggesting that the initial lake level rise of ~60 m (Torfstein et al. 2013b) occurred rapidly within five decades coinciding with an increased flood frequency. After this rapid lake level rise we observe intervals of up to six decades without any event layers even in the ICDP core (Fig. 5-3), probably suggesting stable meromictic conditions without shore or margin disturbance nor local extreme precipitation events. Except for three intervals of increased aragonite sublayer thickness lasting 30-200 years, sedimentation was exceptionally stable for about 800 years (Fig. 5-3). Early signs of approaching the end of this stability only occurred in the last ~130 years of this positive water budget phase, when an increasing number of aadg varves and few primary gypsum laminae (Fig. 3) indicate increasing summer evaporation. According to the improved tephra-based age model (Neugebauer et al. 2021) (Fig. 5-4, supplement S1.4), the ULi-aad coincides with the lateglacial interstadial in Greenland (GI-1) (Rasmussen et al. 2006) and the Bølling/Allerød (Brauer et al. 1999; Müller et al. 2021).

The UGU gypsum deposition, which is correlated with cooling in the North Atlantic during H1 (Bartov et al. 2003; Torfstein et al. 2013b), was repeatedly interrupted by water level rises that caused the four decadal- to centennial-long intercalated varve intervals during the UGU lake level fall between ~17 and 14 ka BP (Fig. 5-4). Varve deposition during this interval suggests the lake level was likely not stable at ~330 m bmsl (Bartov et al. 2003; Stein et al. 2010; Torfstein et al. 2013a), but rose four times to above the threshold for gypsum formation, and formed the meromictic lake conditions required for aragonite precipitation (Ben Dor et al. 2021a). Varve sequences lasting up to 40-years without event layers indicate that even during largely instable lake levels such decadal clustering characterizes both modern and Late Pleistocene climates (Ben Dor et al. 2021b) and several decades of depositional stability may occur.

Following the millennium-long relatively stable high-stand, the AGU gypsum indicates a generally dry interval, interrupted once by a meromictic phase lasting ~210 years, during which water levels rose above the threshold for gypsum formation once more (Fig. 5-4). Even during this period, a single ~40 year-long calm and stable phase without extreme events occurs. Based on tephrochronological dating, the AGU coincides with the Younger Dryas/GS-1 (Neugebauer et al. 2021), thus suggesting generally dry climate in the Levant during this cold phase (supplement S1.4), contradicting previous interpretations of a wet

Younger Dryas (Stein et al. 2010; Torfstein et al. 2013a), reconciling hydroclimatic reconstructions of the DS region with other Eastern Mediterranean records (e.g. Rossignol-Strick 1995; Landmann et al. 1996; Wick et al. 2003), and indicating that climatic influences of prehistoric human developments in the region, such as the rise and demise of the Natufian culture (e.g. Maher et al. 2012), should be revisited.

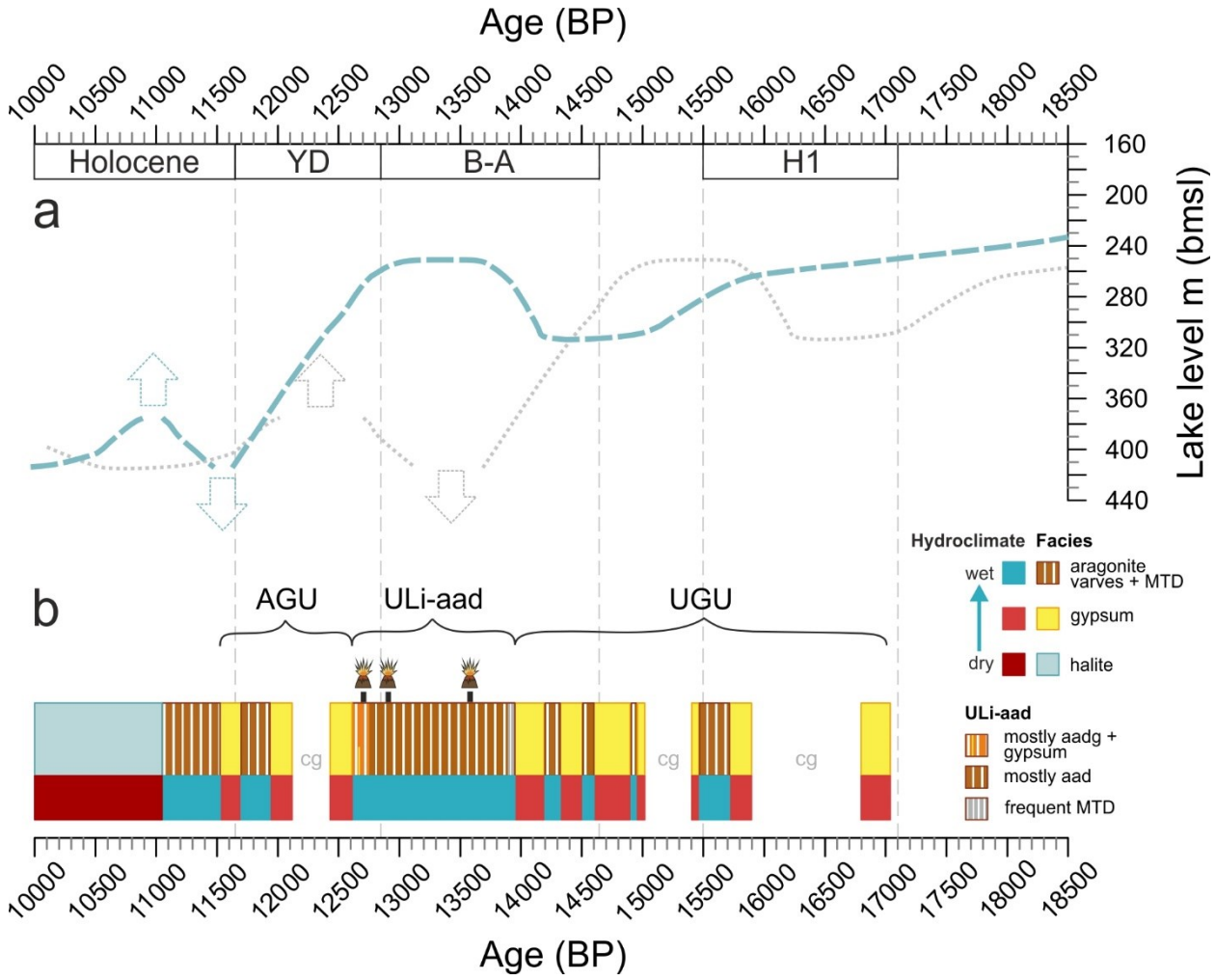

***Figure 5-4**: Lake level curve and fluctuations in lithology. (a) Lake level curve (in m below mean sea level, m bmsl) from* Torfstein et al. (2013b) *for the last glacial-interglacial transition. Dashed grey lake level curve is from* Torfstein et al. (2013b) *and was shifted onto the updated chronology (dashed blue line; supplement S1.4) for correlation with the lithology in b. YD: Younger Dryas, B-A: Bølling/Allerød, H1: Heinrich event 1. (b) Decadal to millennial-scale oscillations between dry and wet phases based on detailed microfacies variations. The data is shown on the updated chronology (supplement S1.4). Note that internal temporal deposition of varve and gypsum phases during the UGU and AGU is only assumed. Yellow boxes: gypsum beds, brown-white streaked boxes: aad phases including intercalated MTDs, boxes with an X mark large core gaps. Blue boxes: wet phases, red boxes: dry phases, dark red box: driest phase below ~400 m bmsl. Position of tephra horizons from the Nemrut V-16 and Süphan swarm eruptions V8-V15* (Neugebauer et al. 2021) *are shown in the ULi-aad by volcanoes. AGU: Additional Gypsum Unit; ULi-aad: Upper Lisan aad; UGU: Upper Gypsum Unit; cg: core gap.*

Between the AGU low-stand and the onset of halite deposition during the early Holocene, which reflects the final lake level fall below the threshold for halite deposition of ~400 m bmsl (Stein et al. 2010), a brief five decades-long lake level rise is indicated by varve and MTD deposition in the deep basin (Fig. 5-4). According to radiocarbon ages (supplement S1.4) this short-term rise occurred during the Lateglacial to Holocene transition (Kitagawa et al. 2017), and sediments associated with this short interval are missing in the littoral zone at Masada due to subsequent erosion.

Our investigation and comparison of the high-resolution sedimentary records from the deep basin and the littoral zone of Lake Lisan reveal new insights into decadal- and centennial-long lake level fluctuations during the Lateglacial, and suggest a complex and variable interplay of hydroclimatic variability during global climatic changes that occurred during this prehistoric crucial interval in the human evolution. Most importantly, periods of relative stability and wet climate were recorded even during a phase of pronounced millennial-scale variability driven by long-term climate change, thus exemplifying the complexity of identifying climatic trends and hydroclimatic shifts from short climatic records, and the importance of paleoclimatic records in unravelling the manifestation of climate change on hydroclimatic variability in situ.

Acknowledgements

This study is a contribution to the PALEX project 'Paleohydrology and Extreme Floods from the Dead Sea ICDP core' funded by the DFG (grant no. BR2208/13-1/-2). We thank B. Brademann for sampling at Masada, thin section preparation and all the other technical support; A. Hendrich for help with figure design; and all people involved in the Dead Sea Deep Drilling Project. This study is further a contribution to the Helmholtz Association (HGF) climate initiative REKLIM Research Theme 3 (RT3) "Extreme events across temporal and spatial scales".

Author Contributions

D.M., Y.B. and M.J.S. sampled at Masada. D.M. performed the microfacies analyses, evaluated the data, compiled the figures, and wrote the manuscript. I.N. performed sedimentological work, and contributed to data acquisition and evaluation. R.T. performed XRF analyses. M.J.S. performed sedimentological work. Y. B. and Y.E. provided information about local lake characteristics, hydrology and sedimentology. Y.E. and

A.B. designed the project and acquired funding. A.B. supervised the project and improved manuscript writing. All co-authors contributed to manuscript writing by proof-reading and discussions.

5.4. Supplementary material

S1. Materials and Methods

S1.1. Sites and sampling

The cores from site 5017-1-A were obtained from the depocenter of the Dead Sea at ~300 m water depth (Fig. 5-1; N31° 30.483' E35° 28.273') during the International Continental Scientific Drilling Program Dead Sea Deep Drilling Project (ICDP-DSDDP) in 2010/2011 (details in Neugebauer et al. 2014). Drilling was performed with the Deep Lake Drilling System (DLDS) operated by the non-profit corporation DOSECC (U.S. Drilling, Observation and Sampling of the Earth's Continental Crust) (Neugebauer et al. 2014). The cores comprise authigenic halite, gypsum, aragonite and clastics (Neugebauer et al. 2014). Especially the sedimentary sequence of the Lisan Formation (MIS2-4) is dominated by varves of alternating authigenic aragonite and allochthonous detritus (aad) (e.g. Machlus et al. 2000; Prasad et al. 2004). This study focusses on the upper Lisan Formation between ~101 and ~88.5 m sediment depth from sections 5017-1-A-47-1, -46, -45, -44, -43 and -42-3 of drilling site A at the depocenter of the lake. Cores 46 to 43 (~9.3 m) were continuously investigated by thin section microscopy (marked by green line in Fig. 5-2), and we provide additional macroscopic information from core catchers (cc), as well as from overlying and underlying sedimentary sections of 87.73-88.48 m (core 42-3) and 100.66-103.15 m (core 47-1) sediment depth, respectively. Five gaps occur due to no core recovery (marked with an X in the lithological profile in Fig. 5-2). In lithozone C3, one gypsum bed was obtained in core catcher 43-cc.

The study interval at Masada (N31° 18.602' E35° 22.489') encompasses the uppermost Lisan Formation from the bottom of the Upper Gypsum Unit (UGU; ~3.8 m) to the top of the Additional Gypsum Unit (AGU; 0 m) that form the terminal deposit at this site. The Lisan Formation at Masada consists of aad varves (e.g. Machlus et al. 2000; Prasad et al. 2004) and several massive gypsum deposits (e.g. Torfstein et al. 2008). About 1.37 m from the uppermost UGU to the lowermost AGU (Fig. 5-2) were sampled continuously with overlap in 2018. After smoothing the outcrop surface with a sharp knife, stainless steel boxes (~34 cm x 5 cm) with removable side walls were pressed along a vertical profile into the sediment with an overlap of several centimeters. A battery-operated dovetail saw was used to cut the hard gypsum sections. The majority of the gypsum units were not sampled for microfacies analyses because the gypsum is too hard and brittle for thin section preparation. However, 3 cm from the top of the UGU and 18 cm from the

bottom of the AGU were recovered and provide basic microfacies data even from gypsum deposits. Because the sampling site is located in an arid region, the sediments were sampled dry, and were not dried before further treatment at the GFZ in Potsdam. The sediment was carefully transferred into aluminum boxes and impregnated with epoxy resin. Then, samples were cut into two halves – one half was impregnated with epoxy resin again and the second half was used for thin section preparation (10x2 cm with 2 cm overlap).

S1.2. Microfacies analyses and varve chronology

At both sites, the study intervals for microscopic investigation were sampled continuously for thin sections following the standard procedure by (Brauer & Casanova 2001) that was adjusted for salty sediments. In total 129 thin sections were prepared, 109 from site 5017-1-A, and 20 from Masada. Thin section analyses were performed using a Zeiss Axiolab pol microscope under plane- and cross-polarized light using magnifications of 50-400x. Photographs were taken with an Olympus BX53F microscope, connected to an Olympus DP72 camera with magnifications between 20- and 400 times. Microfacies analyses included varve counting and measurements of varves and sublayer thickness that were conducted based on determination of varve composition, structure and boundaries. A varve quality index (VQI) from 0 (no varve preservation) to 3 (perfect horizontal varve with sharp boundaries) was assigned to each varve. At both sites, floating varve chronologies were established for lithozones C2 and M2 by microscopic layer counting.

Counting was performed two (C2) and three (M2) times and the sublayer thickness was measured during the second count, which is considered more reliable (Martin-Puertas et al. 2014). The counting difference between the counts was calculated for each thin section. Overcounts (+varves) and undercounts (-varves) are given as counting uncertainty. In lithozone M2, varves were only counted, but not measured in five folded intervals caused by earthquakes (Marco et al. 1996), similar to the method of Prasad et al. (2004)(Prasad et al. 2004).

S1.3. XRF analyses

XRF core scanning was performed on smoothed surfaces of fresh sediment from cores 5017-1-A-46 to -43 with an ITRAX XRF core scanner at the GFZ in Potsdam using a Cr-X-ray source (30 kV, 30 mA), 10 s measurement time and a measurement step size of 200 µm. Element intensities are acquired in counts per second (cps) and displayed as log-ratios reflecting relative variations of the geochemical composition in the ICDP sediment cores (Tjallingii et al. 2007; Weltje & Tjallingii 2008; Weltje et al. 2015).

µ-XRF element mapping was performed on the sedimentary sections collected from both sites – the ICDP core and Masada – on selected impregnated sediment blocks that were also utilized for thin section preparation. The µ-XRF element mapping was performed at the GFZ in Potsdam using a Bruker M4 Tornado µ-XRF scanner. The scanner is equipped with a Rh X-ray source (50 kV, 600 µA) and poly-capillary X-ray optics, which irradiate a spot size of approximately 20 µm. Using a measurement time of 30 ms, measurements were obtained every 50 µm and relative element abundances are visualized as 2D maps using normalized element intensities. µ-XRF element maps reveal compositional differences at sub-annual resolution, thus directly complementing thin section microscopy.

S1.4. Correlation and chronology of Masada and the ICDP core

The chronology for the studied Masada section is based on U/Th- and radiocarbon dating, summarized and re-analysed in the T2013 chronology from Torfstein et al. (2013a) (Fig. S5-5, table S5-1). The lateglacial section of the ICDP core has been dated by 2 aragonite U/Th-ages (T2015; Torfstein et al. 2015), 6 radiocarbon ages in the K2017 chronology from Kitagawa et al. (2017), and 4 tephrochronological ages in the N2021 chronology from Neugebauer et al. (2021) (Fig. S5-5, table S5-1). In T2015, the lower U/Th-age at 102.10 m (18,140 ± 83 (isochron), 18,155 ± 45 BP (single sample)) is obtained from a ~2.3 m thick MTD directly below the UGU, while the upper U/Th-age at 92.2 m (14,067 +1,146/-1,135 (isochron), 12,858 ± 363 (single sample)) is derived from an undisturbed aad section (in this study labelled as ULi-aad) below the AGU. Radiocarbon ages from K2017 are derived from the base of MTDs and were re-calibrated using IntCal20. Based on stratigraphic correlation to dated exposures at the margins of the Dead Sea, the T2015 chronology further includes transferred ages of 17.1 ± 0.5 ka for the base of the UGU (at 101 m sediment depth) and 14.5 ± 0.5 ka for the base of the AGU (91 m sediment depth; Fig. S5-5). In the N2021 chronology, four cryptotephras were identified between 93.3 and 92.0 m that correlate to (i) the Nemrut V-16 eruption at 13,585 ± 1.4% vy BP (Landmann et al. 1996; Schmincke & Sumita 2014) (93.26 m), (ii) the Süphan swarm eruptions V-8 to V-15 at 12,740-13,078 ± 1.4% vy BP (Landmann et al. 1996; Schmincke & Sumita 2014) (92.54 m), (iii) the Santorini PhT1 at ~13,900-10,500 BP (St. Seymour et al. 2004) (92.07 m) and (iv) the Süphan V-13 eruption at 12,740-13,078 1.4% vy BP (Landmann et al. 1996; Schmincke & Sumita 2014) (92.07 m). The latter two are partially derived from the same MTD as a ^{14}C age of 14,161 ± 160 cal. BP at 92.06 m (Kitagawa et al. 2017) and in broad agreement within the uncertainties. Ages for the Nemrut eruption and Süphan swarm eruptions are derived from varve counting in the Lake Van sediment record (Landmann et al. 1996; Schmincke & Sumita 2014) and the Santorini PhT1 tephra age is from an underlying radiocarbon dated peat (St. Seymour et al. 2004). The Süphan swarm eruption ages are about 1500 years

younger than the radiocarbon age at 92.06 m in the K2017 chronology and the transferred U/Th age at 91 m sediment depth in the T2015 chronology.

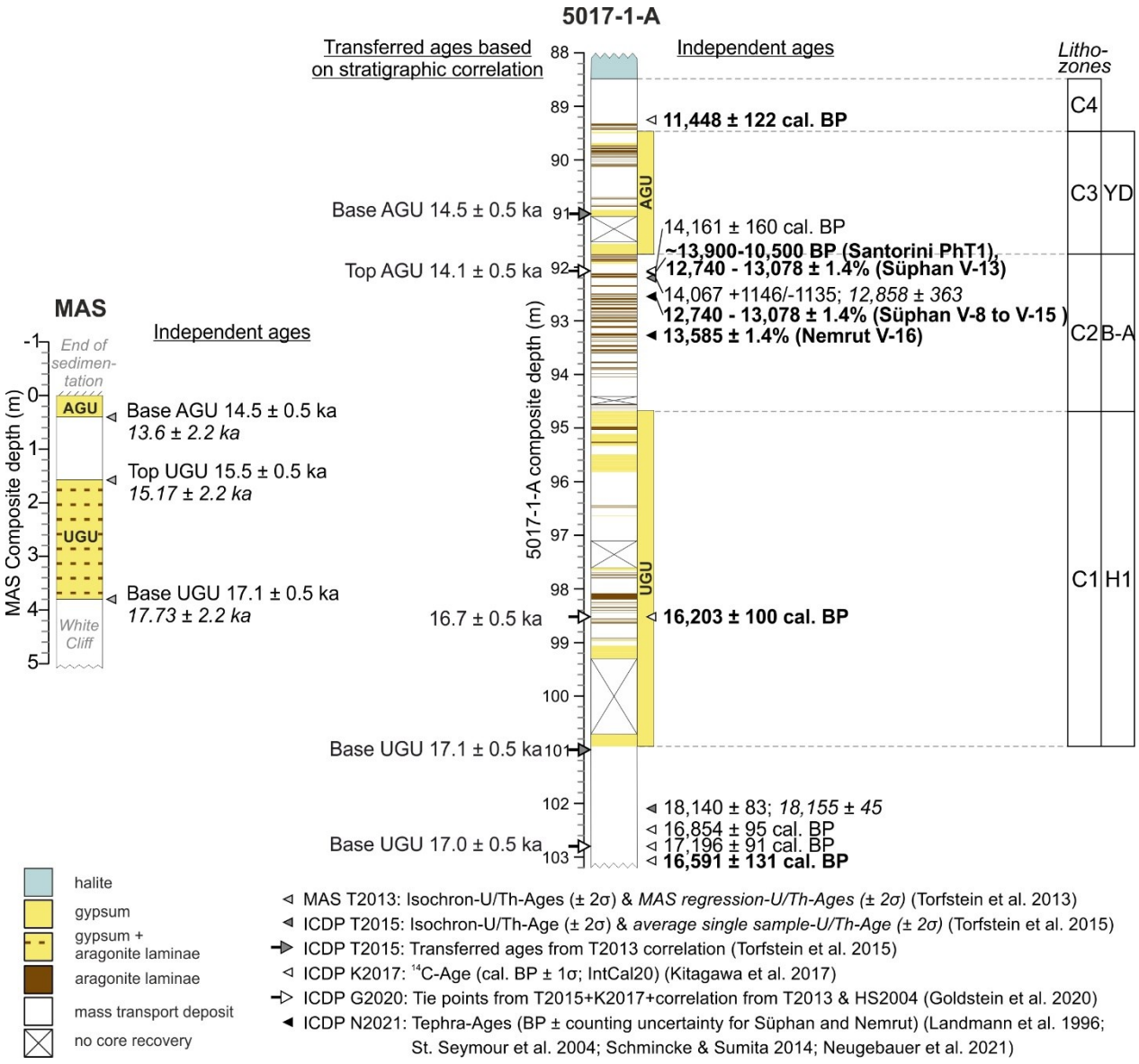

***Figure S5-5**: Lithological profiles of Masada (MAS) and the ICDP core (5017-1-A) with published ages. UGU: Upper Gypsum Unit, AGU: Additional Gypsum Unit, YD: Younger Dryas, B-A: Bølling/Allerød, H1: Heinrich event 1.*

In this study, we define the top of the Lisan Formation at the top of the AGU and accept six ages for our age model – three ^{14}C and three tephra ages. (1) As basal age for the UGU we accept the youngest of the three ^{14}C-ages at 103.07 m (16,591 ± 131 cal BP) from a ~2.3 m thick MTD directly below the base of the

UGU. All three radiocarbon ages from this MTD reveal similar ages around 17 ka and are in agreement within dating uncertainties with the U/Th age for the UGU base in Torfstein et al. (2013) (Fig. S5-5). An aragonite U/Th age obtained from the same MTD as the radiocarbon ages is ~1 ka older. (2) The second date for our chronology is a ^{14}C-age within the UGU at 98.51 m depth (16,203 ± 100 ka BP) that agrees well with transferred U/Th dates from exposed margins (UGU age range 17.1-15.5 ± 0.5 ka; Torfstein et al. 2013a). (3-5) For lithozone C2 (ULi-aad) between the UGU and AGU we accept the Nemrut V-16 tephra age of 13,585 ± 1.4% BP at 93.26 m sediment depth, as well as the Süphan Swarm ages (12,740-13,078 ± 1.4% BP) at 92.54 and 92.07 m sediment depth and the Santorini PhT1 tephra age (~13,900-10,500 BP) at 92.07 m sediment depth. We favour these ages rather than the ~1-1.5 ka older ^{14}C-age from the same sediment section, which we consider reworked due to deposition in the base of a MTD. The tephra ages agree within uncertainties with the U/Th-age from 92.20 m depth in the ICDP core and with the regression-U/Th-age for the base of the AGU at Masada (13.6 ± 2.2 ka BP), whereas the isochron U/Th age of 14.5 ± 0.5 ka appears to be too old (Torfstein et al. 2013a). The tephra ages are further supported by aragonite varve counting between the two tephra horizons at 93.26 m and 92.54 m. (6) The youngest age utilized in our updated chronology is a ^{14}C-age of 11,448 ± 122 cal BP at 89.25 m (Kitagawa et al. 2017) ~20 cm above the top of the AGU.

The main difference of our age model compared to the T2015 chronology is the ~1.5 ka younger age for the AGU base due to the tephrochronological ages which we regard as more reliable than the ^{14}C age and transferred U/Th ages from the marginal outcrops. It should be also mentioned that we define the base of the AGU in the ICDP core at the bottom of the lowermost gypsum bed at 91.76 m and thus lower than in T2015, where this gypsum bed is not included in the AGU.

***Table S5-1**: Published ages for the ICDP core 5017-1-A and Masada. MTD: mass transport deposit, unc.: uncertainty.*

5017-1-A	Age ± unc. (BP)	Type of age	Material	Sediment	Original reference
1	11,448 ± 122	Calibrated ^{14}C-age	terrestrial plant remains	MTD	Kitagawa et al. 2017
2	14,161 ± 160	Calibrated ^{14}C-age	terrestrial plant remains	MTD	Kitagawa et al. 2017
3	~13,900-10,500	Tephra (Santorini PhT1)	glass shards	varves + MTD	Landmann et al. 1996; St. Seymour et al. 2004; Schmincke & Sumita 2014; Neugebauer et al. 2021
3	12,740 - 13,078 ± 1.4%	Tephra (Süphan V-13 eruption)	glass shards	varves + MTD	Landmann et al. 1996; St. Seymour et al. 2004; Schmincke & Sumita 2014; Neugebauer et al. 2021
4	14,067 +1146/-1135	Isochron-U/Th-Age (± 2σ)	aragonite	varves	Torfstein et al. 2015
4	12,858 ± 363	Average single sample-U/Th-Age (± 2σ)	aragonite	varves	Torfstein et al. 2015
5	12,740 - 13,078 ± 1.4%	Tephra (Süphan V-8 to V-15 swarm eruptions)	glass shards	varves + MTD	Landmann et al. 1996; St. Seymour et al. 2004; Schmincke & Sumita 2014; Neugebauer et al. 2021
6	13,585 ± 1.4%	Tephra (Nemrut V-16 eruption)	glass shards	varves + MTD	Landmann et al. 1996; St. Seymour et al. 2004; Schmincke & Sumita 2014; Neugebauer et al. 2021
7	16,203 ± 100	^{14}C-age	terrestrial plant remains	MTD	Kitagawa et al. 2017
8	18,140 ± 83	Isochron-U/Th-Age (± 2σ)	aragonite	varves	Torfstein et al. 2015
8	18,155 ± 45	Average single sample-U/Th-Age (± 2σ)	aragonite	varves	Torfstein et al. 2015
9	16,854 ± 95	Calibrated ^{14}C-age	terrestrial plant remains	MTD	Kitagawa et al. 2017
10	17,196 ± 91	Calibrated ^{14}C-age	terrestrial plant remains	MTD	Kitagawa et al. 2017
11	16,591 ± 131	Calibrated ^{14}C-age	terrestrial plant remains	MTD	Kitagawa et al. 2017
Masada	**Age ± unc. (BP)**	**Type of age**	**Material**	**Sediment**	**Original source**
12	14,500 ± 500	Isochron-U/Th-Age (± 2σ)	aragonite	varves	Torfstein et al. 2013
12	13,600 ± 2,200	Regression-U/Th-Age (± 2σ)	aragonite + organic macrofossils	varves	Torfstein et al. 2013 + Prasad et al. (2004)
13	15,500 ± 500	Isochron-U/Th-Age (± 2σ)	aragonite	varves	Torfstein et al. 2013
13	15,170 ± 2,200	Regression-U/Th-Age (± 2σ)	aragonite + organic macrofossils	varves	Torfstein et al. 2013 + Prasad et al. (2004)
14	17,100 ± 500	Isochron-U/Th-Age (± 2σ)	aragonite	varves	Torfstein et al. 2013
14	17,730 ± 2,200	Regression-U/Th-Age (± 2σ)	aragonite + organic macrofossils	varves	Torfstein et al. 2013 + Prasad et al. (2004)

S2. Sediment facies

Sediments in the studied sections of the ICDP core and Masada consist of three different types of aragonite varves (e.g. Machlus et al. 2000; Prasad et al. 2004), four different types of mass transport deposits (MTD) (Neugebauer et al. 2014) and five different types of gypsum facies.

S2.1. Gypsum

Gypsum grains occur in discrete gypsum deposits, in MTDs and in aragonite laminae at both sites. Interpretation of gypsum deposition is based on the grain form, grain orientation and sedimentary facies. We differentiate two crystal forms – idiomorphic elongated and interlocking rectangular/prismatic. Gypsum mostly is found predominantly in laminae and is rarely non-laminated and massive. We distinguish three laminated gypsum facies and massive gypsum deposits in lithozones C1, C2 and C3, and two laminated gypsum facies in lithozones M1 and M3.

Laminated gypsum facies 1 (gd-l1; Fig. S5-6 a-d) occurs in lithozones C1, C2 and C3 and is the most common type in the ICDP core (~73 %, 215 couplets). The thickness of these couplets is variable (up to 20.4 mm). Two sublayers consist of (i) alternating yellow gypsum (~0.04-16 mm) and (ii) a thinner layer of (dark-) brown fine-grained detritus (~0.04-5.8 mm). Gypsum occurs as interlocking rectangular grains (~10-100 µm) that are occasionally inversely graded and interpreted as rapidly precipitated in the water column (Magee 1991; Kirkland 2003; Mees et al. 2012). Seldom idiomorphic elongated gypsum grains (~20-200 µm) are deposited parallel to laminations, and their morphology often changes upwards to more prismatic gypsum grains, which suggests slow gypsum precipitation (Mees et al. 2012; Reiss et al. 2021). The detrital sublayer consists of scattered rectangular gypsum grains within a clay-sized marl matrix. The lower boundary of the detrital sublayer is sharp, whereas the upper boundary is often gradual. Occasionally, scattered detrital carbonate grains are deposited within the gypsum or both sublayers, suggesting concomitant deposition and thus gypsum precipitation. Similar gypsum laminations in Prungle Lakes, Australia, were tentatively compared to an annual cycle (varves) (Magee 1991).

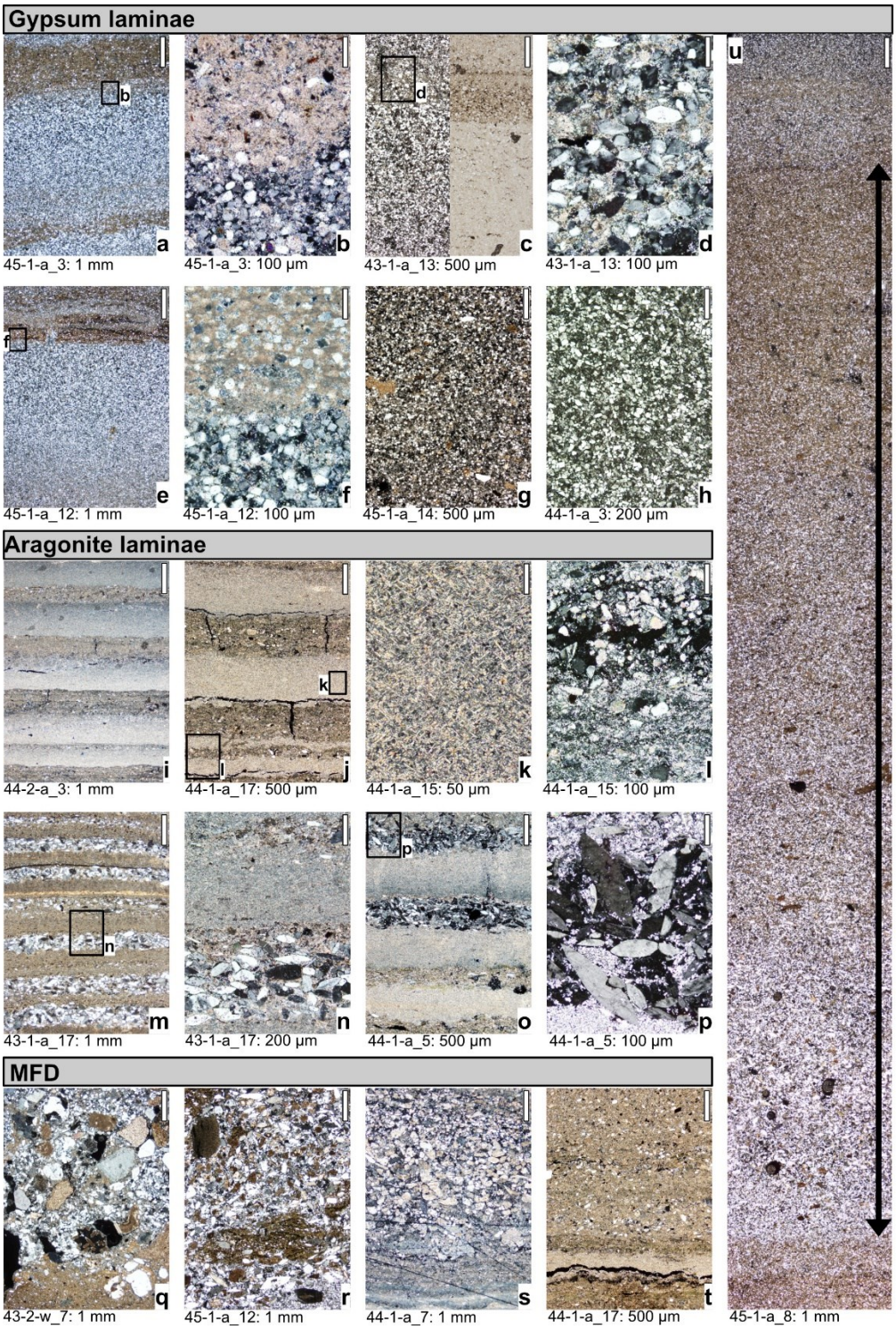

***Figure S5-6**: Microscope images of the different ICDP facies in our study interval. (a-h, u) Gypsum microfacies. (a-d) gd-l1 consisting of rectangular gypsum and a thinner fine detrital sublayer; (e, f) gd-l2 consisting of rectangular gypsum and a thinner top of carbonate cement precipitated between gypsum grains; (g) gypsum grains overlain by coarser detrital grains; (h) solely gypsum grains; (u) gd-l3 consisting of a singlet of rectangular gypsum grains and graded detritus. (i-p) Aragonite varves. (i-l) aad varves consisting of one aragonite and one detrital sublayer. (m-p) aadg varves consisting of couplets of aragonite and idiomorphic elongated gypsum grains. (q-t) base of MFDs. (q-s) MFD-1 with sand-sized detrital grains and basal erosion; (t) matrix-supported MFD-2 with clay to silt-sized detrital grains and rare basal erosion. Note the different scales (white boxes): box scale is specified at the bottom of each picture.*

Laminated gypsum facies 2 (gd-l2; Fig. S5-6e, f) occurs in lithozones C1 and C3, appears mostly intercalated with gd-l1 and comprises 17 % of all gypsum laminae in the ICDP core (50 couplets). These thin couplets (~0.24-11.44 mm thick) comprise (i) yellow often inverse graded gypsum and (ii) carbonate cement. Gypsum occurs usually as interlocking rectangular crystals (~10-80 µm) that commonly show inverse grading, indicating rapid precipitation in the water column (Magee 1991; Kirkland 2003; Mees et al. 2012). More rarely idiomorphic elongated gypsum grains (~20-200 µm), which are deposited parallel to layering occur. Their morphology often changes upwards into more prismatic gypsum grains, thus interpreted as slow growing primary precipitate (Mees et al. 2012; Reiss et al. 2021). The second sublayer consists of few scattered rectangular precipitated gypsum grains surrounded by carbonate cement. The lower boundary of the cement layer is sharp, whereas the upper boundary is often gradual. Formation of carbonate cement is probably not diagenetic (Magee 1991; Mees et al. 2012) and might be explained in the following manner: Higher rainfall that delivers dilute carbonic acid dissolves calcareous dust particles (delivering Ca^{2+} and CO^{3-}) and primary gypsum (delivering Ca^{2+} and S^{2-}) (Magee 1991). When these sources of solutes are mixed, secondary carbonate precipitation might occur around or partly replacing the gypsum crystals (Magee 1991). Fine detrital matter during Lake Lisan mostly comprises quartz and calcite grains (Haliva-Cohen et al. 2012). Altogether, the consideration of the laminae and their structures point to seasonal deposition of the sublayers (gypsum during summer evaporation, cement during winter rains (Magee 1991)) although it cannot be observed under the current settings of the sea.

Laminated gypsum facies 3 (gd-l3; Fig. S5-6u) resembles a mixture of gypsum precipitate and MFD. It occurs in lithozones C1 and C2, and comprises ~5 % of gypsum laminae in the ICDP core (15 layers). This facies represents the thickest gypsum laminae (~9.5-36 mm) occurring one to three times in a sequence. It consists of one layer (singlet) of yellow gypsum and towards the top increasing detrital marl. Gypsum grains occur as interlocking rectangular crystals (up to ~70 µm), thus interpreted as precipitated from the water column (Magee 1991; Kirkland 2003; Mees et al. 2012). The clay-sized detrital marl increases in quantity towards the top, while the gypsum content decreases, further supporting gypsum precipitation from the water column (Mees et al. 2012). In most of the singlets detrital carbonate grains (e.g. fossils) occur syndepositional. Rarely two distinct layers can be differentiated: (i) consisting of interlocking rectangular gypsum and coarse detrital grains (fossils, quartz, gypsum, macro-organic) and (ii) mostly interlocking rectangular gypsum and fine-grained marl.

Laminated gypsum facies 4 (gd-l4; Fig. S5-7c) occurs in lithozone M1. Couplets comprise (i) mostly up to ~200 µm elongated gypsum grains deposited sub-horizontal in distinct layers, and (ii) coarse detrital grains including scattered elongated gypsum grains up to ~200 µm. In both sublayers no displacive growth is

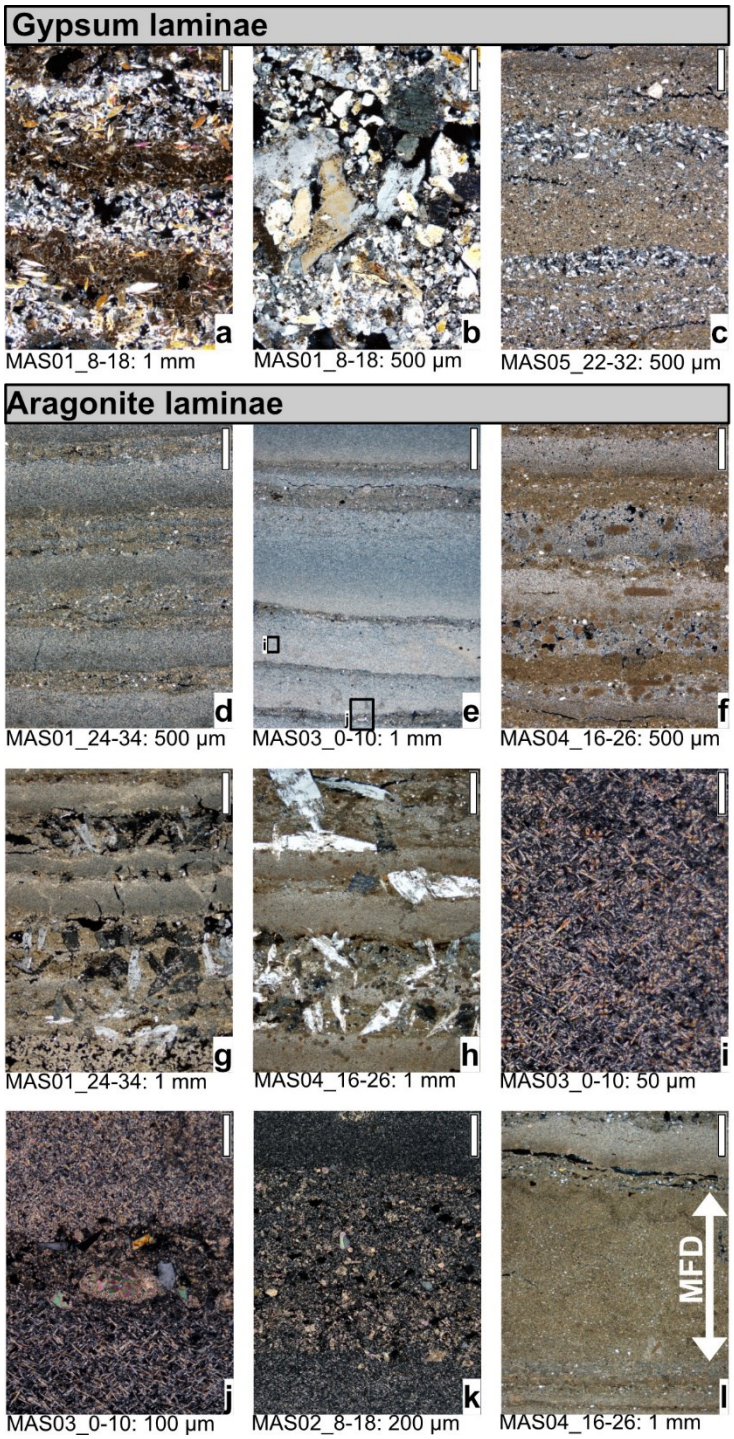

***Figure S5-7**: Microscope pictures of the Masada facies in our study interval. (a-c) Gypsum microfacies. (a, b) gd-l5: gypsum couplets of light idiomorphic elongated gypsum grains and dark detritus. (c) gd-l4: gypsum couplets of light idiomorphic elongated gypsum grains and dark detritus. (d-k) Different aragonite varves. (d-f) aad varves of varying thickness, occasionally including micritic grains (f). (g, h) aadg varves with by gypsum disturbing the boundaries. (i-k) Zoom into aragonite varve sublayers: light aragonite (i, j) and dark detritus (j, k). (l) Matrix-supported MFD-2 within aad varves with clay to silt-sized detrital grains and no basal erosion. Note the different scales (white boxes): box scale is specified at the bottom of each picture.*

visible, and therefore, gypsum is interpreted as reworked (Warren 1982; Magee 1991) from gypsum grains that probably formed by overgrowth (Magee 1991; Torfstein et al. 2008).

Laminated gypsum facies 5 (gd-l5; Fig. S5-7a, b) occurs in lithozone M3. The couplets consist of (i) beige gypsum grains and (ii) brown fine-grained detritus. Gypsum deposition is variable, which is why two further subtypes are defined. In subtype gd-l5a the gypsum sublayer comprises interlocking rectangular gypsum grains (up to ~200 µm) at the base followed by large (up to ~2000 µm) (sub-) vertical oriented elongated gypsum grains that show signs of overgrowth and displacive growth into the overlying detrital sublayer. The detrital sublayer comprises primarily pellets of fine-grained detritus. Interlocking rectangular gypsum grains are interpreted as sub-aqueous rapidly growing precipitate (Magee 1991; Kirkland 2003; Mees et al. 2012), whereas elongated gypsum grains are interpreted as diagenetic overgrowth (Warren 1982; Magee 1991; Torfstein et al. 2008). Subtype gd-l5b comprises couplets of (i) mostly sub-horizontal idiomorphic elongated gypsum grains (up to ~1300 µm) that are often

corroded, fractured and rounded, and (ii) primarily pellets of fine-grained detritus. This structure has been previously interpreted as aeolian reworking/deposition in Australia and Spain (Magee 1991; Mees et al. 2012). In both subtypes, up to ~2800 µm large elongated, displacive and non-oriented gypsum grains can occur within the detrital sublayer that are interpreted as diagenetic (Magee 1991; Mees et al. 2012).

In the shallow-water site Masada, occurrence of mainly reworked or diagenetic gypsum and only minor authigenic precipitated gypsum that alternate with detrital pellets and are deposited in undulose laminae suggest deposition in shallow-waters dominated by wave activity (Warren 1982; Weber et al. 2021) or even seasonal exposure and aeolian reworking/deposition (Magee 1991; Mees et al. 2012). In contrast, in the deep-water 5017 of the ICDP, gypsum grains are primarily authigenic precipitates and alternate with fine-grained detritus or cement indicating deposition in a calm water column (Magee 1991; Kirkland 2003; Mees et al. 2012).

Massive gypsum deposits show no internal structure and occur in ICDP core lithozones C1 (~4.6 cm) and C3 (~11 cm). The deposits consist of yellow gypsum grains, detrital carbonates, carbonate fossils, micritic grains, aragonite needles and clay-sized marl. Gypsum occurs as precipitated interlocked rectangular and elongated idiomorphic crystals (Magee 1991; Kirkland 2003; Mees et al. 2012; Reiss et al. 2021).

Additionally, gypsum grains occur in MTDs and in aragonite laminae at both sites. In aragonite laminae (aadg varves), idiomorphic elongated gypsum grains occur with often random orientation and displacive growth that are interpreted as diagenetic (Magee 1991; Mees et al. 2012). In the ICDP core elongated gypsum grains are up to ~900 µm (C1, C2 and C4) and up to ~1600 µm (C3). Occasionally, elongated gypsum grains are deposited layer-parallel, which might suggest reworking (Warren 1982; Magee 1991) or slow precipitation (Mees et al. 2012). Further, remnants of rectangular gypsum grains can occur that might suggest initial gypsum precipitation followed by overgrowth (Magee 1991; Kirkland 2003; Mees et al. 2012). In Masada diagenetic elongated gypsum grains are up to ~3400 µm and show obvious displacive growth up to complete destruction of layer boundaries and layers.

In the ICDP core, randomly orientated elongated gypsum grains up to ~1500 µm without obvious post-sedimentary displacive growth and fining upwards are included in the grain-supported base of MFD-1, therefore interpreted as reworked(Magee 1991). Rectangular gypsum in patches at the base of few MFD-1 are considered as reworked (e.g. Magee 1991). In Masada, elongated gypsum grains are deposited at the base of one MFD-2 that are interpreted as diagenetic due to their random orientation and displacive growth (Magee 1991; Mees et al. 2012). In the ICDP core homogenites contain randomly-oriented single

elongated gypsum grains up to ~1300 µm scattered within a clay-sized matrix, which is why they are interpreted as diagenetic (Magee 1991; Mees et al. 2012).

S2.2. Aragonite varves

Aragonite varves occur at both sites and are differentiated into three subtypes in the ICDP core and two subtypes in Masada. Alternating aragonite and detritus (aad) varves (e.g. Machlus et al. 2000; Prasad et al. 2004; Neugebauer et al. 2014; Ben Dor et al. 2019) occur in all ICDP core lithozones (Fig. S5-6i-l) and in lithozone M2 in Masada (Fig. S5-7d-f). In the ICDP core ~76 % (1151 couplets) and in Masada ~96% (926 couplets) of all aragonite laminae are typical aad varves. The thickness of these couplets is up to 6.8 mm in the ICDP core and up to 4.8 mm in Masada. The aad facies typically consists of two laminae: (i) white authigenic aragonite needles or stellate aggregates of orthorhombic crystals (~5-30 µm; Fig. S5-6k, S5-7i, j) and (ii) dark allochthonous clay to silt-sized detrital carbonates, quartz, feldspar and clay minerals (Fig. S5-6 i-l; S5-7j, k) (e.g. Begin et al. 1974; Haliva-Cohen et al. 2012). Primary aragonite precipitates during the dry season due to evaporation, while the detritus is deposited by seasonal floods during the rainy season (Neev & Emery 1967; Begin et al. 1974).

A subtype of aad varves (termed 'aadg' varves here) occurs in all lithozones of the ICDP core (Fig. S5-6 m-p) and in lithozone M2 at Masada (Fig. S5-7g, h). The aadg facies occurs in 18 % (268 laminae) of aragonite varves in the ICDP core and in ~4 % (42 laminae) of aragonite varves in Masada. The thickness of these couplets is up to 7 mm in the ICDP core and up to 3.5 mm in Masada. Sublayers are identical to aad varves except for the incorporation of diagenetic idiomorphic elongated gypsum grains (section S2.1) in the detrital sublayer. At Masada gypsum grains also occur within the aragonite sublayer in 21 aadg varves (in previous works referred to as 'disseminated gypsum' (Torfstein et al. 2008)).

A rare aragonite varve subtype termed ld ('laminated detritus'; (Haliva-Cohen et al. 2012; Neugebauer et al. 2014)) occurs solely in lithozone C1 of the ICDP core and amounts to ~6 % (90 laminae) of aragonite varves. The thickness of these laminae is up to 2.7 mm. Two sublayers comprise (i) finer detritus and (ii) coarser grained detritus often incorporating diagenetic elongated gypsum (Magee 1991). Rarely, a third sublayer consisting of aragonite is developed.

S2.3. Mass Transport Deposits

We differentiate MTDs based on previous descriptions (Neugebauer et al. 2014, 2015, 2016; Ahlborn et al. 2018; Kagan et al. 2018) into (i) mass flow deposits (MFD), (ii) homogenites, (iii) slumps and (iv) breccias at both sites. In the ICDP core, between 20 and 43 % of MTDs show erosive structures at their base, whereas at Masada no erosive structure are observed (table S5-2). Mass flow deposits (MFD) are the most

common MTDs (table S5-2) and describe detrital sediments with a coarse sand to silt-sized base and upwards fining. We differentiated two types. MFD-1 (Fig. S5-6 q-s) has an erosional base and typically consist of three sections with decreasing detrital grain sizes and quantity (thickness up to ~64 cm). The base is grain-supported, poorly sorted and encompasses up to sand-sized angular to rounded detrital grains (up to 2 mm; carbonates, reworked gypsum and sub-ordinated quartz, feldspar and organic remains). This MFD type occurs solely in the ICDP core. MFD-2 (Fig. S5-6t, S5-7l) consists of one matrix-supported layer (thickness up to ~8 cm in the ICDP core and up to ~0.8 cm at Masada) with smaller (up to ~0.1 mm) detrital grains and rarely show basal erosion. They either have a coarse base, are fining upwards or are homogenous. MFD-2 are the only MTD occurring at Masada. MFDs in the ICDP core mostly incorporate elongated idiomorphic gypsum interpreted as reworked (section S2.1, Magee 1991). The ICDP core comprises 141 MFDs (30 MFD-1 and 111 MFD-2) with 38 (including all MFD-1) showing erosive structures (e.g. undulating base, dropped grains, half-eroded underlying sublayers). At Masada occur 12 MFD-2 (~0.8 to ~8.4 mm thickness) that show no visible basal erosion.

Homogenites occur only in lithozones C1 and C2 in the ICDP core and are defined as matrix-supported deposits of coarse scattered detrital grains in a marl matrix. They occur three times and are 5-36 cm thick. Due to a missing bottom boundary one could also be defined as MFD. Slumps occur solely in lithozones C2 and C3 of the ICDP core and are in-situ aad laminae that are large-scale folded, fractured and/or dislocated within homogeneous sediments interpreted as subaquatic slope failures. These occur two times and are ~5 cm thick. Breccias, i.e. deposits of broken aad laminae fragments within a fine-grained dark matrix, appear only in lithozones C1 and C2 of the ICDP core. Either they occur as discrete deposit or are incorporated in the base of MFD-1. Discrete breccia deposits appear three times and are 2-2.5 cm thick.

***Table S5-2**: Microfacies data for the lithozones C1-C4 (ICDP core) and M1-M3 (Masada).*

ICDP core 5017-1-A					
Lithozones		**C1**	**C2**	**C3**	**C4**
Unit		**UGU**	**ULi-aad**	**AGU**	
Depth (m)		100.94-94.69	94.69-91.76	91.76-89.46	89.46-88.48
Thickness (m)		6.25	2.93	2.29	0.98
Gypsum	Sum of beds	1.40 m (32%)	0.09 (3%)	0.36 m (21 %)	-
	No. Of beds (#)	7	2	4	-
	Individual beds	Up to 33 cm, Up to ~100 laminae	Up to ~10 cm, up to ~10 laminae	~10-20 cm (laminated lower beds), ~4 cm (upper beds, ~42 % laminated, ~58 % massive)	-
	Gypsum laminae # (thickness %)	224 (97%)	16 (100%)	53 (42%)	-
	Gypsum massive (thickness %)	3%	-	58%	-
	Gypsum laminae type gd-l1	167	15	46	-
	Gypsum laminae type gd-l2	44	-	6	-
	Gypsum laminae type gd-l3	13	1	1	-
Aragonite varves	Sum of aad/aadg packages	0.21 m (5%)	0.76 m (27%)	0.23 m (13 %)	0.08 m (8%)
	aragonite varves No. (#)	339	912	208	50
	aad varves (#)	199	848	102	2
	aadg varves (#)	50	64	106	48
	Sum of ld packages	0.19 m (4 %)	-	-	-
	ld laminae (#)	90	-	-	-
	Max. varves without MTD (#)	36	54	39	23
	aragonite varves between gypsum beds	25-231	-	208	-
MTD	Sum of MTDs	2.60 m (59 %)	1.94 m (70 %)	1.15 m (66 %)	0.91 (92%)
	MTD No. (#)	47	64	27	11
	MTD erosive No. (#)	20 (43%)	13 (20%)	6 (22%)	4 (36%)
	Sum of MFDs	2.26 m (51%)	1.51 m (54%)	1.10 m (63%)	0.91 (92%)
	MFD No. (#)	43	61	26	11
	MFD-1 No. (#)	16 (37%)	6 (10 %)	4 (15%)	4 (36%)
	MFD-1 max. thickness (m)	0.58 m	0.15 m	0.49 m	0.64 m
	MFD-2 No. (#)	27 (63%)	55 (90%)	22 (85%)	7 (64%)
	MFD-2 max. thickness (m)	0.04 m	0.08 m	0.04 m	0.02 m

***Table S5-2 (continued)**: Microfacies data for the lithozones C1-C4 (ICDP core) and M1-M3 (Masada).*

Masada					
Lithozones		**M1**	**M2**	**M3**	**-**
Units		**UGU**	**ULi-aad**	**AGU**	**-**
Depth (m)		3.8-1.55	1.55-0.41	0.41-0	-
Thickness (m)		2.29	1.16	0.41	-
Microscopic analyses		1.6-1.55	1.55-0.41	0.41-0.23	-
Gypsum	Sum of beds	~0.85 m* (37%)	-	0.41 m (100%)	-
	No. Of beds (#)	~9*	-	1	-
	Individual beds	-	-	-	-
	Gypsum laminae (#)	-	-	-	-
	Gypsum type	gd-l4	-	gd-l5	-
Aragonite varves	Sum of aad packages	-	1.13 (97%)	-	-
	aragonite varves No. (#)	-	968	-	-
	aad varves (#)	-	926	-	-
	aadg varves (#)	-	42	-	-
	Sum of ld packages	-	-	-	-
	ld laminae (#)	-	-	-	-
	Max. varve No. without MTD (#)	-	7-297	-	-
	aragonite varves between gypsum beds	-	-	-	-
MTD	Sum of MTDs	-	0.03 (3%)	-	-
	MTD No. (#)	-	12	-	-
	MTD erosive No. (#)	-	0 (0 %)	-	-
	Sum of MFDs	-	0.03 (3%)	-	-
	MFD No. (#)	-	12	-	-
	MFD-1 No. (#)	-	-	-	-
	MFD-1 max. thickness (m)	-	-	-	-
	MFD-2 No. (#)	-	12 (100%)	-	-
	MFD-2 max. thickness (m)	-	0.08 m	-	-

- does not occur
* data from (Torfstein et al. 2008)

S3. Aragonite varve counting and chronologies

In lithozone C1 of the ICDP core, 339 +10/-18 aragonite varves, including aad, aadg and ld laminae, were counted. A floating varve chronology that consists of in total 912 +15/-24 aad/aadg varves (table S5-2) could be constructed solely for lithozone C2. The chronology further shows three weak sections of higher aragonite sublayer thickness that are ~140, ~30, and ~200 years long (Fig. 5-3). The varve thickness ranges from 0.03 to 6.8 mm (mean 0.82 mm) and the aragonite sublayer thickness varies between 0.04 and 1.85

mm (mean 0.63 mm). Here, the varve chronology is interrupted 11 times by erosional events and therefore, an unknown number of eroded varves must be assumed. For lithozone C3, 208 +9/-13 aad/aadg varves and for lithozone C4, 50 +10/-0 aad/aadg varves were counted. A total of 968 +15/-64 aad and aadg varves were counted in lithozone M2 at Masada (table S5-2). Similar to lithozone C2 in the ICDP core, three weak sections of higher aragonite sublayer thickness occur that are ~140, ~30, and ~140 years long (Fig. 5-3). The varve thickness varies between 0.11 and 4.81 mm (mean 1.1 mm) and the thickness of the aragonite sublayer ranges from between 0.04 to 3.2 mm (mean 0.39 mm). In general, varve thicknesses in the deep-water ICDP core have a higher range/amplitude, but thicker varves form more often in the shallow-water at Masada.

S4. Gypsum layer counting

In lithozone C1 occur 224 gypsum laminae comprising mostly gd-l1 and gd-l2 couplets (mean for both ~2.8 mm) and some gd-l3 singlets (mean ~21.8 mm). Lithozone C2 comprises 16 gypsum laminae – mostly gd-l1 couplets (mean ~5.4 mm) and one gd-l3 singlet (9.5 mm). In lithozone C3, 53 gypsum laminae were counted of which almost all are couplets (gd-l1 mean ~3.1 mm, gd-l2 mean ~1.0 mm) and one is a gd-l3 singlet (mean ~24 mm). Due to disturbances, low preservation and indistinct sublayers in the lower part of C3, counting in this section should be considered with care. For details see table S5-2.

S5. XRF analyses

Several element ratios representing the key sedimentary features of our study interval were selected. The log(Ti/Ca) ratio represents input of terrestrial siliciclastic material. Calcium occurring in carbonates and gypsum can be either of detrital or authigenic sources, whereas Ti is exclusively detrital. log(Sr/Ca) reflects aragonite formation since Ca occurs in all carbonates including aragonite and calcite, as well as in gypsum, whereas Sr is only abundant in aragonite. The log(S/Ca) ratio represents gypsum, because S content is elevated in gypsum, but is absent in Ca-carbonate minerals. Gypsum deposits are therefore characterized by high log(S/Ca) ratios, and low log(Ti/Ca) and log(Sr/Ca) ratios. log(S/Ca) ratios are highest in gypsum-dominated segments, second highest in the base of MFDs containing reworked idiomorphic elongated gypsum grains, and third highest in aadg varves comprising diagenetic idiomorphic elongated gypsum (Fig. 5-2). Gypsum deposition is indicated in element maps by Ca and S (orange color, Fig. 5-3a). Aragonite varves show a distinct reversed pattern than observed in gypsum deposits: high log(Ti/Ca) and log(Sr/Ca) ratios, and low log(S/Ca) ratios, with aadg varves being the only exception as all of these ratios are high in this subtype (Fig. 5-2). In element maps, the alternating aragonite (blue Ca and Sr) and detritus (yellow Si) sublayers from aad varves are clearly distinguishable (Fig. 5-3a), and in aadg varves, the gypsum-bearing sublayer is characterized by orange Ca and S maps (Fig. 5-3a).

6. Synthesis

6.1. Summary and conclusion

The main aim of this thesis was to reconstruct climatic and environmental variability during the Lateglacial in detail from two varved lake systems in two different climatic and geographic settings – the Dead Sea (the Levant) and Lake Gościąż (Poland). Therefore, sediments from the deep lake centre of Lake Gościąż, the deep Dead Sea basin and the southwestern margin of the Dead Sea (Masada) have been analysed. To reconstruct the variability in sedimentation processes related to lake-internal and catchment responses to abrupt environmental and climate changes, high resolution microfacies analyses down to seasonal time scales (microscopy of petrographic thin sections, µ-XRF mapping and XRF core scanning) were applied. Additional analyses of sub-decadal resolution (stable oxygen and carbon isotope analyses and temperature reconstructions) were performed on the Lake Gościąż sediments to further improve the understanding of sedimentation characteristics and abrupt climate variability. The reconstruction of a robust chronology is a prerequisite for these high-resolved climate and environmental reconstructions, and for the comparison between the archives. In the following, the main results are summarized, it is concluded how the main objectives of this thesis were achieved, and this work is discussed in a broader scientific context.

6.1.1. What are possibilities to improve chronologies of lacustrine archives?

This objective was accomplished in chapters 2-5. The construction of a novel chronology for the complete sediment profile of Lake Gościąż is described in detail in chapter 2, while the lateglacial part is also presented in chapter 3. In chapter 4, an update for the lateglacial chronology of the Dead Sea record is provided that is further corroborated in chapter 5.

Lake Gościąż

In chapter 2, the new independent chronology of Lake Gościąż (GOS18) is presented, which was constructed from novel sediment cores obtained during lake sediment corings in 2015 and 2018. Based on triple varve counting, Bacon age-depth modelling of a poorly varved section, and further corroborated by ^{137}Cs activity concentration measurements, AMS radiocarbon dating and pollen analysis, the chronology reaches from the late Allerød (12,834 +134/-235 BP) until the time of the first coring in AD 2015. Three sections are distinguished: (i) an upper ~1100 years-long varve chronology, (ii) a poorly to non-varved section that was interpolated using the Bayesian age-depth modelling routine from Bacon (iii), and a lower ~10,000 year-long floating varve chronology. The upper varve chronology is continuous until the sediment-water boundary terminating at the year of coring in AD 2015 and was validated using gamma

measurements that were performed in the uppermost ~1.5 m showing two peaks in AD 1963 and AD 1986 and thus confirming the presence of extremely thick varves up to 70 mm and the varve counting. The lower varve chronology was anchored to the absolute timescale at the bottom of the interpolated section at 2606 ± 80 BP. 15 radiocarbon ages derived from terrestrial plant remains are distributed over the Holocene part of the profile and confirm the established chronology (Fig. 2-5). The high age uncertainty is due to the uncertainty of the interpolated section and added cumulative sum of the varve counting error. Similarity of the pollen data with the previous pollen record from Lake Gościąż (Ralska-Jasiewiczowa et al. 1998b) during the transition zones of the Younger Dryas shows that both records can be correlated and further confirms the chronology. As demonstrated in chapter 3, the Younger Dryas boundaries were defined in the centre of the major shifts in $\delta^{18}O$ of bulk carbonate, which nearly coincide with changes in vegetation (Fig. 3-2; Ralska-Jasiewiczowa et al. 1992).

In contrast to other chronologies of lacustrine archives, varve chronologies are (sub-) annually resolved, providing ages for each depth interval of the varved record, and do not rely on interpolation between chronological tie points. Further, they can be used to precisely date short-term and abrupt climate and environmental changes (e.g. Brauer et al. 1999, 2008), as well as events and/or the time span between events, like e.g. earthquakes (e.g. Migowski et al. 2004), floods (e.g. Czymzik et al. 2010; Ben Dor et al. 2018) or tephra horizons (e.g. Ott et al. 2016), which is demonstrated in chapters 2, 3 and 5, and is further discussed in section 6.1.2. The formation of varves and robustness of the established varve chronology was verified by the good conformity with additional independent dating methods, i.e. radiocarbon dating and ^{137}Cs measurements.

In contrast to the previous investigation of Lake Gościąż in the 20th century (Ralska-Jasiewiczowa et al. 1998b), in the study presented here varve counting was performed continuously on thin sections under the microscope for the complete profile. Although more time-consuming, varve counting on thin sections is more accurate since complex varve types with more than two sublayers and sublayers with low colour contrast, as well as thin varves are easier identified. In contrast, faster counting on fresh cores and core images or using XRF data often underestimates the actual number of varves (e.g. Lotter & Lemcke 1999; Schlolaut et al. 2018; Nzekwe et al. 2021). In comparison to the studies of Lake Gościąż in the 20th century, microscopic varve counting as demonstrated in chapter 2 could show that (i) the lower ~10,000 year-long floating varve chronology is actually 500 years longer than previously assumed, (ii) varves are preserved until the sediment-water boundary (AD 2015) in a ~1100 years-long varve chronology, and (iii) this recognition of additional varves shortened the non-varved interval in between the two varve chronologies by ~5 m. Thus, the study could demonstrate that microscopic varve counting is ideal to construct varve

chronologies, because varves and varve boundaries are identified much more precisely, especially in sections that have a poor varve quality.

Dead Sea

The lateglacial chronology of the DS was previously based on radiocarbon and U/Th-dating in the ICDP cores (Neugebauer et al. 2014; Torfstein et al. 2015; Kitagawa et al. 2017) and at Masada (Prasad et al. 2004; Torfstein et al. 2013a), respectively. Previous lithological correlations and age transfers from on-shore sites onto the deep ICDP core were based on these ages and macroscopic lithological descriptions (Torfstein et al. 2015; Goldstein et al. 2020). In chapter 4, it could be shown that in the deep ICDP core cryptotephrochronology provides a powerful tool to improve the lateglacial chronology of the DS. Five tephra horizons were detected from which six glass samples were analysed in the lateglacial sediment section between the two prominent Upper Gypsum and Additional Gypsum Units (UGU and AGU, respectively). Glass shards from the Nemrut V-16 eruption (Schmincke & Sumita 2014) and Süphan swarm eruptions V-8 to V-15 (Schmincke & Sumita 2014) were identified and provide about 1000 years younger ages than one radiocarbon age from the same sediment section (Kitagawa et al. 2017) and U/Th-dating of the AGU from on-shore sites (Torfstein et al. 2013a). However, one U/Th-age from the ICDP core (Torfstein et al. 2015) and the regression U/Th-ages from Masada (Torfstein et al. 2013a) coincide with the tephra ages within dating uncertainties. Additionally, in chapter 5, the tephra ages are further supported by varve counting between the Nemrut V-16 and Süphan V-8 to V-15 tephra horizons. Further, the study demonstrated that reworking of sediments and glass shards, as well as dispersal of possible tephra correlatives need to be considered during tephra identification and correlation.

As demonstrated in chapter 5, a continuous floating varve chronology of ~1000 varves could be constructed between UGU and AGU in the shallow-water sediments at Masada due to less mass transport deposits (MTDs) than in the deep basin. So far, varve chronologies have been reconstructed for the Last Glacial at exposed sites (~71-24 ka: Marco et al. 1996; ~26.2-17.7 ka: Prasad et al. 2004, 2009) and in the ICDP core (around ~27 and ~18 ka; Ben Dor et al. 2018), as well as during the Holocene in a marginal core (~500-3300 BP; Migowski et al. 2004; Neugebauer et al. 2015). However, it was also shown in chapter 5 that erosion of varves in the deep ICDP core can be quite low during stable phases of high or rising water levels. The study also demonstrated that in the deep lake time series can be established from varve counting of individual varved packages to assess the frequency of intercalated MTDs and gypsum beds. Thus, varve counting again proves as a crucial tool in the analyses of lacustrine sediments (see Lake Gościąż above).

Since dating of sedimentary material in the DS is characterized by large age uncertainties (U/Th-dating) or reworking processes (^{14}C-dating), synchronization and comparison of proxy signals with other archives proved rather difficult, especially at high-resolutions and during abrupt climate changes. To improve the age model of the DS, this study used cryptotephrochronology, which is a powerful tool that not only provides an independent dating method, but also allows for direct synchronization of different terrestrial, marine and ice-core records using the identification of non-visible glass shards (e.g. Wulf et al. 2008, 2013; Lane et al. 2011; for the DS: Neugebauer et al. 2017). The identification of cryptotephra glass shards as demonstrated in chapter 4 shows the great potential of the DS record to connect the Levant with the Mediterranean tephra framework, like e.g. Lake Van.

6.1.2. How do major and abrupt climate and environmental changes affect lake systems?

This objective has been fully met in chapters 3 and 5 in which the climatic and environmental conditions for the Lateglacial were reconstructed from Lake Gościąż (chapter 3) and the Dead Sea (chapter 5). Each study is an independent work focussing on different aspects of climate and environmental changes, which is why the two lake systems are discussed individually below. An overarching comparison of lake system responses to abrupt climate changes from both lake systems is given in the following section 6.1.3.

Lake Gościąż

The development of new analytical techniques and advancement in varve microfacies analyses allowed the re-investigation of the iconic varve record of Lake Gościąż. Climatic and environmental changes in Lake Gościąż were reconstructed at (sub-) annual scale for the Lateglacial (chapter 3), and subsidiary at centennial to millennial scale for the Holocene (chapter 2). During the Holocene, gradual fluctuations in geochemistry and sedimentation processes are recognized, which are caused by (i) changes in local hydrology and/or fluctuations in the water level that were possibly only strengthened during the Holocene Thermal Optimum (at ~7900 BP), (ii) the Homeric Climate Oscillation (at ~2600 BP), (iii) the Little Ice Age (at ~1100 BP), and (iv) eutrophication and human impact (during the last ~500-200 years). However, the last major, abrupt and high-amplitude climate change recorded in the sediments – the YD – occurred during the Lateglacial, and Lake Gościąż is one of the few lake archives in Europe that preserves varves throughout the complete YD. Such a seasonal resolution is vital to track abrupt changes in paleoclimate and paleoenvironment especially during the rapid YD transitions. Therefore, the main focus of climate and environmental reconstructions at Lake Gościąż was placed on the YD and its transitions, as presented in chapter 3. In this study, the seasonally resolved reconstructions focussed on inter-annual variability, short-term trends, and leads and lags of proxy responses to the YD onset and termination, respectively, to improve the understanding of lake system responses to abrupt climate changes.

The lateglacial sediments were analysed using continuous thin section microscopy, XRF core scanning, µ-XRF mapping, stable oxygen and carbon isotope measurements, as well as temperature reconstructions from chironomids. Varve microfacies data included varve composition, as well as varve and sublayer thicknesses for the complete section. Two novelties in comparison to the previous study of Lake Gościąż are both XRF analytical techniques, which depict sub-annual changes in elemental composition, while µ-XRF mapping of the YD transition zones even provides a direct comparison of thin section and element data (Fig. 3-9). Complementing the microfacies data, at (sub-) decadal resolution, changes in air temperature are represented directly by chironomid reconstructions (a novel method applied at Lake Gościąż) and indirectly by $\delta^{18}O_{carb}$. $\delta^{13}C_{org}$ records variability in the aquatic bioproductivity.

Two different biogenic varve types are distinguished: (i) varves during the YD are more complex, variable, thicker, and incorporate diatoms and re-suspended material, whereas (ii) varves during the Allerød and Early Holocene are simpler, less variable, thinner, devoid of diatoms and re-suspended material, and contain more amorphous organic matter. The YD was characterized by low temperatures, however chironomid-based July temperature reconstructions support recent studies indicating warm YD summers (Schenk et al. 2018). A strong water circulation and slightly higher catchment erosion during the YD are reflected in a high aquatic bioproductivity, thin amorphous organic sublayers, re-working of calcite, and deposition of littoral diatoms and some detrital grains in the deep lake centre. Complex sedimentation processes showed high inter-annual variability indicating a dynamic and unstable lake system. These results suggest enhanced westerly winds during the YD, similar to other varved lake records in central Europe (Goslar et al. 1999a; Brauer et al. 2008; Neugebauer et al. 2012). In northern Europe, westerly winds were enhanced during the later YD, indicating a northward movement of the westerlies (Bakke et al. 2009). Already during the last centuries of the YD, changes in temperature and environment (e.g. lower bioproductivity) indicate a weak second half of the YD and initial responses to the major warming at the demise of the YD. Although gradual changes during the YD are evident, a clear bi-partition as in more western lake sites (Brauer et al. 1999; Magny et al. 2001; Bakke et al. 2009) is not observed in the new Lake Gościąż profile. During the warmer Allerød and Early Holocene, sedimentation showed low inter-annual variability, absent diatom bioproductivity and thicker amorphous organic sublayers, suggesting primarily anoxic conditions and less water circulation in a stable lake system due to weaker winds and a denser forest vegetation in the catchment. Cooling at the YD onset (~180 years) was about 100 years longer than warming at the termination (~70 years), and environmental proxies lagged the initial cooling by at least ~90 years, whereas warming and environmental response were simultaneous during the cessation of the YD. In this study, seasonally resolved proxy leads and lags at both YD transition zones are

compared for the first time in Lake Gościąż, while prior studies mainly focussed on the YD/Holocene transition (Ralska-Jasiewiczowa et al. 2003). The YD boundaries and duration agree within dating uncertainties with previous results from Lake Gościąż (Goslar et al. 1993, 1998a, 1999b) and other European sites (table 6-1), although a recently revised age of the Laacher See tephra suggests a slightly older age of the Allerød/Younger Dryas (AL/YD) boundary in Europe (Reinig et al. 2021).

Table 6-1*: Comparison of ages for the boundaries and length of the Younger Dryas (YD) in varved lake sediments on the European mainland and NGRIP ice cores in Greenland. Note that no age uncertainties are listed. Previous Lake Gościąż studies after* Goslar et al. (1998a, 1999b)*, Perespilno after Goslar et al. (1999a), Lake Meerfelder Maar after Brauer et al. (1999), paleolake Rehwiese after Neugebauer et al. (2012), and NGRIP on the GICC05 timescale after Rasmussen et al. (2006). AL: Allerød, PB: Preboreal.*

Record	AL/YD (BP)	YD/PB (BP)	Duration (years)
Lake Gościąż, PL (this study)	12,620	11,470	1149
Lake Gościąż, PL (AD 1998)	12,580	11,440	1140
Lake Gościąż, PL (AD 1999)	12,650	11,510	
Perespilno, PL*	12,635	11,510	1125
Meerfelder Maar, DE	12,680	11,590	1090
Rehwiese, DE**	12,675	11,693	982
NGRIP, GL	12,846	11,653	1193

* no independent chronology: YD/PB boundary was synchronized with Lake Gościąż
** duration of YD is uncertain due to uncertain end of YD

Dead Sea

Several new results from the DS during the transition from the Last Glacial into the Holocene (~17-11 ka BP) were presented and discussed in chapter 5. Climatic and environmental reconstructions are provided at (sub-) annual resolution from two sites recording sediment deposition processes in a shallow- (MAS) and deep-water (ICDP core) environment. The investigation of this time interval was motivated by several aspects: (1) the exact dynamics and duration of the aragonite varve interval between the Upper Gypsum and Additional Gypsum Units (UGU and AGU, respectively) were unknown so far. Therefore, one key aspect of this study was the microfacies analyses and microscopic varve counting between the UGU and AGU at Masada and in the ICDP core. (2) The recovery of (quasi-) continuous sediment cores from the deep DS basin during the ICDP DSDDP (Neugebauer et al. 2014) enabled for the first time the investigation of the complete transition from the Last Glacial into the Holocene including the Younger Dryas. In previous studies of marginal lake sediments (e.g. Yechieli et al. 1993; Haase-Schramm et al. 2004; Stein et al. 2010; Torfstein et al. 2013a) this transition was marked by a hiatus related to the huge lateglacial lake level drop. (3) The first microscopic analyses of gypsum deposits in the Dead Sea were performed, because the gypsum units at exposed sites are typically too hard and brittle.

Similar to recent studies (Neugebauer et al. 2015, 2016; Palchan et al. 2017; Ben Dor et al. 2019), a combination of thin section analyses, XRF core scanning, and µ-XRF mapping was applied for an enhanced understanding of the sedimentation processes related to changing lake levels and precipitation systems.

The more objective XRF analyses thereby also validate the thin section data, while through 2D µ-XRF mapping the elemental sediment composition can be directly compared to the thin section data.

The previous correlation of the UGU and AGU (Torfstein et al. 2015; Goldstein et al. 2020) was updated in chapter 5 based on high-resolution microfacies analyses. In general, the lateglacial DS sediments are heterogeneous, comprising evaporitic aragonite varves, gypsum, and often erosive event layers, labelled as 'mass transport deposits' (MTDs). Erosive MTDs are frequent in the deep lake, which is why the construction of a continuous floating varve chronology was solely possible at Masada, where the influence of MTDs was minimal. However, by means of varve counting of individual varved packages in the deep lake, time series were established that allowed the investigation of the frequency of inter-annual MTD deposition, and hydroclimatically-driven temporal changes in the (micro-) facies similar to recent studies (e.g. Neugebauer et al. 2015; Ahlborn et al. 2018; Ben Dor et al. 2018).

A similar amount of varves were counted between UGU and AGU at both sites indicating nearly one millennium of prolonged relatively stable high or rising lake levels due to higher freshwater influx. At the end of this period, deposition of gypsum in aragonite varves and few separate gypsum laminae is a first indicator for a lake level decline. Within the UGU and AGU, varve counting of varved sequences that alternate with gypsum beds suggests decadal- to centennial-long fluctuations in lake level around the threshold for gypsum formation. This shows that these periods were not continuously dry, but interrupted by wetter phases. Further, MTDs are thinner, less erosive and their intercalation is less frequent in the millennium between UGU and AGU than within the gypsum units, indicating that the wetter phase was also more stable. Yet, even within the gypsum units, phases of up to ~40 uninterrupted aragonite varves suggest decadal-long stable intervals. MTDs in the DS can be triggered by earthquakes (e.g. Marco et al. 1996; Kagan et al. 2018), runoff (e.g. Neugebauer et al. 2015; Ahlborn et al. 2018) or rapid lake level changes (e.g. Haase-Schramm et al. 2004). Phases of instable lake levels are characterized by frequent MTDs (e.g. Haase-Schramm et al. 2004) supporting higher fluctuations in water level during deposition of the gypsum units. One of the key results is also the finding of MTDs and few aragonite varves between the AGU and the halite deposited at the Holocene onset, because this interval was so far absent in the marginal sediments of the DS. Additionally, it could be shown from microfacies analyses that the gypsum facies are different between shallow- and deep-water sites. At both sites, gypsum is mostly deposited in laminae, but in the shallow waters these comprise mostly reworked or diagenetic gypsum alternating with fine-grained detrital pelletal aggregates, while in the deep waters precipitated gypsum alternates with fine-grained detritus or carbonate cement. These characteristics are indicative of the different depositional environments – shallow vs deep water. This study also demonstrated that the combination of thin section

microscopy and especially µ-XRF mapping can greatly advance the understanding of depositional processes and associated variability in hydroclimate.

In agreement with previous studies, the UGU is correlated with H1 (e.g. Bartov et al. 2003; Torfstein et al. 2013b), but one key aspect demonstrated in chapters 4 and 5 is the association of the AGU and underlying aragonite varve interval to the lateglacial stadial and interstadial, respectively, which is for the first time based on exact lithological correlations and on the new tephrochronology, contradicting previous assumptions. Previous dating attributed the AGU to the Bølling/Allerød (B-A; Torfstein et al. 2013a), and the following younger section to the YD (Stein et al. 2010; Torfstein et al. 2013a). However, sediments following the AGU are missing in marginal sites and only in one core a marl sequence, unconformably overlying 21 ± 2 ka BP old sediments, was dated to ~13.2 ka cal. BP (Yechieli et al. 1993; Stein et al. 2010). Therefore, the YD was considered as a wet period thus far (Stein et al. 2010; Torfstein et al. 2013a). The studies in chapter 4 and 5 could however show that (i) the aragonite varve interval between the gypsum units corresponds to the warm B-A, (ii) the AGU was deposited during the cold YD, and (iii) the sediments between the AGU and halite deposit reflect a short period of slightly wetter climate (lake level rise) at the onset of the Holocene, before an abrupt and major lake level drop caused the deposition of halite. Thus, these new results could improve our understanding of the connection between sedimentation processes and abrupt climate fluctuations at the demise of Lake Lisan and its evolution into the hypersaline DS during the Last Glacial-Interglacial transition.

Wet conditions during the B-A in the EM were also reported from Lake Van (e.g. Landmann et al. 1996; Çağatay et al. 2014), Lake Hazar (Eriş et al. 2018; Ön et al. 2018), Yammoûneh paleolake (Develle et al. 2010), and Bekaa Valley (Hajar et al. 2008). Additionally, a dry YD is also reported from several other EM sites: Lake Van (e.g. Landmann et al. 1996; Çağatay et al. 2014), Lake Hazar (Eriş et al. 2018; Ön et al. 2018), Bekaa Valley (Hajar et al. 2008), and Soreq Cave (Bar-Matthews et al. 2003), as well as in an EM composite study including Lake Van, Ghab Valley, and sites in Greece, Western Iran, the Eastern Mediterranean and Arabian Seas (Rossignol-Strick 1995). Solely in Lake Hula, a wet hydroclimate during the YD is suggested, but considering that the record is marked by large dating uncertainties (Rossignol-Strick 1995; Meadows 2005) the temporal correlation should be considered as questionable.

6.1.3. How do varved lake systems in different climate zones respond to hemispheric-scale climate changes (during the same time window)?

During the transition from the Last Glacial to the Holocene several abrupt climate fluctuations (GI-1, GS-1, and H1; Fig. 1-2) (e.g. Sanchez Goñi & Harrison 2010; Rasmussen et al. 2014) occurred that are traced in

different archives throughout the northern hemisphere (e.g. Brauer et al. 1999; Wang et al. 2001; Lea et al. 2003; Rasmussen et al. 2006; Çağatay et al. 2014; Schlolaut et al. 2017). However, depending on the local and regional characteristics, different aspects of these climate changes influence the response at the respective sites. From the individual studies discussed in chapters 2-5 larger conclusions about lake sediment responses to hemispheric-scale abrupt climate changes can be drawn.

When the polar front and atmospheric circulation systems in the northern hemisphere were positioned more southward during the Last Glacial Maximum (LGM; e.g. Enzel et al. 2008; Laîné et al. 2009; Merz et al. 2015) (Fig. 6-1), some ice advances of the Scandinavian Ice Sheet even covered nowadays' location of Lake Gościąż in Europe (Fig. 1-1; Marks et al. 2016). Deglacial ice sheet recession exposed the landscape, leaving behind buried dead ice blocks, from which kettle hole lakes formed after ice melt (Błaszkiewicz et al. 2015). Lake Gościąż developed as such a lake during the late Allerød. Contrastingly, due to its more southern location, the DS region was not covered by ice during the Last Glacial, theoretically enabling climate reconstructions for the complete transition into the Holocene (see discussion in 6.1.2.).

***Figure 6-1**: Schematic map showing positions of polar fronts and westerlies over the North Atlantic, the position of storm tracks over the Eastern Mediterranean (EM), and summer air temperatures and sea surface temperatures (SST) for the northern hemisphere.Topographic map (Arcgis ESRI_Worldmap_Topo) with schematic position of polar fronts, westerlies* (Broecker et al. 1988; Lane et al. 2013; Monegato et al. 2017; Schenk et al. 2018) *and EM storm tracks* (Enzel et al. 2003, 2008) *for the observed time periods. Locations of Lake Gościąż and the Dead Sea are marked by red stars. Simulated July surface air temperature (B) and annual mean SSTs (C) for the YD (~13 ka) (Renssen et al. 2015). (B, C) Circles and squares are proxy-based estimates.*

In general, abrupt climate changes are directly and clearly expressed by changes in sediment deposition in both lake systems. However, in the DS record these facies changes are much more dramatic than in Lake Gościąż (Fig. 6-2). Lake Gościąż forms and preserves varves throughout the complete Lateglacial deposited in the record, while solely the varve composition changes. Contrariwise, in the DS sediment record abrupt changes in authigenic mineralization occur from aragonite varves (higher water levels, wetter hydroclimate (Stein et al. 1997; Ben Dor et al. 2021b)) to gypsum deposition (lower water levels, drier hydroclimate (Stein et al. 1997; Torfstein et al. 2008)) and vice versa during climatic transition zones. Additionally, extreme event layers occur only once in the lateglacial sediments of Lake Gościąż, but repeatedly interrupt the record in the DS, where they are often erosive and change in frequency during the different time periods (see 6.1.2.). Therefore, a detailed study of leads and lags of proxy responses during the transition zones of abrupt climate changes is solely possible at Lake Gościąż, which was shown in chapter 3. On the other hand, the sediment record of the DS covers a longer time span and lake system responses to several abrupt lateglacial climate changes can be investigated, as demonstrated in chapter 5. A direct comparison of the different lake responses to the major and abrupt lateglacial climate changes is only possible since the late Allerød – the time of the onset of varve formation in Lake Gościąż.

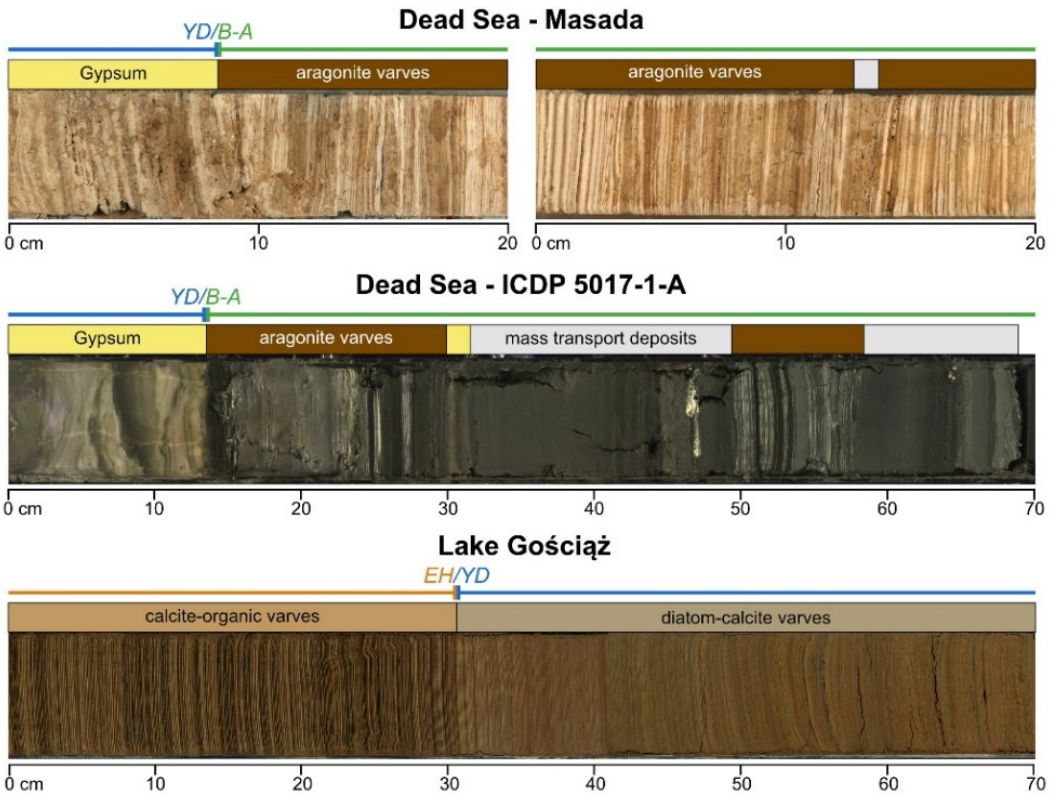

***Figure 6-2**: Different lithologies at both Dead Sea sites and Lake Gościąż. Younger Dryas/Bølling-Allerød (YD/B-A) and Early Holocene/Younger Dryas (EH/YD) boundaries are marked.*

Following the warming and ice sheet melting after the LGM, the lateglacial interstadial (B-A in Europe: e.g. Brauer et al. 1999; GI-1 in Greenland: e.g. Rasmussen et al. 2006) was characterized by general warming and a northward movement of the polar front and associated storm tracks (Fig. 6-1; e.g. Broecker et al. 1988; Schenk et al. 2018). However, this change in atmospheric circulation impacted the two study sites differently. At Lake Gościąż, weaker winds due to the more northward position of storm tracks led to low wind-induced water circulation and wave activity, while denser forest catchment vegetation due to rising temperatures further sheltered the lake from wind-induced mixing. The varved sediments thus showed low aquatic bioproductivity and re-suspension, but high anoxic bottom water conditions associated with calm and stable stratification with mostly meromictic conditions. On the other hand, the Dead Sea was mainly indirectly affected by the northward movement of the polar front leading to abrupt warming of the Mediterranean SST after Heinrich event 1, enhancing the winter air-water-temperature gradient in the Mediterranean and thus cyclogenesis, which led to higher precipitation in its catchment (Torfstein et al. 2013b). Accordingly, water levels rose in the terminal lake, leading to the onset of aragonite varve formation under stable meromictic conditions. While the transition zones are marked by abrupt changes in facies (from gypsum to aragonite varves and vice versa), still small-scale facies changes at the beginning (more frequent MTDs) and end of the period (gypsum-bearing aragonite varves) are observed that indicate changing lake levels. Besides, the occurrence of less frequent and mostly thinner MTDs further suggests prolonged stable conditions in the lake, similar to Lake Gościąż, even when the sediment deposition processes are largely different.

Abrupt cooling during the lateglacial stadial (YD in Europe: e.g. Brauer et al. 1999; GS-1 in Greenland: e.g. Rasmussen et al. 2006) caused a southward shift of the polar front and storm tracks (Fig. 6-1; e.g. Broecker et al. 1988; Brauer et al. 2008; Bakke et al. 2009). In Lake Gościąż, stronger westerly winds caused enhanced water circulation and wave activity (expressed by higher re-suspension, aquatic bioproductivity, and oxygenated bottom waters), whereas sparser forest catchment vegetation provided less lake sheltering and facilitated detrital input. Internal lake conditions were generally dynamic. As also discussed in chapter 5 and in 6.1.2., the study of the lateglacial DS could for the first time show a good lithology-based association with the YD in the DS sediment record: the YD is linked with the AGU, the last gypsum unit of the glacial DS. Gypsum units of the Last Glacial represent drying periods (Torfstein et al. 2008) and have been linked with Heinrich events (e.g. Bartov et al. 2003; Torfstein et al. 2013b). Therefore, it seems plausible to assume that the YD gypsum deposition was caused by the same mechanisms as gypsum deposition during Heinrich events. During Heinrich events (and the YD), the SST of the Atlantic and Mediterranean drops abruptly (Fig. 6-1C), while cold air further reinforces the cooling (Fig. 6-1B), which

leads to a weakened air-water-thermal gradient over the Mediterranean reducing cyclogenesis and thus precipitation in the DS catchment (Bartov et al. 2003; Torfstein et al. 2013b). UGU (H1) and AGU (YD) are further characterized by many and thick MTDs, as well as by intercalated phases of aragonite varves, suggesting high fluctuations in lake level during this time interval (see 6.1.2.), and thus similar dynamic conditions during the YD as in Lake Gościąż.

Northward movement of the polar front and storm tracks at the Holocene onset (Fig. 6-1; e.g. Broecker et al. 1988; Enzel et al. 2008; Lane et al. 2013) is marked in the lake sites by less wind-induced water circulation (Lake Gościąż) and a major drop in lake level (DS). In Lake Gościąż, similar stable and calm lake conditions as during the Allerød develop, marked by low aquatic bioproductivity, high anoxic bottom water conditions and low detrital input due to the weaker winds and catchment reforestation. In the DS record, the age for this section is not well-constrained, but either during the late YD or during the transition to the Holocene, a short rise in lake level is documented. Very tentatively, this might be due to similar causes as the lake level rise during the B-A following the abrupt H1 cooling. However, the consistent northward movement of storm tracks drastically reduces the intensity and frequency of EM cyclones and thus of precipitation at the DS (e.g. Enzel et al. 2003, 2008). Therefore, the lake level drops abruptly leading to the deposition of halite in the DS basin, and marking the onset of the Holocene.

In general, the study of Lake Gościąż showed that the lake system mainly responded between spring and autumn to the influence of westerly winds directly, and to temperature-induced changes in catchment vegetation during the abrupt climate changes of the Lateglacial. On the other hand, the Lateglacial lake system responses to abrupt climate changes in the Dead Sea are primarily influenced by winter precipitation changes in its catchment. These are caused by changes in cyclogenesis in the Mediterranean, which in turn are influenced by temperature changes. Thus, both lake systems respond to different aspects / climate elements of abrupt climate changes (seasons, wind, temperature), but still show similar characteristics (e.g. calmer and more stable conditions during the B-A), even when the sedimentation processes are very different. This further highlights the importance of the understanding of the studied lake system for climate and environmental reconstructions.

6.2. Future perspectives

The sediment records of Lake Gościąż and the Dead Sea provide numerous opportunities for further paleoclimatic and paleoenvironmental reconstructions, as well as investigations of sedimentation processes. In the following, ongoing work with the participation of the doctoral candidate is outlined.

Chronologies

Cryptotephrochronology has been proven as a valuable tool to synchronize different terrestrial, marine, and ice core records (e.g. Wulf et al. 2008, 2013, 2016; Lane et al. 2011; Neugebauer et al. 2017; chapter 4). Unfortunately, conclusive cryptotephra glass shards have not been found at Lake Gościąż thus far (Appendix A2). To allow for better synchronization with other sites, the search will be expanded. In the DS record, this doctoral thesis could show that cryptotephra glass shards occur abundantly in the lateglacial ICDP core and can greatly improve the DS chronology, which is required for a substantiated correlation with climate fluctuations and other archives (chapter 4 and 5). However, older lateglacial sediments (~14-17 ka) were not investigated so far and will be subject to more cryptotephra search to further improve the chronology, including the timing and duration of the Upper Gypsum Unit (Müller et al. forthcoming), which thus far is solely based on ^{14}C- and U/Th-ages in the deep core (Torfstein et al. 2015; Kitagawa et al. 2017).

In earlier studies, the Lisan Formation below the UGU at Masada was dated by radiocarbon (Prasad et al. 2004) and U/Th-dating (Torfstein et al. 2013a). However, between the UGU and AGU at Masada no terrestrial macro-remains or cryptotephra glass shards have been found. This is probably due to the dry nature of the sediments and exposed position of this section at the top of the Lisan Formation, favouring weathering and erosion processes. Thus, radiocarbon dating of pollen samples (e.g. Dinies et al. 2015) could prove useful for the sediments at Masada to further improve the chronology.

Stable isotopes

Stable oxygen ($\delta^{18}O_{carb}$) and carbon ($\delta^{13}C_{carb}$) isotopes have been measured in the previous study of Lake Gościąż from the beginning of lamination until ~1200 BP with low resolution during the Holocene (every 50 years; Ralska-Jasiewiczowa et al. 1998b). Yet, a direct and detailed comparison of stable isotope data with the seasonally-resolved varve microfacies requires (i) a higher resolution of isotopes during the Holocene to detect even small-scale changes, and (ii) analyses performed on the same composite profile and chronology. Therefore, in the new composite profile GOS18 (chapters 2 and 3) stable oxygen ($\delta^{18}O_{carb}$) and carbon isotopes ($\delta^{13}C_{carb}$) were thus far measured between 1897 and ~1150 cm composite depth (ca 12,830-5750 BP; Fig. A3-1; methods for $\delta^{13}C_{carb}$ are the same as for $\delta^{18}O_{carb}$, see 1.6.4). Preliminary results show that the new curves resemble previous ones (Ralska-Jasiewiczowa et al. 1998b), which shows that also during the Holocene the records are not influenced by local effects and are representative for the lake. Further preliminary results are described in Appendix A3. Measurements of stable isotopes until the top of the profile could provide insights into the environmental and hydrological development during the Holocene, especially in terms of leads and lags in proxy responses to climatically and non-climatically-

driven changes (see Appendix A3). This would be especially interesting for the last ~1200 years, which were not investigated so far, but which are marked by human impact and global warming.

In the DS, stable oxygen isotopes of aragonite are heavier (ca 4-6 ‰) during the Last Glacial, whereas they are lighter (ca 2-4 ‰) during the Holocene, which was interpreted as a reflection of the source effect during the Last Glacial (Kolodny et al. 2005). The study also suggested that short-term excursions in $\delta^{18}O$ reflect changes in precipitation (i.e. large floods and droughts) during the Last Glacial, and that the more variable $\delta^{13}C$ data record primary bioproductivity, which was higher during the Last Glacial (Kolodny et al. 2005). To investigate these precipitation-driven short-term fluctuations in $\delta^{18}O$ and $\delta^{13}C$ in direct comparison with the sediment composition, aragonite sublayers were sampled in the about one millennium-long phase of elevated lake levels between the UGU and AGU at Masada and in the deep ICDP core. Methods and preliminary results are provided in Appendix A4. Possibly, this could provide another proxy to reconstruct small-scale hydroclimatic fluctuations and identify precursors of larger-scale hydroclimate changes.

Microfacies of gypsum in the Dead Sea

Within the last glacial Lisan Formation, deposition of gypsum occurred throughout the complete Dead Sea basin during arid periods, when the water level drops (Stein et al. 1997; Torfstein et al. 2008). However, the exact dynamics during these arid periods were not investigated so far, because undisturbed sampling for microfacies analyses in the outcrops proved rather difficult due to the brittleness and hardness of the sediments. As described in chapter 5, it was only possible to sample the transition zones of the gypsum units at Masada and the study focused on the varved sediments between UGU and AGU. However, a detailed investigation of the gypsum facies at the onset of both gypsum units (UGU and AGU) and the termination of the UGU could provide insights into small-scale changes in depositional environments and hydrological conditions linked directly to changes in local hydroclimate at the beginning versus the end of a lake level drop. Therefore, thin sections covering the transition into the UGU were also prepared from Masada (Appendix A5).

Due to the huge lake level variations of the DS, the recovery of the ICDP core enabled first investigations of sediments that thus far were absent in marginal shallow-water sites (chapter 5). From the recovered gypsum units in the ICDP core thin sections could be prepared continuously for microfacies analyses. For the first time, it was possible to study the gypsum facies within a gypsum unit continuously and in detail, which is of special interest considering that the laminae could represent an annual cycle (chapter 5). Preliminary results indicate the occurrence of sub-decadal-long alternations between cement-bearing

gypsum laminae and detritus-bearing gypsum laminae, which could be related to small-scale changes in freshwater input, similar to the decadal-long fluctuations in aragonite sublayer thickness described in chapter 5. This would suggest that even from gypsum laminae within gypsum units small-scale hydroclimatic changes could be inferred.

Heinrich event 1 transitions at Masada

Heinrich event 1 (H1) in the North Atlantic represents a pronounced cooling period that led to drying in the Eastern Mediterranean (Bar-Matthews et al. 2003; Develle et al. 2010; Çağatay et al. 2014). In the ICDP core, the transition into the UGU deposited during H1 is marked by a massive mass transport deposit (>2 m). Therefore, this transition can only be investigated in detail at Masada. In previous studies, a varve chronology was established below the UGU (~26.2-17.7 ka; Prasad et al. 2004, 2009) showing that not only Heinrich events, but also small ice-rafting events in the North Atlantic and even decadal- to century-scale decreases in Greenland temperatures correlate with arid intervals in the DS (Prasad et al. 2004). However, the focus for identification of these fluctuations was based on clastic percentages of the detrital sublayer averaged over 20 and 100 years. A detailed seasonally-resolved investigation of the sediments directly underlying the UGU (Appendix A5) would extend the understanding of the processes signifying an oncoming lake level decline. It could be tested, if the higher deposition of gypsum in aragonite varves (see chapter 5) is a general precursor of lake level decline or if it requires a certain lake level low stand (it is assumed that lake levels during the AGU were lower than during the UGU (Stein et al. 2010; Torfstein et al. 2013b)). Thus, a comparison of the onset of these two lake level declines would enhance our understanding of the commencement of these dry periods, including the identification of possible precursors.

The Younger Dryas in the Tobyłka Bay (Lake Gościąż)

This doctoral thesis demonstrated that the sediments of Lake Gościąż are exceptionally well suited to reconstruct climatic and environmental conditions during the Younger Dryas and its transitions due to the continuous and well-preserved varve formation. The studies in chapters 2 and 3 focussed on the composite profile from the deep lake basin, but do not compare deep- with shallow-water environments. However, varve microfacies analyses were also performed in the Tobyłka Bay – the shallow northern bay of Lake Gościąż (Figs. 1-1, 3-1). In the previous studies in the 20th century (Ralska-Jasiewiczowa et al. 1998b), a core gap prevented continuous investigation of the lowermost Tobyłka Bay sediments. From new cores obtained in 2015, a varve chronology (GT) was established and XRF core scanning was applied (preliminary results are provided in Appendix A6). The same criteria for varve counting and varve thickness

measurements as for the GOS varve chronology (chapters 3.3.2. and 3.3.3.) were applied. Varve formation started ca 100 years earlier than in the deep lake centre and by comparing these shallow- and deep-water sediments, further insights into the similarities and differences of climatically-driven sedimentation processes in different lacustrine environments of the same lake system can be provided (Müller et al. forthcoming). Of interest is also the comparison of the same proxies in the different lake settings to better understand the influence of lake morphometry on proxy signals and advance our understanding of their interpretation.

Mass Spectrometry Imaging (MSI) of the Allerød/YD transition in Lake Gościąż

To reconstruct abrupt climate transitions and investigate lead and lag phases in different archives, annually-resolved archives and analytical methods are crucial (e.g. Brauer et al. 2008; Neugebauer et al. 2012; Lane et al. 2013; Rasmussen et al. 2014; Pauly et al. 2018). Varve microfacies investigations at seasonal resolution have been performed at Lake Gościąż using thin section microscopy, XRF core scanning (chapters 2 and 3) and µ-XRF mapping (chapter 3). Another method at seasonal resolution is Mass Spectrometry Imaging (MSI), which detects and visualizes single biomarkers at µm-scale resolution to reconstruct the dynamic environmental responses to climate changes (e.g. Wörmer et al. 2019; Obreht et al. 2020). MSI has been performed for the Allerød/YD transition in Meerfelder Maar supporting a delayed hydrological response to Greenland, but also showing a correlation between the two sites at annual-resolution (Obreht et al. 2020). Application of MSI to the Lake Gościąż sediments during the Allerød/YD transition would further enhance the understanding of this abrupt onset of climate cooling in central Europe, especially in regard to leads and lags in proxy responses (chapter 3), and enable a direct comparison with Meerfelder Maar and Greenland (Obreht et al. forthcoming).

Bibliography

Adrian, R., Hessen, D. O., Blenckner, T., Hillebrand, H., Hilt, S., Jeppesen, E., Livingstone, D. M. & Trolle, D. 2016: Environmental Impacts—Lake Ecosystems. *In* Quante, M. & Colijn, F. (eds.): *North Sea Region Climate Change Assessment*, 315–340. Springer Nature.

Adrian, R., O'Reilly, C. M., Zagarese, H., Baines, S. B., Hessen, D. O., Keller, W., Livingstone, D. M., Sommaruga, R., Straile, D., Van Donk, E., Weyhenmeyer, G. A. & Winder, M. 2009: Lakes as sentinels of climate change. *Limnology and Oceanography 54*, 2283–2297.

Ahlborn, M., Armon, M., Ben Dor, Y., Neugebauer, I., Schwab, M. J., Tjallingii, R., Shoqeir, J. H., Morin, E., Enzel, Y. & Brauer, A. 2018: Increased frequency of torrential rainstorms during a regional late Holocene eastern Mediterranean drought. *Quaternary Research (United States) 89*, 425–431.

Andersson, G. 1896: Svenska växtvärldens historia. *Geologiska Foereningan i Stockholm. Foerhandlingar 18*, 171–172.

Armon, M., Morin, E. & Enzel, Y. 2019: Overview of modern atmospheric patterns controlling rainfall and floods into the Dead Sea: Implications for the lake's sedimentology and paleohydrology. *Quaternary Science Reviews 216*, 58–73.

Bachmann, O., Schoene, B., Schnyder, C. & Spikings, R. 2010: The 40Ar/39Ar and U/Pb dating of young rhyolites in the Kos-Nisyros volcanic complex, Eastern Aegean Arc, Greece: Age discordance due to excess 40Ar in biotite. *Geochemistry, Geophysics, Geosystems 11*, Q0AA08.

Bakke, J., Lie, Ø., Heegaard, E., Dokken, T., Haug, G. H., Birks, H. H., Dulski, P. & Nilsen, T. 2009: Rapid oceanic and atmospheric changes during the Younger Dryas cold period. *Nature Geoscience 2*, 202–205.

Bar-Matthews, M., Ayalon, A., Gilmour, M., Matthews, A. & Hawkesworth, C. J. 2003: Sea - land oxygen isotopic relationships from planktonic foraminifera and speleothems in the Eastern Mediterranean region and their implication for paleorainfall during interglacial intervals. *Geochimica et Cosmochimica Acta 67*, 3181–3199.

Bar-Matthews, M., Ayalon, A. & Kaufman, A. 1997: Late Quaternary Paleoclimate in the Eastern Mediterranean Region from Stable Isotope Analysis of Speleothems at Soreq Cave, Israel. *Quaternary Research 47*, 155–168.

Bar-Matthews, M., Ayalon, A., Kaufman, A. & Wasserburg, G. J. 1999: The Eastern Mediterranean paleoclimate as a reflection of regional events: Soreq cave, Israel. *Earth and Planetary Science Letters 166*, 85–95.

Bard, E., Hamelin, B., Arnold, M., Montaggioni, L., Cabioch, G., Faure, G. & Rougerie, F. 1996: Deglacial sea-level record from Tahiti corals and the timing of global meltwater discharge. *Nature 382*, 241–244.

Bartczak, A., Słowińska, S., Tyszkowski, S., Kramkowski, M., Kaczmarek, H., Kordowski, J. & Słowiński, M. 2019: Ecohydrological changes and resilience of a shallow lake ecosystem under intense human pressure and recent climate change. *Water (Switzerland) 11*, 32.

Bartolomé, M., Moreno, A., Sancho, C., Stoll, H. M., Cacho, I., Spötl, C., Belmonte, Á., Edwards, R. L., Cheng, H. & Hellstrom, J. C. 2015: Hydrological change in Southern Europe responding to increasing North Atlantic overturning during Greenland Stadial 1. *PNAS 112*, 6568–6572.

Bartov, Y., Goldstein, S. L., Stein, M. & Enzel, Y. 2003: Catastrophic arid episodes in the Eastern Mediterranean linked with the North Atlantic Heinrich events. *Geology 31*, 439–442.

Bartov, Y., Stein, M., Enzel, Y., Agnon, A. & Reches, Z. 2002: Lake levels and sequence stratigraphy of Lake Lisan, the late Pleistocene precursor of the Dead Sea. *Quaternary Research 57*, 9–21.

Beck, H. E., Zimmermann, N. E., McVicar, T. R., Vergopolan, N., Berg, A. & Wood, E. F. 2018: Present and future Köppen-Geiger climate classification maps at 1-km resolution. *Scientific Data 5*, 1–12.

Begin, Z. B., Ehrlich, A. & Nathan, Y. 1974: *Lake Lisan: the Pleistocene Precursor of the Dead Sea*. 45 pp. Ministry of Commerce and Industry, Geological Survey of Israel, Jerusalem.

Begin, Z. B., Nathan, Y. & Ehrlich, A. 1980: Stratigraphy and facies distribution in the Lisan Formation—new evidence from the area south of the Dead Sea, Israel. *Israel Journal of Earth Sciences 29*, 182–189.

Beit-Arieh, I. 1997: The Dead Sea Region: an archaeological perspective. *In* Niemi, T. M. Ben-Avraham, Z. & Gat, J. R. (eds.): *The Dead Sea. The Lake and Its Setting*, 249–251. Oxford University Press, Inc., New York.

Ben-Avraham, Z., Lazar, M., Garfunkel, Z., Reshef, M., Ginzburg, A., Rotstein, Y., Frieslander, U., Bartov, Y. & Shulman, H. 2012: Structural styles along the Dead Sea Fault. *In* Roberts, D. G. & Bally, A. W. (eds.): *Regional Geology and Tectonics: Phanerozoic Passive Margins, Cratonic Basins and Global Tectonic Maps*, 616–633. Elsevier B.V.

Ben-Avraham, Z., Niemi, T. M., Heim, C., Negendank, J. & Nur, A. 1999: Holocene stratigraphy of the Dead Sea: Correlation of high-resolution seismic reflection profiles to sediment cores. *Journal of Geophysical Research: Solid Earth 104*, 17617–17625.

Ben Dor, Y., Armon, M., Ahlborn, M., Morin, E., Erel, Y., Brauer, A., Schwab, M. J., Tjallingii, R. & Enzel, Y. 2018: Changing flood frequencies under opposing late Pleistocene eastern Mediterranean climates. *Scientific Reports 8*, 1–10.

Ben Dor, Y., Flax, T., Levitan, I., Enzel, Y., Brauer, A. & Erel, Y. 2021a: The paleohydrological implications of aragonite precipitation under contrasting climates in the endorheic Dead Sea and its precursors revealed by experimental investigations. *Chemical Geology 576*, 120261.

Ben Dor, Y., Marra, F., Armon, M., Enzel, Y., Brauer, A., Schwab, M. J. & Morin, E. 2021b: Hydroclimatic variability of opposing Late Pleistocene climates in the Levant revealed by deep Dead Sea sediments. *Climate of The Past 17*, 2653–2677.

Ben Dor, Y., Neugebauer, I., Enzel, Y., Schwab, M. J., Tjallingii, R., Erel, Y. & Brauer, A. 2019: Varves of the Dead Sea sedimentary record. *Quaternary Science Reviews 215*, 173–184.

Bentor, Y. K. 1961: Some geochemical aspects of the Dead Sea and the question of its age. *Geochimica et Cosmochimica Acta 25*, 239–260.

Berglund, B. E. & Ralska-Jasiewiczowa, M. 1986: Handbook of Holocene palaeoecology and palaeohydrology. *Wiley-Interscience. John Wiley & Sons Ltd. Chicester*.

Beug, H.-J. 2004: *Leitfaden der Pollenbestimmung für Mitteleuropa und angrenzende Gebiete (Guide to Pollen Analysis for Central Europe and the Adjacent Areas)*. 542 pp. Friedrich Pfeil, Munich.

Birks, H. H. & Birks, H. J. B. 2014: To what extent did changes in July temperature influence Lateglacial vegetation patterns in NW Europe? *Quaternary Science Reviews 106*, 262–277.

Björck, S. 2007: Younger Dryas Oscillation, Global Evidence. *In* Scott, E. (ed.): *Encyclopedia of Quaternary Science*, 1987–1994. Elsevier.

Björck, S., Bennike, O., Rosén, P., Andresen, C. S., Bohncke, S., Kaas, E. & Conley, D. 2002: Anomalously mild Younger Dryas summer conditions in southern Greenland. *Geology 30*, 427–430.

Björck, S., Kromer, B., Johnsen, S., Bennike, O., Hammarlund, D., Lemdahl, G., Possnert, G., Rasmussen, T. L., Wohlfarth, B., Hammer, C. U. & Spurk, M. 1996: Synchronized Terrestrial-Atmospheric Deglacial Records Around the North Atlantic. *Science 274*, 1155–1160.

Blaauw, M. & Christen, J. A. 2011: Flexible Paleoclimate Age-Depth Models Using an Autoregressive Gamma Process. *Bayesian Analysis 6*, 457–474.

Blanchet, C. L., Osborne, A. H., Tjallingii, R., Ehrmann, W., Friedrich, T., Timmermann, A., Brückmann, W. & Frank, M. 2021: Drivers of river reactivation in North Africa during the last glacial cycle. *Nature Geoscience 14*, 97–103.

Błaszkiewicz, M. 2011: Timing of the final disappearance of permafrost in the central European Lowland, as reconstructed from the evolution of lakes in N Poland. *Geological Quarterly 55*, 361–374.

Błaszkiewicz, M., Piotrowski, J. A., Brauer, A., Gierszewski, P., Kordowski, J., Kramkowski, M., Lamparski, P., Lorenz, S., Noryśkiewicz, A. M., Ott, F., Słowiński, M. & Tyszkowski, S. 2015: Climatic and morphological controls on diachronous postglacial lake and river valley evolution in the area of Last Glaciation, northern Poland. *Quaternary Science Reviews 109*, 13–27.

Blockley, S. P. E., Lane, C. S., Lotter, A. F. & Pollard, A. M. 2007: Evidence for the presence of the Vedde Ash in Central Europe. *Quaternary Science Reviews 26*, 3030–3036.

Blockley, S. P. E., Pyne-O'Donnell, S. D. F., Lowe, J. J., Matthews, I. P., Stone, A., Pollard, A. M., Turney, C. S. M. & Molyneux, E. G. 2005: A new and less destructive laboratory procedure for the physical separation of distal glass tephra shards from sediments. *Quaternary Science Reviews 24*, 1952–1960.

Bonk, A., Kinder, M., Enters, D., Grosjean, M., Meyer-Jacob, C. & Tylmann, W. 2016: Sedimentological and geochemical responses of Lake Żabińskie (north-eastern Poland) to erosion changes during the last millennium. *Journal of Paleolimnology 56*, 239–252.

Bonk, A., Müller, D., Ramisch, A., Kramkowski, M. A., Noryśkiewicz, A. M., Sekudewicz, I., Gąsiorowski, M., Luberda-Durnaś, K., Słowiński, M., Schwab, M., Tjallingii, R., Brauer, A. & Błaszkiewicz, M. 2021: Varve microfacies and chronology from a new sediment record of Lake Gościąż (Poland). *Quaternary Science Reviews 251*, 106715.

Bonk, A., Tylmann, W., Amann, B., Enters, D. & Grosjean, M. 2015a: Modern limnology and varve-formation processes in Lake Żabińskie, northeastern Poland: comprehensive process studies as a key to understand the sediment record. *Journal of Limnology 74*, 358–370.

Bonk, A., Tylmann, W., Goslar, T., Wacnik, A. & Grosjean, M. 2015b: Comparing varve counting and ^{14}C-AMS chronologies in the sediments of lake Żabińskie, Northeastern Poland: Implications for accurate ^{14}C dating of lake sediments. *Geochronometria 42*, 157–171.

Bookman (Ken-Tor), R., Enzel, Y., Agnon, A. & Stein, M. 2004: Late Holocene lake levels of the Dead Sea. *Geological Society of America Bulletin 116*, 555–571.

Borzenkova, I., Zorita, E., Borisova, O., Kalniņa, L., Kisielienė, D., Koff, T., Kuznetsov, D., Lemdahl, G.,

Sapelko, T., Stančikaitė, M. & Subetto, D. 2015: Climate Change During the Holocene (Past 12,000 Years). *In* The BACC II Author Team (ed.): *Second Assessment of Climate Change for the Baltic Sea Basin. Regional Climate Studies*, 25–49. Springer, Cham., Heidelberg.

Botta, F., Dahl-Jensen, D., Rahbek, C., Svensson, A. & Nogués-Bravo, D. 2019: Abrupt Change in Climate and Biotic Systems. *Current Biology 29*, R1045–R1054.

Bourne, A. J., Albert, P. G., Matthews, I. P., Trincardi, F., Wulf, S., Asioli, A., Blockley, S. P. E., Keller, J. & Lowe, J. J. 2015: Tephrochronology of core PRAD 1-2 from the Adriatic Sea: insights into Italian explosive volcanism for the period 200-80 ka. *Quaternary Science Reviews 116*, 28–43.

Bourne, A. J., Lowe, J. J., Trincardi, F., Asioli, A., Blockley, S. P. E., Wulf, S., Matthews, I. P., Piva, A. & Vigliotti, L. 2010: Distal tephra record for the last ca 105,000 years from core PRAD 1-2 in the central Adriatic Sea: implications for marine tephrostratigraphy. *Quaternary Science Reviews 29*, 3079–3094.

Brauer, A. 2004: Annually laminated lake sediments and their palaeoclimatic relevance. *In* Fischer, H. Kumke, T. Lohmann, G. Flöser, G. Miller, H. von Storch, H. & Negendank, J. F. W. (eds.): *The Climate in Historical Times. GKSS School of Environmental Research*, 109–127. Springer, Berlin, Heidelberg.

Brauer, A. & Casanova, J. 2001: Chronology and depositional processes of the laminated sediment record from Lac d'Annecy, French Alps. *Journal of Paleolimnology 25*, 163–177.

Brauer, A., Endres, C., Günter, C., Litt, T., Stebich, M. & Negendank, J. F. W. 1999: High resolution sediment and vegetation responses to Younger Dryas climate change in varved lake sediments from Meerfelder Maar, Germany. *Quaternary Science Reviews 18*, 321–329.

Brauer, A., Haug, G. H., Dulski, P., Sigman, D. M. & Negendank, J. F. W. 2008: An abrupt wind shift in western Europe at the onset of the Younger Dryas cold period. *Nature Geoscience 1*, 520–523.

Broecker, W. S. 1994: Massive iceberg discharges as triggers for global climate change. *Nature 372*, 421–424.

Broecker, W. S. 2006: Geology. Was the Younger Dryas triggered by a flood? *Science (New York, N.Y.) 312*, 1146–1148.

Broecker, W. S., Andree, M., Wolfli, W., Oeschger, H., Bonani, G., Kennett, J. & Peteet, D. 1988: The chronology of the last Deglaciation: Implications to the cause of the Younger Dryas Event. *Paleoceanography 3*, 1–19.

Broecker, W. S., Denton, G. H., Edwards, R. L., Cheng, H., Alley, R. B. & Putnam, A. E. 2010: Putting the Younger Dryas cold event into context. *Quaternary Science Reviews 29*, 1078–1081.

Bronk Ramsey, C., Albert, P. G., Blockley, S. P. E., Hardiman, M., Housley, R. A., Lane, C. S., Lee, S., Matthews, I. P., Smith, V. C. & Lowe, J. J. 2015a: Improved age estimates for key Late Quaternary European tephra horizons in the RESET lattice. *Quaternary Science Reviews 118*, 18–32.

Bronk Ramsey, C., Housley, R. A., Lane, C. S., Smith, V. C. & Pollard, A. M. 2015b: The RESET tephra database and associated analytical tools. *Quaternary Science Reviews 118*, 33–47.

Butz, C., Grosjean, M., Poraj-Górska, A., Enters, D. & Tylmann, W. 2016: Sedimentary Bacteriopheophytin α as an indicator of meromixis in varved lake sediments of Lake Jaczno, north-east Poland, CE 1891–2010. *Global and Planetary Change 144*, 109–118.

Çağatay, M. N., Öğretmen, N., Damci, E., Stockhecke, M., Sancar, Ü., Eriş, K. K. & Özeren, S. 2014: Lake

level and climate records of the last 90 ka from the Northern Basin of Lake Van, eastern Turkey. *Quaternary Science Reviews 104*, 97–116.

Çağatay, M. N., Wulf, S., Sancar, Ü., Özmaral, A., Vidal, L., Henry, P., Appelt, O. & Gasperini, L. 2015: The tephra record from the Sea of Marmara for the last ca. 70 ka and its palaeoceanographic implications. *Marine Geology 361*, 96–110.

Canales, F. A., Gwoździej-Mazur, J., Jadwiszczak, P., Struk-Sokołowska, J., Wartalska, K., Wdowikowski, M. & Kaźmierczak, B. 2020: Long-Term Trends in 20-Day Cumulative Precipitation for Residential Rainwater Harvesting in Poland. *Water 12*, 1932.

Cheddadi, R. & Rossignol-Strick, M. 1995: Eastern Mediterranean Quaternary paleoclimates from pollen and isotope records of marine cores in the Nile Cone Area. *Paleoceanography 10*, 291–300.

Choiński, A., Ptak, M. & Skowron, R. 2014: Trends to changes in ice phenomena in Polish lakes in the years 1951-2010. *Przegląd Geograficzny 86*, 23–40.

Churski, Z. & Marszelewski, W. 1998: Hydrology and sedimentation conditions in Lake Gościąż. *In* Ralska-Jasiewiczowa, M. Goslar, T. Madeyska, T. & Starkel, L. (eds.): *Lake Gościąż, central Poland. A monographic study. Part I*, 39–45. W. Szafer Institute of Botany, Polish Academy of Sciences, Kraków.

Clark, P. U., Shakun, J. D., Baker, P. A., Bartlein, P. J., Brewer, S., Brook, E., Carlson, A. E., Cheng, H., Kaufman, D. S., Lui, Z., Marchitto, T. M., Mix, A. C., Morrill, C., Otto-Bliesner, B. L., Pahnke, K., Russell, J. M., Whitlock, C., Adkins, J. F., Blois, J. L., Clark, J., Colman, S. M., Curry, W. B., Flower, B. P., He, F., Johnson, T. C., Lynch-Stieglitz, J., Markgraf, V., McManus, J., Mitrovica, J. X., Moreno, P. I. & Williams, J. W. 2012: Global climate evolution during the last deglaciation. *PNAS 109*, E1134–E1142.

Çoban, H., Topuz, G., Roden, M. F., Hoang, N. & Schwarz, W. H. 2019: 40Ar-39Ar dating and petrology of monzonite ejecta in tephra from Quaternary Gölcük volcano (Isparta, SW Turkey): tear-related contrasting metasomatic symptoms in extensional mantle-derived magmas. *Lithos 330–331*, 160–176.

Cook, E. R., D'Arrigo, R. D. & Briffa, K. R. 1998: A reconstruction of the North Atlantic Oscillation using tree-ring chronologies from North America and Europe. *The Holocene 8*, 9–17.

Croudace, I. W., Rindby, A. & Rothwell, R. G. 2006: ITRAX: description and evaluation of a new multi-function X-ray core scanner. *In* Rothwell, R. G. (ed.): *New Techniques in Sediment Core Analysis*, 51–63. Geological Society, London, Special Publications 267.

Czymzik, M., Dulski, P., Plessen, B., Von Grafenstein, U., Naumann, R. & Brauer, A. 2010: A 450 year record of spring-summer flood layers in annually laminated sediments from Lake Ammersee (southern Germany). *Water Resources Research 46*, W11528.

Dansgaard, W., Clausen, H. B., Gundestrup, N., Hammer, C. U., Johnsen, S. F., Kristinsdottir, P. M. & Reeh, N. 1982: A new Greenland deep ice core. *Science 218*, 1273–1277.

Dansgaard, W., Johnsen, S. J., Clausen, H. B., Dahl-Jensen, D., Gundestrup, N. S., Hammer, C. U., Hvidberg, C. S., Steffensen, J. P., Sveinbjörnsdóttir, Á. E., Jouzel, J. & Bond, G. C. 1993: Evidence for general instability of past climate from a 250-kyr ice-core record. *Nature 364*, 218–220.

Davies, S. M. 2015: Cryptotephras: The revolution in correlation and precision dating. *Journal of Quaternary Science 30*, 114–130.

Davies, S. M., Abbott, P. M., Pearce, N. J. G., Wastegård, S. & Blockley, S. P. E. 2012: Integrating the INTIMATE records using tephrochronology: rising to the challenge. *Quaternary Science Reviews 36*, 11–27.

Davies, S. M., Wastegård, S. & Wohlfarth, B. 2003: Extending the limits of the Borrobol Tephra to Scandinavia and detection of new early Holocene tephras. *Quaternary Research 59*, 345–352.

Deino, A. L., Orsi, G., de Vita, S. & Piochi, M. 2004: The age of the Neapolitan Yellow Tuff caldera-forming eruption (Campi Flegrei caldera - Italy) assessed by $^{40}Ar/^{39}Ar$ dating method. *Journal of Volcanology and Geothermal Research 133*, 157–170.

Delfino, J. J. & Lee, G. F. 1971: Variation of manganese, dissolved oxygen and related chemical parameters in the bottom waters of Lake Mendota, Wisconsin. *Water Research 5*, 1207–1217.

Denton, G. H., Alley, R. B., Comer, G. C. & Broecker, W. S. 2005: The role of seasonality in abrupt climate change. *Quaternary Science Reviews 24*, 1159–1182.

Denton, G. H., Anderson, R. F., Toggweiler, J. R., Edwards, R. L., Schaefer, J. M. & Putnam, A. E. 2010: The Last Glacial Termination. *Science 328*, 1652–1656.

Develle, A.-L., Gasse, F., Vidal, L., Williamson, D., Demory, F., Van Campo, E., Ghaleb, B. & Thouveny, N. 2011: A 250 ka sedimentary record from a small karstic lake in the Northern Levant (Yammoûneh, Lebanon). Paleoclimatic implications. *Palaeogeography, Palaeoclimatology, Palaeoecology 305*, 10–27.

Develle, A.-L., Herreros, J., Vidal, L., Sursock, A. & Gasse, F. 2010: Controlling factors on a paleo-lake oxygen isotope record (Yammoûneh, Lebanon) since the Last Glacial Maximum. *Quaternary Science Reviews 29*, 865–886.

Develle, A.-L., Williamson, D., Gasse, F. & Walter-Simonnet, A.-V. 2009: Early Holocene volcanic ash fallout in the Yammoûneh lacustrine basin (Lebanon): Tephrochronological implications for the Near East. *Journal of Volcanology and Geothermal Research 186*, 416–425.

Dinies, M., Plessen, B., Neef, R. & Kürschner, H. 2015: When the desert was green: Grassland expansion during the early Holocene in northwestern Arabia. *Quaternary International 382*, 293–302.

Dräger, N., Theuerkauf, M., Szeroczyńska, K., Wulf, S., Tjallingii, R., Plessen, B., Kienel, U. & Brauer, A. 2017: Varve microfacies and varve preservation record of climate change and human impact for the last 6000 years at Lake Tiefer See (NE Germany). *The Holocene 27*, 450–464.

Druitt, T. H., Edwards, L., Mellors, R. M., Pyle, D. M., Sparks, R. S. J., Lanphere, M., Davies, M. & Barreirio, B. 1999: Santorini Volcano. *Geological Society Memoir 19*, 165.

Dulski, P., Brauer, A. & Mangili, C. 2015: Combined µ-XRF and Microfacies Techniques for Lake Sediment Analyses. *In Micro-XRF Studies of Sediment Cores*, 325–349. Springer, Dordrecht.

Dusini, D. S., Foster, D. L., Shore, J. A. & Merry, C. 2009: The effect of Lake Erie Water Level Variations on Sediment Resuspension. *Journal of Great Lakes Research 35*, 1–12.

Enzel, Y., Amit, R., Dayan, U., Crouvi, O., Kahana, R., Ziv, B. & Sharon, D. 2008: The climatic and physiographic controls of the eastern Mediterranean over the late Pleistocene climates in the southern Levant and its neighboring deserts. *Global and Planetary Change 60*, 165–192.

Enzel, Y., Bookman (Ken Tor), R., Sharon, D., Gvirtzman, H., Dayan, U., Ziv, B. & Stein, M. 2003: Late Holocene climates of the Near East deduced from Dead Sea level variations and modern regional

winter rainfall. *Quaternary Research 60*, 263–273.

EPICA community members: Augustin, L., Barbante, C., Barnes, P. R. F., Barnola, J. M., Bigler, M., Castellano, E., Cattani, O., Chappellaz, J., Dahl-Jensen, D., Delmonte, B., Dreyfus, G., Durand, G., Falourd, S., Fischer, H., Flückiger, J., Hansson, M. E., Huybrechts, P., Jugie, G., Johnsen, S. J., Jouzel, J., Kaufmann, P., Kipfstuhl, J., Lambert, F., Lipenkov, V. Y., Littot, G. C., Longinelli, A., Lorrain, R., Maggi, V., Masson-Delmotte, V., Miller, H., Mulvaney, R., Oerlemans, J., Oerter, H., Orombelli, G., Parrenin, F., Peel, D. A., Petit, J. R., Raynaud, D., Ritz, C., Ruth, U., Schwander, J., Siegenthaler, U., Souchez, R., Stauffer, B., Steffensen, J. P., Stenni, B., Stocker, T. F., Tabacco, I. E., Udisti, R., Wal, R. S. W., Broeke, M., Weiss, J., Wilhelms, F., Winther, J. G., Wolff, E. W. & Zucchelli, M. 2004: Eight glacial cycles from an Antarctic ice core. *Nature 429*, 623–628.

Eriş, K. K. 2013: Late Pleistocene-Holocene sedimentary records of climate and lake-level changes in Lake Hazar, eastern Anatolia, Turkey. *Quaternary International 302*, 123–134.

Eriş, K. K., Ön, S. A., Çağatay, M. N., Ülgen, U. B., Ön, Z. B., Gürocak, Z., Nagihan Arslan, T., Akkoca, D. B., Damcı, E., İnceöz, M. & Okan, Ö. Ö. 2018: Late Pleistocene to Holocene paleoenvironmental evolution of Lake Hazar, Eastern Anatolia, Turkey. *Quaternary International 486*, 4–16.

Fabbro, G. N., Druitt, T. H. & Scaillet, S. 2013: Evolution of the crustal magma plumbing system during the build-up to the 22-ka caldera-forming eruption of Santorini (Greece). *Bulletin of Volcanology 75*, 767 (2013).

Fairbanks, R. G. 1989: A 17,000-year glacio-eustatic sea level record: influence of glacial melting rates on the Younger Dryas event and deep-ocean circulation. *Nature 342*, 637–642.

Fairbanks, R. G. & Matthews, R. K. 1978: The Marine Oxygen Isotope Record in Pleistocene Coral, Barbados, West Indies. *Quaternary Research 10*, 181–196.

Federman, A. N. & Carey, S. N. 1980: Electron Microprobe Correlation of Tephra Layers from Eastern Mediterranean Abyssal Sediments and the Island of Santorini. *Quaternary Research 13*, 160–171.

Firestone, R. B., West, A., Kennett, J. P., Becker, L., Bunch, T. E., Revay, Z. S., Schultz, P. H., Belgya, T., Kennett, D. J., Erlandson, J. M., Dickenson, O. J., Goodyear, A. C., Harris, R. S., Howard, G. A., Kloosterman, J. B., Lechler, P., Mayewski, P. A., Montgomery, J., Poreda, R., Darrah, T., Hee, S. S. Q., Smith, A. R., Stich, A., Topping, W., Wittke, J. H. & Wolbach, W. S. 2007: Evidence for an extraterrestrial impact 12,900 years ago that contributed to the megafaunal extinctions and the Younger Dryas cooling. *Proceedings of the National Academy of Sciences 104*, 16016–16021.

Fojutowski, M., Gierszewski, P., Brykała, D., Bonk, A., Błaszkiewicz, M. & Kramkowski, M. 2021: Spatio-temporal differences of sediment accumulation rate in the Lake Gościąż (Central Poland) as a response of meteorological conditions and lake basin morphometry. *Geographical Research Letters 47*, 391–413.

Frisia, S., Borsato, A., Spötl, C., Villa, I. & Cucchi, F. 2005: Climate variability in the SE Alps of Italy over the past 17 000 years reconstructed from a stalagmite record. *Boreas 34*, 445–455.

Gałka, M., Miotk-Szpiganowicz, G., Goslar, T., Jęśko, M., van der Knaap, W. O. & Lamentowicz, M. 2013: Palaeohydrology, fires and vegetation succession in the southern Baltic during the last 7500 years reconstructed from a raised bog based on multi-proxy data. *Palaeogeography, Palaeoclimatology, Palaeoecology 370*, 209–221.

Garfunkel, Z. 1981: Internal structure of the Dead Sea leaky transform (rift) in relation to plate

kinematics. *Tectonophysics 80*, 81–108.

Gasse, F., Vidal, L., Van Campo, E., Demory, F., Develle, A.-L., Tachikawa, K., Elias, A., Bard, E., Garcia, M., Sonzogni, C. & Thouveny, N. 2015: Hydroclimatic changes in northern Levant over the past 400,000 years. *Quaternary Science Reviews 111*, 1–8.

Genty, D., Blamart, D., Ghaleb, B., Plagnes, V., Causse, C., Bakalowicz, M., Zouari, K., Chkir, N., Hellstrom, J., Wainer, K. & Bourges H, F. 2006: Timing and dynamics of the last deglaciation from European and North African d 13 C stalagmite profiles—comparison with Chinese and South Hemisphere stalagmites. *Quaternary Science Reviews 25*, 2118–2142.

Gertman, I. 2012: Dead Sea. *In* Bengtsson, L. Herschy, R. W. & Fairbridge, R. W. (eds.): *Encyclopedia of Lakes and Reservoirs*, Springer, Dordrecht.

Giaccio, B., Hajdas, I., Isaia, R., Deino, A. & Nomade, S. 2017: High-precision ^{14}C and $^{40}Ar/^{39}$ Ar dating of the Campanian Ignimbrite (Y-5) reconciles the time-scales of climatic-cultural processes at 40 ka. *Scientific Reports 7*, 1–10.

Gierszewski, P. 1993: Chemical denudation within the drainage basin of the Ruda River in 1990 hydrological year. *Zeszyty Instytutu Geografii i Przestrzennego Zagospodarowania PAN 12*, 29-45 (in Polish with English summary).

Gierszewski, P. 2000: *Charakterystyka Środowiska Hydrochemicznego Wód Powierzchniowych Zachodniej Części Kotliny Płockiej [in Polish]*. 18–35 pp. Instytut Geografii i Przestrzennego Zagospodarowania PAN im. Stanisława Leszczyckiego, Warszawa.

Giziński, A., Kentzer, A., Mieszczankin, T., Żbikowski, J. & Żytkowicz, R. 1998: Hydrobiological characteristics and modern sedimentation of Lake Gościąż. *In* Ralska-Jasiewiczowa, M. Goslar, T. Madeyska, T. & Starkel, L. (eds.): *Lake Gościąż, central Poland. A monographic study. Part 1*, 49–61. W. Szafer Institute of Botany, Polish Academy of Sciences, Kraków.

Goldstein, S. L., Kiro, Y., Torfstein, A., Kitagawa, H., Tierney, J. & Stein, M. 2020: Revised chronology of the ICDP Dead Sea deep drill core relates drier-wetter-drier climate cycles to insolation over the past 220 kyr. *Quaternary Science Reviews 244*, 1–13.

Goslar, T. 1993: Chronologia warwowa osadu laminowanego jeziora Gościąż [in Polish]. *In* Ralska-Jasiewiczowa, M. (ed.): *Jezioro Gościąż - Stan Badań Nad Osadami Dennymi I Środowiskiem Współczensym. Materiały Spotkania Roboczego W Gliwicach*, 105–119. W. Szafer Institute of Botany, Polish Academy of Sciences, Kraków.

Goslar, T. 1998a: Chronology of the Lake Gościąż sediments. *In* Ralska-Jasiewiszowa, M. Goslar, T. Madeyska, T. & Starkel, L. (eds.): *Lake Gościąż, central Poland. A monographic study. Part I*, 97–115. W. Szafer Institute of Botany, Polish Academy of Sciences, Kraków.

Goslar, T. 1998b: Lake Gościąż: Palaeogeography of the Holocene. *In* Ralska-Jasiewiczowa, M. Goslar, T. Madeyska, T. & Starkel, L. (eds.): *Lake Gościąż, central Poland. A monographic study. Part I*, 187–196. W. Szafer Institute of Botany, Polish Academy of Sciences, Kraków.

Goslar, T. 1998c: Record of laminae thickness of the Lake Gościąż sediments, and its correlation with absolutely dated tree-ring width sequences. *In* Ralska-Jasiewiczowa, M. Goslar, T. Madeyska, T. & Starkel, L. (eds.): *Lake Gościąż, central Poland. A monographic study. Part 1*, 104–110. W. Szafer Institute of Botany, Polish Academy of Sciences, Kraków.

Goslar, T. 1998d: Late-Glacial sediments of Lake Gościąż – chronological background. *In* Ralska-

Jasiewiczowa, M. Goslar, T. Madeyska, T. & Starkel, L. (eds.): *Lake Gościąż, central Poland. A monographic study. Part 1*, 119–124. W. Szafer Institute of Botany, Polish Academy of Sciences, Kraków.

Goslar, T., Arnold, M., Bard, E., Kuc, T., Pazdur, M. F., Ralska-Jasiewiczowa, M., Różański, K., Tisnerat, N., Walanus, A., Wicik, B. & Więckowski, K. 1995: High concentration of atmospheric ^{14}C during the Younger Dryas cold episode. *Nature 377*, 414–417.

Goslar, T., Arnold, M. & Pazdur, M. F. 1998a: Variations of atmospheric ^{14}C concentrations at the Pleistocene/Holocene transition, reconstructed from the Lake Gościąż sediments. *In* Ralska-Jasiewiczowa, M. Goslar, T. Madeyska, T. & Starkel, L. (eds.): *Lake Gościąż, central Poland. A monographic study. Part 1*, 162–171. W. Szafer Institute of Botany, Polish Academy of Sciences, Kraków.

Goslar, T., Arnold, M., Tisnerat-Laborde, N., Czernik, J. & Więckowski, K. 2000: Variations of Younger Dryas atmospheric radiocarbon explicable without ocean circulation changes. *Nature 403*, 877–880.

Goslar, T., Bałaga, K., Arnold, M., Tisnerat, N., Starnawska, E., Kuźniarski, M., Chróst, L., Walanus, A. & Więckowski, K. 1999a: Climate-related variations in the composition of the lateglacial and early Holocene sediments of Lake Perespilno (eastern Poland). *Quaternary Science Reviews 18*, 899–911.

Goslar, T., Kuc, T., Pazdur, M. F., Ralska-Jasiewiczowa, M., Różański, K., Szeroczyńska, K., Walanus, A., Wicik, B., Wieckowski, K., Arnold, M. & Bard, E. 1992: Possibilities for reconstructing radiocarbon level changes during the Late Glacial by using a laminated sequence of Gościąż Lake. *Radiocarbon 34*, 826–832.

Goslar, T., Kuc, T., Ralska-Jasiewiczowa, M., Różański, K., Arnold, M., Bard, E., van Geel, B., Pazdur, M. F., Szeroczyńska, K., Wicik, B., Więckowski, K. & Walanus, A. 1993: High-resolution lacustrine record of the Late Glacial/Holocene transition in Central Europe. *Quaternary Science Reviews 12*, 287–294.

Goslar, T., Pazdur, A., Pazdur, M. F. & Walanus, A. 1989: Radiocarbon and Varve Chronologies of Annually Laminated Lake Sediments of Gościąz Lake, Central Poland. *Radiocarbon 31*, 940–947.

Goslar, T., Ralska-Jasiewiczowa, M., Starkel, L., Demske, D., Kuc, T., Łącka, B., Szeroczyńska, K., Wicik, B. & Więckowski, K. 1998b: Discussion of the Late-Glacial recorded in the Lake Gościąż sediments. *In* Ralska-Jasiewiczowa, M. Goslar, T. Madeyska, T. & Starkel, L. (eds.): *Lake Gościąż, central Poland. A monographic study. Part 1*, 171–175. W. Szafer Institute of Botany, Polish Academy of Sciences, Kraków.

Goslar, T., Wohlfarth, B., Björck, S., Possnert, G. & Björck, J. 1999b: Variations of atmospheric ^{14}C concentrations over the Allerød-Younger Dryas transition. *Climate Dynamics 15*, 29–42.

Gray, L. J., Beer, J., Geller, M., Haigh, J. D., Lockwood, M., Matthes, K., Cubasch, U., Fleitmann, D., Harrison, G., Hood, L., Luterbacher, J., Meehl, G. A., Shindell, D., van Geel, B. & White, W. 2010: Solar influences on climate. *Reviews of Geophysics 48*, 1–53.

Gražulis, S., Chateigner, D., Downs, R. T., Yokochi, A. F. T., Quirós, M., Lutterotti, L., Manakova, E., Butkus, J., Moeck, P. & Le Bail, A. 2009: Crystallography Open Database - An open-access collection of crystal structures. *Journal of Applied Crystallography 42*, 726–729.

Greenbaum, N., Ben-Zvi, A., Haviv, I. & Enzel, Y. 2006: The hydrology and paleohydrology of the Dead Sea tributaries. *Geological Society of America Special Papers 401*, 63–93.

Haase-Schramm, A., Goldstein, S. L. & Stein, M. 2004: U-Th dating of Lake Lisan (late Pleistocene Dead

Sea) aragonite and implications for glacial East Mediterranean climate change. *Geochimica et Cosmochimica Acta 68*, 985–1005.

Hajar, L., Khater, C. & Cheddadi, R. 2008: Vegetation changes during the late Pleistocene and Holocene in Lebanon: a pollen record from the Bekaa Valley. *The Holocene 18*, 1089–1099.

Hajdas, I. 2008: Radiocarbon dating and its applications in Quaternary studies. *E&G Quaternary Science Journal 57*, 2–24.

Haliva-Cohen, A., Stein, M., Goldstein, S. L., Sandler, A. & Starinsky, A. 2012: Sources and transport routes of fine detritus material to the Late Quaternary Dead Sea basin. *Quaternary Science Reviews 50*, 55–70.

Hamann, Y., Wulf, S., Ersoy, O., Ehrmann, W., Aydar, E. & Schmiedl, G. 2010: First evidence of a distal early Holocene ash layer in Eastern Mediterranean deep-sea sediments derived from the Anatolian volcanic province. *Quaternary Research 73*, 497–506.

Hartman, A., Torfstein, A. & Almogi-Labinc, A. 2020: Climate swings in the northern Red Sea over the last 150,000 years from εNd and Mg/Ca of marine sediments. *Quaternary Science Reviews 231*, 106205.

Hartz, N. & Milthers, V. 1901: Det senglaciale ler i Allerød Teglværksgrav. *Meddelelser Dansk Geologisk Foreningen 8*, 31–60.

Havens, K. & Jeppesen, E. 2018: Ecological responses of lakes to climate change. *Water 10*, 917. https://doi.org/10.3390/w10070917.

Hazan, N., Stein, M., Agnon, A., Marco, S., Nadel, D., Negendank, J. F. W., Schwab, M. J. & Neev, D. 2005: The late Quaternary limnological history of Lake Kinneret (Sea of Galilee), Israel. *Quaternary Research 63*, 60–77.

Heikkilä, M. & Seppä, H. 2010: Holocene climate dynamics in Latvia, eastern Baltic region: a pollen-based summer temperature reconstruction and regional comparison. *Boreas 39*, 705–719.

Heim, C., Nowaczyk, N. R., Negendank, J. F. W., Leory, S. A. G. & Ben-Avraham, Z. 1997: Near East Desetification: Evidence from the Dead Sea. *Naturwissenschaften 84*, 398–401.

Heinrich, H. 1988: Origin and consequences of cyclic ice rafting in the Northeast Atlantic Ocean during the past 130,000 years. *Quaternary Research 29*, 142–152.

Hershkovitz, I., Weber, G. W., Quam, R., Duval, M., Grün, R., Kinsley, L., Ayalon, A., Bar-Matthews, M., Valladas, H., Mercier, N., Arsuaga, J. L., Martinón-Torres, M., de Castro, J. M. B., Fornai, C., Martín-Francés, L., Sarig, R., May, H., Krenn, V. A., Slon, V., Rodríguez, L., García, R., Lorenzo, C., Carretero, J. M., Frumkin, A., Shahack-Gross, R., Mayer, D. E. B.-Y., Cui, Y., Wu, X., Peled, N., Groman-Yaroslavski, I., Weissbrod, L., Yeshurun, R., Tsatskin, A., Zaidner, Y. & Weinstein-Evron, M. 2018: The earliest modern humans outside Africa. *Science 359*, 456–459.

Hochman, A., Alpert, P., Kunin, P., Rostkier-Edelstein, D., Harpaz, T., Saaroni, H. & Messori, G. 2020: The dynamics of cyclones in the twentyfirst century: the Eastern Mediterranean as an example. *Climate Dynamics 54*, 561–574.

Hochman, A., Mercogliano, P., Alpert, P., Saaroni, H. & Bucchignani, E. 2018: High-resolution projection of climate change and extremity over Israel using COSMO-CLM. *International Journal of Climatology 38*, 5095–5106.

Hunt, J. B. & Hill, P. G. 1996: Inter-laboratory comparison of electron probe microanalysis of glass

geochemistry. *Quaternary International 34–36*, 229–241.

IPCC 2014: *Climate Change 2014: Synthesis Report. Contribution of Working Groups I, II and III to the Fifth Assessment Report of the Intergovernmental Panel on Climate Change*, IPCC. 151 pp. Geneva, Switzerland.

IPCC 2021: Summary for Policymakers. *In* Masson-Delmotte, V. Zhai, P. Pirani, A. Connors, S. L. Péan, C. Berger, S. Caud, N. Chen, Y. Goldfarb, L. Gomis, M. I. Huang, M. Leitzell, K. Lonnoy, E. Matthews, J. B. R. Maycock, T. K. Waterfield, T. Yelekçi, O. Yu, R. & Zhou, B. (eds.): *Climate Change 2021: The Physical Science Basis. Contribution of Working Group I to the Sixth Assessment Report of the Intergovernmental Panel on Climate Change*, 41. Cambridge University Press. In Press.

Isarin, R. F. B., Renssen, H. & Vandenberghe, J. 1998: The impact of the North Atlantic Ocean on the Younger Dryas climate in northwestern and central Europe. *Journal of Quaternary Science 13*, 447–453.

Jennings, A. E., Hald, M., Smith, M. & Andrews, J. T. 2006: Freshwater forcing from the Greenland Ice Sheet during the Younger Dryas: Evidence from southeastern Greenland shelf cores. *Quaternary Science Reviews 25*, 282–298.

Jochum, K. P., Stoll, B., Herwig, K., Willbold, M., Hofmiann, A. W., Amini, M., Aarburg, S., Abouchami, W., Hellebrand, E., Mocek, B., Raczek, I., Stracke, A., Alard, O., Bouman, C., Becker, S., Dücking, M., Brätz, H., Klemd, R., de Bruin, D., Canil, D., Cornell, D., de Hoog, C.-J., Dalpé, C., Danyushevshy, L., Eisenhauer, A., Gao, Y., Snow, J. E., Groschopf, N., Günther, D., Latkoczy, C., Guillong, M., Hauri, E. H., Höfer, H. E., Lahaye, Y., Horz, K., Jacob, D. E., Kasemann, S. A., Kent, A. J. R., Ludwig, T., Zack, T., Mason, P. R. D., Meixner, A., Rosner, M., Misawa, K., Nash, B. P., Pfänder, J., Premo, W. R., Sun, W. D., Tiepolo, M., Vannucci, R., Vennemann, T., Wayne, D. & Woodhead, J. D. 2006: MPI-DING reference glasses for in situ microanalysis: New reference values for element concentrations and isotope ratios. *Geochemistry, Geophysics, Geosystems 7*, Q02008.

Johnsen, S. J., Clausen, H. B., Dansgaard, W., Fuhrer, K., Gundestrup, N., Hammer, C. U., Iversen, P., Jouzel, J., Stauffer, B. & Steffensen, J. P. 1992: Irregular glacial interstadials recorded in a new Greenland ice core. *Nature 359*, 311–313.

Jouve, G., Francus, P., Lamoureux, S., Provencher-Nolet, L., Hahn, A., Haberzettl, T., Fortin, D. & Nuttin, L. 2013: Microsedimentological characterization using image analysis and µ-XRF as indicators of sedimentary processes and climate changes during Lateglacial at Laguna Potrok Aike, Santa Cruz, Argentina. *Quaternary Science Reviews 71*, 191–204.

Juggins, S. 2007: *C2 Version 1.5 User Guide. Software for Ecological and Palaeoecological Data Analysis and Visualisation*. 73 pp. Newcastle University, Newcastle upon Tyne.

Kagan, E., Stein, M. & Marco, S. 2018: Integrated Paleoseismic Chronology of the Last Glacial Lake Lisan: From Lake Margin Seismites to Deep-Lake Mass Transport Deposits. *Journal of Geophysical Research: Solid Earth 123*, 2806–2824.

Kearney, R., Albert, P. G., Staff, R. A., Pál, I., Veres, D., Magyari, E. & Bronk Ramsey, C. 2018: Ultra-distal fine ash occurrences of the Icelandic Askja-S Plinian eruption deposits in Southern Carpathian lakes: New age constraints on a continental scale tephrostratigraphic marker. *Quaternary Science Reviews 188*, 174–182.

Keller, J., Ryan, W. B. F., Ninkovich, D. & Altherr, R. 1978: Explosive volcanic activity in the Mediterranean over the past 200,000 yr as recorded in deep-sea sediments. *Geological Society of America Bulletin*

89, 591–604.

Kelts, K. & Hsü, K. J. 1978: Freshwater Carbonate Sedimentation. *In* Lerman, A. (ed.): *Lakes. Chemistry, Geology, Physics*, 295–323. Springer, New York.

Kępczyński, K. & Noryśkiewicz, A. 1998: Vegetation of the Gostynińskie Lake District. *In* Ralska-Jasiewiczowa, M. Goslar, T. Madeyska, T. & Starkel, L. (eds.): *Lake Gościąż, central Poland. A monographic study. Part 1*, 29–33. W. Szafer Institute of Botany, Polish Academy of Sciences, Kraków.

Kinder, M., Tylmann, W., Rzeszewski, M. & Zolitschka, B. 2020: Varves and mass-movement deposits record distinctly different sedimentation dynamics since the late glacial (Lake Szurpiły, northeastern Poland). *Quaternary Research (United States) 93*, 299–313.

Kinder, M., Wulf, S. & Appelt, O. 2021: Detection of the historical Askja AD 1875 and modern Icelandic cryptotephras in varved lake sediments – results from a first systematic search in northern Poland. *Journal of Quaternary Science 36*, 1–7.

Kirkland, D. W. 2003: An explanation for the varves of the Castile evaporites (Upper Permian), Texas and New Mexico, USA. *Sedimentology 50*, 899–920.

Kitagawa, H., Stein, M., Goldstein, S. L., Nakamura, T. & Lazar, B. 2017: Radiocarbon Chronology of the DSDDP Core at the Deepest Floor of the Dead Sea. *Radiocarbon 59*, 383–394.

Kolodny, Y., Stein, M. & Machlus, M. 2005: Sea-rain-lake relation in the Last Glacial East Mediterranean revealed by $\delta^{18}O$-$\delta^{13}C$ in Lake Lisan aragonites. *Geochimica et Cosmochimica Acta 69*, 4045–4060.

Kotrys, B., Płóciennik, M., Sydor, P. & Brooks, S. J. 2020: Expanding the Swiss-Norwegian chironomid training set with Polish data. *Boreas 49*, 89–107.

Kruczkowska, B., Błaszkiewicz, M., Jonczak, J., Uzarowicz, Ł., Moska, P., Brauer, A., Bonk, A. & Słowiński, M. 2020: The Late Glacial pedogenesis interrupted by aeolian activity in Central Poland – records from the Lake Gościąż catchment. *Catena 185*, 104286. https://doi.org/10.1016/j.catena.2019.1042.

Kuc, T., Różański, K. & Duliński, M. 1998: Isotopic indicators of the Late-Glacial/Holocene transition recorded in the sediments of Lake Gościąż. *In* Ralska-Jasiewiczowa, M. Goslar, T. Madeyska, T. & Starkel, L. (eds.): *Lake Gościąż, central Poland. A monographic study. Part 1*, 158–162. W. Szafer Institute of Botany, Polish Academy of Sciences, Kraków.

Kuehn, S. C., Froese, D. G., Shane, P. A. R. & INTAV Intercomparison Participants 2011: The INTAV intercomparison of electron-beam microanalysis of glass by tephrochronology laboratories: Results and recommendations. *Quaternary International 246*, 19–47.

Kuzucuoglu, C., Pastre, J.-F., Black, S., Ercan, T., Fontugne, M., Guillou, H., Hatté, C., Karabiyikoglu, M., Orth, P. & Türkecan, A. 1998: Identification and dating of tephra layers from Quaternary sedimentary sequences of Inner Anatolia, Turkey. *Journal of Volcanology and Geothermal Research 85*, 153–172.

Kwiecien, O., Arz, H. W., Lamy, F., Wulf, S., Bahr, A., Röhl, U. & Haug, G. H. 2008: Estimated reservoir ages of the Black Sea since the Last Glacial. *Radiocarbon 50*, 99–118.

Łącka, B., Starnawska, E., Kuźniarski, M. & Chróst, L. 1998: Mineralogy and geochemistry of the Lake Gosciaz Holocene sediments. *In* Ralska-Jasiewiczowa, M. Goslar, T. Madeyska, T. & Starkel, L. (eds.):

Lake Gościąż, central Poland. A monographic study. Part I, 196–202. W. Szafer Institute of Botany, Polish Academy of Sciences, Kraków.

Laîné, A., Kageyama, M., Salas-Mélia, D., Voldoire, A., Rivière, G., Ramstein, G., Planton, S., Tyteca, S. & Peterschmitt, J. Y. 2009: Northern hemisphere storm tracks during the last glacial maximum in the PMIP2 ocean-atmosphere coupled models: energetic study, seasonal cycle, precipitation. *Climate Dynamics 32*, 593–614.

Lamy, F., Arz, H. W., Bond, G. C., Bahr, A. & Pätzold, J. 2006: Multicentennial-scale hydrological changes in the Black Sea and northern Red Sea during the Holocene and the Arctic/North Atlantic Oscillation. *Paleoceanography 21*, 1–11.

Landmann, G., Reimer, A., Lemcke, G. & Kempe, S. 1996: Dating Late Glacial abrupt climate changes in the 14,570 yr long continuous varve record of Lake Van, Turkey. *Palaeogeography, Palaeoclimatology, Palaeoecology 122*, 107–118.

Lane, C. S., Blockley, S. P. E., Bronk Ramsey, C. & Lotter, A. F. 2011: Tephrochronology and absolute centennial scale synchronisation of European and Greenland records for the last glacial to interglacial transition: A case study of Soppensee and NGRIP. *Quaternary International 246*, 145–156.

Lane, C. S., Brauer, A., Blockley, S. P. E. & Dulski, P. 2013: Volcanic ash reveals time-transgressive abrupt climate change during the Younger Dryas. *Geology 41*, 1251–1254.

Lane, C. S., Cullen, V. L., White, D., Bramham-Law, C. W. F. & Smith, V. C. 2014: Cryptotephra as a dating and correlation tool in archaeology. *Journal of Archaeological Science 42*, 42–50.

Lane, C. S., Lowe, D. J., Blockley, S. P. E., Suzuki, T. & Smith, V. C. 2017: Advancing tephrochronology as a global dating tool: Applications in volcanology, archaeology, and palaeoclimatic research. *Quaternary Geochronology 40*, 1–7.

Langgut, D. 2018: Late Quaternary Nile flows as recorded in the Levantine Basin: The palynological evidence. *Quaternary International 464*, 273–284.

Lauterbach, S., Brauer, A., Andersen, N., Danielopol, D. L., Dulski, P., Hüls, M., Milecka, K., Namiotko, T., Obremska, M. & von Grafenstein, U. 2011a: Environmental responses to Lateglacial climatic fluctuations recorded in the sediments of pre-Alpine Lake Mondsee (northeastern Alps). *Journal of Quaternary Science 26*, 253–267.

Lauterbach, S., Brauer, A., Andersen, N., Danielopol, D. L., Dulski, P., Hüls, M., Milecka, K., Namiotko, T., Plessen, B., Grafenstein, U. Von & Participants, D. 2011b: Multi-proxy evidence for early to mid-Holocene environmental and climatic changes in northeastern Poland. *Boreas 40*, 57–72.

Lea, D. W., Pak, D. K., Peterson, L. C. & Hughen, K. A. 2003: Synchroneity of tropical and high-latitude Atlantic temperatures over the last glacial termination. *Science (New York, N.Y.) 301*, 1361–1364.

Lencewicz, S. 1929: Jeziora Gostynińskie [in Polish]. *Przegląd Geograficzny* 9.

Leng, M. J. 2006: *Isotopes in Palaeoenvironmental Research*. 307 pp. Springer, Dordrecht.

Lensky, N. G., Dvorkin, Y., Lyakhovsky, V., Gertman, I. & Gavrieli, I. 2005: Water, salt, and energy balances of the Dead Sea. *Water Resources Research 41*, 1–13.

Limburg, E. M. & Varekamp, J. C. 1991: Young pumice deposits on Nisyros, Greece. *Bulletin of Volcanology 54*, 68–77.

Lind, E. M. & Wastegård, S. 2011: Tephra horizons contemporary with short early Holocene climate fluctuations: New results from the Faroe Islands. *Quaternary International 246*, 157–167.

Lisiecki, L. E. & Raymo, M. E. 2005: A Pliocene-Pleistocene stack of 57 globally distributed benthic $\delta^{18}O$ records. *Paleoceanography 20*, 1–17.

Litt, T., Brauer, A., Goslar, T., Merkt, J., Bałaga, K., Müller, H., Ralska-Jasiewiczowa, M., Stebich, M. & Negendank, J. F. W. 2001: Correlation and synchronisation of Lateglacial continental sequences in northern central Europe based on annually laminated lacustrine sediments. *Quaternary Science Reviews 20*, 1233–1249.

Locke, S. & Thunell, R. C. 1988: Paleoceanographic record of the Last Glacial/Interglacial cycle in the Red Sea and Gulf of Aden. *Palaeogeography, Palaeoclimatology, Palaeoecology 64*, 163–187.

Lotter, A. F. 1991: How long was the Younger Dryas? Preliminary evidence from annually laminated sediments of Soppensee (Switzerland). *Hydrobiologia 214*, 53–57.

Lotter, A. F. & Anderson, N. J. 2012: Limnological Responses to Environmental Changes at Inter-annual to Decadal Time-Scales. *In* Birks, H. J. B. Lotter, A. F. Juggins, S. & Smol, J. P. (eds.): *Tracking Environmental Change Using Lake Sediments. Data Handling and Numerical Techniques*, 557–578. Springer Dordrecht Heidelberg New York London.

Lotter, A. F. & Lemcke, G. 1999: Methods for preparing and counting biochemical varves. *Boreas 28*, 243–252.

Lougheed, B. C. & Obrochta, S. P. 2016: MatCal : Open Source Bayesian ^{14}C Age Calibration in Matlab. *Journal of Open Research Software 4*, e42.

Lowe, D. J. 2011: Tephrochronology and its application: A review. *Quaternary Geochronology 6*, 107–153.

Lowe, J. J., Ramsey, C. B., Housley, R. A., Lane, C. S., Tomlinson, E. L., RESET Team & RESET Associates 2015: The RESET project: constructing a European tephra lattice for refined synchronisation of environmental and archaeological events during the last c. 100 ka. *Quaternary Science Reviews 118*, 1–17.

Lücke, A. & Brauer, A. 2004: Biogeochemical and micro-facial fingerprints of ecosystem response to rapid Late Glacial climatic changes in varved sediments of Meerfelder Maar (Germany). *Palaeogeography, Palaeoclimatology, Palaeoecology 211*, 139–155.

Lücke, A., Schleser, G. H., Zolitschka, B. & Negendank, J. F. W. 2003: A Lateglacial and Holocene organic carbon isotope record of lacustrine palaeoproductivity and climatic change derived from varved lake sediments of Lake Holzmaar, Germany. *Quaternary Science Reviews 22*, 569–580.

Luoto, T. P., Kotrys, B. & Płóciennik, M. 2019: East European chironomid-based calibration model for past summer temperature reconstructions. *Climate Research 77*, 63–76.

MacAyeal, D. R. 1993: Binge/purge oscillations of the Laurentide Ice Sheet as a cause of the North Atlantic's Heinrich events. *Paleoceanography 8*, 775–784.

Machlus, M., Enzel, Y., Goldstein, S. L., Marco, S. & Stein, M. 2000: Reconstructing low levels of Lake Lisan by correlating fan-delta and lacustrine deposits. *Quaternary International 73–74*, 137–144.

Magee, J. W. 1991: Late Quaternary lacustrine, groundwater, aeolian and pedogenic gypsum in the Prungle Lakes, southeastern Australia. *Palaeogeography, Palaeoclimatology, Palaeoecology 84*, 3–42.

Magny, M., Guiot, J. & Schoellammer, P. 2001: Quantitative reconstruction of Younger Dryas to Mid-Holocene paleoclimates at Le Locle, Swiss Jura, using pollen and lake-level data. *Quaternary Research 56*, 170–180.

Maher, L. A., Richter, T. & Stock, J. T. 2012: The Pre-Natufian Epipaleolithic: Long-Term Behavioral Trends in the Levant. *Evolutionary Anthropology 21*, 69–81.

Mangerud, J., Andersen, S. T., Berglund, B. E. & Donner, J. J. 1974: Quaternary stratigraphy of Norden, a proposal for terminology and classification. *Boreas 3*, 109–126.

Marciniak, B. & Szeroczyńska, K. 1998: Development of the Lake Gościąż biota during the Late-Glacial. *In* Ralska-Jasiewiczowa, M. Goslar, T. Madeyska, T. & Starkel, L. (eds.): *Lake Gościąż, central Poland. A monographic study. Part 1*, 143–158. W. Szafer Institute of Botany, Polish Academy of Sciences, Kraków.

Marco, S., Stein, M. & Agnon, A. 1996: Long-term earthquake clustering: A 50,000-year paleoseismic record in the Dead Sea Graben. *Journal of Geophysical Research 101*, 6179–6191.

Marcott, S. a, Clark, P. U., Padman, L., Klinkhammer, G. P., Springer, S. R., Liu, Z., Otto-Bliesner, B. L., Carlson, A. E., Ungerer, A., Padman, J., He, F., Cheng, J. & Schmittner, A. 2011: Ice-shelf collapse from subsurface warming as a trigger for Heinrich events. *Proceedings of the National Academy of Sciences of the United States of America 108*, 13415–13419.

Marks, L., Gałązka, D. & Woronko, B. 2016: Climate, environment and stratigraphy of the last Pleistocene glacial stage in Poland. *Quaternary International 420*, 259–271.

Marra, F., Armon, M., Adam, O., Zoccatelli, D., Gazal, O., Garfinkel, C. I., Rostkier-Edelstein, D., Dayan, U., Enzel, Y. & Morin, E. 2021: Toward Narrowing Uncertainty in Future Projections of Local Extreme Precipitation. *Geophysical Research Letters 48*, e2020GL091823.

Martin-Puertas, C., Brauer, A., Wulf, S., Ott, F., Lauterbach, S. & Dulski, P. 2014: Annual proxy data from Lago Grande di Monticchio (southern Italy) between 76 and 112 ka: new chronological constraints and insights on abrupt climatic oscillations. *Climate of the Past 10*, 2099–2114.

Martin-Puertas, C., Matthes, K., Brauer, A., Muscheler, R., Hansen, F., Petrick, C., Aldahan, A., Possnert, G. & van Geel, B. 2012: Regional atmospheric circulation shifts induced by a grand solar minimum. *Nature Geoscience 5*, 397–401.

Martin-Puertas, C., Tjallingii, R., Bloemsma, M. & Brauer, A. 2017: Varved sediment responses to early Holocene climate and environmental changes in Lake Meerfelder Maar (Germany) obtained from multivariate analyses of micro X-ray fluorescence core scanning data. *Journal of Quaternary Science 32*, 427–436.

Matthews, I. P., Trincardi, F., Lowe, J. J., Bourne, A. J., MacLeod, A., Abbott, P. M., Andersen, N., Asioli, A., Blockley, S. P. E., Lane, C. S., Oh, Y. A., Satow, C. S., Staff, R. A. & Wulf, S. 2015: Developing a robust tephrochronological framework for Late Quaternary marine records in the Southern Adriatic Sea: new data from core station SA03-11. *Quaternary Science Reviews 118*, 84–104.

Mayewski, P. A., Meeker, L. D., Twickler, M. S., Whitlow, S., Yang, Q., Lyons, W. B. & Prentice, M. 1997: Major features and forcing of high-latitude northern hemisphere atmospheric circulation using a 110,000-year-long glaciochemical series. *Journal of Geophysical Research: Oceans 102*, 26345–26366.

McManus, J. F., Francois, R., Gherardi, J.-M., Keigwin, L. D. & Brown-Leger, S. 2004: Collapse and rapid

resumption of Atlantic meridional circulation linked to deglacial climate changes. *Nature 428*, 834–837.

Meadows, J. 2005: The Younger Dryas episode and the radiocarbon chronologies of the Lake Huleh and Ghab Valley pollen diagrams, Israel and Syria. *The Holocene 15*, 631–636.

Mees, F., Castenẽda, C., Herrero, J. & Van Ranst, E. 2012: The Nature and Significance of Variations in Gypsum Crystal Morphology in Dry Lake Basins. *Journal of Sedimentary Research 82*, 37–52.

Merz, N., Raible, C. C. & Woollings, T. 2015: North Atlantic Eddy-driven Jet in Interglacial and Glacial Winter Climates. *Journal of Climate 28*, 3977–3997.

Miebach, A., Chen, C., Schwab, M. J., Stein, M. & Litt, T. 2017: Vegetation and climate during the Last Glacial high stand (ca. 28–22 ka BP) of the Sea of Galilee, northern Israel. *Quaternary Science Reviews 156*, 47–56.

Miebach, A., Stolzenberger, S., Wacker, L., Hense, A. & Litt, T. 2019: A new Dead Sea pollen record reveals the last glacial paleoenvironment of the southern Levant. *Quaternary Science Reviews 214*, 98–116.

Migowski, C. 2001: Untersuchung laminierter holozäner Sedimente aus dem Toten Meer: Rekonstruktion von Paläoklima und -seismizität. 99 pp.

Migowski, C., Agnon, A., Bookman, R., Negendank, J. F. W. & Stein, M. 2004: Recurrence pattern of Holocene earthquakes along the Dead Sea transform revealed by varve-counting and radiocarbon dating of lacustrine sediments. *Earth and Planetary Science Letters 222*, 301–314.

Migowski, C., Stein, M., Prasad, S., Negendank, J. F. W. & Agnon, A. 2006: Holocene climate variability and cultural evolution in the Near East from the Dead Sea sedimentary record. *Quaternary Research 66*, 421–431.

Mix, A. C., Bard, E. & Schneider, R. 2001: Environmental processes of the ice age: Land, oceans, glaciers (EPILOG). *Quaternary Science Reviews 20*, 2001.

Monegato, G., Scardia, G., Hajdas, I., Rizzini, F. & Piccin, A. 2017: The Alpine LGM in the boreal ice-sheets game. *Scientific Reports 7*, 1–8.

Müller, D. 2017: Reconstructing climatic conditions at the last Glacial – Interglacial – Transition using varved lake sediments from Lake Gościąż (central Poland). 67 pp. University of Potsdam.

Müller, U. C., Pross, J., Tzedakis, P. C., Gamble, C., Kotthoff, U., Schmiedl, G., Wulf, S. & Christanis, K. 2011: The role of climate in the spread of modern humans into Europe. *Quaternary Science Reviews 30*, 273–279.

Müller, D., Tjallingii, R., Płóciennik, M., Luoto, T. P., Kotrys, B., Plessen, B., Ramisch, A., Schwab, M. J., Błaszkiewicz, M., Słowiński, M. & Brauer, A. 2021: New insights into lake responses to rapid climate change: the Younger Dryas in Lake Gościąż, central Poland. *Boreas 50*, 535–555.

Myhre, G., Alterskjær, K., Stjern, C. W., Hodnebrog, Ø., Marelle, L., Samset, B. H., Sillmann, J., Schaller, N., Fischer, E., Schulz, M. & Stohl, A. 2019: Frequency of extreme precipitation increases extensively with event rareness under global warming. *Scientific Reports 9*, 16063.

Narcisi, B. & Vezzoli, L. 1999: Quaternary stratigraphy of distal tephra layers in the Mediterranean - an overview. *Global and Planetary Change 21*, 31–50.

Neev, D. & Emery, K. O. 1967: *The Dead Sea. Depositional Processes and Environments of Evaporites*. 169 pp. Monson Press, Jerusalem.

Neugebauer, I. 2015: Reconstructing climate from the Dead Sea sediment record using high-resolution micro-facies analyses. University of Potsdam.

Neugebauer, I., Brauer, A., Dräger, N., Dulski, P., Wulf, S., Plessen, B., Mingram, J., Herzschuh, U. & Brande, A. 2012: A Younger Dryas varve chronology from the Rehwiese palaeolake record in NE-Germany. *Quaternary Science Reviews 36*, 91–102.

Neugebauer, I., Brauer, A., Schwab, M. J., Dulski, P., Frank, U., Hadzhiivanova, E., Kitagawa, H., Litt, T., Schiebel, V., Taha, N. & Waldmann, N. D. 2015: Evidences for centennial dry periods at ~3300 and ~2800 cal. yr BP from micro-facies analyses of the Dead Sea sediments. *The Holocene 25*, 1358–1371.

Neugebauer, I., Brauer, A., Schwab, M. J., Waldmann, N. D., Enzel, Y., Kitagawa, H., Torfstein, A., Frank, U., Dulski, P., Agnon, A., Ariztegui, D., Ben-Avraham, Z., Goldstein, S. L. & Stein, M. 2014: Lithology of the long sediment record recovered by the ICDP Dead Sea Deep Drilling Project (DSDDP). *Quaternary Science Reviews 102*, 149–165.

Neugebauer, I., Müller, D., Schwab, M. J., Blockley, S., Lane, C. S., Wulf, S., Appelt, O. & Brauer, A. 2021: Cryptotephras in the Lateglacial ICDP Dead Sea sediment record and their implications for chronology. *Boreas 50*, 844–861.

Neugebauer, I., Schwab, M. J., Waldmann, N. D., Tjallingii, R., Frank, U., Hadzhiivanova, E., Naumann, R., Taha, N., Agnon, A., Enzel, Y. & Brauer, A. 2016: Hydroclimatic variability in the Levant during the early last glacial (∼117-75 ka) derived from micro-facies analyses of deep Dead Sea sediments. *Climate of the Past 12*, 75–90.

Neugebauer, I., Wulf, S., Schwab, M. J., Serb, J., Plessen, B., Appelt, O. & Brauer, A. 2017: Implications of S1 tephra findings in Dead Sea and Tayma palaeolake sediments for marine reservoir age estimation and palaeoclimate synchronisation. *Quaternary Science Reviews 170*, 269–275.

Neumann, F. H., Kagan, E. J., Schwab, M. J. & Stein, M. 2007: Palynology, sedimentology and palaeoecology of the late Holocene Dead Sea. *Quaternary Science Reviews 26*, 1476–1498.

Neumann, F. H., Kagan, E. J., Stein, M. & Agnon, A. 2009: Assessment of the effect of earthquake activity on regional vegetation - High-resolution pollen study of the Ein Feshka section, Holocene Dead Sea. *Review of Palaeobotany and Palynology 155*, 42–51.

Niewiarowski, W. & Noryśkiewicz, B. 1999: Environmental changes in the vicinity of Biskupin in selected periods of the last six thousand years and their reflection in pollen diagrams. *In Acta Palaeobotanica (Suppl. 2)*, 581–588.

Nzekwe, O. P., Lapointe, F., Francus, P., St-Onge, G., Lajeunesse, P., Fortin, D., Jenny, J.-P., De Coninck, A., Philippe, É. G. H. & Labarre, T. 2021: A new ~ 900-year varved record in Lake Walker, Québec North Shore, eastern Canada: insight on late Holocene climate mode of variability. *Journal of Paleolimnology*.

Obreht, I., Wörmer, L., Brauer, A., Wendt, J., Alfken, S., De Vleeschouwer, D., Elvert, M. & Hinrichs, K.-U. 2020: An annually resolved record of Western European vegetation response to Younger Dryas cooling. *Quaternary Science Reviews 231*, 106198.

Ön, Z. B., Akçer-Ön, S., Özeren, M. S., Eriş, K. K., Greaves, A. M. & Çağatay, M. N. 2018: Climate proxies

for the last 17.3 ka from Lake Hazar (Eastern Anatolia), extracted by independent component analysis of μ-XRF data. *Quaternary International 486*, 17–28.

Ott, F., Kramkowski, M., Wulf, S., Plessen, B., Serb, J., Tjallingii, R., Schwab, M., Słowiński, M., Brykała, D., Tyszkowski, S., Putyrskaya, V., Appelt, O., Błaszkiewicz, M. & Brauer, A. 2017: Site-specific sediment responses to climate change during the last 140 years in three varved lakes in Northern Poland. *The Holocene 28*, 464–477.

Ott, F., Wulf, S., Serb, J., Słowiński, M., Obremska, M., Tjallingii, R., Błaszkiewicz, M. & Brauer, A. 2016: Constraining the time span between the Early Holocene Hässeldalen and Askja-S Tephras through varve counting in the Lake Czechowskie sediment record, Poland. *Journal of Quaternary Science 31*, 103–113.

Palchan, D., Neugebauer, I., Amitai, Y., Waldmann, N. D., Schwab, M. J., Dulski, P., Brauer, A., Stein, M., Erel, Y. & Enzel, Y. 2017: North Atlantic controlled depositional cycles in MIS 5e layered sediments from the deep Dead Sea basin. *Quaternary Research (United States) 87*, 168–179.

Paterne, M., Guichard, F. & Labeyrie, J. 1988: Explosive activity of the South Italian volcanoes during the past 80,000 years as determined by marine tephrochronology. *Journal of Volcanology and Geothermal Research 34*, 153–172.

Pauly, M., Helle, G., Miramont, C., Büntgen, U., Treydte, K., Reinig, F., Guibal, F., Sivan, O., Heinrich, I., Riedel, F., Kromer, B., Balanzategui, D., Wacker, L., Sookdeo, A. & Brauer, A. 2018: Subfossil trees suggest enhanced Mediterranean hydroclimate variability at the onset of the Younger Dryas. *Scientific Reports 8*, 13980.

Pawłowski, D., Płóciennik, M., Brooks, S. J., Luoto, T. P., Milecka, K., Nevalainen, L., Peyron, O., Self, A. & Zieliński, T. 2015: A multiproxy study of Younger Dryas and Early Holocene climatic conditions from the Grabia River paleo-oxbow lake (central Poland). *Palaeogeography, Palaeoclimatology, Palaeoecology 438*, 34–50.

Pazdur, A., Fontugne, M. R., Goslar, T. & Pazdur, M. F. 1995: Lateglacial and holocene water-level changes of the Gościąż Lake, Central Poland, derived from carbon isotope studies of laminated sediment. *Quaternary Science Reviews 14*, 125–135.

Pazdur, A., Pazdur, M. F., Goslar, T., Wicik, B. & Arnold, M. 1994: Radiocarbon chronology of late Glacial and Holocene sedimentation and water-level changes in the area of the Gościąż Lake Basin. *Radiocarbon 36*, 187–202.

Pędziszewska, A., Tylmann, W., Witak, M., Piotrowska, N., Maciejewska, E. & Latałowa, M. 2015: Holocene environmental changes reflected by pollen, diatoms, and geochemistry of annually laminated sediments of Lake Suminko in the Kashubian Lake District (N Poland). *Review of Palaeobotany and Palynology 216*, 55–75.

Peel, M. C., Finlayson, B. L. & McMahon, T. A. 2007: Updated world map of the Köppen-Geiger climate classification. *Hydrology and Earth System Sciences 11*, 1633–1644.

Peeters, F., Straile, D., Lorke, A. & Livingstone, D. M. 2007: Earlier onset of the spring phytoplankton bloom in lakes of the temperate zone in a warmer climate. *Global Change Biology 13*, 1898–1909.

Perşoiu, A., Onac, B. P., Wynn, J. G., Blaauw, M., Ionita, M. & Hansson, M. 2017: Holocene winter climate variability in Central and Eastern Europe. *Scientific Reports 7*, 1–8.

Piotrowski, W. 1995: Biskupin - the fortified settlement from the first millennium BC. *Quaternary Studies*

in Poland 13, 89–99.

Platevoet, B., Scaillet, S., Guillou, H., Blamart, D., Nomade, S., Massault, M., Poisson, A., Elitok, Ö., Özgür, N., Yağmurlu, F. & Yilmaz, K. 2008: Pleistocence eruptive chronology of the Gölcük volcano, Isparta Angle, Turkey. *Quaternaire 19*, 147–156.

Poli, S., Chiesa, S., Gillot, P. Y., Gregnanin, A. & Guichard, F. 1987: Chemistry versus time in the volcanic complex of Ischia (Gulf of Naples, Italy): evidence of successive magmatic cycles. *Contributions to Mineralogy and Petrology 95*, 322–335.

Prasad, S., Negendank, J. F. W. & Stein, M. 2009: Varve counting reveals high resolution radiocarbon reservoir age variations in palaeolake Lisan. *Journal of Quaternary Science 24*, 690–696.

Prasad, S., Vos, H., Negendank, J. F. W., Waldmann, N., Goldstein, S. L. & Stein, M. 2004: Evidence from Lake Lisan of solar influence on decadal- To centennial-scale climate variability during marine oxygen isotope stage 2. *Geology 32*, 581–584.

Przybylak, R. 2016: Poland's climate in the last millennium. *In Oxford Research Encyclopedia of Climate Science*, 36. Oxford University Press.

Punt, W., Blackmore, S., Hoen, P. P. & Stafford, P. 2003: *Northwest European Pollen Flora (Volumes I-VIII)*, Elsevier. Amsterdam.

Quinlan, R. & Smol, J. P. 2001: Setting minimum head capsule abundance and taxa deletion criteria in chironomid-based inference models. *Journal of Paleolimnology 26*, 327–342.

Rach, O., Brauer, A., Wilkes, H. & Sachse, D. 2014: Delayed hydrological response to Greenland cooling at the onset of the Younger Dryas in western Europe. *Nature Geoscience 7*, 109–112.

Rach, O., Engels, S., Kahmen, A., Brauer, A., Martín-Puertas, C., van Geel, B. & Sachse, D. 2017: Hydrological and ecological changes in western Europe between 3200 and 2000 years BP derived from lipid biomarker δD values in lake Meerfelder Maar sediments. *Quaternary Science Reviews 172*, 44–54.

Rahmstorf, S. 2002: Ocean circulation and climate during the past 120,000 years. *Nature 419*, 207–214.

Ralska-Jasiewiczowa, M., Demske, D. & van Geel, B. 1998a: Late-Glacial vegetation history recorded in the Lake Gościąż sediments. *In* Ralska-Jasiewiczowa, M. Goslar, T. Madeyska, T. & Starkel, L. (eds.): *Lake Gościąż, central Poland. A monographic study. Part 1*, 128–143. W. Szafer Institute of Botany, Polish Academy of Sciences, Kraków.

Ralska-Jasiewiczowa, M., Goslar, T., Madeyska, T. & Starkel, L. 1998b: *Lake Gościąż, central Poland. A monographic study. Part 1.* 340 pp. W. Szafer Institute of Botany, Polish Academy of Sciences, Kraków.

Ralska-Jasiewiczowa, M., Goslar, T., Madeyska, T. & Starkel, L. 1998c: Introduction. *In* Ralska-Jasiewiczowa, Magdalena Goslar, Tomasz Madeyska, Teresa & Starkel, Leszek (eds.): *Lake Gościąż, central Poland. A monographic study. Part 1*, 10–16. W. Szafer Institute of Botany, Polish Academy of Sciences, Kraków.

Ralska-Jasiewiczowa, M., Goslar, T., Różański, K., Wacnik, A., Czernik, J. & Chróst, L. 2003: Very fast environmental changes at the Pleistocene/Holocene boundary, recorded in laminated sediments of Lake Gościąż, Poland. *Palaeogeography, Palaeoclimatology, Palaeoecology 193*, 225–247.

Ralska-Jasiewiczowa, M. & van Geel, B. 1998: Human impact on the vegetation of the Lake Gościąż

surroundings in prehistoric and early-historic times. *In* Ralska-Jasiewiczowa, M. Goslar, T. Madeyska, T. & Starkel, L. (eds.): *Lake Gościąż, central Poland. A monographic study. Part I*, 267–294. W. Szafer Institute of Botany, Polish Academy of Sciences, Kraków.

Ralska-Jasiewiczowa, M., van Geel, B. & Demske, D. 1998d: Holocene regional vegetation history recorded in the Lake Gościąż sediments. *In* Ralska-Jasiewiczowa, M. Goslar, T. Madeyska, T. & Starkel, L. (eds.): *Lake Gościąż, central Poland. A monographic study. Part 1*, 202–219. W. Szafer Institute of Botany, Polish Academy of Sciences, Kraków.

Ralska-Jasiewiczowa, M., van Geel, B., Goslar, T. & Kuc, T. 1992: The record of the Late Glacial/Holocene transition in the varved sediments of lake Gosciaz, central Poland. *Sveriges Geologiska Undersökning, Ser. Ca 81*, 257–268.

Ralska-Jasiewiczowa, M., Wicik, B. & Więckowski, K. 1987: Lake Gościąż - a site of annually laminated sediments covering 12000 years. *Bulletin of the Polish Academy of Sciences. Earth Sciences 35*, 127–137.

Ramisch, A., Tjallingii, R., Hartmann, K., Diekmann, B. & Brauer, A. 2018: Echo of the Younger Dryas in Holocene Lake Sediments on the Tibetan Plateau. *Geophysical Research Letters 45*, 11,154-11,163.

Ramsey, C. B., Staff, R. A., Bryant, C. L., Brock, F., Kitagawa, H., van der Plicht, J., Schlolaut, G., Marshall, M. H., Brauer, A., Lamb, H. F., Payne, R. L., Tarasov, P. E., Haraguchi, T., Gotanda, K., Yonenobu, H., Yokoyama, Y., Tada, R. & Nakagawa, T. 2012: A Complete Terrestrial Radiocarbon Record for 11.2 to 52.8 kyr B.P. *Science 338*, 370–374.

Rasmussen, S. O., Andersen, K. K., Svensson, A. M., Steffensen, J. P., Vinther, B. M., Clausen, H. B., Siggaard-Andersen, M.-L., Johnsen, S. J., Larsen, L. B., Dahl-Jensen, D., Bigler, M., Röthlisberger, R., Fischer, H., Goto-Azuma, K., Hansson, M. E. & Ruth, U. 2006: A new Greenland ice core chronology for the last glacial termination. *Journal of Geophysical Research: Atmospheres 111*, D06102. https://doi.org/10.1029/2005JD006079.

Rasmussen, S. O., Bigler, M., Blockley, S. P., Blunier, T., Buchardt, S. L., Clausen, H. B., Cvijanovic, I., Dahl-Jensen, D., Johnsen, S. J., Fischer, H., Gkinis, V., Guillevic, M., Hoek, W. Z., Lowe, J. J., Pedro, J. B., Popp, T., Seierstad, I. K., Steffensen, J. P., Svensson, A. M., Vallelonga, P., Vinther, B. M., Walker, M. J. C., Wheatley, J. J. & Winstrup, M. 2014: A stratigraphic framework for abrupt climatic changes during the Last Glacial period based on three synchronized Greenland ice-core records: refining and extending the INTIMATE event stratigraphy. *Quaternary Science Reviews 106*, 14–28.

Rasmussen, S. O., Vinther, B. M., Clausen, H. B. & Andersen, K. K. 2007: Early Holocene climate oscillations recorded in three Greenland ice cores. *Quaternary Science Reviews 26*, 1907–1914.

Reimer, P. J., Bard, E., Bayliss, A., Beck, J. W., Blackwell, P. G., Ramsey, C. B., Buck, C. E., Cheng, H., Edwards, R. L., Friedrich, M., Grootes, P. M., Guilderson, T. P., Haflidason, H., Hajdas, I., Hatté, C., Heaton, T. J., Hoffmann, D. L., Hogg, A. G., Hughen, K. A., Kaiser, K. F., Kromer, B., Manning, S. W., Niu, M., Reimer, R. W., Richards, D. A., Scott, E. M., Southon, J. R., Staff, R. A., Turney, C. S. M. & van der Plicht, J. 2013: Intcal13 and Marine13 Radiocarbon Age Calibration Curves 0–50,000 Years cal BP. *Radiocarbon 55*, 1869–1887.

Reinig, F., Wacker, L., Jöris, O., Oppenheimer, C., Guidobaldi, G., Nievergelt, D., Adolphi, F., Cherubini, P., Engels, S., Esper, J., Land, A., Lane, C., Pfanz, H., Remmele, S., Sigl, M., Sookdeo, A. & Büntgen, U. 2021: Precise date for the Laacher See eruption synchronizes the Younger Dryas. *Nature 595*, 66–69.

Reiss, A. G., Gavrieli, I., Rosenberg, Y. O., Reznik, I. J., Luttge, A., Emmanuel, S. & Ganor, J. 2021: Gypsum Precipitation under Saline Conditions: Thermodynamics, Kinetics, morphology, and Size Distribution. *Minerals 11*, 1–38.

Renssen, H., Geel, B. van, Plicht, J. van der & Magny, M. 2000: Reduced solar activity as a trigger for the start of the Younger Dryas? *Quaternary International 68–71*, 373–383.

Renssen, H., Mairesse, A., Goosse, H., Mathiot, P., Heiri, O., Roche, D. M., Nisancioglu, K. H. & Valdes, P. J. 2015: Multiple causes of the Younger Dryas cold period. *Nature Geoscience 8*, 946–949.

Rossignol-Strick, M. 1985: Mediterranean Quaternary sapropels, an immediate response of the African monsoon to variation of insolation. *Palaeogeography, Palaeoclimatology, Palaeoecology 49*, 237–263.

Rossignol-Strick, M. 1995: Sea-land correlation of pollen records in the Eastern Mediterranean for the glacial-interglacial transition: Biostratigraphy versus radiometric time-scale. *Quaternary Science Reviews 14*, 893–915.

Rothe, M., Frederichs, T., Eder, M., Kleeberg, A. & Hupfer, M. 2014: Evidence for vivianite formation and its contribution to long-term phosphorus retention in a recent lake sediment: a novel analytical approach. *Biogeosciences 11*, 5169–5180.

Rothe, M., Kleeberg, A. & Hupfer, M. 2016: The occurrence, identification and environmental relevance of vivianite in waterlogged soils and aquatic sediments. *Earth-Science Reviews*.

Rozanski, K., Klisch, M. A., Wachniew, P., Gorczyca, Z., Goslar, T., Edwards, T. W. D. & Shemesh, A. 2010: Oxygen-isotope geothermometers in lacustrine sediments: New insights through combined $\delta^{18}O$ analyses of aquatic cellulose, authigenic calcite and biogenic silica in Lake Gościąż, central Poland. *Geochimica et Cosmochimica Acta 74*, 2957–2969.

Różański, K., Kuc, T., Duliński, M. & Wachniew, P. 1998: Oxygen and carbon isotope composition of authigenic carbonates in the Holocene part of the Lake Gościąż sediments. *In* Ralska-Jasiewiczowa, M. Goslar, T. Madeyska, T. & Starkel, L. (eds.): *Lake Gościąż, central Poland. A monographic study. Part I*, 229–232. W. Szafer Institute of Botany, Polish Academy of Sciences, Kraków.

Rychel, J., Woronko, B., Błaszkiewicz, M. & Karasiewicz, T. 2018: Aeolian processes records within last glacial limit areas based on the Płock Basin case (Central Poland). *Bulletin of the Geological Society of Finland 90*, 223–237.

Samuels, R., Hochman, A., Baharad, A., Givati, A., Levi, Y., Yosef, Y., Saaroni, H., Ziv, B., Harpaz, T. & Alpert, P. 2018: Evaluation and projection of extreme precipitation indices in the Eastern Mediterranean based on CMIP5 multi-model ensemble. *International Journal of Climatology 38*, 2280–2297.

Sanchez Goñi, M. F. & Harrison, S. P. 2010: Millennial-scale climate variability and vegetation changes during the Last Glacial: Concepts and terminology. *Quaternary Science Reviews 29*, 2823–2827.

Satow, C., Tomlinson, E. L., Grant, K. M., Albert, P. G., Smith, V. C., Manning, C. J., Ottolini, L., Wulf, S., Rohling, E. J., Lowe, J. J., Blockley, S. P. E. & Menzies, M. A. 2015: A new contribution to the Late Quaternary tephrostratigraphy of the Mediterranean: Aegean Sea core LC21. *Quaternary Science Reviews 117*, 96–112.

Schenk, F., Bennike, O., Väliranta, M., Avery, R., Björck, S. & Wohlfarth, B. 2020: Floral evidence for high summer temperatures in southern Scandinavia during 15–11 cal ka BP. *Quaternary Science Reviews*

233, 106243. https://doi.org/10.1016/j.quascirev.2020.1.

Schenk, F., Väliranta, M., Muschitiello, F., Tarasov, L., Heikkilä, M., Björck, S., Brandefelt, J., Johansson, A. V., Näslund, J.-O. & Wohlfarth, B. 2018: Warm summers during the Younger Dryas cold reversal. *Nature Communications 9*, 1–13.

Schlolaut, G., Brauer, A., Nakagawa, T., Lamb, H. F., Tyler, J. J., Staff, R. A., Marshall, M. H., Bronk Ramsey, C., Bryant, C. L. & Tarasov, P. E. 2017: Evidence for a bi-partition of the Younger Dryas Stadial in East Asia associated with inversed climate characteristics compared to Europe. *Scientific Reports 7*, 44983.

Schlolaut, G., Staff, R. A., Brauer, A., Lamb, H. F., Marshall, M. H., Ramsey, C. B. & Nakagawa, T. 2018: An extended and revised Lake Suigetsu varve chronology from ~50 to ~10 ka BP based on detailed sediment micro-facies analyses. *Quaternary Science Reviews 200*, 351–366.

Schmincke, H.-U. & Sumita, M. 2014: Impact of volcanism on the evolution of Lake Van (eastern Anatolia) III: Periodic (Nemrut) vs. episodic (Süphan) explosive eruptions and climate forcing reflected in a tephra gap between ca. 14 ka and ca. 30 ka. *Journal of Volcanology and Geothermal Research 285*, 195–213.

Schmitt, A. K., Danišík, M., Aydar, E., Şen, E., Ulusoy, I. & Lovera, O. M. 2014: Identifying the volcanic eruption depicted in a Neolithic painting at Çatalhöyük, Central Anatolia, Turkey. *PLoS ONE 9*, e84711.

Schmitt, A. K., Danišík, M., Evans, N. J., Siebel, W., Kiemele, E., Aydin, F. & Harvey, J. C. 2011: Acigöl rhyolite field, Central Anatolia (part 1): high-resolution dating of eruption episodes and zircon growth rates. *Contributions to Mineralogy and Petrology 162*, 1215–1231.

Schwander, J., Eicher, U. & Ammann, B. 2000: Oxygen isotopes of lake marl at Gerzensee and Leysin (Switzerland), covering the Younger Dryas and two minor oscillations, and their correlation to the GRIP ice core. *Palaeogeography, Palaeoclimatology, Palaeoecology 159*, 203–214.

Schweingruber, F. H. 1988: *Tree Rings: Basics and Applications of Dendrochronology*. 275 pp. Kluwer Academic Publishers, Dordrecht, Holland.

Seager, R. & Battisti, D. S. 2007: Challenges to our understanding of the General Circulation: Abrupt climate change. *In The Global Circulation of the Atmosphere*, 331–371.

Shackleton, N. J. & Opdyke, N. D. 1973: Oxygen Isotope and Palaeomagnetic Stratigraphy of Equatorial Pacific Core V28-238: Oxygen Isotope Temperatures and Ice Volumes on a 10^5 year and 10^6 Year Scale. *Quaternary Research 3*, 39–55.

Siani, G., Sulpizio, R., Paterne, M. & Sbrana, A. 2004: Tephrostratigraphy study for the last 18,000 ^{14}C years in a deep-sea sediment sequence for the South Adriatic. *Quaternary Science Reviews 23*, 2485–2500.

Siebel, W., Schmitt, A. K., Kiemele, E., Danišík, M. & Aydin, F. 2011: Acigöl rhyolite field, central Anatolia (part II): geochemical and isotopic (Sr-Nd-Pb, $\delta^{18}O$) constraints on volcanism involving two high-silica rhyolite suites. *Contributions to Mineralogy and Petrology 162*, 1233–1247.

Sillasoo, Ü., Mauquoy, D., Blundell, A., Charman, D., Blaauw, M., Daniell, J. R. G., Toms, P., Newberry, J., Chambers, F. M. & Karofeld, E. 2007: Peat multi-proxy data from Männikjärve bog as indicators of late Holocene climate changes in Estonia. *Boreas 36*, 20–37.

Sirota, I., Enzel, Y., Mor, Z., Ben Moshe, L., Eyal, H., Lowenstein, T. K. & Lensky, N. G. 2020: Sedimentology and stratigraphy of a modern halite sequence formed under Dead Sea level fall. *Sedimentology 68*, 1069–1090.

Słowiński, M., Marcisz, K., Płóciennik, M., Obremska, M., Pawłowski, D., Okupny, D., Słowińska, S., Borówka, R., Kittel, P., Forysiak, J., Michczyńska, D. J. & Lamentowicz, M. 2016: Drought as a stress driver of ecological changes in peatland - A palaeoecological study of peatland development between 3500 BCE and 200 BCE in central Poland. *Palaeogeography, Palaeoclimatology, Palaeoecology 461*, 272–291.

Słowiński, M., Zawiska, I., Ott, F., Noryśkiewicz, A. M., Plessen, B., Apolinarska, K., Rzodkiewicz, M., Michczyńska, D. J., Wulf, S., Skubała, P., Kordowski, J., Błaszkiewicz, M. & Brauer, A. 2017: Differential proxy responses to late Allerød and early Younger Dryas climatic change recorded in varved sediments of the Trzechowskie palaeolake in Northern Poland. *Quaternary Science Reviews 158*, 94–106.

Środoń, J., Drits, V. A., McCarty, D. K., Hsieh, J. C. C. & Eberl, D. D. 2001: Quantitative X-ray diffraction analysis of clay-bearing rocks from random preparations. *Clays and Clay Minerals 49*, 514–528.

St. Seymour, K., Christanis, K., Bouzinos, A., Papazisimou, S., Papatheodorou, G., Moran, E. & Dénès, G. 2004: Tephrostratigraphy and tephrochronology in the Philippi peat basin, Macedonia, Northern Hellas (Greece). *Quaternary International 121*, 53–65.

Stabel, H.-H. 1986: Calcite precipitation in Lake Constance: Chemical equilibrium, sedimentation, and nucleation by algae. *Limnology and Oceanography 31*, 1081–1094.

Starkel, L., Goslar, T., Ralska-Jasiewiczowa, M., Demske, D., Różański, K., Łącka, B., Pelisiak, A., Szeroczyńska, K., Wicik, B. & Więckowski, K. 1998: Discussion of the Holocene events recorded in the Lake Gościąż sediments. *In* Ralska-Jasiewiczowa, Magdalena Goslar, Tomasz Madeyska, T. & Starkel, Leszek (eds.): *Lake Gościąż, central Poland. A monographic study. Part 1*, 239–246. W. Szafer Institute of Botany, Polish Academy of Sciences, Kraków.

Starkel, L., Pazdur, A., Pazdur, M. F., Wicik, B. & Wieckowski, K. 1996: Lake-level and groundwater-level changes in the Lake Gosciaz area, Poland: Palaeoclimatic implications. *The Holocene 6*, 213–224.

Stein, M. 2001: The sedimentary and geochemical record of neogene-quaternary water bodies in the Dead Sea basin - Inferences for the regional paleoclimatic history. *In Journal of Paleolimnology*, 271–282. Kluwer Academic Publishers.

Stein, M. 2014: The Evolution of Neogene-Quaternary Water- Bodies in the Dead Sea Rift Valley. *In* Garfunkel, Z. Ben-Avraham, Z. & Kagan, E. J. (eds.): *Dead Sea Transform Fault System: Reviews*, Springer Science+ Business Media Dordrecht.

Stein, M., Ben-Avraham, Z. & Goldstein, S. L. 2011: Dead Sea Deep Cores : A Window Into Past Climate and Seismicity. *Eos, Transactions American Geophysical Union 92*, 453–454.

Stein, M. & Goldstein, S. L. 2006: U-Th and radiocarbon chronologies of late Quaternary lacustrine records of the Dead Sea basin: methods and applications. *Geological Society of America Special Papers 401*, 141–154.

Stein, M., Starinsky, A., Katz, A., Goldstein, S. L., Machlus, M. & Schramm, A. 1997: Strontium isotopic, chemical, and sedimentological evidence for the evolution of Lake Lisan and the Dead Sea. *Geochimica et Cosmochimica Acta 61*, 3975–3992.

Stein, M., Torfstein, A., Gavrieli, I. & Yechieli, Y. 2010: Abrupt aridities and salt deposition in the post-glacial Dead Sea and their North Atlantic connection. *Quaternary Science Reviews 29*, 567–575.

Stockhecke, M., Timmermann, A., Kipfer, R., Haug, G. H., Kwiecien, O., Friedrich, T., Menviel, L., Litt, T., Pickarski, N. & Anselmetti, F. S. 2016: Millennial to orbital-scale variations of drought intensity in the Eastern Mediterranean. *Quaternary Science Reviews 133*, 77–95.

Stockmarr, J. A. 1971: Tablets with spores used in absolute pollen analysis. *Pollen et Spores 13*, 615–621.

Sumita, M. & Schmincke, H.-U. 2013: Impact of volcanism on the evolution of Lake Van II: Temporal evolution of explosive volcanism of Nemrut Volcano (eastern Anatolia) during the past ca. 0.4Ma. *Journal of Volcanology and Geothermal Research 253*, 15–34.

Szymaniak, M. & Wieckowski, K. 1984: The Nature of bottom deposits in some chosen Gostynin Lakes. *Miscellanea Geographica. Regional Studies on Development 1*, 109–114.

Tarasov, L. & Peltier, W. R. 2005: Arctic freshwater forcing of the Younger Dryas cold reversal. *Nature 435*, 662–665.

Teller, J. T., Leverington, D. W. & Mann, J. D. 2002: Freshwater outbursts to the oceans from glacial Lake Agassiz and their role in climate change during the last deglaciation. *Quaternary Science Reviews 21*, 879–887.

Tjallingii, R., Röhl, U., Kölling, M. & Bickert, T. 2007: Influence of the water content on X-ray fluorescence core-scanning measurements in soft marine sediments. *Geochemistry, Geophysics, Geosystems 8*, 1–12.

Tomlinson, E. L., Arienzo, I., Civetta, L., Wulf, S., Smith, V. C., Hardiman, M., Lane, C. S., Carandente, A., Orsi, G., Rosi, M., Müller, W. & Menzies, M. A. 2012a: Geochemistry of the Phlegraean Fields (Italy) proximal sources for major Mediterranean tephras: Implications for the dispersal of Plinian and co-ignimbritic components of explosive eruptions. *Geochimica et Cosmochimica Acta 93*, 102–128.

Tomlinson, E. L., Kinvig, H. S., Smith, V. C., Blundy, J. D., Gottsmann, J., Müller, W. & Menzies, M. A. 2012b: The Upper and Lower Nisyros Pumices: Revisions to the Mediterranean tephrostratigraphic record based on micron-beam glass geochemistry. *Journal of Volcanology and Geothermal Research 243–244*, 69–80.

Tomlinson, E. L., Smith, V. C., Albert, P. G., Aydar, E., Civetta, L., Cioni, R., Çubukçu, E., Gertisser, R., Isaia, R., Menzies, M. A., Orsi, G., Rosi, M. & Zanchetta, G. 2015: The major and trace element glass compositions of the productive Mediterranean volcanic sources: tools for correlating distal tephra layers in and around Europe. *Quaternary Science Reviews 118*, 48–66.

Torfstein, A. & Enzel, Y. 2017: Dead Sea Lake Level Changes and Levant Paleoclimate. *In* Enzel, Y. & Bar-Yosef, O. (eds.): *Quaternary of the Levant: Environments, Climate Change, and Humans*, 115–125. Cambridge University Press, Cambridge.

Torfstein, A., Gavrieli, I., Katz, A., Kolodny, Y. & Stein, M. 2008: Gypsum as a monitor of the paleo-limnological-hydrological conditions in Lake Lisan and the Dead Sea. *Geochimica et Cosmochimica Acta 72*, 2491–2509.

Torfstein, A., Goldstein, S. L., Kagan, E. J. & Stein, M. 2013a: Integrated multi-site U-Th chronology of the last glacial Lake Lisan. *Geochimica et Cosmochimica Acta 104*, 210–231.

Torfstein, A., Goldstein, S. L., Kushnir, Y., Enzel, Y., Haug, G. & Stein, M. 2015: Dead Sea drawdown and

monsoonal impacts in the Levant during the last interglacial. *Earth and Planetary Science Letters 412*, 235–244.

Torfstein, A., Goldstein, S. L., Stein, M. & Enzel, Y. 2013b: Impacts of abrupt climate changes in the Levant from Last Glacial Dead Sea levels. *Quaternary Science Reviews 69*, 1–7.

Torfstein, A., Haase-Schramm, A., Waldmann, N., Kolodny, Y. & Stein, M. 2009: U-series and oxygen isotope chronology of the mid-Pleistocene Lake Amora (Dead Sea basin). *Geochimica et Cosmochimica Acta 73*, 2603–2630.

Tylmann, W., Bonk, A., Goslar, T., Wulf, S. & Grosjean, M. 2016: Calibrating ^{210}Pb dating results with varve chronology and independent chronostratigraphic markers: Problems and implications. *Quaternary Geochronology 32*, 1–10.

Tylmann, W., Głowacka, P. & Szczerba, A. 2017: Tracking climate signals in varved lake sediments: research strategy and key sites for comprehensive process studies in the Masurian Lakeland. *Limnological Review 17*, 159–166.

van Geel, B., Buurman, J. & Waterbolk, H. T. 1996: Archaeological and palaeoecological indications of an abrupt climate change in The Netherlands, and evidence for climatological teleconnections around 2650 BP. *Journal of Quaternary Science 11*, 451–460.

van Geel, B., Heijnis, H., Charman, D. J., Thompson, G. & Engels, S. 2014: Bog burst in the eastern Netherlands triggered by the 2.8 kyr BP climate event. *The Holocene 24*, 1465–1477.

van Geel, B., Raspopov, O. M., Renssen, H., van der Plicht, J., Dergachev, V. A. & Meijer, H. A. J. 1999: The role of solar forcing upon climate change. *Quaternary Science Reviews 18*, 331–338.

van Raden, U. J., Colombaroli, D., Gilli, A., Schwander, J., Bernasconi, S. M., van Leeuwen, J., Leuenberger, M. & Eicher, U. 2013: High-resolution late-glacial chronology for the Gerzensee lake record (Switzerland): δ^{18}O correlation between a Gerzensee-stack and NGRIP. *Palaeogeography, Palaeoclimatology, Palaeoecology 391*, 13–24.

Vinci, A. 1985: Distribution and chemical composition of tephra layers from Eastern Mediterranean abyssal sediments. *Marine Geology 64*, 143–155.

von Grafenstein, U., Erlenkeuser, H., Brauer, A., Jouzel, J. & Johnsen, S. J. 1999: A Mid-European Decadal Isotope-Climate Record from 15,500 to 5000 Years B.P. *Science 284*, 1654–1657.

Walanus, A. & Nalepka, D. 1999: POLPAL. Program for counting pollen grains, diagrams plotting and numerical analysis. *Acta Palaeobotanica 2*, 659–661.

Waldmann, N., Stein, M., Ariztegui, D. & Starinsky, A. 2009: Stratigraphy, depositional environments and level reconstruction of the last interglacial Lake Samra in the Dead Sea basin. *Quaternary Research 72*, 1–15.

Wang, Y. J., Cheng, H., Edwards, R. L., An, Z. S., Wu, J. Y., Shen, C. C. & Dorale, J. A. 2001: A High-Resolution Absolute-Dated Late Pleistocene Monsoon Record from Hulu Cave, China. *Science 294*, 2345–2348.

Warren, J. K. 1982: The hydrological setting, occurrence and significance of gypsum in late Quaternary salt lakes in South Australia. *Sedimentology 29*, 609–637.

Weber, N., Lazar, B., Gavrieli, I., Yechieli, Y. & Stein, M. 2021: Gypsum Deltas at the Holocene Dead Sea linked to Grand Solar Minima. *Geophysical Research Letters 48*, 1–10.

Weltje, G. J., Bloemsma, M. R., Tjallingii, R., Heslop, D., Röhl, U. & Croudace, I. W. 2015: Prediction of geochemical composition from XRF core scanner data: A new multivariate approach including automatic selection of calibration samples and quantification of uncertainties. *In* Croudace, I. & Rothwell, R. (eds.): *Micro-XRF Studies of Sediment Cores. Developments in Paleoenvironmental Research, 17*, 507–534. Springer, Dordrecht.

Weltje, G. J. & Tjallingii, R. 2008: Calibration of XRF core scanners for quantitative geochemical logging of sediment cores: Theory and application. *Earth and Planetary Science Letters 274*, 423–438.

Wick, L., Lemcke, G. & Sturm, M. 2003: Evidence of Lateglacial and Holocene climatic change and human impact in eastern Anatolia: high-resolution pollen, charcoal, isotopic and geochemical records from the laminated sediments of Lake Van, Turkey. *The Holocene 13*, 665–675.

Wohlfarth, B., Blaauw, M., Davies, S. M., Andersson, M., Wastegård, S., Hormes, A. & Possnert, G. 2006: Constraining the age of Lateglacial and early Holocene pollen zones and tephra horizons in southern Sweden with Bayesian probability methods. *Journal of Quaternary Science 21*, 321–334.

Wójcik, G. & Przybylak, R. 1998: Present-day climatic conditions of the Lake Gościąż region. *In* Ralska-Jasiewiczowa, M. Goslar, T. Madeyska, T. & Starkel, L. (eds.): *Lake Gościąż, central Poland. A monographic study. Part 1*, 22–26. W. Szafer Institute of Botany, Polish Academy of Sciences, Kraków.

Wörmer, L., Wendt, J., Alfken, S., Wang, J.-X., Elvert, M., Heuer, V. B. & Hinrichs, K.-U. 2019: Towards multiproxy, ultra-high resolution molecular stratigraphy: Enabling laser-induced mass spectrometry imaging of diverse molecular biomarkers in sediments. *Organic Geochemistry 127*, 136–145.

Wulf, S., Dräger, N., Ott, F., Serb, J., Appelt, O., Gudmundsdóttir, E., van den Bogaard, C., Słowiński, M., Błaszkiewicz, M. & Brauer, A. 2016: Holocene tephrostratigraphy of varved sediment records from Lakes Tiefer See (NE Germany) and Czechowskie (N Poland). *Quaternary Science Reviews 132*, 1–14.

Wulf, S., Hardiman, M. J., Staff, R. A., Koutsodendris, A., Appelt, O., Blockley, S. P. E., Lowe, J. J., Manning, C. J., Ottolini, L., Schmitt, A. K., Smith, V. C., Tomlinson, E. L., Vakhrameeva, P., Knipping, M., Kotthoff, U., Milner, A. M., Müller, U. C., Christanis, K., Kalaitzidis, S., Tzedakis, P. C., Schmiedl, G. & Pross, J. 2018: The marine isotope stage 1–5 cryptotephra record of Tenaghi Philippon, Greece: Towards a detailed tephrostratigraphic framework for the Eastern Mediterranean region. *Quaternary Science Reviews 186*, 236–262.

Wulf, S., Keller, J., Paterne, M., Mingram, J., Lauterbach, S., Opitz, S., Sottili, G., Giaccio, B., Albert, P. G., Satow, C., Tomlinson, E. L., Viccaro, M. & Brauer, A. 2012: The 100-133 ka record of Italian explosive volcanism and revised tephrochronology of Lago Grande di Monticchio. *Quaternary Science Reviews 58*, 104–123.

Wulf, S., Keller, J., Satow, C., Gertisser, R., Kraml, M., Grant, K. M., Appelt, O., Vakhrameeva, P., Koutsodendris, A., Hardiman, M., Schulz, H. & Pross, J. 2020: Advancing Santorini's tephrostratigraphy: New glass geochemical data and improved marine-terrestrial tephra correlations for the past ~360 kyrs. *Earth-Science Reviews 200*, 102964.

Wulf, S., Kraml, M., Brauer, A., Keller, J. & Negendank, J. F. W. 2004: Tephrochronology of the 100ka lacustrine sediment record of Lago Grande di Monticchio (southern Italy). *Quaternary International 122*, 7–30.

Wulf, S., Kraml, M. & Keller, J. 2008: Towards a detailed distal tephrostratigraphy in the Central Mediterranean: The last 20,000 yrs record of Lago Grande di Monticchio. *Journal of Volcanology*

and Geothermal Research 177, 118–132.

Wulf, S., Kraml, M., Kuhn, T., Schwarz, M., Inthorn, M., Keller, J., Kuscu, I. & Halbach, P. 2002: Marine tephra from the Cape Riva eruption (22 ka) of Santorini in the Sea of Marmara. *Marine Geology 183*, 131–141.

Wulf, S., Ott, F., Słowiński, M., Noryśkiewicz, A. M., Dräger, N., Martin-Puertas, C., Czymzik, M., Neugebauer, I., Dulski, P., Bourne, A. J., Błaszkiewicz, M. & Brauer, A. 2013: Tracing the Laacher See Tephra in the varved sediment record of the Trzechowskie palaeolake in central Northern Poland. *Quaternary Science Reviews 76*, 129–139.

Yechieli, Y., Magaritz, M., Levy, Y., Weber, U., Kafri, U., Woelfli, W. & Bonani, G. 1993: Late quaternary geological history of the dead sea area, Israel. *Quaternary Research 39*, 59–67.

Zaarur, S., Affek, H. P. & Stein, M. 2016: Last glacial-Holocene temperatures and hydrology of the Sea of Galilee and Hula Valley from clumped isotopes in <I>Melanopsis</I> shells. *Geochimica et Cosmochimica Acta 179*, 142–155.

Zanchetta, G., Sulpizio, R., Roberts, N., Cioni, R., Eastwood, W. J., Siani, G., Caron, B., Paterne, M. & Santacroce, R. 2011: Tephrostratigraphy, chronology and climatic events of the Mediterranean basin during the Holocene: An overview. *The Holocene 21*, 33–52.

Zander, P. D., Żarczyński, M., Vogel, H., Tylmann, W., Wacnik, A., Sanchini, A. & Grosjean, M. 2021: A high-resolution record of Holocene primary productivity and water-column mixing from the varved sediments of Lake Żabińskie, Poland. *Science of the Total Environment 755*, 143713.

Żarczyński, M., Szmańda, J. & Tylmann, W. 2019a: Grain-size distribution and structural characteristics of varved sediments from lake Żabińskie (Northeastern Poland). *Quaternary 2*, 8.

Żarczyński, M., Tylmann, W. & Goslar, T. 2018: Multiple varve chronologies for the last 2000 years from the sediments of Lake Żabińskie (northeastern Poland) – Comparison of strategies for varve counting and uncertainty estimations. *Quaternary Geochronology 47*, 107–119.

Żarczyński, M., Wacnik, A. & Tylmann, W. 2019b: Tracing lake mixing and oxygenation regime using the Fe/Mn ratio in varved sediments: 2000 year-long record of human-induced changes from Lake Żabińskie (NE Poland). *Science of the Total Environment 657*, 585–596.

Zolitschka, B., Francus, P., Ojala, A. E. K. & Schimmelmann, A. 2015: Varves in lake sediments - a review. *Quaternary Science Reviews 117*, 1–41.

Appendix

A1. Overview of sediment cores and blocks at Lake Gościąż and the Dead Sea

***Table A1-1**: Overview of sediment cores at Lake Gościąż and the deep basin of the Dead Sea (ICDP drilling) investigated in this doctoral thesis.*

Lake	Coring site	Cores	GPS	Water depth [m]	Date of coring	Coring equipment	Core diameter [mm]
Lake Gościąż	GOS15-S1	S1	52° 34.963' N 19° 20.400' E	21.3	04.09.2015	Uwitec Piston corer	90
	GOS15-A	A1 - A10	52° 34.963' N, 19° 20.401' E	21.3	02.09.2015 - 04.09.2015	Uwitec Piston corer	90
	GOS15-B	B1 - B10	52° 34.961' N, 19° 20.392' E	21.4	04.09.2015 - 06.09.2015	Uwitec Piston corer	90
	GOS15-C	C1 - C7	52° 34.967' N 19° 20.395' E	21.5	06.09.2015 - 07.09.2015	Uwitec Piston corer	90
	GOS18-G	G1 - G3	52° 35.015' N 19° 20.353' E	20.1	28.05.2018	Uwitec Piston corer	90
	GOS18-H	H1 - H5	52° 35.015' N 19° 20.341' E	19.6	29.05.2018 - 30.05.2018	Uwitec Piston corer	90
Dead Sea	ICDP DSDDP 5017-1-A	43 - 47	31° 30.483' N, 35° 28.273' E	-297.46	23.11.2010 - 24.11.2010	top-head-drive rotary rig (Atlas Copco T3WDH): rotating extended core bit ('Alien')	74

***Table A1-2**: Overview of sediment blocks at Masada (MAS) investigated in this doctoral thesis.*

Lake	Sampling site	Blocks	GPS	Altitude [m]	Date of sampling	Sampling equipment	block dimensions [mm]
Dead Sea	MAS	01 - 05	31° 18.602' N, 35° 22.489' E	-349	27.11.2018	stainless steel boxes with removable side walls	340 x 50

A2. Cryptotephra from Lake Gościąż

Four different tephras (Askja-AD1875, Askja-S, Hässeldalen and Laacher See Tephra (LST)) were expected in Lake Gościąż due to their discovery in northern polish lakes (Wulf et al. 2013, 2016; Ott et al. 2016; Kinder et al. 2021), but unfortunately none could be identified so far. Lacustrine sedimentation in GOS probably initiated slightly after the Laacher See eruption (Brauer et al. 1999; Reinig et al. 2021), which is why the LST was not found in the lake sediments. The search for the other cryptotephras was unsuccessful so far. However, glass shards from an unknown Askja ash occur that coincide temporally with the age of the Askja-S tephra (Fig. A2-1), but glass geochemical data from electron probe microanalyses (EPMA) do not precisely match published data for the Askja-S tephra from other European sites (e.g. Davies et al. 2003; Lane et al. 2011; Wulf et al. 2016; Kearney et al. 2018): especially the SiO_2 values are lower, while the Al_2O_3 and MgO values are higher in the glass shards found in GOS. Due to these ambiguous results, this Askja-like tephra was not included in the age-depth-model.

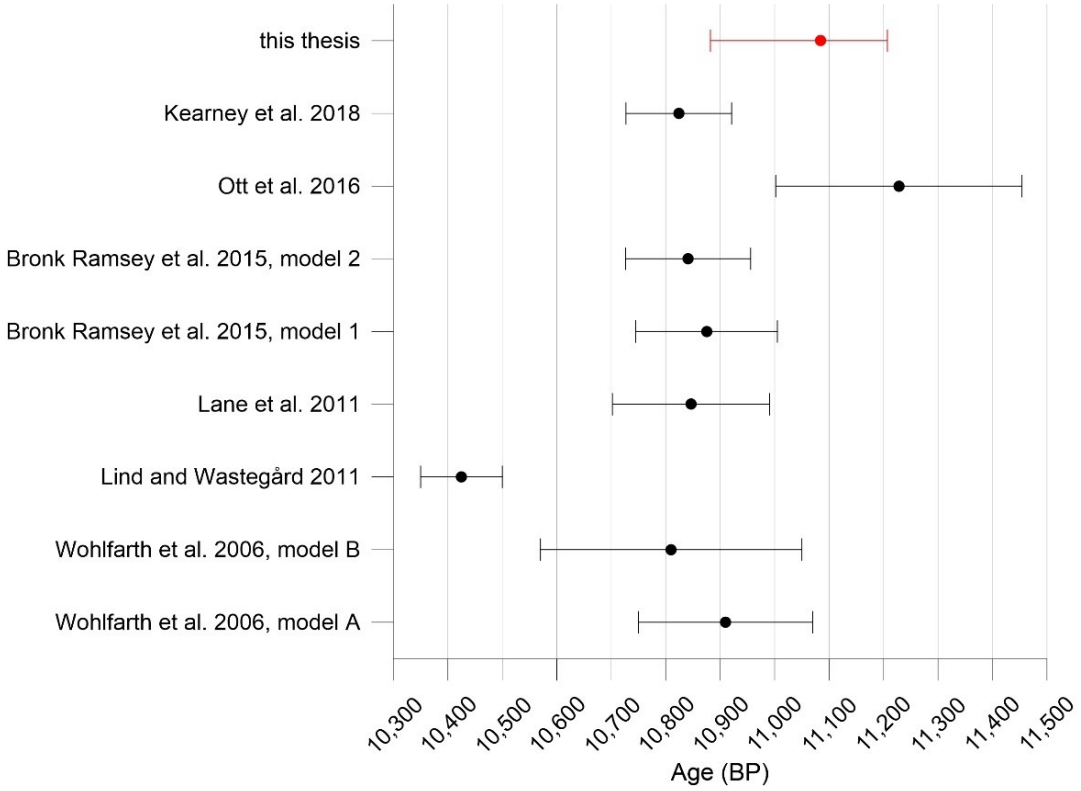

***Figure A2-1**: Age ranges of the Askja-S tephra from different studies (references are displayed on the left).*

A3. Stable oxygen and carbon isotopes from Lake Gościąż

Preliminary results show that a gradual shift starts at ~1450 cm that is steeper between ~1450 and ~1350 cm (~8850-7750 BP), and less steep between ~1350 and ~1150 cm (~7750-5750 BP). The steeper part encircles the abrupt shift in XRF elemental data at ~1370 cm (~7940 BP), while a gradual shift is also observed in varve composition from ~1420-1280 cm (~8500-7000 BP) as presented in chapter 2. Therefore, it seems likely that the shift in stable isotope data is related to the same processes as the other proxy data, meaning to the change in hydrology (water level decline, and formation of the four lake Na Jazach system and the Ruda stream). Interestingly, the XRF data are elevated between ~1370 and ~1170 cm (7940-5870 BP; chapter 2), which coincides with the here observed less steep decrease in $\delta^{18}O_{carb}$ and increase in $\delta^{13}C_{carb}$.

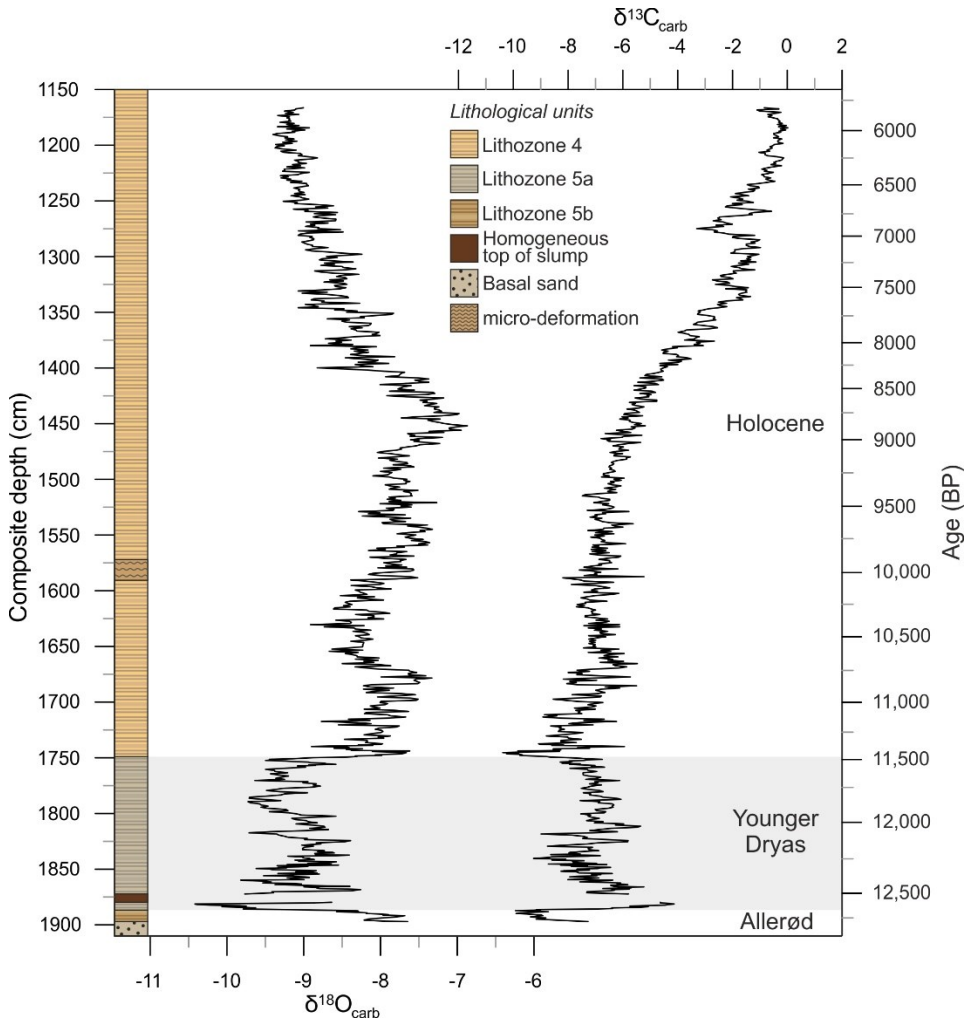

***Figure A3-1**: Stable oxygen ($\delta^{18}O_{carb}$) and carbon ($\delta^{13}C_{carb}$) isotopes from the carbonate fraction of the Lake Gościąż sediments measured between ca 1897-1150 cm composite depth (ca 12,830-5750 BP). Grey box indicates the extent of the Younger Dryas.*

A4. Stable oxygen and carbon isotopes from the DS

In the ICDP core and at Masada, stable carbon and oxygen isotope measurements were performed on aragonite sublayers of aragonite varves ($\delta^{18}O_{aragonite}$, $\delta^{13}C_{aragonite}$), because within the water column precipitated aragonite reflects the isotopic water composition at the time of sediment deposition, which is influenced by precipitation (Kolodny et al. 2005). In contrast, detrital sublayers represent the catchment signal, which is influenced not only by in situ signals. This different signal influence at the DS was previously shown by different isotopic values for the respective sediment fractions (Neugebauer 2015). At Masada, varve formation is continuous (chapter 5), which is why several aragonite laminae (n=398) could be sampled between UGU and AGU. Individual aragonite sublayers were drilled in the fresh surface of the impregnated ~34 cm long sediment blocks. In the ICDP core, varve formation is frequently interrupted by MTDs and aragonite sublayers are thinner than at Masada (chapter 5), which is why less aragonite sublayers (n=166) between the UGU and AGU could be sampled. Here, phases comprising (i) thicker aragonite sublayers, (ii) thinner aragonite sublayers, and (iii) gypsum-bearing aragonite varves were selected for analyses. Here, individual aragonite laminae were drilled on the fresh surface of impregnated sediment blocks that were also used for thin section preparation. Depending on laminae thickness, sampling was performed using 0.3-0.5 mm thick corers. At both DS sites, each sample represents one year, because single aragonite sublayers were drilled. Yet, aragonite sublayers are often disturbed and/or too thin for the corers, which is why not every year could be sampled, even at Masada. About 90-120 mg of the drilled powdery sediment was transferred into glass tubes and dried at 40°C. The samples were subsequently measured with an automated carbonate device (KIEL IV), which is connected to a MAT253 Isotope Ratio Mass Spectrometer (IRMS, Thermo Fisher Scientific). Like for $\delta^{18}O_{carb}$ (chapter 3.3.6.), the isotope compositions are given relative to Vienna PeeDee Belemnite (VPDB) standard, the data was calibrated against NBS-19 and C1, and standard errors are 0.06‰. Results and interpretations described below are preliminary as data evaluation is still ongoing.

Preliminary results show $\delta^{18}O_{aragonite}$ values between ~2-6 ‰, and more variable $\delta^{13}C_{aragonite}$ values between ~-5 and 4 ‰ in the ICDP core and -3 and 3 ‰ at Masada (Fig. A4-1). The higher variability in $\delta^{13}C_{aragonite}$ values, probably representing primary productivity, coincides with results from Kolodny et al. (2005). Although correlation between $\delta^{18}O_{aragonite}$ and $\delta^{13}C_{aragonite}$ is generally weak, it seems like it is higher in the ICDP core (Masada $R^2 = 0.03$; ICDP core $R^2 = 0.12$) between UGU and AGU. At both sites, multiple samples have been drilled from the same laminae in some aragonite sublayers to test the spatial distribution of the isotope signals. The results show similar values within one aragonite sublayer of proximal and distal samples. Interestingly, in few thick aragonite sublayers samples were drilled successively, and the lower

sample is in most cases lighter in $\delta^{18}O_{aragonite}$ and heavier in $\delta^{13}C_{aragonite}$, which possibly represents the higher dilution of the DS water at the beginning of aragonite precipitation.

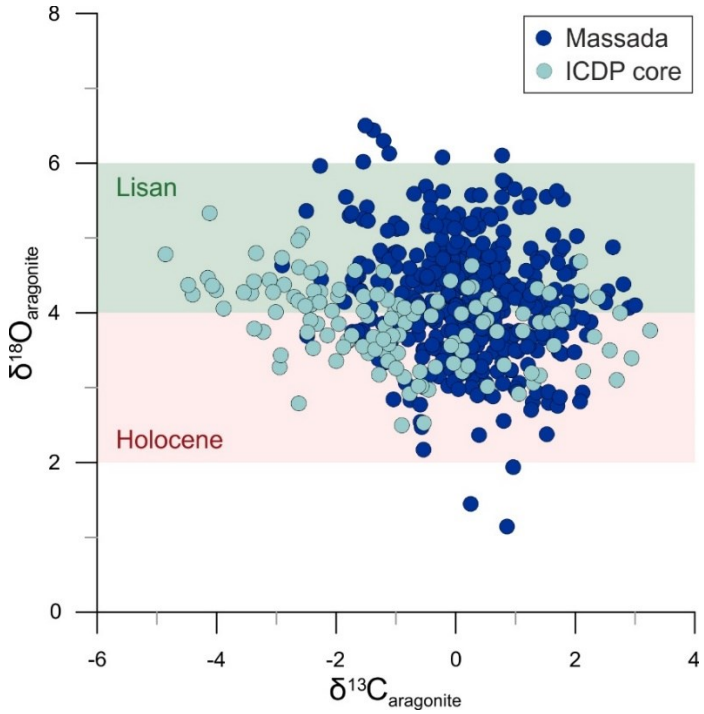

***Figure A4-1**: Stable oxygen ($\delta^{18}O_{aragonite}$) versus stable carbon ($\delta^{13}C_{aragonite}$) between the Upper and Additional Gypsum Units (ULi-aad) in the ICDP core (light blue) and Masada (blue). $\delta^{18}O_{aragonite}$ data range from Kolodny et al. (2005). Note that here all samples from the ICDP core are shown.*

At Masada (Fig. A4-2), most $\delta^{18}O_{aragonite}$ values fall between ~3-6 ‰, which roughly falls in the data range for typical heavy Lisan Formation values (~4-6 ‰; Kolodny et al. 2005), but also already shows a trend towards lighter values more typical for the Holocene (~2-4 ‰; Kolodny et al. 2005). This might suggest that although the millennium of stable sedimentation (ULi-aad) during the transition from the Last Glacial to the Holocene represents a positive water budget phase (chapter 5), the general long-term change from wet glacial (heavy isotope values) to dry interglacial (lighter isotope values) climate at the DS is already reflected in the $\delta^{18}O_{aragonite}$ values. About decadal-long fluctuations between heavier and lighter $\delta^{18}O_{aragonite}$ values might suggest small-scale changes in hydroclimate between slightly wetter and drier phases. However, no direct correlation between isotope values und sedimentation was observed thus far. Interestingly, the 15- and 31-data point average in $\delta^{13}C_{aragonite}$ show nearly the same pattern indicating decadal- to centennial-scale variations, whereas the 15-data point average in $\delta^{18}O_{aragonite}$ shows more variability than the 31-data point average suggesting higher frequency changes in hydroclimate on decadal

scales. The uppermost ~250 cm comprise slightly heavier $\delta^{18}O_{aragonite}$ and steadier $\delta^{13}C_{aragonite}$ values, which might be interpreted as a precursor of the oncoming drying and lake level decline. Since the long-term trends in $\delta^{18}O_{aragonite}$ values reflect the source water, i.e. the Mediterranean seawater (Kolodny et al. 2005), cooling at the YD onset (AGU) would have caused heavier $\delta^{18}O$ values in the Mediterranean and thus also at the DS. Further, this phase of heavier $\delta^{18}O_{aragonite}$ values coincides with the occurrence of more aadg varves indicating increasing summer evaporation at the end of this depositional stability (chapter 5).

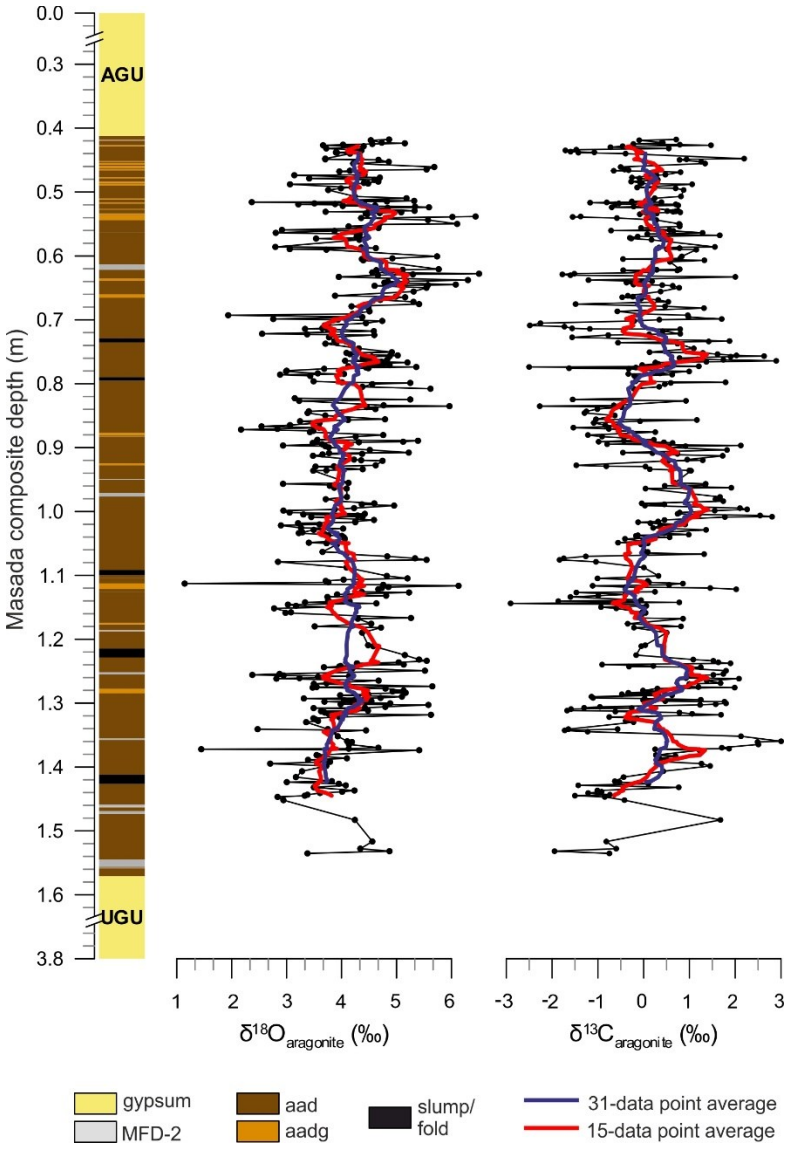

***Figure A4-2**: Stable oxygen ($\delta^{18}O_{aragonite}$) and carbon ($\delta^{13}C_{aragonite}$) isotopes from aragonite sublayers at Masada between the Upper Gypsum Unit (UGU) and Additional Gypsum Unit (AGU). Lithological column on the left. Data points represent single years. MFD: mass flow deposit.*

In the ICDP core (Fig. A4-3), $\delta^{18}O_{aragonite}$ values occur in a similar range (~3-5.5 ‰) than at Masada, however most values fall between ~3-4.5 ‰ and thus coincide more with Holocene values (~2-4 ‰; Kolodny et al. 2005). This might be due to the proximity of Masada to the freshwater inflow, which is why even small-scale changes can be recorded there and the long-term trend towards generally more drying at the end of the Last Glacial is observed in the depocenter. In the aragonite sublayers directly below the AGU (Fig. A4-3A), the lower $\delta^{18}O_{aragonite}$ values are heavier than in the underlying varve phases (Fig. A4-3B-C) consistent with the general trend in the uppermost isotopes at Masada, while the upper $\delta^{18}O_{aragonite}$ values are lighter probably representing a small-scale fluctuation in data, which is also occurring in the uppermost $\delta^{18}O_{aragonite}$ values at Masada. However, it needs to be stressed that not all drilled aragonite sublayers were evaluated in the ICDP core thus far and only a subset of the data is shown in figure A4-3.

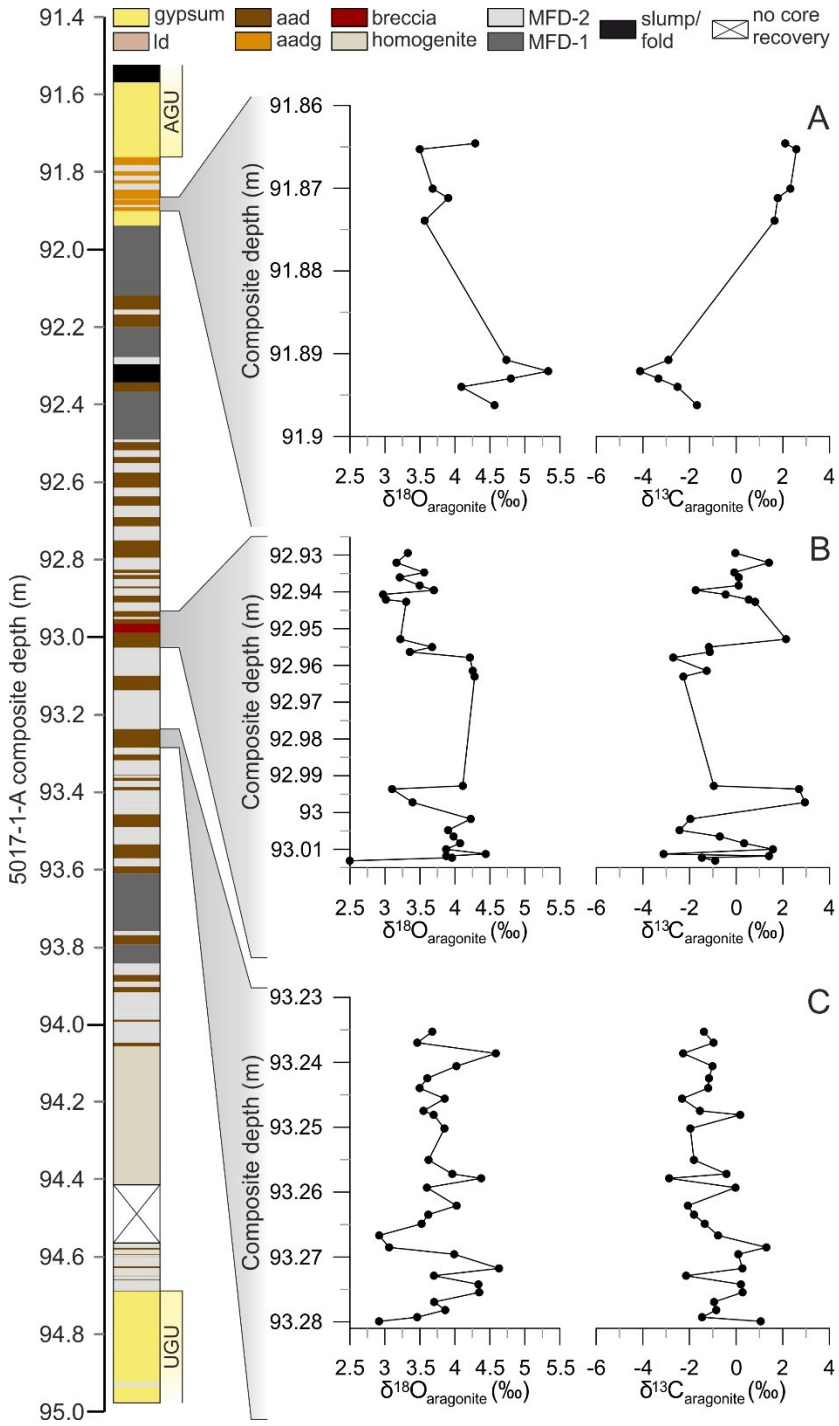

***Figure A4-3**: Stable oxygen ($\delta^{18}O_{aragonite}$) and carbon ($\delta^{13}C_{aragonite}$) isotopes from aragonite sublayers from varved sections of the ICDP core 5017-1-A between the Upper Gypsum Unit (UGU) and Additional Gypsum Unit (AGU). Lithological column on the left. Varved sequences include gypsum (aadg varves, A), have thin (B) or thick aragonite sublayers (C). MFD: mass flow deposit. Note that these sections only represent a fraction of samples, because not all samples have been evaluated thus far.*

A5. Upper Lisan Formation directly below the UGU at Masada

***Table A5-1**: Overview of additional sediment blocks 06 – 07 at Masada in comparison to blocks 01 – 05 (see table A1-1).*

Lake	Sampling site	Blocks	GPS	Altitude [m]	Date of sampling	Sampling equipment	block dimensions [mm]
Dead Sea	MAS	01 - 05	31° 18.602' N, 35° 22.489' E	-349	27.11.2018	stainless steel boxes with removable side walls	340 x 50
	MAS	06 - 07	31° 18.588' N, 35° 22.492' E	-347	27.11.2018	stainless steel boxes with removable side walls	340 x 50

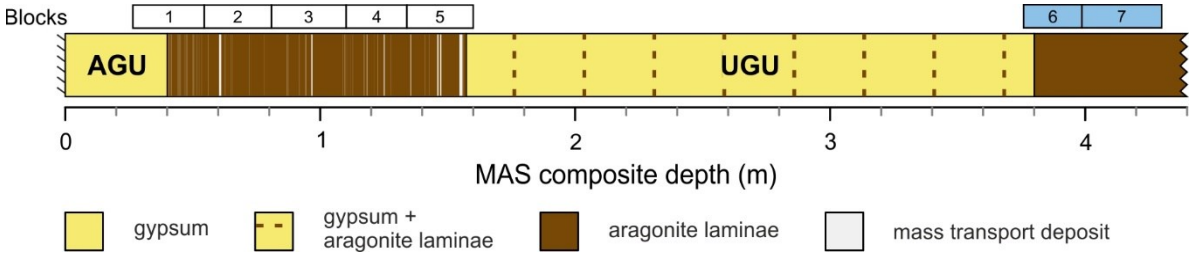

***Figure A5-1**: Sediment blocks sampled at Masada. Blocks 1-5 cover the ULi-aad between Upper Gypsum Unit (UGU) and Additional Gypsum Unit (AGU) and were investigated in chapter 5. Blocks 6 and 7 (blue) cover the transition into the UGU.*

A6. Tobyłka Bay at Lake Gościąż

The profiles from the deep centre (GOS; water depth ~22 m) and the shallow Tobyłka Bay (GT; water depth ~2 m) were preliminarily correlated (Fig. A6-1) using the biostratigraphic boundaries of the YD, and ages were transferred from GOS unto GT. The shift in XRF data at the YD boundaries is completed contemporaneously in both profiles, supporting the preliminary correlation. Deposition of thick planktonic diatom sublayers in both profiles occurs mostly only during the YD, supporting the interpretation demonstrated in chapter 3 that stronger winds during the YD lead to stronger water circulation, and thus nutrient upwelling leading to spring and autumn diatom blooms.

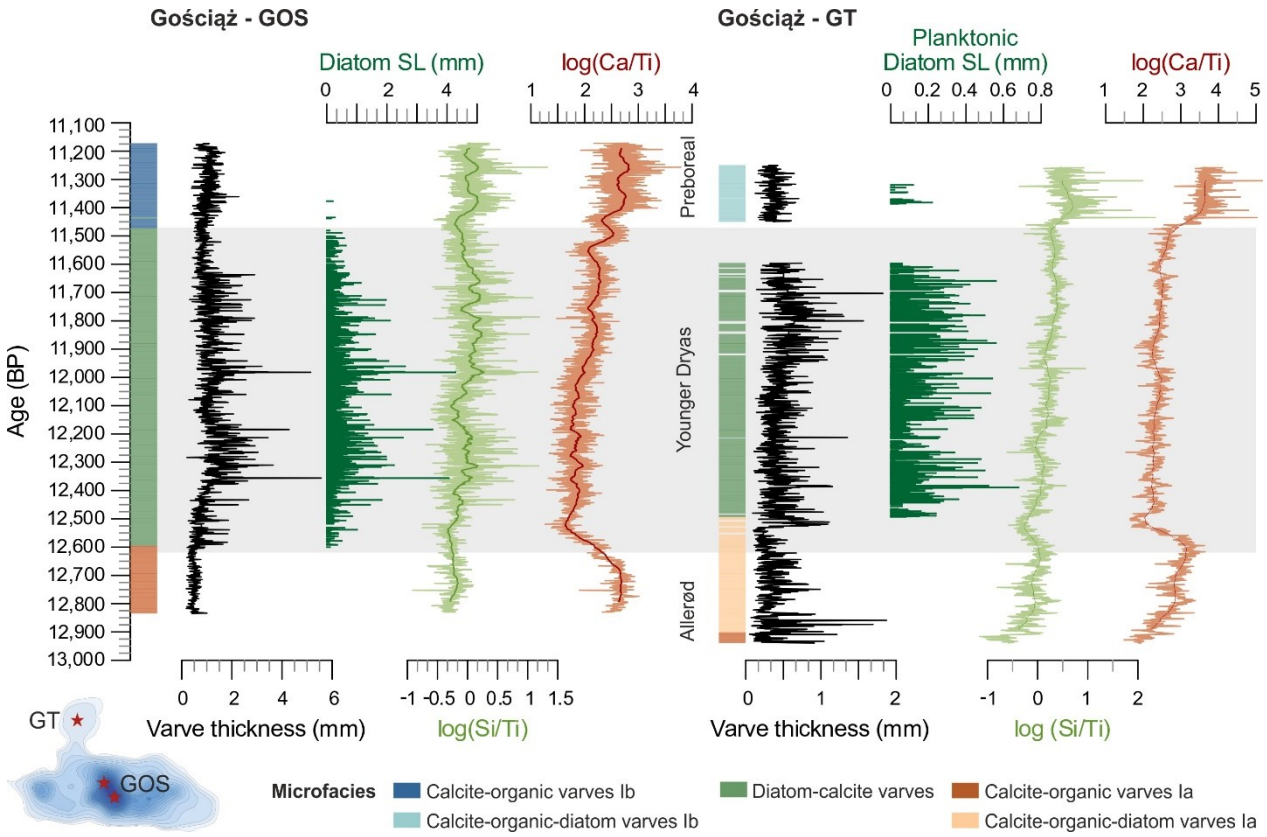

***Figure A6-1**: Comparison of selected data for the composite profiles of the main basin (GOS, chapter 3) and the Tobyłka Bay (GT). GT was anchored to the age model of GOS using the biostratigraphic YD boundaries in both profiles. Note that correlation between profiles is preliminary. In the lower left, the locations of GOS and GT are marked in the bathymetric map of the lake. Grey box marks the extent of the YD in GOS. SL: Sublayer.*

Nevertheless, some differences in the varve chronologies are also visible: (1) the GT varve chronology starts about ~100 years earlier than GOS at ~ 12,940 BP. It was assumed that the varve chronology in the Tobyłka Bay is longer than in any other cores, which however could not be proven previously due to the

core gap (Goslar 1998d). These preliminary results show that the continuous chronology indeed starts about one century earlier than in the deep lake, in the mid-Allerød. Earlier varve formation in GT than in GOS probably is because the Tobyłka Bay depression was isolated from the main water body during the early Lateglacial, and its dead ice block was smaller melting earlier than in the main depression more southwards (Ralska-Jasiewiczowa et al. 1998a). (2) At the end of the YD, when varve thicknesses are very low in GOS, varves are no longer preserved in GT and a gap of ~150 varves occurs. The late YD sedimentation rates in GT must have decreased dramatically, because varve interpolation of this section using the surrounding 40 varves underestimated the gap by ~60 years. (3) Due to the shallow water depth of GT, littoral diatoms are deposited even in the Allerød and Preboreal, when they are missing in GOS. (4) Varve thickness is mostly thinner in GT than in GOS, which likely is related to higher bottom steepness in the lake centre and reworking of material from the shallow bay into the deep lake as indicated by recent monitoring in Lake Gościąż (Fojutowski et al. 2021). Additionally, the main water body is larger (e.g. Fig. 2-1) providing more sedimentation sources. (5) Interestingly, the XRF data during the YD transitions display the same pattern in both profiles, but while log(Si/Ti) values shift nearly contemporaneously in both profiles, the log(Ca/Ti) values shift about twice as fast in GT than in GOS. The shifts are completed contemporaneously in both profiles for log(Si/Ti) and log(Ca/Ti), respectively. Independent dating of the composite profile of GT is needed to reliably anchor the floating varve chronologies to the absolute timescale (independently from the GOS profile) enabling the direct and detailed comparison of the shallow- and deep-water environments in Lake Gościąż.

A7. Table of content of data CD

1) Pdf file of the doctoral thesis by Daniela Müller
2) Curriculum Vitae and list of publications by Daniela Müller
3) Data related to chapter 2
4) Data related to chapter 3
5) Data related to chapter 4
6) Data related to chapter 5